



The University of
Nottingham

DEPARTMENT OF CIVIL ENGINEERING

**IMPACT LOAD-INDUCED MICROSTRUCTURAL DAMAGE OF
CONCRETE MADE WITH UNCONVENTIONAL AGGREGATES**

Savaş Erdem

Thesis submitted to the University of Nottingham
for the degree of Doctor of Philosophy

January 2012

Abstract

Understanding the correlation between the mix proportions, micro structural characteristics, and macro-scale properties of concrete (i.e. the process-structure-properties relationship) is fundamental to achieving a more advanced understanding of how to apply and optimise this abundant engineering material. Although, concrete has been traditionally evaluated by its physico-mechanical and functional properties; development of advanced and effective inspection techniques during the last decade has demonstrated that fundamental macro-level properties of concrete depend, to a great extent, on its properties at the micro- and nano levels. This research was intended to make a quantitative assessment of impact load-induced micro-structural damage in concrete and, more particularly, to investigate the influence of ITZ micro- and nano local properties (as influenced by aggregate characteristics) on the impact load-induced cracking behaviour of concrete.

Five different types of concrete mixtures were designed with the same total water cement ratio either by using natural aggregates as reference or by totally replacing the natural coarse aggregate with unconventional aggregates (such as copper slag, blue brick, sintered fly ash and tyre rubber) having significant differences in strength, shape and surface texture, porosity and roughness, and elasticity. A range of advanced techniques including X-ray diffraction, mercury porosimetry, 3D X-ray computed tomography coupled with digital image analysis, laser surface profilometry, 3D nanotech vertical scanning interferometer and scanning electron microscopy fitted with energy-dispersive X-ray spectrometer were used to characterize the aggregates and the concrete micro-structures. Based on the results obtained a possible mechanism for the micro-structural damage in concrete was proposed.

Poorer aggregate characteristics alone could be responsible for a greater ITZ deterioration after loading but the results demonstrated that in fact, the aggregate causes a change in the ITZ conditions and it is these altered ITZ conditions that have a major effect on overall mix behaviour and govern the damaging process of concrete under impact loading. It was also concluded that the presence of a weak and porous ITZ has two opposite effects on the failure process. First, the chemical and porosity heterogeneities within the ITZ can cause fluctuations/disordering in the cracking (fracture) path, resulting in an increase in the tortuosity and corresponding fracture energy dissipation. Second, a weak and porous ITZ transfers less stress from the matrix to the aggregate particles. This leads to a lower compressive strength but increased toughness due to micro crack path lengthening and energy dissipation.

Finally, the effect of the aggregate on the surface area roughness of the ITZ was established for the first time in the concrete literature. The roughness number of the area near the ITZ was found to positively correlate with dissipated surface fracture energy. An increase in the roughness number is associated with an increase in the dissipated fracture energy. The significance of this correlation however, lies in the fact that the rougher near – ITZ fraction of the bulk paste is more resistant to cracking at the macro level.

Findings from this study will lead to a better understanding of the impact load-induced micro-structural damage phenomena. In addition, the micro-structural data from SEM and X-ray CT obtained during impact and mechanical testing of the concrete mixtures could be used to develop a multi-scale finite element model to simulate and predict the behaviour and fracture damage of concrete subjected to dynamic loading.

*Three grand essentials to happiness in this life are
something to do, something to love and something to hope for.*

Joseph Addison



*Why should anyone be afraid of change? What can take place without it?
What can be more pleasing or more suitable to universal nature? Can you
take your bath without the firewood undergoing a change? And can anything
useful be done without change? Don't you see that for you to change is just
the same, and is equally necessary for universal nature?*

Marcus Aurelius

ACKNOWLEDGEMENT

When I started my PhD, I did not really think that there would be many contributors in this project. I can now claim that writing the acknowledgement section of a thesis is much harder than one might think. This research project was completed with the great helps and unconditional supports of many people whom I would like to thank.

First of all, I would like to express my most sincere gratitude to Andrew Dawson and Nick Thom, who were my project supervisors, for their perfect guidance, motivation, supports and offered me this journey to the fascinating world of experimental adventure. I guess they (in particular Andrew) were tired of reading and commenting on the drafts for many times as I am not a native English writer. Probably, I could not write my thesis without their supports. I have learned a lot teaching and writing skills from them. Their breadth of experience, professionalism and integrity as a researcher and an exceptional supervisor will always be a source of inspiration for me. Thank you very much Andrew and Nick for all that you have done for me.

I would like also to express my sincere gratitude to my PhD committee; Professor Marious Soutsos and Assoc. Prof. Matthew Hall. Special thanks to Professor Marious Soutsos who agreed to review this work and come to Nottingham for my examination and Dr. Matthew Hall for his great helps through the correction process. I would also like thank to Prof. Dragos Axinte (Director of University of Nottingham`s Technology Centre) for allowing me to use his research facilities and Dr. Mohammed Bassuoni for the input of helpful discussion and advices.

Thanks to all technical staff of NTEC (Nottingham Transportation Engineering Centre) and Structural & Concrete Laboratory, specifically Mr. Mick Winfield, Mr. Mike Langford, Mrs. Nancy Hodge, Mr. Balbir Loyla and Mr. Nigel Rook for helping me in concrete casting and testing, cutting my samples, and conducting the X-ray CT tests.

I really appreciate the support and company of my colleagues: Marva, Rose, Pejman, Norhidayah, Usama, Mahmoud, Khalid, Mahmoud Mohamed, Ameer, Adam, Alan, Chao, Olu, Xibo, Chen and all the other researchers in NTEC. Marva and Rose! Sorry for all the trouble that I gave you. Sure! You wanted to put me in the quarantine for a quite long time and even to get lost me in the stock of samples☹ I would also like thank to my special friend Ridvan Ata from Sheffield University. Nearly five years ago, we began this journey together from Turkey. I have never ever forgotten the date we arrived in the UK (3rd June 2007). Thank you very much my dear friend.

Special thanks must also go to Dr. Kevin Brown and Dr. Nigel Neate for their valuable helps during the impact tests, and the SEM and XRD analysis. I would like to gratefully acknowledge Ms. Lindy Heath and Ms. Vikki Archibald, Mr. David Clift and Mrs. Ezgi Demir for their great helps and comments during the TGA, EDX and micro-hardness analyses.

My gratitude goes to my family for their patience and encouragement. I cannot thank them enough for their love and support. It is time to go back home!

Finally, I also would like to thank to this lovely country: Charles Dickens-Great Expectations, Pink Floyd- Another Brick in the Wall (Hey teacher! Leave them kids alone), heavy raining and very little sun, fish and chips, tea with milk (I enjoyed so much- I am honest), green hills and long history.

*This thesis is dedicated to “the apples of my eye”
(my mother and my father) who have given me
everything...*

DECLARATION

The work described in this thesis was conducted at the Department of Civil Engineering, University of Nottingham between October 2008 and October 2011. I declare that the work is my own and has not submitted for a degree of another university.

Savas ERDEM

Nottingham

December 2011

Table of Contents

Abstract.....	ii
Acknowledgement	v
Dedication	vii
Table of Contents.....	ix
List of Tables	xii
List of Figures	xiii
Abbreviations and Notations	xx
1 INTRODUCTION	
1.1 Background and Motivation for Research.....	1
1.2 Aim and Objectives.....	4
1.2.1 Scientific novelty	5
1.2.2 Approval of the dissertation results	6
1.3 Research Description	7
References	9
2 MICROSTRUCTURE AND PROPERTIES OF INTERFACIAL ZONE BETWEEN THE CEMENT PASTE-AGGREGATE IN CONCRETE	
11	
2.1 General.....	11
2.2 An Introduction to Concrete Microstructure	12
2.3 The Nature of the ITZ in Concrete.....	14
2.4 The Paste-Aggregate Interfacial Bond.....	16
2.5 Micro-cracking at Paste-Aggregate Interface	17
2.6 Properties of the ITZ.....	18
2.6.1 Porosity and Thickness of the ITZ	18
2.6.2 Micro-hardness of the ITZ	20
2.6.3 Elemental Composition at the ITZ	21
2.7 Relationships between the Properties of the ITZ and the Properties of Concrete	22
2.7.1 Overview.....	22
2.7.2 Relationships between the ITZ and Strength, Cracking and Failure Mechanism	23
2.8 Concluding Remarks	34
References	36
3 IMPACT PHENOMENA IN CONCRETE	
41	
3.1 General.....	41
3.2 Introduction of Impact Phenomena in Concrete.....	42
3.3 Concrete Behaviour under Impact.....	43
3.3.1 Mechanism of Impact Damage.....	43
3.3.2 Failure Mechanism and Cracking Behaviour of Concrete under Impact.....	45
3.4 Analysis of Impact Resistance	56
3.4.1 Damage Mechanics	56
3.4.2 Energy Dissipation	58
3.5 Concluding Remarks	61
References.....	63

4 ASSESSING MECHANICAL BEHAVIOUR OF CONCRETE MIXTURES UNDER STATIC LOADING66

4.1	General.....	66
4.2	Materials, Casting and Concrete Mix Design.....	67
4.2.1	Materials Used	67
4.2.2	Mixture Proportions.....	72
4.2.3	Mixing, Specimen Preparation and Curing	73
4.3	Test Procedures and Apparatus for Aggregate.....	74
4.3.1	X-ray Diffraction Analysis.....	74
4.3.2	Quantification of Aggregate Shape Parameters.....	76
4.3.3	Surface Texture Analysis with Optical Microscope	78
4.3.4	Total Porosity (Mercury Porosimetry) of Aggregates.....	78
4.3.5	Surface Roughness by Contact Surface Profilometer	79
4.3.6	Physico-mechanical Properties of Aggregates.....	79
4.4	Routine Mechanical Tests for Concrete.....	80
4.4.1	Compressive Strength	80
4.4.2	Static Elastic Modulus.....	80
4.4.3	Ultrasonic (Dynamic) Modulus of Elasticity	81
4.4.4	Flexural Response and Fracture Energy.....	81
4.5	Thermogravimetric Analysis Procedure	84
4.6	X-ray Computed Tomography with Digital Image Analysis	87
4.7	Aggregate Properties Results and Discussion	89
4.7.1	Mineralogical Analysis of the Aggregates Used	89
4.7.2	Surface Roughness of the Aggregates Used	89
4.7.3	Physico-mechanical and Geometrical Properties of the Aggregates... ..	90
4.8	Mechanical Concrete Properties Results and Discussion	96
4.8.1	Engineering Properties of Concrete.....	96
4.8.1.1	Thermogravimetric Analysis (Degree of Hydration)	100
4.8.1.2	X-ray CT (Void Content)	103
4.8.2	Flexural Response and Fracture Energy	108
4.9	Concluding Remarks	110
	References	112

5 QUANTITATIVE ASSESSMENTS OF MICROSTRUCTURE OF THE INTERFACIAL TRANSITION ZONE IN CONCRETE MIXTURES116

5.1	General.....	116
5.2	Test Procedures for Characterization of the ITZ.....	117
5.2.1	Scanning Electron Microscopy (SEM)	117
5.2.1.1	Working Principle of the SEM.....	117
5.2.1.2	Sample Preparation	120
5.2.2	Micro-mechanical Properties of the ITZ	120
5.2.2.1	Porosity in ITZ	120
5.2.2.2	Measurement of ITZ Thickness	121
5.2.2.3	Measurement of ITZ Micro-hardness.....	122
5.2.2.4	Elements Analysis in the ITZ	122
5.2.2.5	Measurement of Surface Roughness of ITZ.....	123
5.3	Results and Discussion of the Micro-mechanical Local Properties of the ITZ	124
5.3.1	Surface Roughness of the ITZ.....	124
5.3.2	Chemistry of the Hydrous Phases in the ITZ	128
5.3.3	Thickness and Porosity of the ITZ	132
5.3.4	Interconnectivity of the ITZ.....	137

5.3.5	Micro-hardness of ITZ	138
5.4	Concluding Remarks	141
	References	143
6	DAMAGE ANALYSIS OF THE CONCRETE MIXTURES UNDER IMPACT LOADING	145
6.1	General.....	145
6.2	Equipment Development for Impact Testing	146
6.2.1	Review	146
6.2.2	Initial Apparatus Development in the Present Study.....	149
6.2.3	Rosand Falling Weight Apparatus	152
6.2.3.1	Instrumentation Used.....	155
6.3	Characterization of Fracture Surfaces	157
6.3.1	Fracture Roughness using 3D Non-contact Surface Profilometer	157
6.3.2	Crack Tortuosity and Density.....	159
6.3.3	Fractal Dimension and Dissipated Fracture Energy	160
6.4	Impact Response Test Results and Discussion	161
6.4.1	Results from the Manual Drop-Weight Apparatus.....	162
6.4.2	Results from the Rosand Impact Equipment.....	173
6.5	Concluding Remarks	182
	References.....	184
7	OVERALL DISCUSSION AND EVALUATION: MICRO-MECHANICAL STRUCTURE-PROPERTY RELATIONSHIPS	187
7.1	General.....	187
7.2	Pore Structure Testing Procedure.....	188
7.3	Summary of Material Behaviours	190
7.4	Bridging between the Scales (from Micro to Macro)	195
7.4.1	Micro-hardness- Strength Relationship.....	195
7.4.2	Compressive strength vs. ITZ Porosity	196
7.4.3	ITZ Micro-hardness vs. Impact Load.....	197
7.4.4	ITZ Surface Roughness vs. Dissipated Surface Fracture Energy	199
7.4.5	ITZ Crack Width vs. Coarse Aggregate Type	202
7.4.6	ITZ Thickness vs. Impact Induced Stress Wave Propagation	204
7.4.7	ITZ Surface Roughness vs Surface Crack Tortuosity.....	204
7.4.8	Compressive Strength/Flexural Energy vs. Impact Strength/Impact Energy	205
7.5	Pore Structure Characterisation after Impact	207
7.6	Concluding Remarks	212
	References.....	214
8	CONCLUSIONS AND SUGGESTIONS FOR FUTURE RESEARCH	216
8.1	Introduction	216
8.2	Main conclusions	217
8.3	Suggestions for Future Research	219

APPENDIXES

LIST OF TABLES

Table 3.1: Typical strain rates for various types of loading (CEB, 1988)	43
Table 4.1: Physical and chemical properties of cement	67
Table 4.2: Physico-mechanical properties of fibres.....	72
Table 4.3: Mix proportions for 1 m ³	73
Table 4.4: The physico-mechanical properties of the aggregates used	94
Table 4.5: Engineering properties of the concrete mixtures.....	97
Table 4.6: First crack loads, peak loads and corresponding deflections	110
Table 5.1: Average atomic ratios of analyses in the ITZ of hydrous materials .	129
Table 6.1: The results of drop-weight impact test.....	161
Table 6.2: Micro-crack density of the ITZ	162
Table 6.3: Internal cracking features of the concrete mixtures	169
Table 6.4: Changes in the dynamic modulus of specimens after impact	169
Table 7.1: Relative values of results for all mixes	194
Table 7.2: The calculated percentage of the micro and macro-pores after impact	210

LIST OF FIGURES

Figure 1.1: Impact Damage on Structures a) The World Trade Centre (Buyukozturk and Gunes, 2011) and b) Japan Earthquake and Tsunami 2011 (National Geographic, 2011)	3
Figure 1.2: Flowchart presentation for the research project	8
Figure 2.1: Concrete at different length scales (Mondal, 2008).....	12
Figure 2.2: Basic microscopic view of concrete composition	14
Figure 2.3: The hydration products with porosity (Esping, 2007)	14
Figure 2.4: a-) packing expected without aggregate wall, b-) packing with aggregate wall in place (Scrivener et al., 2004)	16
Figure 2.5: Mechanism at the interfaces between the aggregate and the matrix (Zhang and Gjorv, 1995)	17
Figure 2.6: Basic types of micro-cracks in concrete (Hsu et al., 1963).....	16
Figure 2.7: Porosity profiles in the ITZ (Diamond and Huang, 2001)	18
Figure 2.8: Vickers micro-hardness distribution in concrete containing different types of aggregates (Hussin and Poole, 2011)	19
Figure 2.9: Fracture paths in different concretes (Adapted Newman and Owens, 2003)	24
Figure 2.10: Schematic description of the micro-fracture process in plain concrete (Lofgren, 2005)	25
Figure 2.11: X-ray CT view of improving of the transition zone via internal curing process (Bentz et al., 2006)	27
Figure 2.12: Schematic view of improving of the transition zone via internal curing process (ESCSI, 2006)	28

Figure 2.13: X-ray powder diffraction patterns of the products formed at the ITZ at 1 week (Tasong et al., 1998)	29
Figure 2.14: Individual stress-strain response of cement paste, aggregate and concrete (Scrivener et al., 2004)	30
Figure 2.15: ITZ crack density as a function of w/c and stress level for three types of concretes: low, medium and high strength mortars (Akcaoglu et al., 2005).....	32
Figure 2.16: σ_{xx} distribution for $\dot{\epsilon} = 4/s$ (Zhou and Hao, 2008)	34
Figure 3.1: Back face spalling and shock wave propagation (Millard et al, 2010)	44
Figure 3.2: Fracture region in concrete subjected to impact (Zhang et al., 2005).....	45
Figure 3.3: Some toughening mechanism in plain concrete (Shah et al., 1995)	46
Figure 3.4: Differences between static and impact fracture (Zhang, 2008).....	47
Figure 3.5: Crack pattern of both normal and RAC beams a) and b) normal concrete, c) RAC with 25 %, d) RAC with 50 %, e) and f) RAC with 100 % RCA (Rao et al., 2011).....	50
Figure 3.6: SEM micrograph of the CSRC (Wu et al., 2010)	51
Figure 3.7: Dynamic compressive stress-strain relationships of a) control concrete and b) 100 % copper slag concrete (Wu et al., 2010)	52
Figure 3.8: SEM for normal strength concrete: a) no imposed damaging effect, b) after impact damaging effect (Soroushian and Elzafraney, 2005).....	53
Figure 3.9: SEM for high-strength concrete: a) no imposed damaging effect, b) after impact damaging effect. White indicates cracks (Soroushian and Elzafraney, 2005)	53
Figure 3.10: Schematic description of the effect of fibres on the fracture process in concrete (Lofrigen, 2005)	54
Figure 3.11: Failure modes of plain and fibre-reinforced lightweight concrete (Swamy and Jojagha, 1982).....	55

Figure 3.12: Load vs. deformation curves of a fibre-reinforced mix under static and impact loading (Zhang, 2008)	57
Figure 3.13: Air void distribution along the depth of specimen (Ying, 2010)	58
Figure 3.14: 3D air void distribution along the specimen depthh (Ying, 2010) ...	58
Figure 3.15: Fracture process zone in concrete (Shah et al., 1995)	59
Figure 4.1: Grading curve of the fine aggregate	68
Figure 4.2: Grading curve of the coarse aggregate	68
Figure 4.3: Photograph of the aggregates used	72
Figure 4.4: Steel fibres (a) and synthetic fibres (b) used for concrete reinforcement	75
Figure 4.5: Schematic view of image analyzer set up (Adapted from Kwan et al., 1999)	77
Figure 4.6: Measurement in Image Pro Plus Version 4.5	78
Figure 4.7: Surface profilometer for aggregate roughness (Tasong et al., 1998)	79
Figure 4.8: Elastic modulus test set up	81
Figure 4.9: Instrumentation of the concrete beam used for the four-point bending test	83
Figure 4.10: Definition of flexural toughness indices (ASTM C 1018-1989)	84
Figure 4.11: Photograph of thermogravimetric analyzer	86
Figure 4.12: Typical TGA and DTG curves (Loukili et al., 1999)	86
Figure 4.13: Three major stages of image analysis technique (Masad et al., 1999)	88
Figure 4.14: X-ray CT system at NTEC, University of Nottingham	89
Figure 4.15: XRD patterns of the aggregates used	91
Figure 4.16: Typical surface roughness profiles of the aggregates	93
Figure 4.17: Surface texture views of the aggregates via optical microscope	95

Figure 4.18: Cumulative intrusion vs. Pore diameter curves of the fly ash-Lytag and gravel aggregates	96
Figure 4.19: DTA/TGA curves of the mixes.....	101
Figure 4.20: Images of lightweight concrete a) original X-ray b) pseudo colour transformation	105
Figure 4.21: Images of brick concrete a) original X-ray b) pseudo colour transformation	106
Figure 4.22: Air void distribution of the mixtures (a) and 3D air void simulation (b)	107
Figure 4.23: Flexural load-deformation curves of the mixtures.....	109
Figure 5.1: Interaction between the beam and sample (Adapted from Fens, 2000)	118
Figure 5.2: Schematic view of the interaction volume and the regions of the various signals	119
Figure 5.3: Illustrations of the variation in the interaction volume shape, E: electron beam accelerating voltage and Z: the average specimen atomic number (Hemavibool, 2007)	119
Figure 5.4: Thresholding criteria for the segmentation of the constituents in concrete, DIP:dense inner hydration products; Anh: unhydrated cement paste (Hemavibool, 2007)	122
Figure 5.5: Nanotech vertical scanning interferometer	123
Figure 5.6: Surface roughness profile of the ITZ in the gravel mixture and example of camera view of the area.....	125
Figure 5.7: Surface roughness profiles of the paste matrix in the copper slag mixtures with mesh application and different views of angles.....	126
Figure 5.8: Surface roughness profile of the ITZ paste matrix of the blue brick (a) and rubberised mix.....	127

Figure 5.9: Surface roughness profile of the ITZ of the lightweight mixture.....	128
Figure 5.10: Energy dispersive spectroscopy analysis in the ITZ.....	130
Figure 5.11: EDX spectrums of the ITZ of some mixtures.....	130
Figure 5.12: Internal structure of the lightweight (a) and the rubberised mix (b)	131
Figure 5.13: SEM micrographs of the pastes surrounding the aggregates	133
Figure 5.14: Interfacial porosity profiles of the mixes as a function of the distance from the aggregate surface.....	133
Figure 5.15: Close-up views of the ITZs of some of the mixtures.....	134
Figure 5.16: EDX spectrum analysis of the fly ash/Lytag aggregate	136
Figure 5.17: Results of continuum models used to determine interfacial zone percolation in mortars with varying sand contents and ITZ thickness (Synder et al., 1992)	137
Figure 5.18: Connectivity of the ITZ zone a) initial stage and b) connectivity of solid phases (Ye, 2003)	138
Figure 5.19: Micro-hardness values of the ITZs of the concrete mixes.....	139
Figure 5.20: Normalized hardness values of the copper slag and gravel aggregate mixes	140
Figure 5.21: Schematic description of the process for the reduction due to restrain of the stress field (a) and reduction due to physical interaction of the penetrating indenter and the rigid inclusion (Igarashi et al., 1996)	140
Figure 6.1: The drop-weight impact test set up (Adapted from Banthia et al., 1987)	147
Figure 6.2: Split Hopkinson Pressure Bar Test Apparatus (Minging, 2010).....	148
Figure 6.3: The falling mass for the test set up	150
Figure 6.4: Support connection for the drop weight test set up	150
Figure 6.5: Schematic view of the impact test set up developed by the author	152

Figure 6.6: Schematic of Rosand Instrumented Falling Weight Drop Tower (Adapted from Brown, 2007)	154
Figure 6.7: Photograph of drop tower impact machine	156
Figure 6.8: Talysurf CLI 1000 Laser Profilometer.....	158
Figure 6.9: Texture profile and different roughness regimes (Tasong et al.,1998)	158
Figure 6.10: Digitized actual crack profile (a) and schematic of crack profile (b) (Akhavan et al., 2011)	159
Figure 6.11: The box-counting method (Chiaia et al., 1997)	160
Figure 6.12: Debonded interfaces after impact	164
Figure 6.13: Micro-roughness profiles of the concrete mixes.....	165
Figure 6.14: Digitized crack maps and fractal fracture energy of the lightweight concrete.....	167
Figure 6.15: Digitized crack maps and fractal fracture energy of the gravel concrete	168
Figure 6.16: Polar diagrams for the changes in air void distribution across the depth of the concrete mixes	171
Figure 6.17: Reaction force-time curves of all specimens at the first drop of impact	175
Figure 6.18: Broken surfaces of the specimens after impact	175
Figure 6.19: Ettringite deposition in air void.....	176
Figure 6.20: Reaction force-deformation curves of the specimens at the first drop of impact.....	178
Figure 6.21: Images of the impacted blue brick concrete a)original and b) pseudo colour transformation.....	180
Figure 6.22: Reaction force-displacement curves of the specimens	181
Figure 6.23: Failure pattern of the specimens after impact.....	182

Figure 7.1: Micromeritics Autopore IV Mercury Porosimetry	189
Figure 7.2: Schematic illustration of mercury intrusion and extrusion (Ye, 2003)	190
Figure 7.3: Schematic representation of pore connectivity in matrix under loading	193
Figure 7.4: Relationships between the ITZ micro-hardness and concrete compressive strength	195
Figure 7.5: Relationships between the ITZ porosity and concrete compressive strength	196
Figure 7.6: The micro-hardness before and after first drop of impact (a) and the peak force load at first cycle of impact (b).....	198
Figure 7.7: An example of the digitized crack path of the surfaces of the concrete mixtures a) gravel, b) blue brick c) lightweight, d) copper slag and e) rubberised mix.	200
Figure 7.8: Relationship between the ITZ roughness and dissipated surface fracture energy	201
Figure 7.9: Fracture propagation with a single aggregate: black lines show contact forces (Katsaga, 2010)	201
Figure 7.10: Measured ITZ crack widths	202
Figure 7.11: Pre-loading cracks in the rubberised mix.....	203
Figure 7.12: Relationships between the ITZ thickness and the time for stress wave propagation	204
Figure 7.13: Relationship between the ITZ roughness and surface crack tortuosity	205
Figure 7.14: Relationship between the compressive and impact strength.....	206
Figure 7.15: Relationship between the flexural toughness and impact energy.	207
Figure 7.16: Cumulative intrusion volume vs. pore diameter curves after impact	209

Figure 7.17: Low resolution image of air voids (a) and high-resolution images of air void showing connectivity in air-void layer	211
---	-----

LIST OF ABBREVIATIONS AND NOTATIONS

ACI	American Concrete Institute
AFm	Monosulphate
AFt	Ettringite
BSE	Back Scattered Electron
BS EN	British European Standard
CEB	European Committee for Concrete
CH	Calcium Hydroxide
C-S-H	Calcium Silicate Hydrate
CSRC	Copper Slag Reinforced Concrete
CT	Computed Tomography
DIP	Digital Image Processing
DTG	Differential Thermogravimetric
EDX	Energy Dispersive X-ray
FRC	Fibre-reinforced Concrete
HV	Hardness Value
ITZ	Interfacial Transition Zone
MIP	Mercury Intrusion Porosimetry
RAC	Recycled Aggregate Concrete
RCA	Recycled Concrete Aggregate
SEM	Scanning Electron Microscopy
TGA	Thermogravimetric Analysis
UH	Unhydrated Cement
XRD	X-ray Diffraction
a	Euclidean length
A	Initial area of undamaged section
\bar{A}	Effective cross sectional area in the damaged state

d	Distance between lattice planes in the crystal
dp	Mercury intruded pore diameter
D_{d-1}	Fractal dimension of surface cracks
E	Impact energy
Ea	Modulus of elasticity of aggregate
E₁	Potential energy before impact
E₂	Kinetic energy during impact
ΔE	Energy change
g	Earth`s gravitational acceleration
G_f	Fracture energy
h	Drop height
L	Length of projected profile
L_e	Effective length
m	Impactor mass
MW_{CH}	Molecular weight of Portlandite
MW_H	Molecular weight of water
n	Integer
n*	Integer
N	Number of blows
P	Contact force
P_{In}	Intrusion pressure
Ra	Micro-roughness
X_{max}	Entire nominal length
V_I	Impact speed
Ws	Dissipated total energy
WL_{CH}	Weight loss occurring during CH dehydration
Z	Reference length
z(x)	Central-line profile

γ	Surface tension of mercury
θ	Contact angle between mercury and solid
θ^*	Incident/diffracted angle
ρ_a	Density of aggregate
δ	Deflection at first crack
λ	Segment length
λ^*	Wavelength of scattered wave
τ	Tortuosity

CHAPTER 1

INTRODUCTION

1.1 Background and Motivation for Research

“Concrete is one of the most basic building blocks of modern life that most people take for granted”

(Prof Adam Neville, 1963)

There is absolutely no doubt that the Ancient Egyptians, Romans or Chinese would be jealous of the options we have these days to build their fabulous Pyramid, Coliseum or Great Wall. Unfortunately, they used a combination of mud, straw, gypsum and the other minerals to bind their stones together. However, with the invention of Portland cement in 1824, a new construction material that is the foundation of modern life regardless of if we live in Kyoto, Mumbai, Rome or Las Vegas, had been born ([Lane, 2011](#)). It is estimated that the present consumption of concrete in the world is more than 11 billion metric tonnes every year. Its success stems from the fact that it is comparatively cheap and made of widely available raw materials, highly versatile and functional, and possesses excellent resistance to water ([Mehta and Monterio, 2006](#)).

The new millennium brings new challenges to the concrete industry. In addition to economic pressures, there is a rapidly growing public concern that we can no longer continue to ignore the issues of environmental pollution problems on the one hand, and the unrestricted depletion of natural resources on the other. As a major consumer of limited natural resources and the most important player in infrastructural development, the concrete industry has an obligation to incorporate environment-friendly technologies ([Mehta, 1999](#)). According to one estimate, the concrete industry in the UK consumed approximately 160 million tonnes of natural aggregates in 2005. In volume terms, this quantity would be enough to fill the bowl of Wembley Stadium up to the roof more than 70 times ([British Geological Survey Report, 2008](#)).

One approach to contribute sustainable construction is to partially or totally replace natural aggregates with recycled and secondary (industrial by-products) aggregates. The figures in 2009 obtained from [European Topic Centre on Sustainable Consumption and Production](#) demonstrate that 850 million tonnes of construction and demolition (C&D) waste arise per year, and 74 % of this C&D waste was land filled. Similarly, statistics ([ECOBA, 2008](#)) showed that about 64 million tonnes of ash in Europe were generated in 2004, and only 22 million of this production was utilized by the construction industry. However, new European regulations prohibit the storage of such wastes in landfill sites ([Muller and Rubner, 2006](#)). As such, there is an urgent need to recycle and reuse these wastes. The utilization of some waste materials in structural concrete seems to be very attractive idea from an economic and environmental sustainability point of views. However, our knowledge about how concrete made with these materials bears loads- particularly under short duration dynamic loads- in laboratory conditions, which in turn assist us to predict how it will behave in real life, is still very limited.

There are two very important events in our recent history that we cannot easily forget. First, the terrorist attacks that took place in the September 11, 2001 in New York City resulted in thousands of lives lost and the collapse of the twin towers of the World Trade Centre (Fig.1.1a). Second, the 8.9 magnitude mega earthquake accompanied by a devastating tsunami that swept away cars, ships and even some buildings, in Japan on March 11, 2011 - marked as black Friday in Japan`s history (Fig.1.1b). These two tragedies have not only caused disquiet across the world, but have also demonstrated the importance of understanding the design of concrete members to withstand impact loads. Civil engineers today face new challenges, including a better understanding of the behaviour of concrete materials under such dynamic loads, and development of new methods to enhance these materials.



Fig.1.1: Impact Damage on Structures a) The World Trade Centre ([Büyükoztürk and Güneş, 2011](#)) and b-) Japan Earthquake and Tsunami ([National Geographic, 2011](#))

Development of advanced and effective inspection techniques during the last decade has demonstrated that the atomic level (nano and micro) properties of concrete have a profound effect upon its macro-level properties, and these structure-property relationships lie at the heart of research in modern concrete technology. The role of mortar-aggregate interfaces, also called the Interfacial Transition Zone (ITZ), is generally accepted as a key factor on the behaviour of concrete under loading. The failure process in concrete is usually initiated when micro-cracks form at the aggregate- mortar matrix interface and propagate through the surrounding matrix with increased localized stress and strain ([Akçaoğlu et al., 2005](#)). The structure of the ITZ is mainly influenced by the properties of coarse aggregate, and the interfacial bond strength forms as a result of some combination of chemical bonding, physical bonding and mechanical interlocking between the cement paste and the aggregate ([Zhang and Gjørv, 1990](#)). Researchers have explored the damage in concrete to some extent but accurate prediction of concrete performance is still difficult due to complex material nature. For this reason, an advanced understanding of the aggregate-cementitious matrix interfaces from the viewpoint of aggregate properties is very important to determine the actual damage mechanism under loading and hence to provide a basis for enhancing the performance.

1.2 Aim and Objectives

The overall aim of this research project is to further understanding of the performance of concrete made with “unconventional” aggregates (such as copper slag, blue brick, sintered lightweight fly ash and rubber) subjected to high strain-rate impact loading. The idea is not so much to make better concrete, but to try to understand better how cracks propagate through the aggregate, the mortar matrix or the interface between the two, and more importantly, to investigate the changes in the impact behaviour and mechanical performance of concrete

associated with the changes in the micromechanical properties of the ITZ as influenced by the characteristics of the coarse aggregate.

The specific objectives of this research are as follows:

1. Develop specialist research methods to examine the influence of local properties of the ITZ on the impact behaviour and mechanical response (strength, stiffness and fracture energy) of concrete containing different types of aggregates when the concrete is subjected to impact loading.
2. Investigate the progression of impact-induced damage through concrete using a range of advance techniques.
3. Quantify the damage at a microscopic scale, and relate it to changes in macro-structural properties such as impact resistance and static strength.

1.2.1 Scientific novelty

Research conducted prior to this thesis is still too limited to answer the question of how changes in the micro- and nano level properties of the ITZ and of the aggregate-mortar interface itself affect overall concrete behaviour. Moreover, to the author's best knowledge, there has been no study to evaluate the influence of the local properties of the ITZ on concrete behaviour under impact loading. An attempt was therefore made to investigate the changes in the impact behaviour and mechanical performance of concrete associated with changes in the micromechanical properties of the ITZ that resulted from the influence of the characteristics of coarse aggregate. The merit of this research is to provide a quantitative micro-structural analysis from which it may be possible, in the future, to establish a numerical model for the fracture process or to correlate the microstructure of concrete with its mechanical properties.

1.2.2 Approval of the dissertation results

Four research papers on the topic of the dissertation have been published by the most prestigious journals in civil engineering. The work presented in this doctoral thesis is mainly based on the work contained in these papers. The following is a list of the papers:

- S. Erdem, A.R. Dawson, N.H. Thom, “Impact load-induced micro-structural damage and microstructure associated mechanical response of concrete made with different surface roughness and porosity aggregates” [Published](#). [Cement and Concrete Research](#).
- S. Erdem, A.R. Dawson, N.H. Thom, “Influence of the Micro- and Nano-scale Local Mechanical Properties of the Interfacial Transition Zone on Impact Behaviour of Concrete made with different aggregates” [Published](#). [Cement and Concrete Research](#).
- S. Erdem, A.R. Dawson, N.H. Thom, “Micromechanical Structure-Property Relationships for the Damage Analysis of Impact Loaded Sustainable Concrete”. [Published](#). [American Society of Civil Engineering-Journal of Materials in Civil Engineering](#).
- S. Erdem, A.R. Dawson, N.H. Thom, “Microstructure-linked Strength properties and Impact Response of Conventional and Recycled Concrete Reinforced with Steel and Synthetic Macro Fibres” [Published](#). [Construction and Building Materials](#).

During the course of this work, one conference paper entitled “Comparative study on the rheological and durability characteristics of conventional and glass-enriched self compacting concrete” has been also published and presented on 6th International Structural Engineering and Construction Conference, June 21-26 2011, Zurich-Switzerland.

1.3 Research Description

Chapter 1 has provided the general background and problem definition of this work. The objectives and research approaches are also presented.

Chapter 2 reviews pertinent literature on the microstructure and properties of the ITZ and its influence on macro-level concrete properties. In addition, it is also highlighted that how conventional and unconventional aggregates affect the cracks and cracking scenarios in concrete. Since this understanding forms an important background in conducting this research project.

Chapter 3 covers a comprehensive literature review related to the behaviour and micro-analysis of concrete under impact loading.

Chapter 4 first introduces the details of experimental programme, mix proportions, specimen preparation and test methods. Then, it presents the results of physico-mechanical and mineralogical characterization of the aggregates, and mechanical and fracture performance of the concrete mixtures under static loading.

Chapter 5 describes test procedures for quantifying the structure and mechanical properties of the ITZ. Following that, the results of micro-structural characteristics of the transition zone are presented and discussed in this chapter.

Chapter 6 begins with an overview of the types of equipment that are available for impact testing and then describes in detail the apparatus used or developed in the project. Finally, it gives the details of the results of the impact responses and the crack patterns and failure modes of the concrete mixtures under impact loading.

Chapter 7 provides, based on the findings of this work, a technical discussion on the micromechanical structure-property relationships of concrete under impact loading.

Chapter 8 summarizes the major conclusions of the work and makes recommendations for the future research.

A flowchart (Fig. 1.2) describes the way in which the various strands of this research project interact and contribute to meet the final aim.

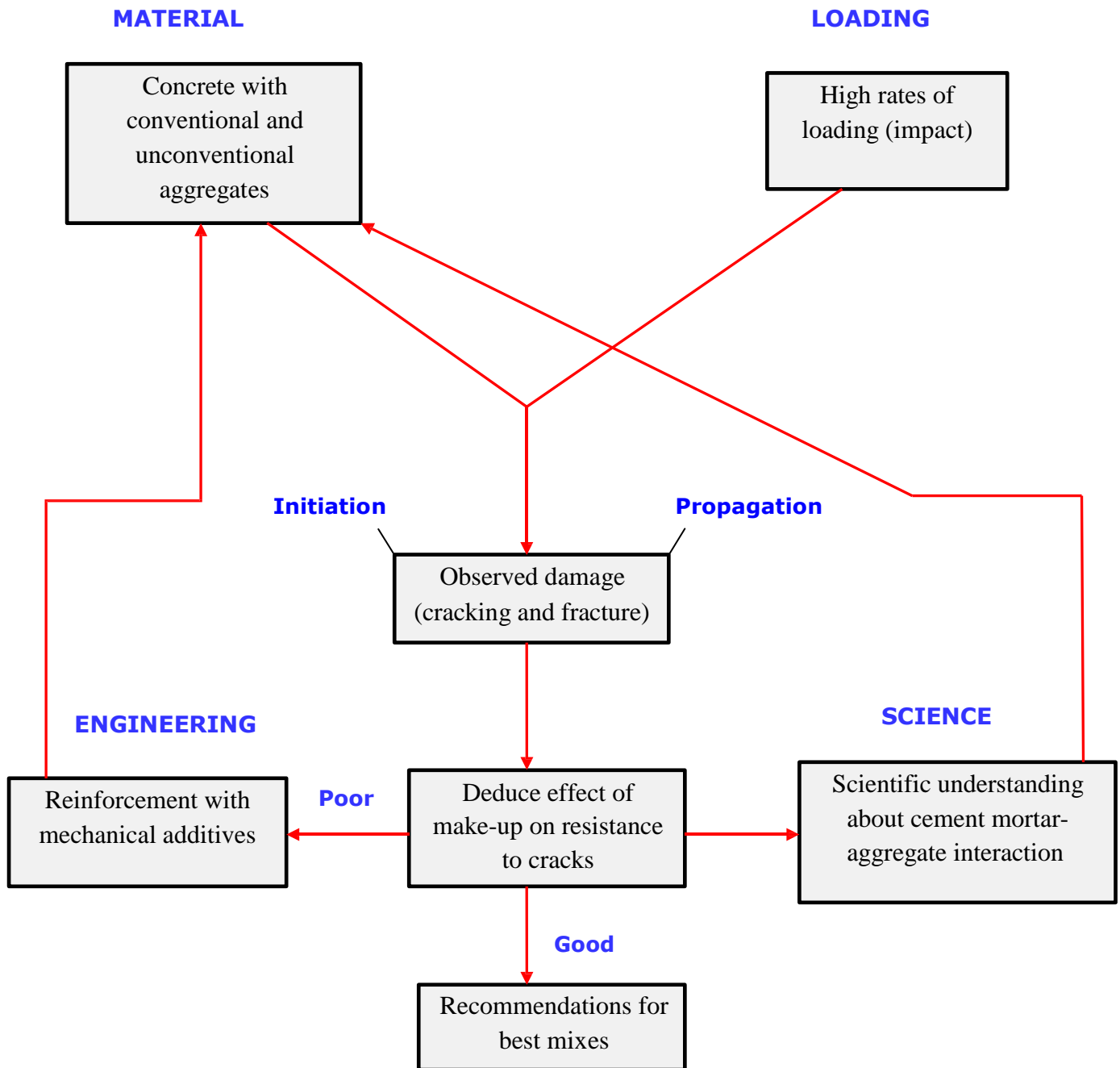


Fig.1.2: Flowchart presentation for the research project

References:

- [1] Akçaoğlu T., Tokyay, M., and Çelik, T., (2005). “Assessing the ITZ micro-cracking via scanning electron microscope and its effect on the failure behaviour of concrete”. Cement and Concrete Research 35 (2) 358-363.
- [2] British Geological Survey Report (2008) “The need for indigenous aggregates production in England”. http://nora.nerc.ac.uk/3711/1/Aggregates_-_Final_Report_June_2008.pdf.
- [3] Büyükoztürk, O., and Güneş, M., (2011) “The Collapse of Twin Towers: Causes and Effects”. Keynote Lecture, EFCA 2004 Conference and GAM. Istanbul-Turkey.
- [4] ECOBA (2009). Fly ash utilization in concrete. <http://www.ecoba.com/ecobaccpexs.html>.
- [5] European Topic Centre on Sustainable Consumption and Production working paper (2009) “EU as a Recycling Society-Present recycling levels of Municipal Waste and Construction and Demolition Waste in the EU”, <http://scp.eionet.europa.eu/publications>.
- [6] Lane, A., (2011). “From Rome to Las Vegas: Concrete is Everywhere”. <http://ezinearticles.com/?Concrete-is-Everywhere&id=1367080>.
- [7] Mehta, P.K., (1999). “Concrete Technology for Sustainable Development-An Overview of Essential Principles”. CANMET/ACI International Symposium on Concrete Technology for Sustainable Development.
- [8] Mehta, P.K., and Monterio P.J.K., (2006). “Concrete: Microstructure, Properties and Materials”. McGraw-Hill, Third Edition, New York.
- [9] Müller, U., and Rübner, K., (2006). “The micro-structure of concrete made with municipal waste incinerator bottom ash as an aggregate component”. Cement and Concrete Research 36 (8): 1434-43.
- [10] National Geographic (2011). “Japan Tsunami 20 unforgettable pictures.” <http://news.nationalgeographic.com/news/2011/03/pictures/110315-nuclear-reactor-japan-tsunami-earthquake-world-photos-meltdown/>.

[11] Zhang, M.H., and Gjrv O.E., (1990). "Microstructure of the interfacial zone between lightweight aggregate and cement paste". Cement and Concrete Research 20 (4): 610-618.

CHAPTER 2

MICROSTRUCTURE AND PROPERTIES OF INTERFACIAL ZONE BETWEEN THE CEMENT PASTE-AGGREGATE IN CONCRETE

2.1 General:

This chapter covers specific areas that either contribute or are involved in the basic understanding of the properties and performance of concrete that relate to its microstructure. The first section will begin by outlining a brief introduction of concrete microstructure in general. Following that, interfaces between different phases in a concrete system will be described, focusing on the interface between hardened Portland cement paste and aggregate. The next section will deal with the micro- and nano scale local mechanical properties of the paste aggregate interfaces and the influence of coarse aggregate characteristics on this structure (physical and chemical interactions between aggregate and paste matrix). Finally, microstructure-property relationships are discussed with respect to their influence on the strength, micro-crack initiation and propagation, and damage mechanism of concrete.

2.2 An introduction to concrete microstructure

Concrete is a `non-homogeneous` material at all length scale, as shown in Fig. 2.1, and has been generally regarded as a multiphase composite made of three phases at microscopic level: coarse aggregate, mortar and an interfacial transition zone (ITZ) between the aggregate and the mortar matrix (Fig. 2.2).

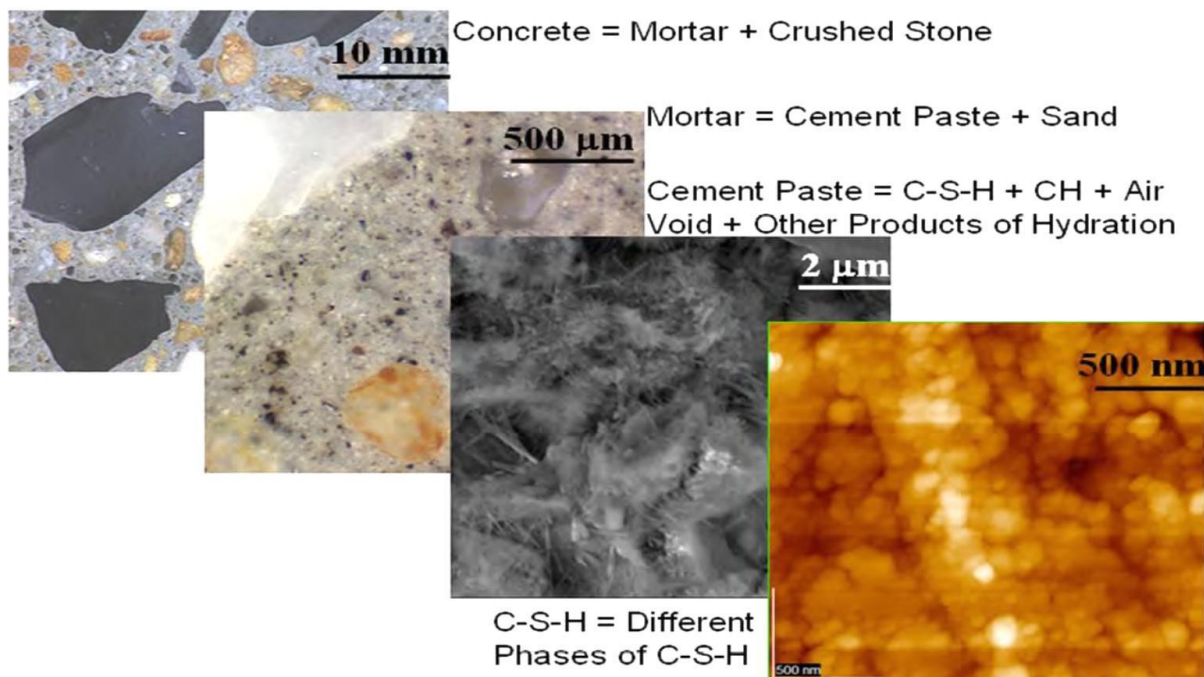


Fig.2.1: Concrete at different length scales [Mondal, 2008]

Mortar is `again` a composite mixture of sand, cement paste and an ITZ in between. Cement powder, when dispersed in water, undergoes a set of reactions to produce hydration products which in time form a firm and hard `heterogeneous` structure in nature. The main phases present in hydrated cement paste (hcp) can be listed as: calcium silicate hydrates (CSH), calcium hydroxide (CH), ettringite, monosulfate, unhydrated cement grains and pores [Mondal, 2008]. The products associated with the stages of cement hydration and the change of porosity and permeability are presented in Fig.2.3. As the hydration proceeds, capillary pores are gradually emptied and the hydration products progressively fill the void spaces in

the paste matrix. As the pores will be smaller, the total volume of pores (porosity) will decrease, which, in turn, leads to decreased permeability and to increased strength and durability of the paste ([Esping, 2007](#)).

Each of the phases in the structure of concrete may have heterogeneity in its composition, which makes predictions of concrete behaviour from its microstructure more challenging than predictions of other materials ([Kurtis, 2007](#)). Development of advanced and effective inspection techniques during the last decade has demonstrated that the atomic level (nano and micro) properties of concrete have a profound effect upon its macro-level properties, and these structure-property relationships lie at the heart of modern concrete technology. Understanding structure-property relationships of concrete under different loading states is an essential yet challenging task for the concrete technologist.

Although modern concrete actually contains a number of different interfaces including those between the cement paste and unhydrated or partially hydrated cement grains; between the cement paste and steel reinforcement or between the coarse aggregate and cement paste ([Mindess, 1996](#)), the last of those is probably the most critical for the overall performance of concrete ([Giaccio and Zerbino, 1998](#)) which is why the work in this thesis has focussed on these interfaces.

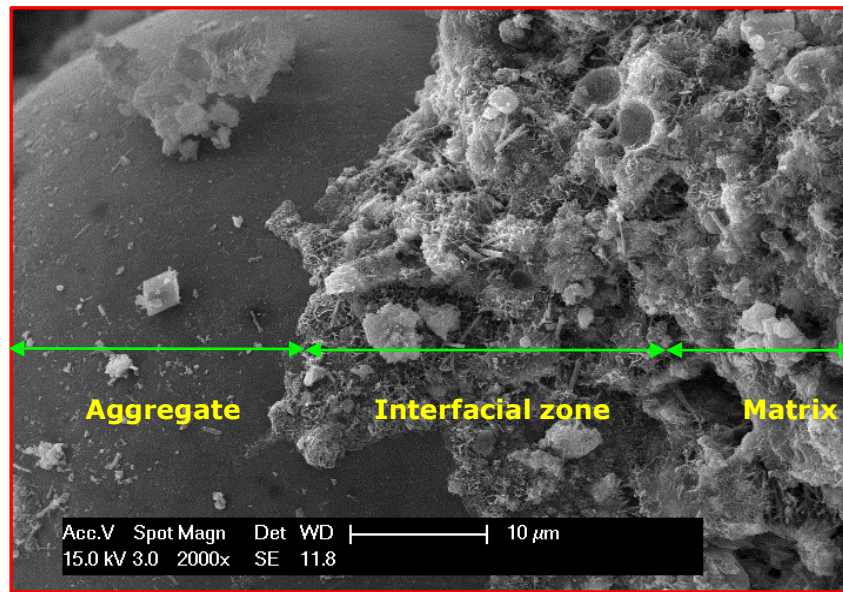


Fig.2.2: Basic microscopic view of concrete components

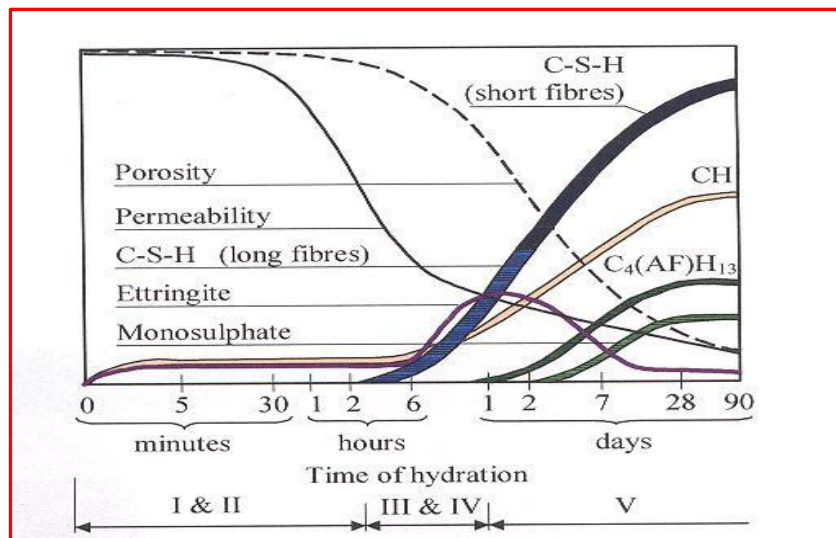


Fig.2.3: The hydration products with porosity (Esping, 2007)

2.3 The Nature of the ITZ in Concrete

During mixing, compaction and placement of concrete, the interaction of the aggregate particles with the paste matrix causes a difference of microstructure and properties of the hydrated cement paste adjacent to the coarse aggregate particles (Larbi, 1991). It has been generally established that the origin of the ITZ lies in:

- “A wall effect” sourced by the aggregate particles. The aggregates appear locally flat to the cement grains due to their several orders of magnitude larger sizes compared to cement grains and do not effectively allow the proper packing of the cement grains leading to smaller grains in the zone close the aggregate, as schematically shown in Fig.2.4 ([Scrivener et al. 2004](#)).
- “A local increase in water cement ratio” in the vicinity of coarse aggregates as a result of upward displacement of mix water, known as micro-bleeding ([Bentur and Odler, 1996](#)). In this case the water can accumulate beneath the aggregate particles leading to a local weakness at the interface and easily prone to micro-cracking.

As a result of these effects, the ITZ is structurally inferior and locally composed of a duplex film, formed by CH (calcium hydroxide) crystals and C-S-H gels about 0.5 μm thick at the surface of the coarse aggregate. Further away from the aggregate, there is the main interfacial zone about 50 μm thick, containing the hydration products with larger crystals of Portlandite without any unhydrated cement. The presence of large crystals of portlandite signifies that the porosity at the ITZ is much higher than elsewhere while the complete hydration of cement signifies that the w/c ratio at the ITZ is higher than elsewhere ([Neville, 1995](#)).

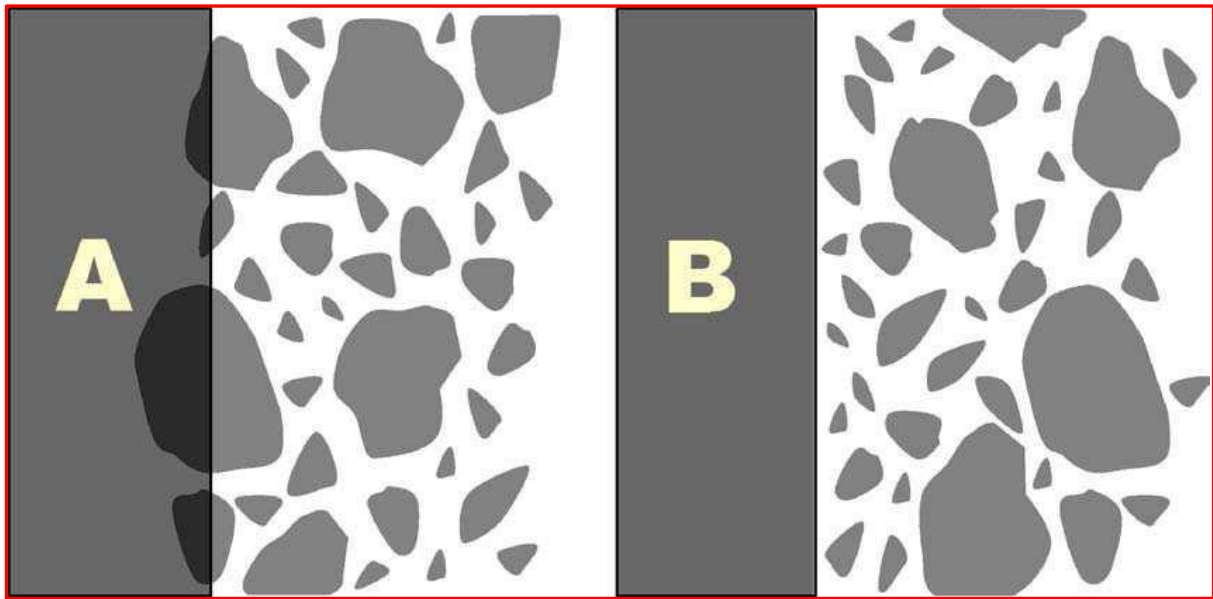


Fig. 2.4: a) packing expected without aggregate wall, b) packing with aggregate wall in place
([Scrivener et al. 2004](#))

2.4 The Paste-Aggregate Interfacial Bond

Cohesive forces generated at the interfaces are one of the main mechanisms that results in bonding in the concrete composite. In this way, interfaces contribute to transferring of stresses depending on the degree of the bond formed. [Zhang and Gjrv \(1995\)](#) reported that three types of potential mechanisms may be observed at the interface for the transfer of forces, as shown in Fig.2.5.

- **Physical interaction:** For well-polished aggregates and no chemical interaction with the cement paste, negligible bond strength may develop in the system. The ITZ is the weakest link in the system (Fig.2.5a)
- **Physico-chemical interaction:** For rock based aggregates (i.e. limestone, dolomite) which have a chemical interaction with the matrix, a strong chemical bond between the cement paste and the aggregate may be observed (Fig.2.5b).

- **Mechanical interlocking:** In the case of porous aggregates or aggregates with a rough surface (i.e. lightweight aggregates), cement hydration products may penetrate into pores on the aggregate surfaces leading to an increase of interfacial density and an improved mechanical interlocking (Fig.2.5c).

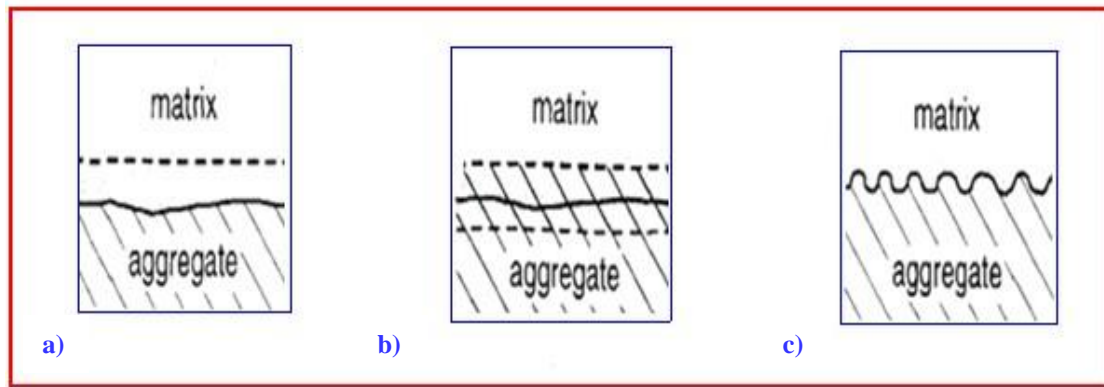


Fig.2.5: Mechanism at the interfaces between the aggregate and the matrix

(Zhang and Gjrv, 1995)

2.5 Micro-cracking at Paste-Aggregate Interface

Hsu and his colleagues (1963) from Cornell University pioneered the study of the internal micro-cracking of concrete and, they made significant contribution to our current knowledge on the topic. They fundamentally divided internal micro-cracks into three categories depending on their locations: bond cracks, mortar cracks, and aggregate cracks as shown in Fig.2.6.

Bond Cracks: Bond cracks are cracks which are present at the interface between the coarse aggregate and mortar matrix.

Mortar Cracks: Mortar cracks are micro-cracks within the mortar matrix.

Aggregate Cracks: Aggregate cracks refer to cracks through the aggregate.

Under load, Carrasquillo et al. (1981) categorized cracks into two types, namely simple (or isolated) and combined (or connected) cracks. The simple cracks are a single crack which consists of bond or mortar cracks but are not connected to any other cracks. The combined cracks, on other hand, refer to a combination of bond and mortar cracks that means two or more cracks connect to each other. These authors also made one further sub-division for the combined cracks, which are Type 1 and Type 2. A Type 1 combined crack encompasses a combination of one bond crack and one mortar crack, which is uncommon, or the connection of two bond cracks with a mortar crack, which is common. A Type 2 combined crack contains a combination of at least two bond cracks and two mortar cracks.

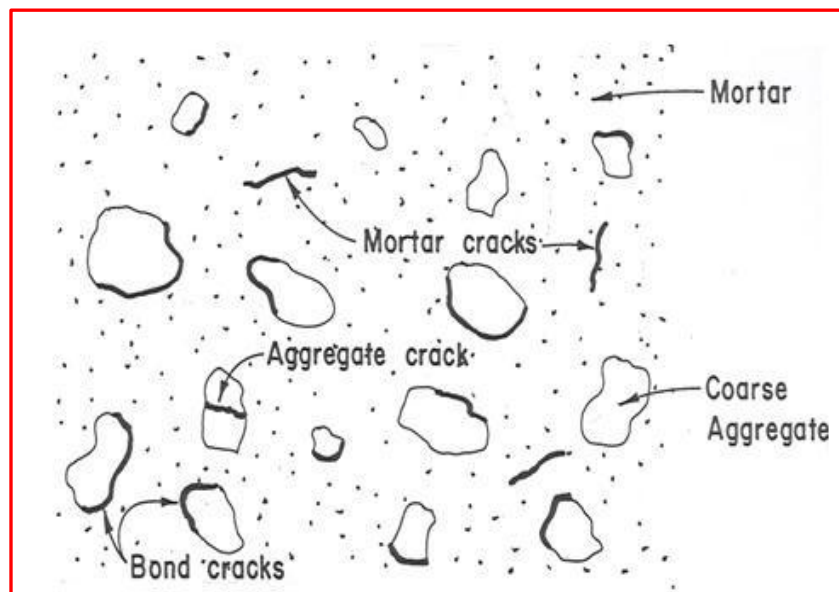


Fig.2.6: Basic Types of Micro-cracks in Concrete (Hsu et al., 1963)

2.6 Properties of the ITZ

2.6.1 Porosity and Thickness of the ITZ

Considering much coarser pores, and easily cleavable and highly soluble CH crystals-as mentioned before- it would be logical to expect a much higher porosity at the ITZ than in the bulk cement paste. The quantification of the porosity in the ITZ can be quantitatively

performed using image analysis of flat polished surfaces observed by scanning electron microscopy (SEM). The technique was first developed by [Scrivener and Pratt \(1988\)](#). An example of data obtained by this technique has been presented in Fig. 2.7. The general consensus for the porosity in the ITZ is that the porosity is highest at the interface and it decreases with the distance from the aggregate surface, as confirmed in Fig.2.7. This also supports the wall effect hypothesis.

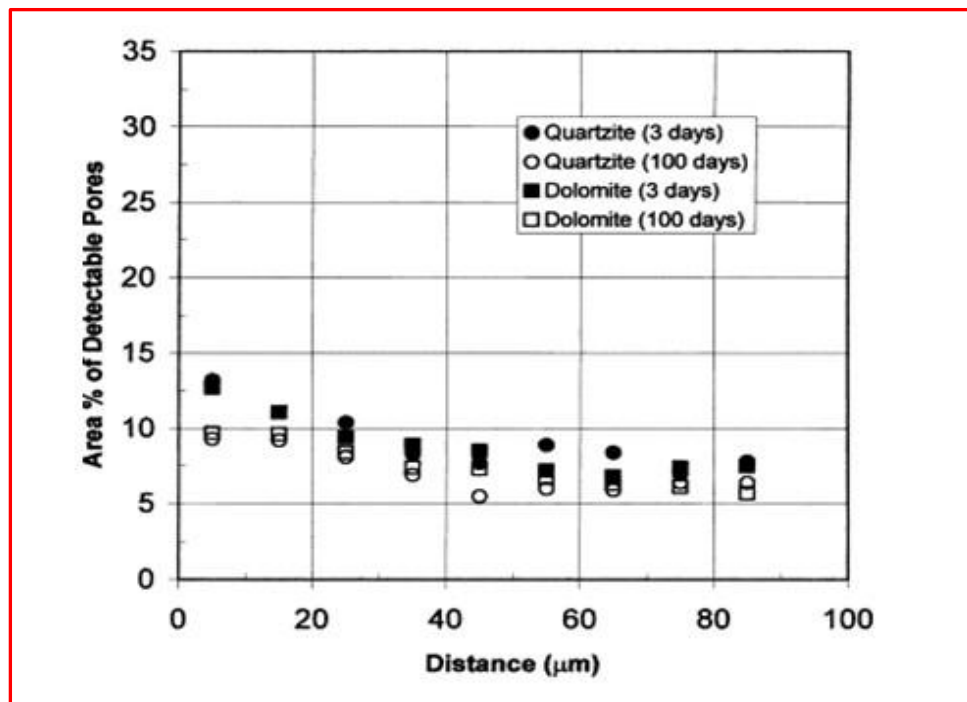


Fig.2.7: Porosity profiles in the ITZ ([Diamond and Huang, 2001](#))

The ITZ thickness has been regarded as the distance from the aggregate surface where the porosity curves intersect with the observed porosity of the bulk paste. The thickness of the ITZ is basically dependent of the type of aggregate and cement used, w/c ratio, the age of the composite, the nature of bonding between the aggregate and the paste, and the method used to compute it ([Larbi, 1991](#)). However, typical thickness is reported as about 50 μm ([Olivier et al. 1995](#); [Mindess, 1996](#)).

2.6.2 Micro-hardness of the ITZ

Micro-hardness is a comprehensive parameter for various characteristics of the ITZ encompassing the information of mean crystal size, crystal orientation index of CH and pore microstructure ([Gao et al. 2005](#)). This test provides direct information about the mechanical performance of the interfacial zone. A lower value indicates that the cement paste is either soft or contains a higher amount of micropores, which is an indication of higher interfacial porosity ([Larbi, 1991](#)).

In the first reported work, [Lyubimova and Pinus \(1962\)](#) investigated the micro-hardness profiles of a variety of cement paste-aggregate interfaces. Their results revealed a variation in the micro-hardness numbers from the aggregate interface into the bulk paste. At a distance of 3-5 μm from the aggregate surface, a micro-hardness value of $H_v = 18$ was measured. This was followed by a softer region with $H_v = 4$, and then in another zone 15-50 μm thick into the bulk paste, a constant micro-hardness value of about 10 was recorded.

A more recent work carried out by [Hussin and Poole \(2011\)](#) investigated the micro-hardness characteristics of concretes made with four different types of aggregates (Johor granite (JG), Mountsorrel granite (MG), Shap granite (SG) and Coldstone limestone (CL)) and obtained similar micro-hardness distribution. They observed that the ITZ from concretes containing granite had a higher micro-hardness value compared to the concrete made with limestone aggregate (Fig.2.8). As stated by the authors, this was confusing because if porous aggregate is used, this usually results in a very dense ITZ and consequently a stronger interfacial layer as the hydration products tend to migrate into the pores of the aggregate. This possibly

suggests that a chemical interaction between the Coldstone limestone aggregate and the matrix would lead to a weakness in the ITZ.

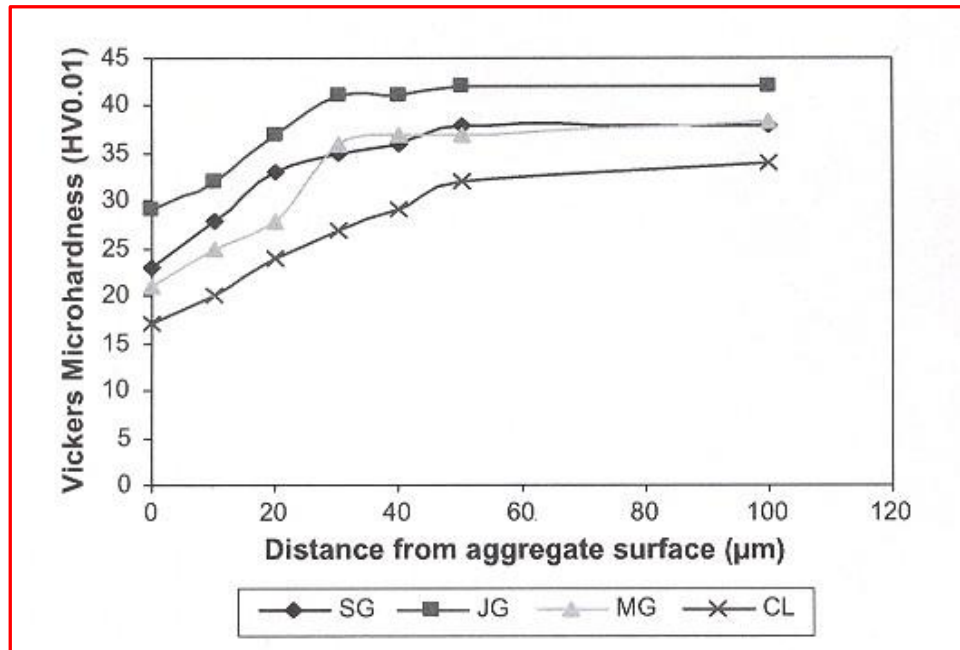


Fig.2.8: Vickers micro-hardness distribution in concrete containing different types of aggregates: SG=Shap granite, JG=Johor granite, MG=Mountsorrel granite and CL=Coldstone limestone (Hussin and Poole, 2011)

2.6.3 Elemental Composition at the ITZ

The SEM fitted with an energy dispersive X-ray (EDX) spectrometer is usually used for investigation of the elemental composition of the ITZ. At the same time, X-ray line scanning analyses are made in the region of the aggregate-cement paste interfaces of the specimens to quantify the various elements. Trägårdh (1999) used the following classification in order to distinguish hydrates rich in C-S-H, rich in calcium hydroxide (CH) and monosulfate (AFm).

C-S-H: $0.8 \leq \text{Ca/Si} \leq 2.5$, $(\text{Al} + \text{Fe})/\text{Ca} \leq 0.2$

CH: $\text{Ca/Si} \geq 10$, $(\text{Al} + \text{Fe})/\text{Ca} \leq 0.4$, $\text{S/Ca} \leq 0.04$

AFm: $\text{Ca/Si} \geq 4$, $(\text{Al} + \text{Fe})/\text{Ca} \leq 0.40$, $\text{S/Ca} > 0.15$

As previously reported and shown by [Bentz et al., \(1992\)](#), the Ca/Si molar ratio in cement paste increases significantly in the interfacial region when the aggregate surface is approached. Since initially (before hydration) the Ca/Si ratio could be constant, hydration process is resulting in a preferential increase of Ca rather than Si in the interfacial region which is in agreement with the frequently observed large crystal of calcium hydroxide deposition in this region.

2.7 Relationships between the Properties of the ITZ and the Properties of Concrete

2.7.1 Overview

In the study of the ITZ, the key question that needs to be answered is to what extent the existence of the ITZ has any practical influences on the engineering properties of concrete or is it just a peculiarity of academic interest ([Bentur et al. 2000](#))? Actually, as [Mehta and Monterio \(2006\)](#) pointed out, the answers of many enigmatic questions on concrete behaviour lie in the interfacial zone. For instance, have we ever wondered why

- Concrete is relatively weak and brittle in tension but relatively strong in compression?
- The response of the components (aggregate and cement paste) of concrete individually under compression remains elastic until fracture while concrete itself exhibits inelastic behaviour?

- At a given cement content, w/c ratio and age of hydration, cement mortar will always be stronger than the corresponding concrete? Also, why does the strength of concrete decreases as the coarse aggregate size is increased?
- When concrete is exposed to fire, the elastic modulus of a concrete drops more rapidly than its compressive strength?
- The permeability of a concrete containing even a very dense aggregate will be bigger by an order of magnitude than the permeability of the corresponding cement paste?

However, as stated by [Wang et al. \(2009\)](#), there are two contrary opinions: On the one hand, some researchers ([Nemati et al., 1998](#); [Wong et al., 2009](#)) claim that since the ITZ is the weakest part of the micro-structural system and the place where cracking initiates; it plays a significant role on the mechanical and transport properties of concrete. On the other hand, some researchers ([Diamond and Huang, 2001](#)) suggest that there is no obvious reason to assume that the ITZ might have significant negative effects on the permeance and mechanical performance of concrete, even for concrete with a w/c ratio of 0.50. The conflicting arguments from various resources indicate that the significance of the ITZ with regard to the overall concrete behaviour, it seems, remains uncertain.

2.7.2 Relationships between the ITZ and Strength, Cracking and Failure Mechanism

Conventional wisdom has it that the interfacial zone is the weakest link in normal strength concrete, while the aggregate itself is the strongest component. Thus, the micro-cracks tend to propagate through the matrix-aggregate interface. In high strength concrete, however, low w/c ratio and use of pozzolanic materials such as silica fume consume calcium hydroxide, and modify the zone as well as improve the strength of cement paste and the ITZ.

Consequently, the aggregates become the weakest part and thus, micro-cracks tend to develop through aggregate particles, as shown in Fig.2.9 (Lee et al., 1992; Van Mier, 1997; Zhang et al., 2005).

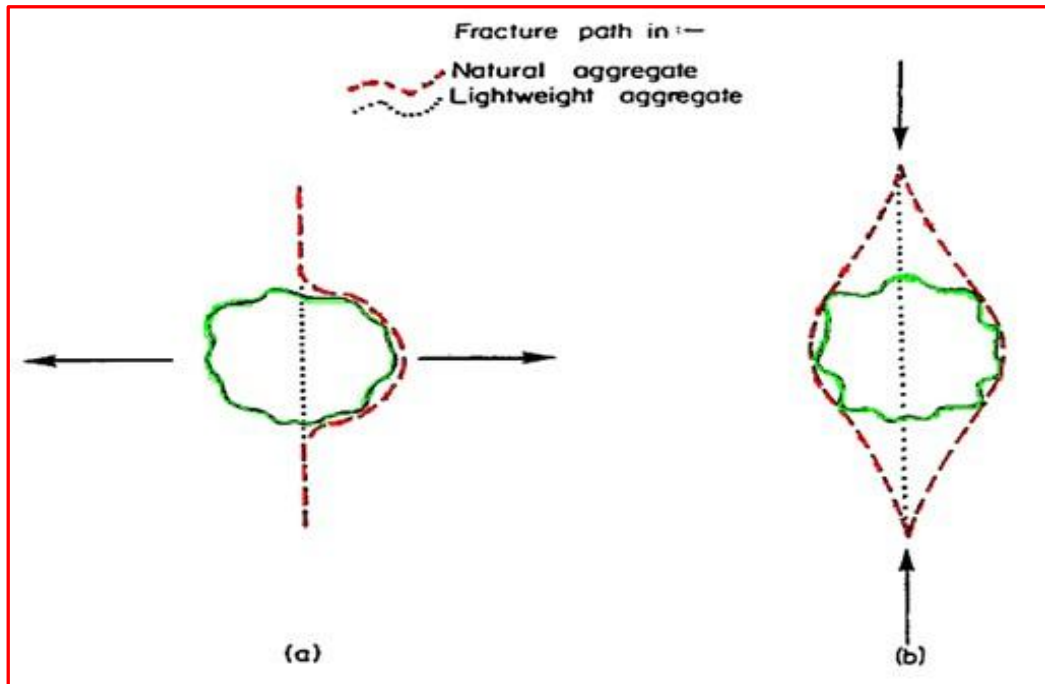


Fig.2.9: Fracture paths in different concretes (Adapted from Newman and Owens, 2003)

At this point, this difference gives rise to several questions that will be addressed in the following paragraphs.

- How do changes in the aggregates affect cracks and cracking scenarios in concrete?
- What effects do the micro- and nano level properties of ITZ have on the overall concrete behaviour?

Under externally exposed loads and environmental effects, the occurrence of tensile stress leads to the growth of micro-cracks in the ITZ both (Fig.2.10) in size and number (A), and the penetration of the ITZ cracks into the surrounding matrix (B). Once the peak stress is reached (C), micro-cracks propagate in an unstable manner and crack localisation occurs,

with the result that the micro-cracks yield large cracks and leading to the stress drop (D). Crack bridging and crack branching (D-E) is the main mechanism responsible for the long softening tail (Löfgren, 2005).

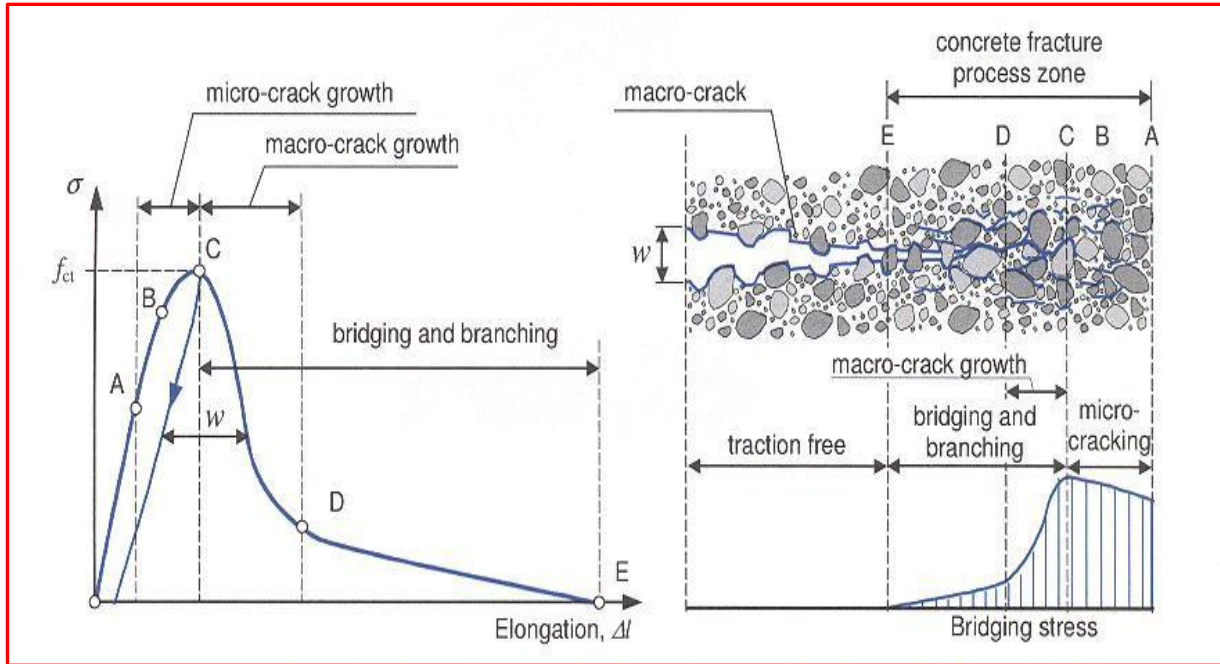


Fig.2.10: Schematic description of the micro-fracture process in concrete (Löfgren, 2005)

In conventional concrete as just mentioned, there is a “wall effect”, in which the aggregates appear locally flat to the cement grains and disrupt their packing. By contrast, in concretes made with some unconventional aggregates (i.e. sintered fly ash lightweight aggregates), this does not exist and a nearly continuous uniform microstructure of hydration products abuts and partially penetrates the lightweight aggregates (Bentz, 2009). Moreover, the lightweight aggregate-cement paste can be characterized by a mechanical interlocking in combination with a chemical interaction in the form of pozzolanic reaction (Zhang and GjØrv, 1990) and lightweight aggregates can act as an internal water reservoir (“internal curing”) when they are saturated (pre-wetted) and may increase the degree of hydration of cement (Weber and

[Reinhardt, 1999](#)). This situation is experimentally determined using X-ray computed tomography (CT) technique and schematically illustrated in Fig. 2.11 and 12, respectively.

As a result of these effects, the lightweight aggregate-cement paste bond strength is usually higher than the conventional aggregate-cement paste bond strength. This difference has a pronounced effect on crack initiation and propagation. For this type of concrete, aggregate rupture may occur, which reduces the bridging effect and results in a more brittle fracture process. Although the affected part of the mix is small, this can also have a very significant influence on the concrete strength if the interface would otherwise be the weakest part of the micro-structural system.

Lightweight aggregate is usually weaker than both conventional aggregate and cement mortar. On this basis one might expect the concrete to be weaker, too. If, however, the lightweight aggregate is stronger than the ITZ in conventional mix, then this expectation might not be met. For example, a recent study conducted by [Kayali \(2008\)](#) showed that concrete produced with sintered fly ash lightweight aggregates was 20 % stronger in compression than concrete made with conventional aggregates under the same mix design conditions although the lightweight aggregate was weaker than the ordinary aggregates. Unfortunately, the author did not conduct any quantitative micro-structural work, and based on qualitative analysis, the author attributed the higher strength to the strong bonding characteristics that develop at the cement paste and the lightweight aggregate. In addition, it was observed that cracking did not initiate at the interfaces but rather was arrested by the interfacial zone. This means that the ITZ in conventional concrete could be weaker than the ITZ in lightweight aggregate concrete and, thus, the high strength of other materials is inconsequential if failure is primarily in the ITZ.

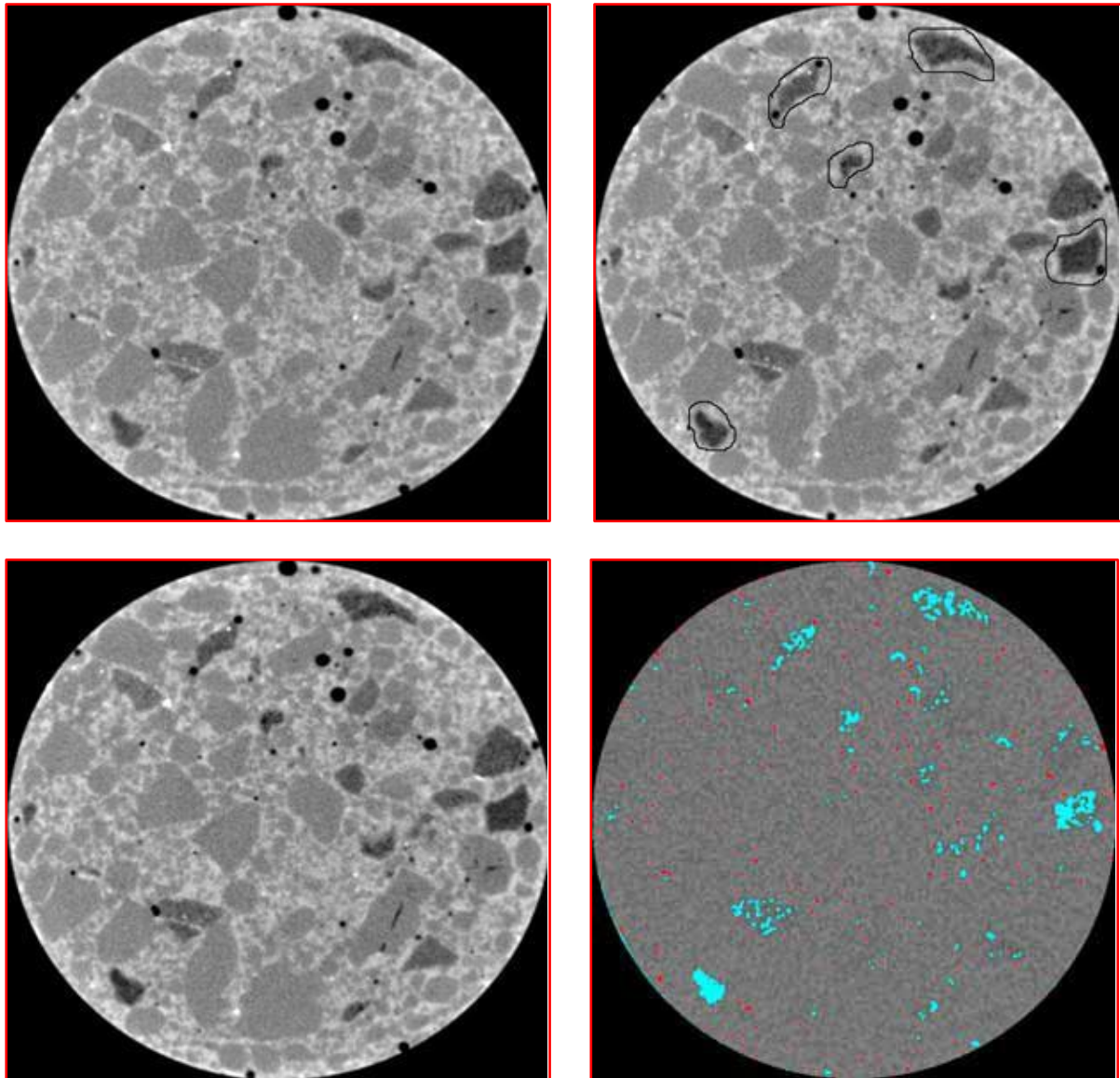


Fig.2.11: X-ray CT view of improving of the transition zone via internal curing process: upper left-mortar after immediately mixing, upper right-mortar about 1 d of hydration, lower left mortar about 2 d of hydration and lower right-subtracted colour-coded image of 1 d - aqua indicates regions of drying and red indicates regions of wetting- ([Bentz et al., 2006](#)).

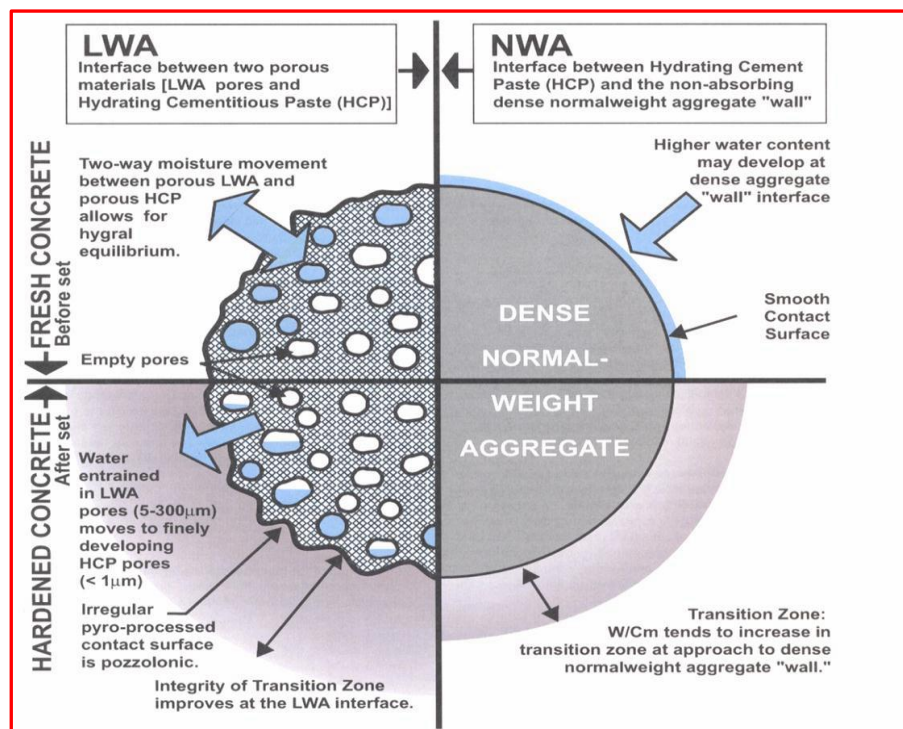


Fig.2.12: Schematic view of improving of the transition zone via internal curing process

(ESCSI, 2006- <http://www.escsi.org>)

Most studies with regards to the cement paste-aggregate bond strength found that increasing the paste-aggregate bond strength will results in 20-40 % improvements to the strength of concrete (Alexander and Mindess, 2005). Darwin and Slate (1970), on other hand, observed only a slight reduction in the modulus of elasticity of concrete, although the bond strength dramatically reduced. However, a study conducted by Tasong et al. (1998) showed that the chemical interaction between the matrix and some rock-based aggregates would cause a reduction rather than increase in bond strength, particularly at early ages, due to the release of CO₂ gas and the presence of large crystals of calcite (as confirmed by X-ray diffraction analysis- Fig.2.13) which results in a very porous and weak ITZ.

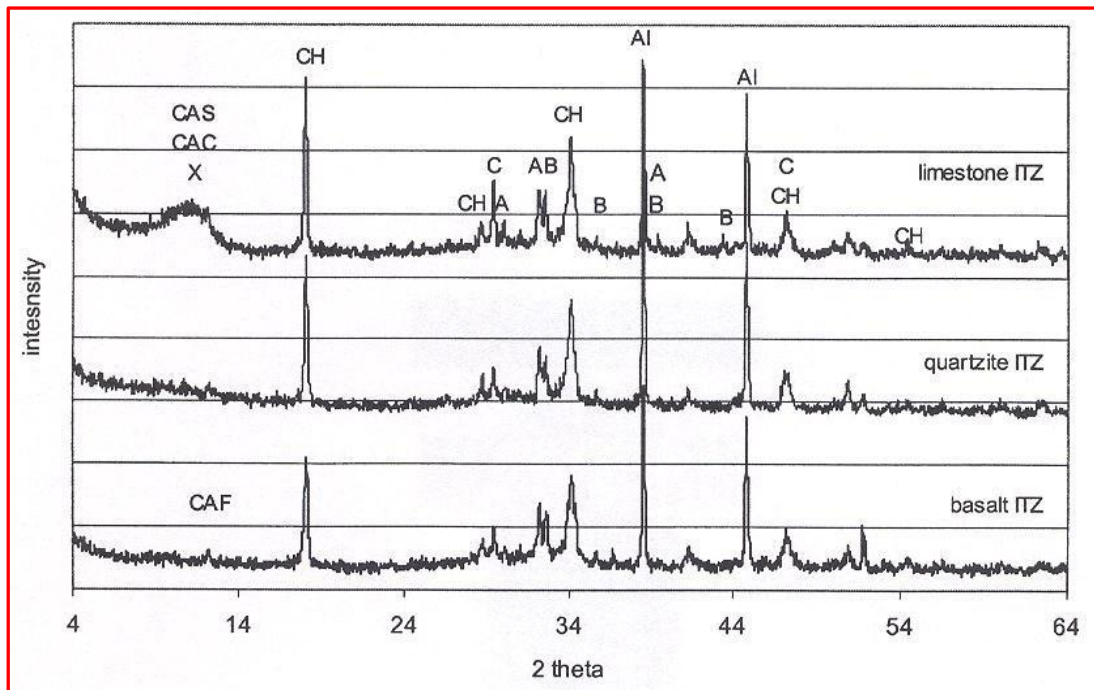


Fig.2.13: X-ray powder diffraction patterns of the products formed at the ITZ at 1 week.

CAS= tetra calcium aluminate monosulphate, CAC= tetra calcium aluminate carbonate, CH= calcium hydroxide, A= alite, B= belite, C=calcite, CAF= ferrite and Al= aluminium (Tasong et al., 1999).

In addition, so far considerable research has been conducted to investigate the relationship between the micro-crack development and the stress-strain behaviour. It is generally agreed that the development of the micro-cracks at the interface leads to a non-linear stress-strain response for concrete composite, although the response of the cement paste and aggregate alone is highly linear (Neville, 1996; Scrivener et al., 2004). This behaviour is illustrated in Fig.2.14.

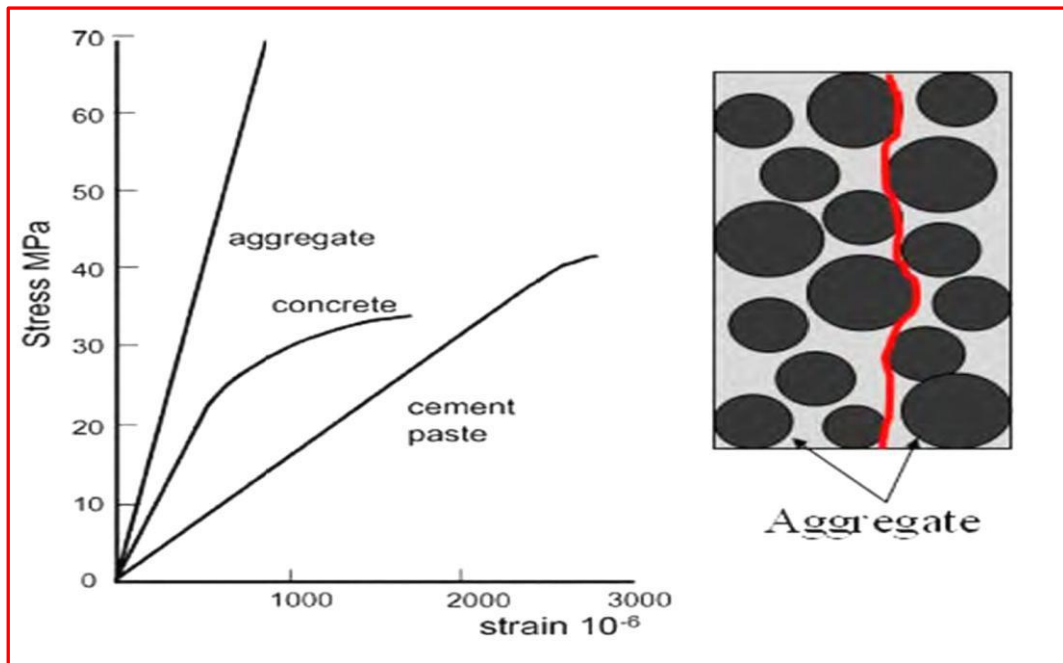


Fig.2.14: Individual stress-strain response of cement paste, aggregate and concrete
([Scrivener et al., 2004](#))

[Giaccio and Zerbino \(1998\)](#) investigated the failure mechanism of high strength and conventional concrete made with coarse aggregates having significant differences in strength, shape and surface texture, and porosity and water absorption, and arrived at very valuable results. In general, they concluded that when concretes were produced with the aggregates having very smooth surface textures, the failure mechanism shows almost no changes in different strength concrete and the failure mainly stems from extensive debonding. By contrast, when concretes were prepared with the aggregates having irregular shape and rough texture as well as very “low” strength and very “high” water absorption, an excellent interface bonds developed which led to behaviour more similar to a “homogeneous” material such as mortar. In addition, the main failure mechanism with cracking through aggregates was observed in both concretes. However, there were no increases in the fracture energy of these concretes (the lowest energy was recorded in these concretes) although compressive

strength was considerably increased from 33.1 to 79.4 MPa. The study conducted by [Chiaia et al. \(1998\)](#) gave some support to the results but interestingly, the author reported that weaker elements (the aggregate, the bond zone and a very weak matrix) including in the composite can increase ductility. This probably reflects the fact that the improved compatibility between the mortar matrix and aggregate phases gives a concrete with a lower overall modulus of elasticity (larger deflection) at each increment of the load which is much more preferable under dynamic conditions due to the greater ability to absorb energy without yield. Their interesting and important results opened the door for the investigation of micro-structural aspect of the failure process of concrete made with unconventional aggregates such as steel slag.

A further study conducted by [Akçaoğlu et al. \(2005\)](#) focused on the understanding of the bond between the matrix and the aggregate for special cases using very rigid, nonporous and smooth-surfaced aggregates and the subsequent failure process of concrete under compression. At low stress levels, the micro-crack density at the ITZ increased linearly with increasing w/c ratio likely due to the low quality of the ITZ (Fig.2.15a). However, at higher stress levels, the mortar strength, its strength difference with the ITZ and the ITZ thickness were observed to be the deciding factor for the tensile strength. The authors showed that a narrower ITZ in the concrete led to more condensed stress concentrations and micro-cracks at the interfacial zone leading to a sudden failure (Fig.2.15b). More importantly, the presence of very rigid and smooth surface aggregates contributed to the sudden failure as they increased the flow of the matrix around the aggregate resulting in higher lateral tensile stresses.

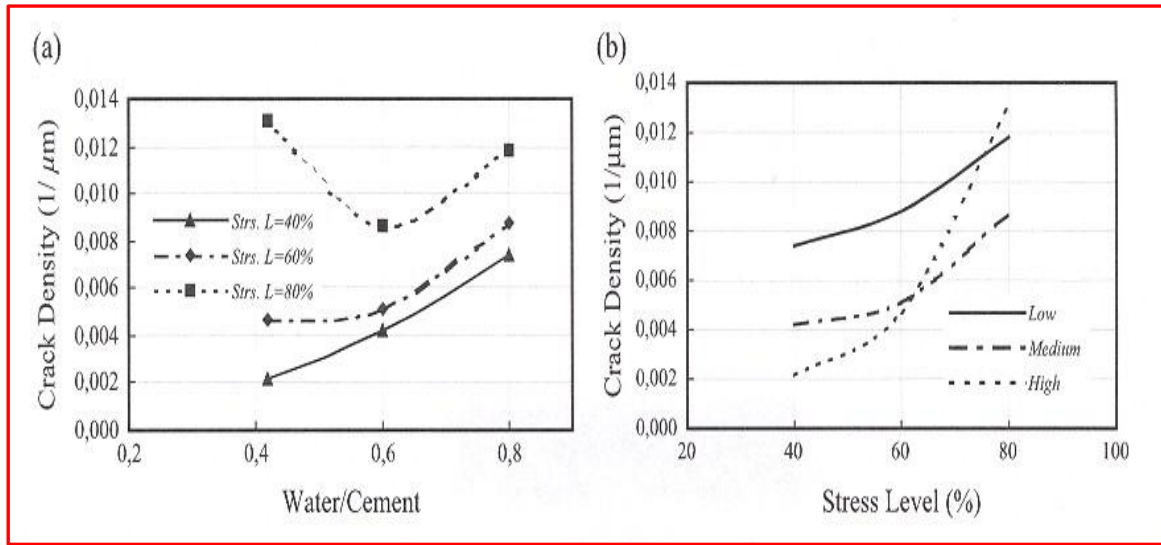


Fig.2.15: ITZ crack density as a function of w/c and stress level for three types of composites: low, medium strength and high strength mortars (Akçaoğlu et al., 2005)

Another important property of the ITZ that could have a significant influence on concrete response at macro-scale is its surface roughness. The only available study in this subject was carried out Zampini et al. (1998). The authors evaluated the roughness of the region near the interface between the cement paste and the aggregate by digitizing images from a confocal tandem scanning microscope, and found that the average roughness of the paste was closely related to fracture parameters K_{IC} (critical stress intensity factor) and Δa_c (critical crack extension), as determined by the two-parameter fracture model in which three-point bending specimens is loaded up to the maximum stress, and then exposed to unloading and reloading cycle. The increase in paste roughness, associated with the increased paste-aggregate interfaces, resulted in an increase in the toughness of the paste and of concrete signifying that the paste-aggregate interface can toughen the paste by increasing its roughness.

As can be seen the cited papers, a number of research studies have been performed for investigating the effect of the ITZ and aggregate characteristics when concrete is subjected to

static loading. However, no paper has been found in open literature with regard to the influence of the microstructure and properties of the ITZ when concrete subjected to high-strain rate (impact) loading. The paucity of such data leads to the objective of this project. But, it must be noted that only one paper by [Zhou and Hao \(2008\)](#) “numerically” analysed the effect of the ITZ (thickness and strength) and aggregate distribution on the dynamic tensile behaviour of concrete. For this, a mesoscale heterogeneous model (three-phase concrete material with a single circular aggregate bounded by a thin ITZ) was constructed. But it can be claimed that most of the assumption in model were not reasonable. For instance, the authors assumed the ITZ thickness to be 0.2 mm which is much larger than the real typical thickness.

However, based on their own meso-scale model, they concluded that when the ITZ is thicker, the failure time is earlier and the tensile strength is lower. Similarly, the tensile strength of the sample increases and the failure occurs after a delayed time when the ITZ strength increases. Fig.2.16 illustrates the stress (σ_{xx} stress along vertical axis) for $\dot{\epsilon} = 4/s$ at different time instants. For comparison, three different cases (case I, II and V) are displayed in the figure. As the material properties for three phases were not the same, the distribution of the aggregate and the properties of the ITZ affects the stress wave propagation. As can be seen in the case V, the stress distribution is obviously not as continuous as that in case I, probably reflecting that the stress state in some ITZ elements could differ a lot from their adjacent elements.

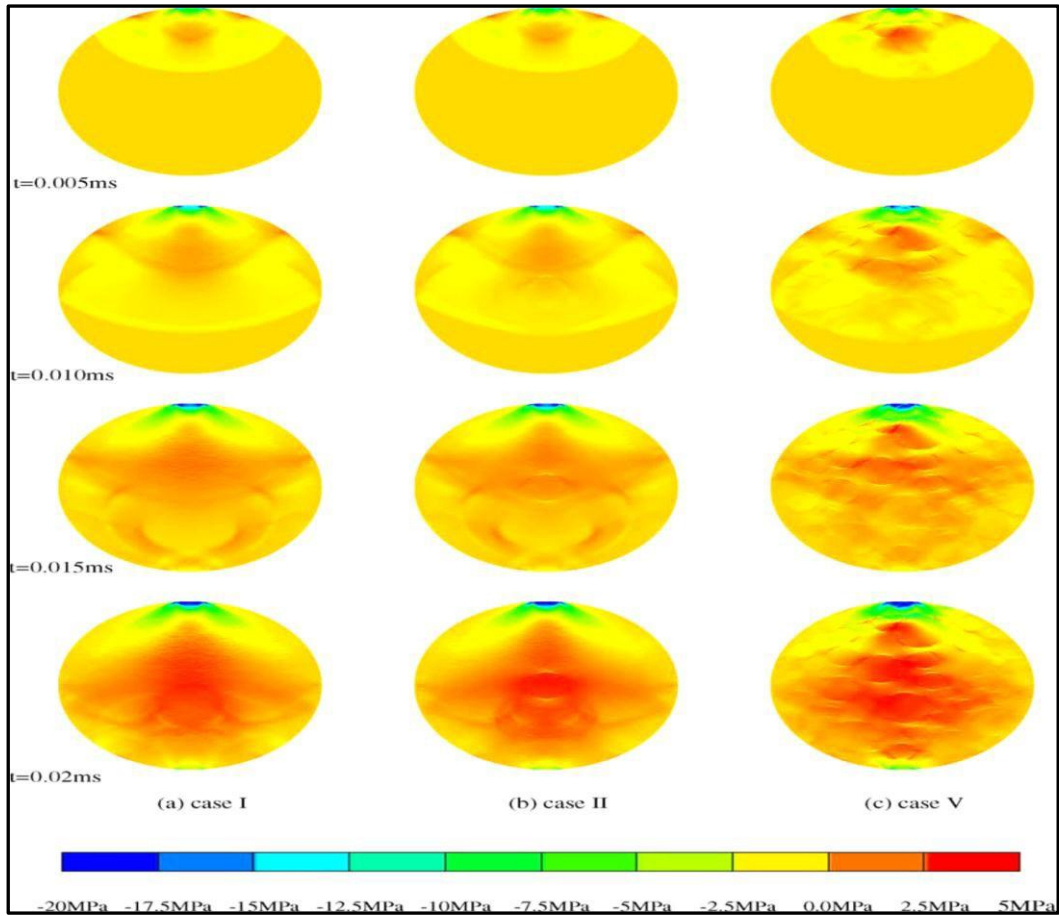


Fig.2.16: σ_{xx} distribution for $\dot{\epsilon}=4/s$ (Zhou and Hao, 2008)

2.8 Concluding Remarks

- The interface among concrete components seems to have distinct micro-structural features. Compared to the matrix, the ITZ can generally be characterized by a higher porosity, higher concentrations of calcium hydroxide crystals and larger spaces. Indeed, it may play a significant role on the overall understanding of mechanical performance of concrete, and contribute to load transfer mechanism in concrete composite system.

- Although the previous studies had elaborated the nature of the ITZ, the role of aggregate variation in the development of ITZ microstructure and the influence of ITZ on the dynamic (impact) behaviour of concrete are still inconclusive.
- Three types of binding mechanism at the interface can occur: physical interaction, physical-chemical interaction, and mechanical interlock. Thus, the bond in concrete composite is basically as a result of the combination of different mechanisms. The nature of these mechanisms depends on the micro-structural characteristics of aggregates. Normally, the bond developed with siliceous aggregates is greater than that with carbonate aggregates.
- Factors that have been observed to significantly influence micro-damage processes in concrete are aggregate shape (i.e. roughness and angularity), stiffness and surface texture. Use of large, stiff and dense aggregates increases the tensile stress concentrations at the ITZ. Moreover, it has been demonstrated that the aggregate in some types of concrete, such as lightweight concrete, has more contribution to an effective stress transfer mechanism as a result fundamentally of higher fracture toughness of the interface and a better modular match.
- From a fracture mechanics standpoint, when the adhesive bonds between the aggregate and the matrix are damaged under applied loads, the concrete weakens, and cracks develop and propagate either through the particles or around them. The type of propagation influences the energy consumption and the interlocking effect.

References:

- [1] Akçaoğlu, T., Tokyay, M., and Çelik, T. (2005). “Assessing the ITZ micro-cracking via scanning electron microscope and its effect on the failure behaviour of concrete.” *Cement and Concrete Research* 35 (2) 358-363.
- [2] Alexander, M. G., and Mindess, S., (2005). “Aggregates in Concrete.” Taylor & Francis, New York.
- [3] Bentur, A., Alexander, M.G., Bentz, D., Büyükoztürk, O., Elsen, J., Hooton, D., Jennings, H., Katzs, A., Kjellsen, K.O., Kronlof, A., Lagerblad, B., Mindess, S., Ollivier, J.P., Scrivener, K., and Skalny, J., et al., (2002). “Review of the work of the RILEM TC 159-ETC: Engineering of the Interfacial transition zone in cementitious composites, *Materials and Structures* 33(2) 82-87.
- [4] Bentur, A., and Odler, I., (1996). “Development of interfacial microstructure.” In: J.C. Maso Editor, *Interfacial Transition Zone in Concrete RILEM Report 11 E & FN Spon*, London, pp. 47–63.
- [5] Bentz, D.P., Stutzman, P.E., and Garboczi, E.J., (1992). “Experimental and simulation studies of the interfacial zone in concrete.” *Cement and Concrete Research* 22 (5) 891-902.
- [6] Bentz, D.P., Halleck, P.M., and Grader, A.S., (2006). “Four-dimensional X-ray microtomography study of water movement during internal curing.” In *Proceedings of the International RILEM Conference*, Eds. Jensen, O.M., Lura, P., and Kovler, K., France.
- [7] Bentz, D.P., (2009). “Influence of internal curing using lightweight aggregates on interfacial transition zone percolation and chloride ingress in mortars.” *Cement and Concrete Composites* 31 (5) 285-289.
- [8] Carrasquillo, R.L., Nilson, A.H., and Slate, F.O., (1981). “Properties of high strength concrete subject to short term loads.” *ACI Materials Journal* 78 (3) 171–178.

- [9] Chiaia, B., Van Mier, J.G.M., and Vervuurt, A., (1998). “Crack growth mechanism in four different concretes: Microscopic observations and fractal analysis.” *Cement and Concrete Research* 28 (1) 103-114.
- [10] Darwin, D., and Slate, F.O., (1970). “Effect of Paste-Aggregate Bond Strength on Behaviour of Concrete.” *Journal of Materials* 5 (1) 86–98.
- [11] Diamond, S., and Huang, J., (2001). “The ITZ in concrete – a different view based on image analysis and SEM observations.” *Cement and Concrete Composites* 23(3) 179-188.
- [12] Esping, O., (2007). “Early age properties of self-compacting concrete-effects of fine aggregate and limestone filler.” PhD Thesis. Chalmers University of Technology, Sweden.
- [13] Expanded Shale, Clay and Slat Institute (2006). “Internal curing using expanded shale, clay and slate lightweight aggregate.”
http://www.escsi.org/uploadedFiles/Technical_Docs/Structural_Lightweight_Concrete/4362.0%20Internal%20Curing%20-%20Using%20ESCS%20LWA.pdf.
- [14] Gao, J.M., Qian, C.X., Liu, H.F., Wang, B., and Li, L., (2005). “ITZ microstructure of concrete containing ggbs.” *Cement and Concrete Research* 35 (7) 1299-1304.
- [15] Giaccio, G., and Zerbina, R., (1998). “Failure mechanism of concrete- combined effects of coarse aggregates and strength level.” *Advanced Cement Based Materials* 7 (2) 41-48.
- [16] Hsu, T.T.C., Slate F.O., Sturman, G.M., and Winter, G. (1963). “Micro-cracking of plain concrete and the shape of the stress-strain curve”. *ACI Journal of Materials* 60 (2) 209–224.
- [17] Hussin, A., and Poole, C., (2011). “Petrography evidence of the interfacial transition zone (ITZ) in the normal strength concrete containing granitic and limestone aggregate.” *Construction and Building Materials* 25 (5) 2298-2303.
- [18] Kayali, O., (2008). “Fly ash lightweight aggregates in high performance concrete.” *Construction and Building Materials* 22 (12) 2393-2399.

- [19] Kurtis, K.E., (2007). “Structure of the hydrated cement paste.” CEE 8813B Materials Science of Concrete, Lecture Notes.
- [20] Larbi, J.A. (1991). “The cement paste-aggregate interfacial zone in concrete.” PhD Thesis. Technical University of Delft, The Netherlands.
- [21] Lee, K.M., Büyükoztürk, O., and Oumera, A., (1992). “Fracture analysis of mortar-aggregate interfaces in concrete.” *Journal of Engineering Mechanics*, ASCE 118 (10) 2031–2047.
- [22] Lofgren, I., (2005). “Fibre-reinforced concrete for industrial construction- a fracture mechanics approach to material testing and structural analysis.” PhD Thesis. Chalmers University of Technology, Sweden.
- [23] Lyubimova, T.Y., and Pinus, E.R., (1962). “Crystallization structure in the contact zone between aggregate and cement in concrete.” *Colloid Journal* 24 (5) 491-498.
- [24] Mehta, P.K., and Monterio, P., (2006). “Concrete: microstructure, properties, and materials.” McGraw-Hill, New York.
- [25] Mondal, P., (2008). “Nanomechanical properties of cementitious materials.” PhD Thesis. Northwestern University, USA.
- [26] Mindess, S., (1996). “Test to determine the mechanical properties of the interfacial zone”. In: J.C. Maso Editor, *Interfacial Transition Zone in Concrete RILEM Report 11 E & FN* Spon, London, 47–63.
- [27] Nemati, K.M., Monterio, P.J.M., and Scrivener, K.L., (1998). “Analysis of compressive stress-induced cracks in concrete.” *ACI Materials Journal* 95 (8) 617-630.
- [28] Neville, A.M. (1996). “Properties of Concrete.” (4th edn. ed.), Wiley, New York, USA.
- [29] Newman, J., and Owens, P., (2003). “Properties of Lightweight Concrete (Chapter 2)”. In: J. Newman and B.S. Choo, Editors, “Advanced concrete technology constituent materials 3”. Wiley, New York, 72–98.

- [30] Ollivier, J.P., Maso, J.C., and Bourdette, B., (1995). "Interfacial transition zone in concrete." *Advanced Cement Based Materials* 2 (1) 30-38.
- [31] Scrivener, K.L., and Pratt, P.L., (1986). "A preliminary study of the microstructure of the cement/sand bond in mortars. Proceedings of 8th International Congress of the Chemistry of Cement, Rio de Janeiro, 466-471.
- [32] Scrivener, K.L., Crumbie, A.K., and Laugesen, P., (2004). "The interfacial transition zone (ITZ) between cement paste and aggregate in concrete." *Interface Science* 12 (4) 411-421.
- [33] Tasong, W.A., Lynsdale, C.J., and Cripps, J.C., (1999). "Aggregate-cement paste interface Part 1: Influence of aggregate geochemistry." *Cement and Concrete Research* 29 (7) 1019-1025.
- [34] Trägårdh, J., (1999). "Micro-structural features and related properties of self-compacting concrete." In: A. Skarendahl and O. Petersson (Editors), *Proceedings of the First International RILEM Symposium on Self Compacting Concrete*, RILEM, Cachan, Cedex, 175-186.
- [35] Zhou, X.Q., and Hao, H., (2008). "Mesoscale modelling of concrete tensile failure mechanism at high strain rates." *Computer and Structures* 86 (21-22), 2013-2026.
- [36] Van Mier, J.G.M., (1997). "Fracture processes of concrete." CRC Press, New York.
- [37] Wang, X.H., Jacobsen, S., He, J.Y., Zhang, Z.L., and Lee, S.F., (2009). "Application of nano-indentation testing to study of the interfacial transition zone in steel fibre reinforced mortar." *Cement and Concrete Research* 39 (8) 701-715.
- [38] Weber, S., and Reinhardt, H.W., (1997). "A new generation of high performance concrete: concrete with autogeneous curing." *Advanced Cement Based Materials* 6 (2) 59-68.

- [39] Zampini, D., Jennings, H.M., and Shah, S.P., (1995). "Characterization of the paste-aggregate interfacial transition zone surface roughness and its relationship to the fracture toughness of concrete." *Journal of Material Science* 30 (12), 3149-3154.
- [40] Zhang, M.H., and Shim, V.P.W., Lu, G., and Chew, C.W., (2005). "Resistance of high-strength concrete to projectile impact." *International Journal of Impact Engineering* 31 (7) 825–841.
- [41] Zhang, M.H., and GjØrv, O.E., (1990). "Microstructure of the interfacial zone between lightweight aggregate and cement paste". *Cement and Concrete Research* 20 (4) 610–618.

CHAPTER 3

IMPACT PHENOMENA IN CONCRETE

3.1 General:

This chapter aims to provide a general review of the literature on concrete under impact loading but, in particular, it presents a background for understanding the damage mechanism of concrete under impact loading from a micro-structural point of view.

Topics addressed in this chapter include:

- Introduction to impact load characteristics and sources
- Strain rate effects on concrete
- Failure mechanism under impact loading
- Cracking behaviour of concrete under impact, and the influence of aggregate and reinforcement on that behaviour.

3.2 Introduction of Impact Phenomena in Concrete

Concrete and concrete structures in many civil engineering applications can often be subjected to a range of accidental or deliberate impact loads, apart from static loads. Typical examples of such loads are generated from sources such as

- terrorist attacks using bombs or rockets, and missiles or airplane collision to symbolic and military buildings,
- ship collision to offshore platform and into bridge piers,
- boulder moved by waves hitting flood defences,
- natural disasters such as tornados and tsunamis,
- earthquakes,
- vehicle crash into concrete barriers,
- pile driving,
- columns in underground car parks, overpass bridges and medium to low rise buildings located close to major roads and intersections,
- rock falls on the roadways in mountain areas,

(Grote et al., 2001; Mougin et al., 2005; Remennikov and Kaewunruen, 2006; Thilakarathna et al., 2010).

Typical characteristics of such dynamic loads are to generate very high strain-rates and to transmit large amounts of energy to the structure. Typical strain rates during some impact and explosive loads are given in Table 3.1 (CEB, 1988).

Table 3.1: Typical strain rates for various types of loading ([CEB, 1988](#))

Type of Loading	Strain rate (/s)	Tests and machines
Static loading: creep, etc.	10^{-7}	Static test
Traffic	$10^{-7} - 10^{-4}$	Quasi-static test
Gas explosions	$5 \times 10^{-5} - 5 \times 10^{-4}$	Seismic effect test
Earthquake	$5 \times 10^{-3} - 5 \times 10^{-1}$	Shake table test
Pile driving, airplane impact, vehicle hitting bridge pier, hard impact	$10^{-2} - 10^1$	Special hydraulic machine with high-capacity servo-valves; impact test; impact or drop weight machine, Split-Hopkinson pressure bar
Hypervelocity impact	$10^2 - 10^6$	Explosion or bombing adjacent to buildings

3.3 Concrete Behaviour under Impact

3.3.1 Mechanism of Impact Damage

Before discussion cracking behaviour of concrete under impact, it would be useful to provide a brief review on how impact damage is caused “in general” not specifically in concrete.

When an explosion impinges on a solid element, a high-speed pressure wave will be released. A proportion of the energy will be reflected back and a significant portion will propagate through the affected solid body as a compressive stress wave and reflect a tension wave at the rear side of the element which can cause back face spalling as the concrete fails in tension (Fig.3.1.) and particles are ejected from the back surface at high speed. Depending on the location of the loading source, major disintegration effects can also occur. For example, the entire solid section can fail in flexure if an explosion loading originating from a standoff location, or a localised mode of failure (shear-punching behaviour) can occur when an explosion occurring at a small standoff to the solid body ([Millard et al., 2010](#)).

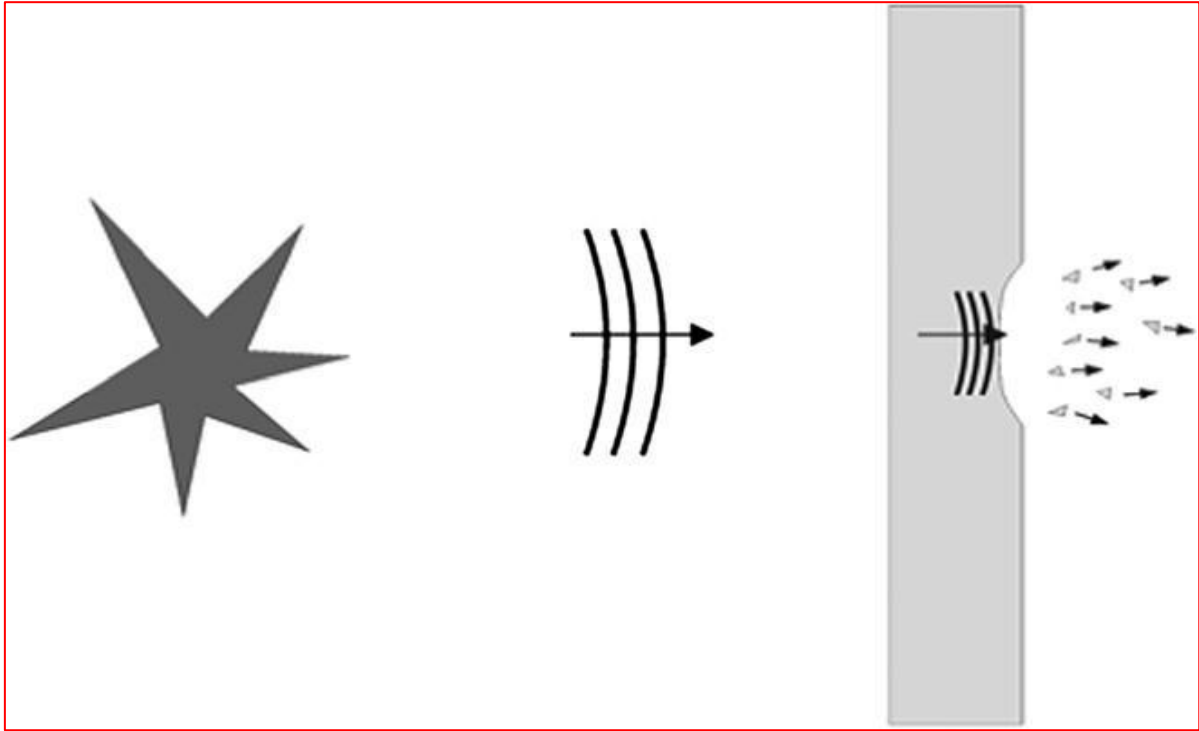


Fig.3.1: Back face spalling and shock wave propagation (Millard et al, 2010)

In the case of concrete, as depicted by Clifton (1982), three major damage regions (Fig.3.2) are formed, namely: crater region, crushed aggregate region and extensive cracking region due to the propagation and reflection of the impact-induced stress waves from specimen boundaries (Zhang et al. 2005). In addition, they noted that scabbing, which is a violent separation of mass of material from the distal face of a slab subjected to an impact loading, may occur probably due to reflected shock waves as just mentioned.

When the concrete is subjected to an impact or load due to contact / near contact explosion, a crater is produced as a result of the concentrated forces at the surface of the concrete. These forces are transmitted inwards, thereby crushing the concrete in the crater region. The crushed aggregate region can be regarded as an interfacial region in which the concrete has both plastic and elastic response to impact loading. The concrete in this region is fractured by the original compressive wave and possibly further fractured by the reflected tensile waves.

The final (cracking) region involves the propagation of elastic stress waves with little dispersion or attenuation from the point of impact. Compressive longitudinal wave propagate spherically into the concrete. When the wave reaches an opposite free surface, it is reflected at normal incidences as a tensile wave. The superposition of the original compressive wave and the reflected tensile waves results, firstly, in a decreasingly compressive and then an increasingly tensile wave (see Fig.3.1). Within the concrete itself, internal stress wave reflections can occur due to the impedance mismatches between the cement paste and aggregates.

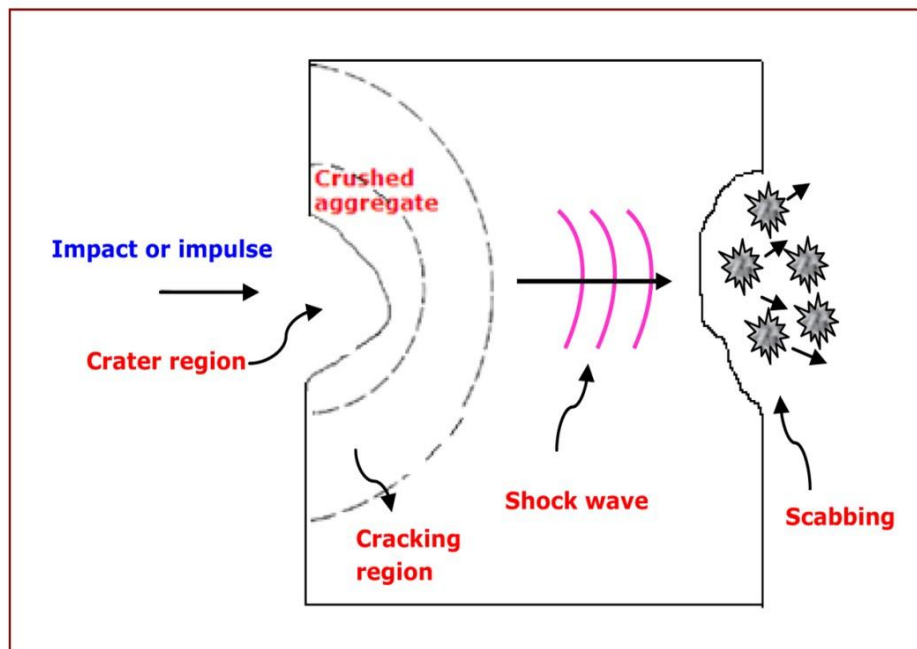


Fig.3.2: Fracture region in concrete subjected to impact (Adapted from [Zhang et al. 2005](#))

3.3.2 Failure Mechanism and Cracking Behaviour of Concrete under Impact Loading

Fig.3.3 illustrates the toughening mechanisms involved in the fracture process of concrete described by [Shah et al., 1995](#). During fracture, the high-stress state developed near the crack tip leads to micro-cracking at flaws. Such flaws stem from water-filled pores, air voids and shrinkage cracks. This phenomenon is known as micro-crack shielding (Fig.3.3-I) and consumes a part of external energy. When the path of least resistance is around a relatively

stiff particle or along a weak interfacial region, crack deflection takes place (Fig.3.3-II). By contrast, the aggregate bridging process, which is the major toughening mechanism in plain concrete, occurs when the crack has advanced beyond an aggregate that continues to transfer stresses until it is fractured or pulled-out (Fig.3.3-III). During aggregate pull-out or the opening of a tortuous crack, interlock between the cracked faces (Fig.3.3-IV) may exist which, in turn, can cause energy dissipation and load transfer through the friction across the crack. If the crack tip is terminated by internal voids (Fig.3.3-V) which generate a blunt tip, additional energy is required for crack propagation with a new blunt tip. Finally, crack branching (Fig.3.3- VI) might occur due to concrete heterogeneities. If this is the case, more energy should be consumed in creating the crack branches.

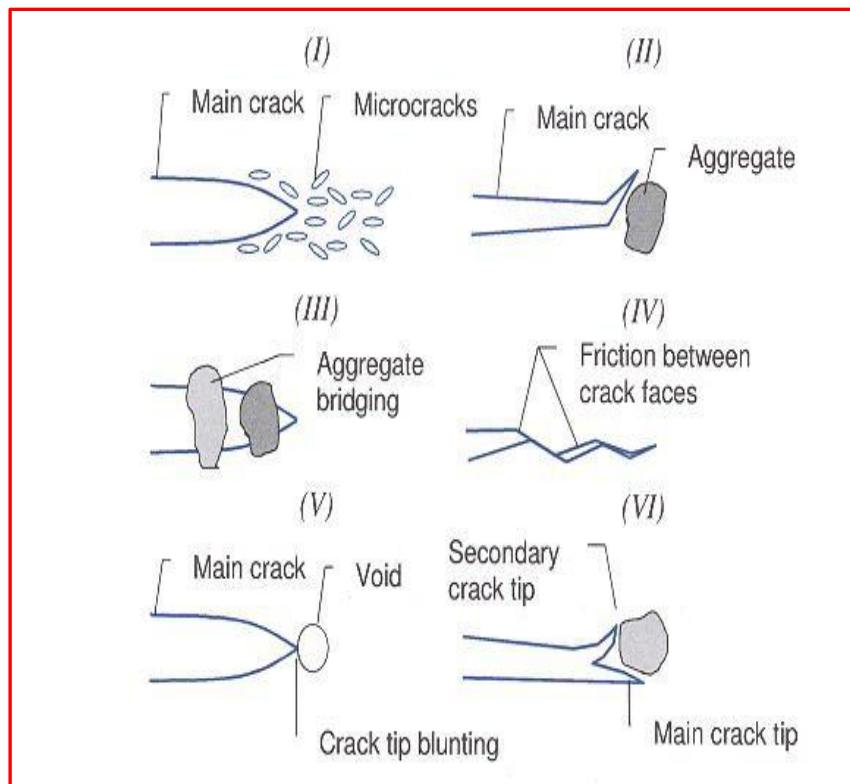


Fig.3.3: Some toughening mechanism in plain concrete (Shah et al., 1995)

When it comes to impact behaviour of concrete, not to mention from the University of British Columbia's civil engineering professors Sidney Mindess and Nemkumar Banthia would be a big disrespect. They have made very significant contribution to our understanding of the response of concrete to impact loading and showed that strain rate sensitivity of concrete is generally attributed to the visco-elastic nature of cement paste (a viscoelastic material whose rate sensitivity is controlled by the viscous time-dependent movement of free water through voids and pores), and to the time-dependent nature of crack growth as a function of the loading rate (Mindess et al., 2002). The rapid increase in strain rates experienced under impact loading conditions will drive a large number of micro-cracks (that already exist in the microstructure of concrete even before the concrete has been loaded) to grow simultaneously. Thus, the propagating cracks can be forced to develop along the paths of higher resistance, i.e. through the aggregate particles rather than growing around them (Zhang, 2008) which in turn results in an increase in strength, as schematically illustrated in Fig.3.4.

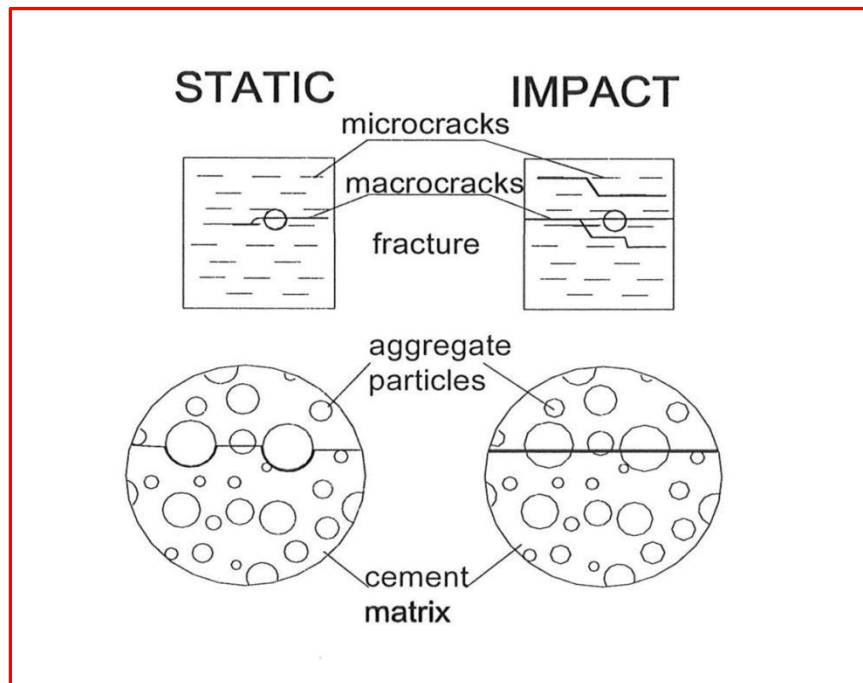


Fig.3.4: Differences between static and impact fracture (Zhang, 2008)

Unfortunately, previous studies on the impact phenomena in concrete have focused on determination of the number of cycles that leads to first crack and ultimate failure. Thus, our knowledge is scarce on the way in which concrete cracks and on the micro-cracking induced by impact loading. How the cracks propagate under impact; through the aggregate, the paste or the interface between the two, and what aggregate factors are most influential in deciding which of these happens?

An experimental study conducted by [Hughes and Gregory \(1972\)](#) on concrete subjected to high-rates of loading in compression showed that, of all of the concrete variables, the type of coarse aggregate plays the most important role in the resistance to impact. His view was supported by other researchers. [Zhang et al., \(2005\)](#) showed that if coarse aggregate is present, the degree of crack propagation may be dramatically reduced. Moreover, increasing the coarse aggregate content and decreasing the water-cement ratio may significantly contribute to the improvement of the impact resistance.

In a very recent work, [Rao et al. \(2011\)](#) attempted to study the physical and mechanical properties of recycled coarse aggregate (RCA) and their influence on the behaviour of recycled aggregate concrete (RAC) beams subjected to repeated drops of impact. Their analysis revealed that the recycled aggregate concrete is more sensitive to the high strain rate of loading, and the acceleration and maximum displacement of RAC are more than conventional concrete at a given impact energy (energy imparted by the hammer per blow) and they increased with the increase in drop number. This suggests that the lower stiffness and density in the case of RAC resulted in a lower velocity and higher displacement.

Another interesting finding was that the cracks initiated at the bottom vertically at or near the impact point in both conventional and RAC beams except in the RAC with 100 % RCA in which the cracks initiated away from the impact point (Fig.3.5). The failure in the RAC with 100 % RCA occurred through the aggregate in addition to those at the weaker interfaces between aggregate and old and new mortars. This could possibly provide much larger distances between the cracks (holding energy) and displace the site at which shock-wave induced stress exceeds a critical value and cracks begin.

[Wu et al. \(2010\)](#) carried out research to examine the dynamic mechanical properties of concrete with various contents of copper slag (CSRC) as a replacement of sand using a 50 mm diameter Split Hopkinson pressure bar system. Based on the results obtained, they found out that a significant difference in the microstructure of CSRCs was seen when the substituted amounts of copper slag exceeded 40 % such as larger voids, larger density of micro-cracks, wider capillary channels spacing and more voids and capillary channels connected together (Fig.3.6). This in turn led to a sharp decline of dynamic compressive strength of the concretes (Fig.3.7) as the weakest links of the internal voids and micro-cracks accelerate the damage of concrete forming a network of destructive fracture lines. The reason for such behaviour was attributed to “glassy” (smooth) surface texture of the copper slag particle that would diminish the cohesion between the cement paste and coarse aggregate and lower water absorption capacity compared to sand. Also, the low absorptivity of copper slag for water could cause excessive bleeding and consequently, a poor interfacial zone.

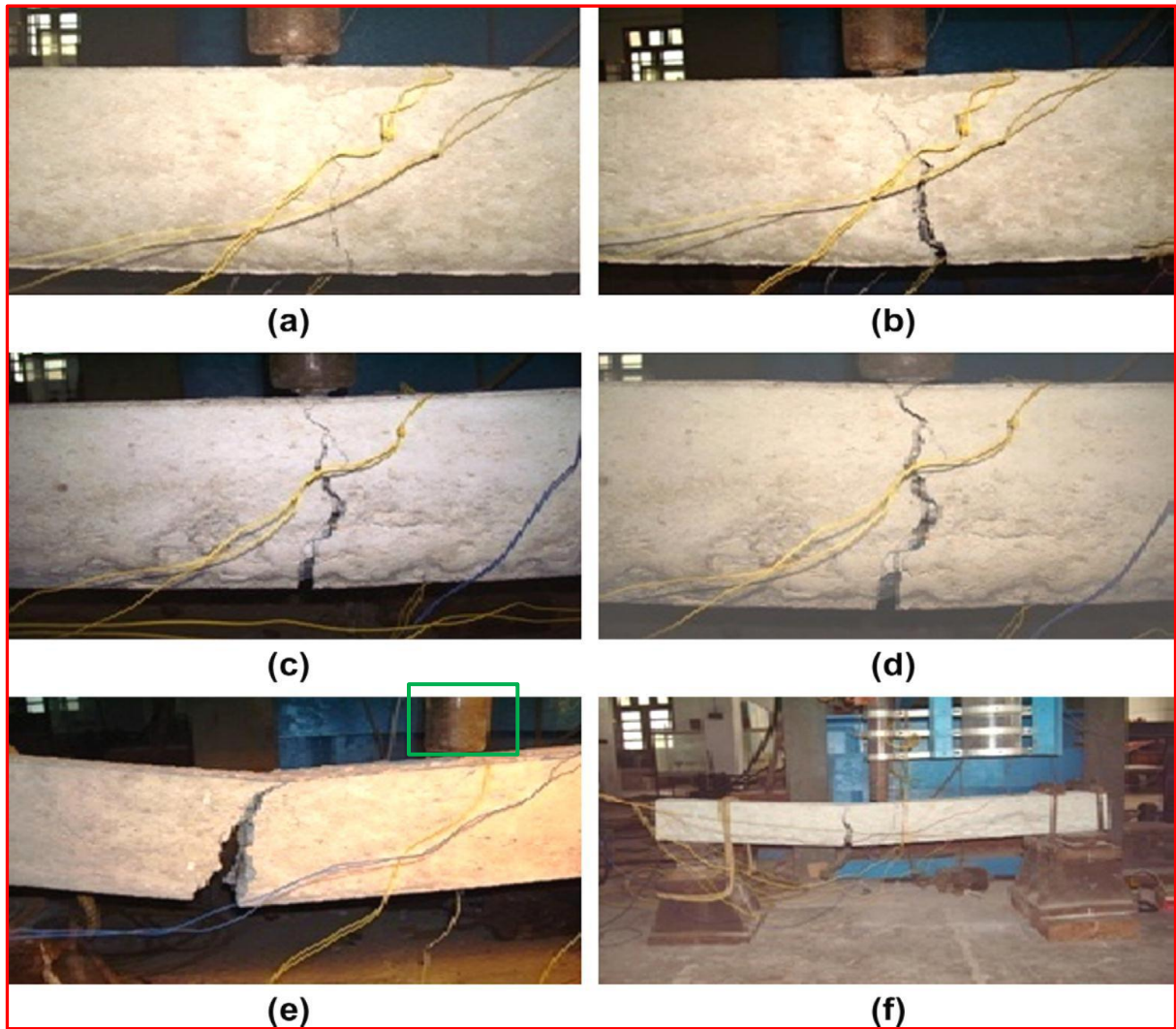


Fig.3.5: Crack pattern of both normal and RAC beams: a) and b) are normal concrete, c) RAC with 25 % RCA, d) RAC with 50 % RCA, e) and f) RAC with 100 % RCA ([Rao et al., 2011](#))

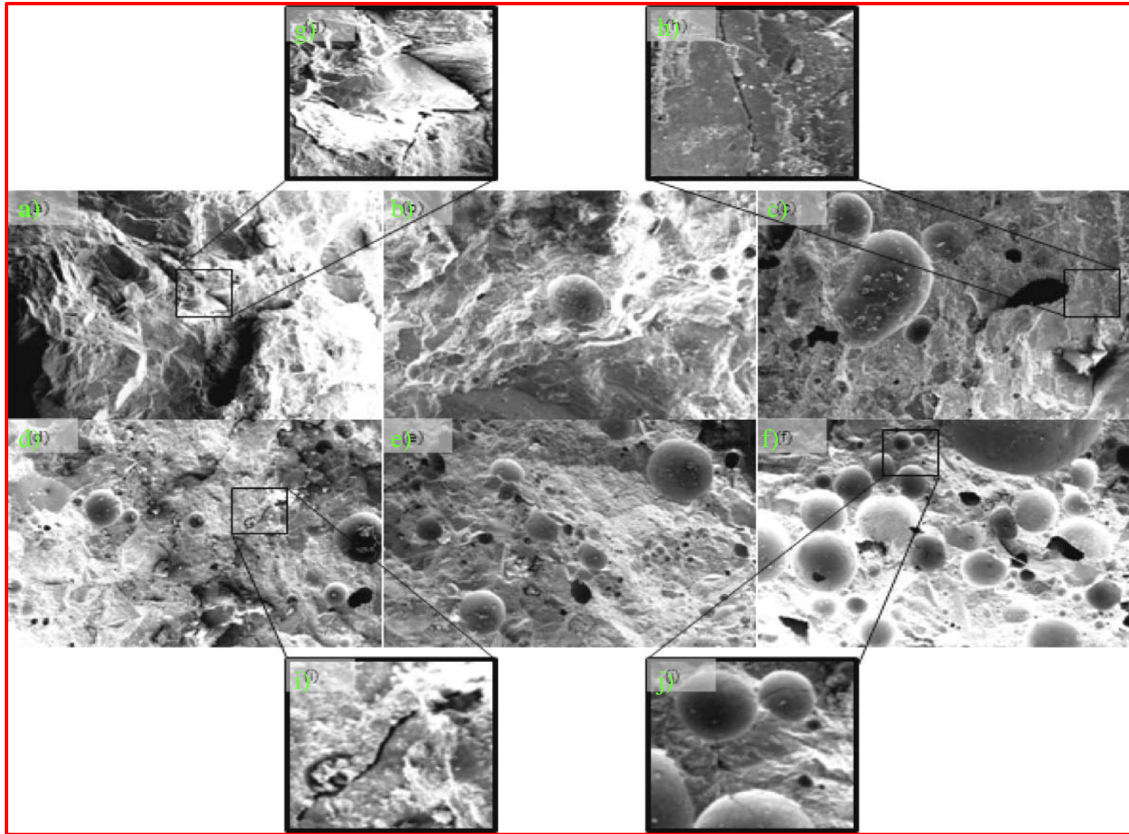


Fig.3.6: SEM micrograph of the CSRC (50 x): a) control concrete, b) concrete with 20 % copper slag, c) concrete with 40 % copper slag, d) concrete with 60 % copper slag, e) concrete with 80 % copper slag, f) concrete with 100 % copper slag, g) micro-cracks in control concrete, h) micro-cracks in the concrete with 40 % copper slag, i) capillary channel between pores in the concrete with 60 % copper slag, j) pores in the concrete with 100 % copper slag (Wu et al., 2010).

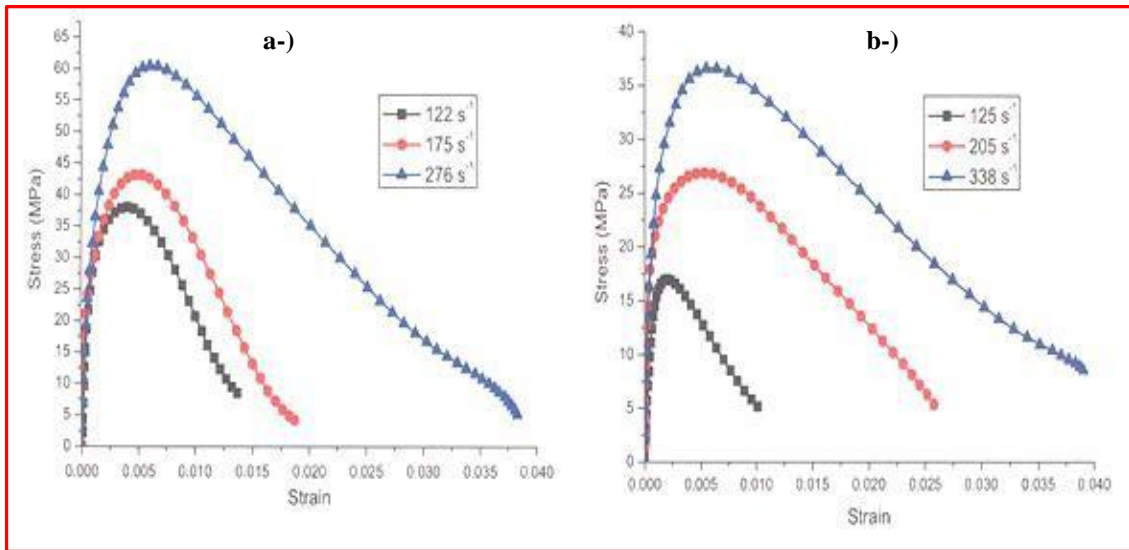


Fig.3.7: Dynamic compressive stress-strain relationships of a) control concrete and b) 100 % copper slag concrete (Wu et al., 2010).

A comprehensive quantitative micro-structural investigation performed by Elzafraney and Soroushian (2004) on normal-strength and relatively high strength concrete specimens subjected to different load and damaging environmental phenomena provided substantial insight into the performance and failure mechanisms of concrete. Their analysis revealed that relatively high-strength concrete experienced more extensive micro-crack growth under impact loading than normal-strength concrete; however it was observed that the number of micro-cracks per unit area in high-strength concrete was less than that in normal-strength concrete - this was attributed to the more brittle nature of high strength compared to normal-strength concrete. By contrast, under compression damage, the normal strength concrete exhibited more extensive micro-crack growth. The authors attributed, however, such behaviour to the concentrations of stresses around air voids, such voids being more frequent in the case of normal-strength concrete. This led to a conclusion that micro-crack characteristics are governed by significantly different mechanisms in normal and high-strength concretes under application of different damaging effects.

A further similar qualitative work from the same authors ([Soroushian and Elzafraney, 2004](#)) arrived at the conclusion that, for the concrete specimens subjected to impact loading, micro-cracks seem to still be confined to interfacial transition zone but a more pronounced increase in their widths is apparent when compared with undamaged specimens (see Fig.3.8 and 9).

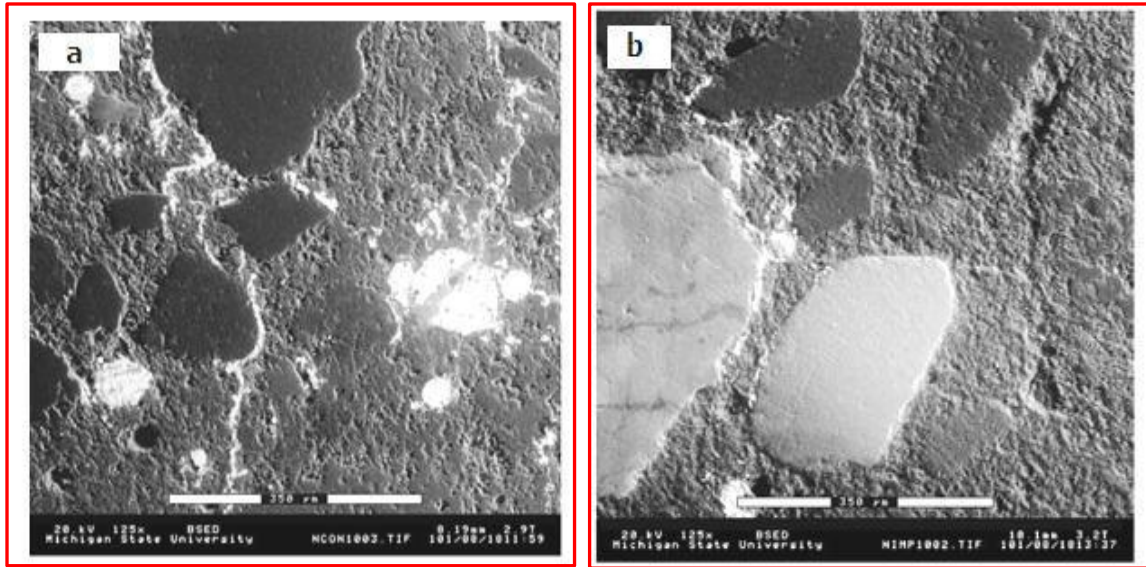


Fig.3.8: SEM for normal strength concrete: a-) no imposed damaging effect, b-) after impact damaging effect. White indicates a crack. ([Soroushian and Elzafraney, 2004](#)).

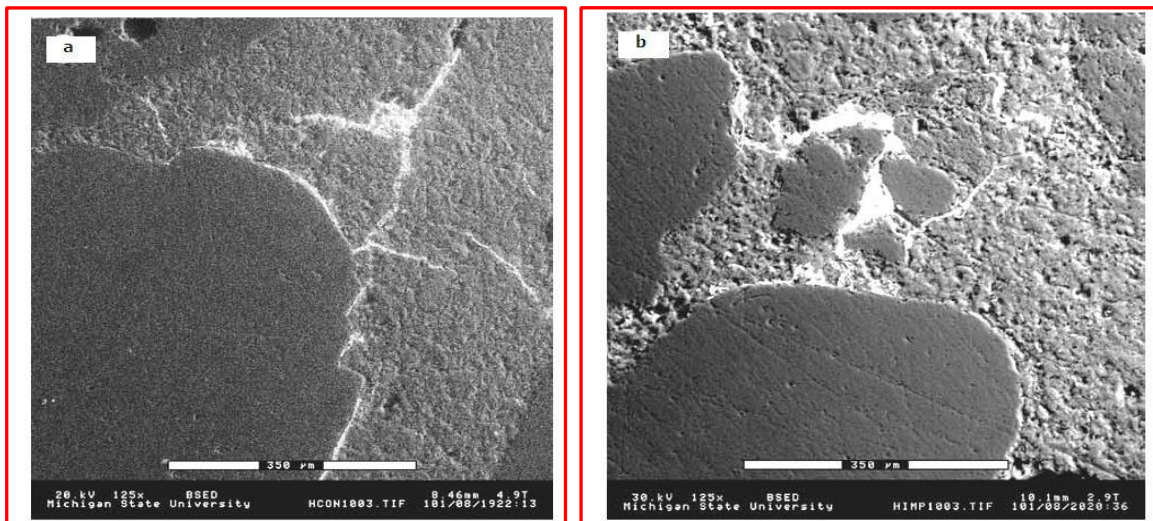


Fig.3.9: SEM for high-strength concrete: a-) no imposed damaging effect, b-) after impact damaging effect. White indicates a crack ([Soroushian and Elzafraney, 2004](#)).

Several researchers have demonstrated that fibre-reinforcement can be quite effective in improving the impact resistance of plain concrete (Nataraja et al., 1999; Song et al., 2005). Compared to plain concrete, for a fibre-reinforced concrete (FRC), there will be a combined effect of aggregate and fibre-bridging, and thus the critical crack opening and the fracture energy considerably increases (Fig.3.10- Löfgren, 2005). From the figure, three distinct zones would be highlighted as: a traction-free zone, which takes place for relatively large crack openings; a bridging zone, where stress is transferred by fibre-pull-out and aggregate bridging but the aggregate bridging has a relatively short working range in comparison to the fibres; and a zone of micro-cracking and macro-crack growth.

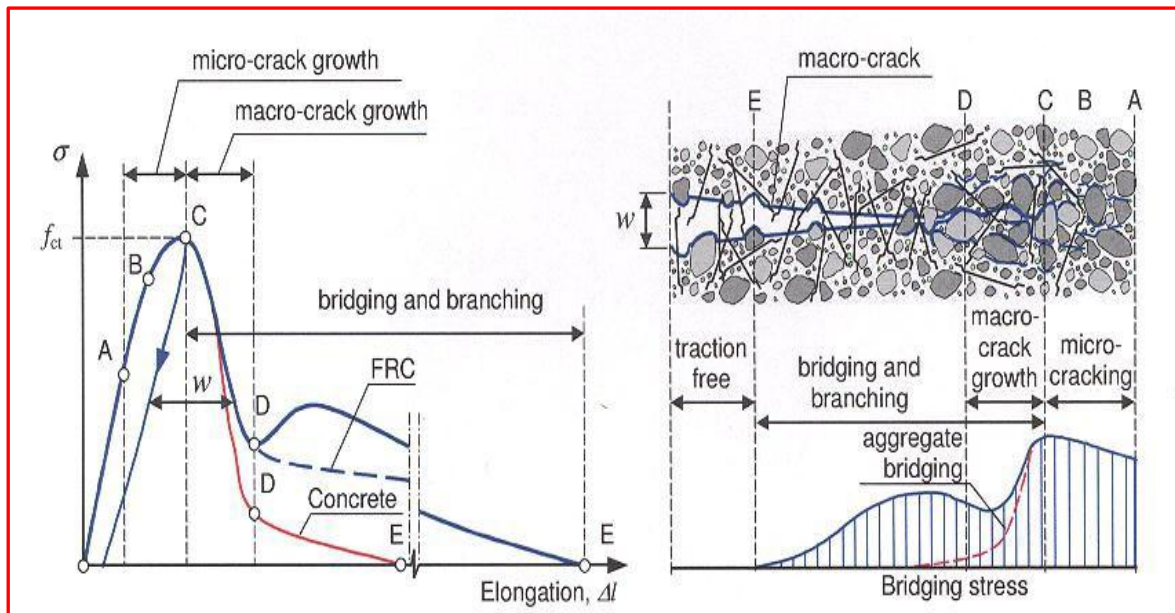


Fig.3.10: Schematic description of the effect of fibres on the fracture process in concrete (Löfgren, 2005)

An earlier experimental work by Swamy and Jojagha (1982) on the impact response of structural lightweight (pulverized fly ash aggregates-Lytag) concrete reinforced with steel fibres reported that the mode of failure of concrete under a repeated falling weight impact test

is closely related to the aggregate strength, as well as the matrix strength, the aggregate-matrix bond strength and with fibres, to the fibre-matrix bond strength.

Their experimental analysis showed that the predominant mode (72 % of failure) of fracture of plain lightweight aggregate concrete specimens occurred by failing in 3 pieces (see Fig.3.11a) signifying the tensile nature of the failure process likely due to (relatively) much lower particle strength and stiffness compared to the surrounding matrix and strong bond developed at the interface. By contrast, the concrete reinforced with long fibres with high aspect and surface irregularities produces a complex mode of failure under impact involving multiple cracking, crushing, shearing and disintegration (Fig. 3.11b). As can be seen from the cited studies, the major toughening mechanism in a plain concrete is mainly due to aggregate bridging mechanism, while in a fibre-reinforced concrete, fibres act as an additional bridging mechanism holding together the two sides of a cracked matrix.

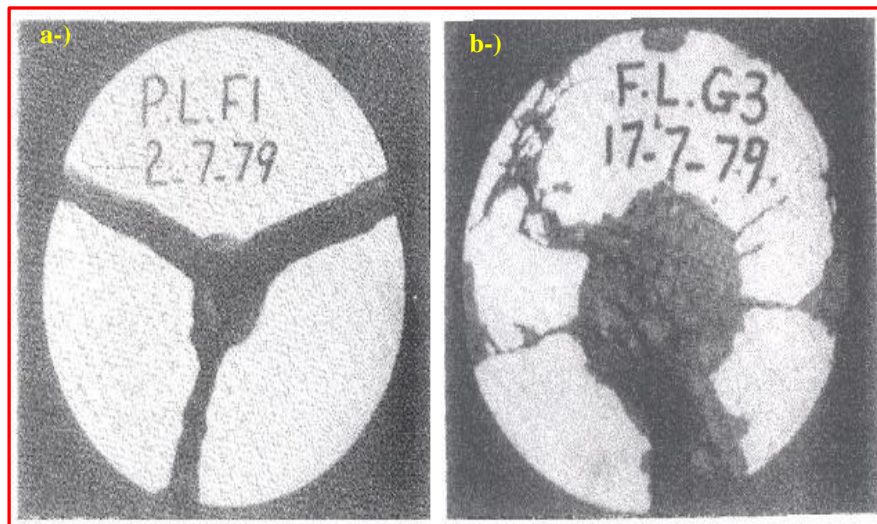


Fig.3.11: Failure modes of plain and fibre-reinforced lightweight concrete

(Swamy and Jojagha, 1982)

3.4 Analysis of Impact Resistance

3.4.1 Damage Mechanics

In the initial state, real materials generally contain already a multitude of defects such as voids and micro-cracks. During the deformation process, these internal flaws may grow and create new micro-defects. This leads to a change of the macroscopic properties of the material and its strength decreases. Such a process of structural deterioration of material which stems from the creation, growth and coalescence of micro-defects is called damage. It causes a complete loss of the material's integrity in the final stage and the formation of macroscopic cracks ([Gross and Seelig, 2006](#)).

Concrete is obviously damaged when subjected to impact loading. This damage could be internal, with no visible signs on the surface of the specimens; or external, with macro-crack until failure. Measurement of damage could be evaluated by a number of traditional methods such as variation of elastic modulus, or variation of density, or a reduction of strain energy. Fig. 3.12 displays an example of a load vs. deformation curves of a fibre-reinforced concrete (FRC) mix under impact loading conditions. The author reloaded the specimen under the static load and then measured the difference of elastic modulus between the virgin specimen and the impacted specimen to assess the damage of the FRC specimen. As can be seen from the figure, the author concluded that although the specimen did not break and there was no physical damage observed, its internal microstructure was deteriorated under impact loading.

However, with the development of highly-sophisticated material characterization techniques, researchers have obtained a chance to look at concrete in new, microscopic ways giving us new insights. Very recently, X-ray computed tomography coupled with digital image analysis technique was successfully employed by [Ying \(2010\)](#) to quantify the level of damage in

“asphalt” mixes in the dynamic complex modulus and the flow number tests. The author used a scalar variable ξ to quantify the levels of damage in the specimens as follows: $\xi = 1 - (\bar{A}/A)$ where A is the initial area of the undamaged section and \bar{A} is the effective cross sectional area in the current damaged state, which was calculated by subtracting the areas of air voids from the total cross sectional area. Fig.3.13 and 14 presents an example of his analysis. As shown in the figures, a significant increase in air voids occurred in the specimens after testing. The specimens had also highly heterogeneous air void distribution along the specimens` heights with much higher air void concentrations in the middle third of the specimens which is indicative of the damage taking place in a localized area of the specimen. Unfortunately, there is no such data reported in the concrete literature for the damage analysis of concrete under impact or any type of loading.

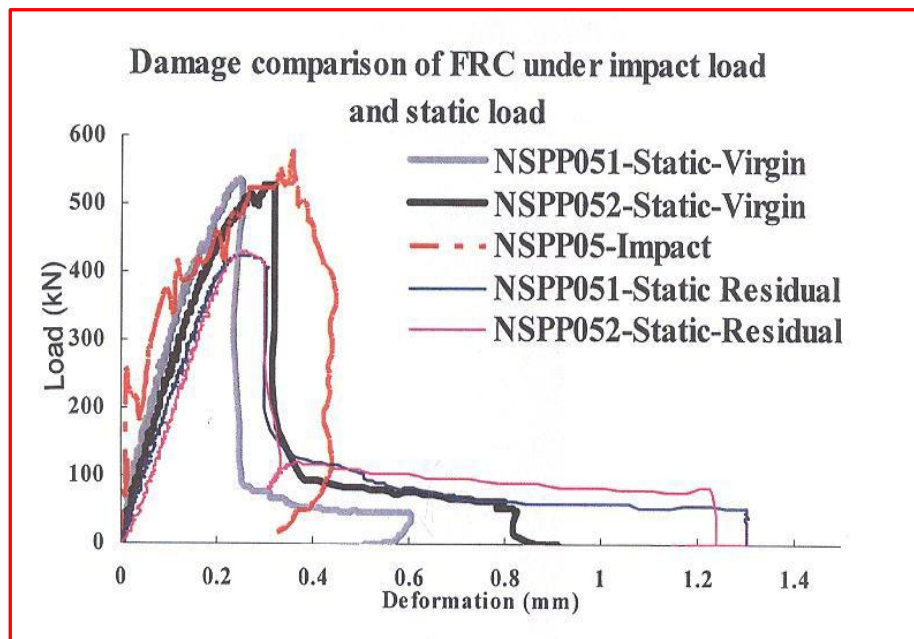


Fig.3.12: Load vs. deformation curves of a fibre reinforced mix under static and impact loading (Zhang, 2008).

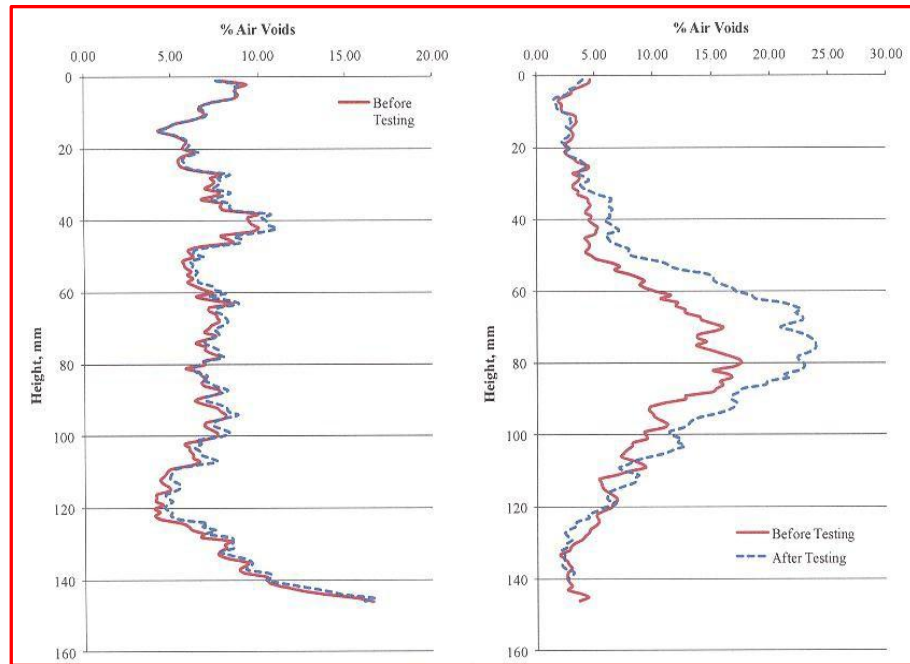


Fig.3.13: Air voids distribution along the depth of specimen (Ying, 2010)

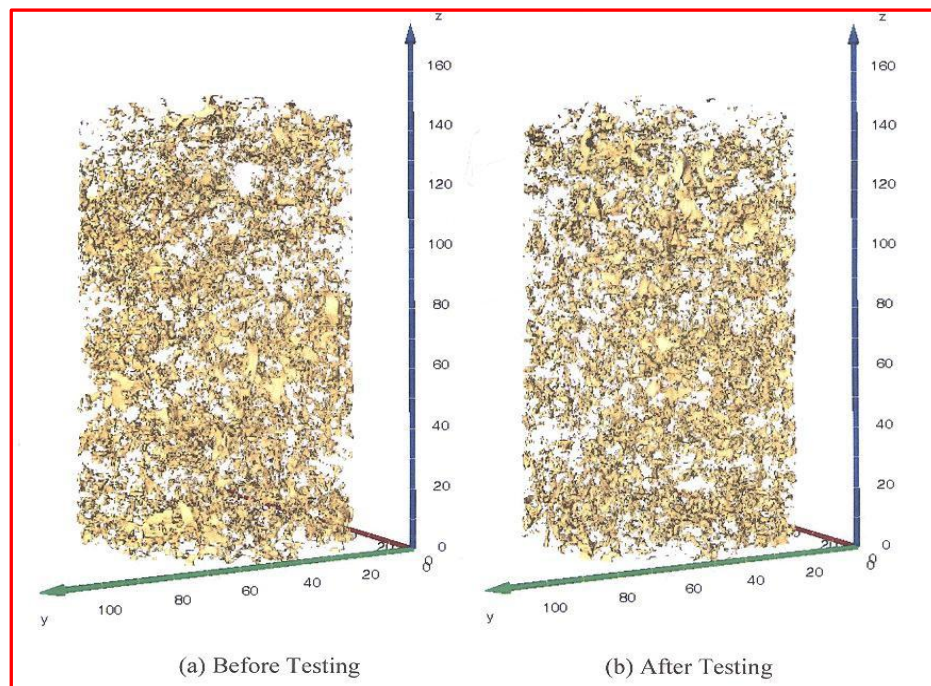


Fig.3.14: 3D air voids distribution along specimen depth (Ying, 2010)

3.4.2 Energy Dissipation

As is well-established (Banthia, 1989), the failure process for a brittle material consists of the breaking of the atomic bonds and the propagation of cracks. Since there is resistance to crack

growth (provided by aggregate, fibre or combined), energy has to be supplied to create new crack surfaces. However, in the case of concrete, the formation of a fracture process zone, which is a micro-cracked zone and exists at the tip of crack (Fig.3.15), requires energy and thus, the crack resistance in concrete consists not only of the surface energy component but also of the micro-cracking component.

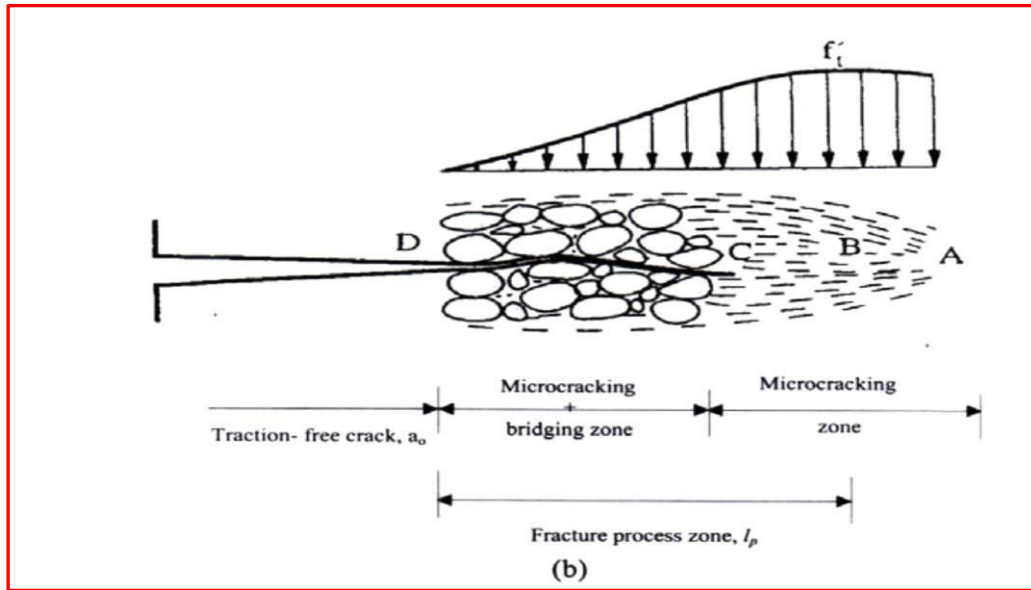


Fig.3.15: Fracture process zone in concrete (Shah et al., 1995)

Based on physical approaches, if a concrete material is subjected to an object of mass released from a defined height, a loss of potential energy is expected which is converted to elastic strain energy, leading to crack formations.

Using the impulse-momentum principle,

$$\int P(t) dt = m\Delta V \quad (3.1)$$

$$\Delta V = \sqrt{2gh} \quad (3.2)$$

P = contact impulse (force)

m = mass of the dropping object

g = earth`s gravitational acceleration

h =height of drop of the mass

ΔV = Velocity difference between V_0 and V_1 and

Hence $\int P(t) dt = m\sqrt{2gh}$

If the frictional and other loses of energy are ignored, the following equation can be written in accordance with conservation of energy;

$$\Delta E = E_1 - E_2 \quad (3.3)$$

E_1 = Potential Energy before impact

E_2 = Kinetic Energy during the impact

ΔE = Energy change

In the light of these formulas, the impact energy delivered to the specimen generated by each blow can be calculated as:

$$E = 1/2 * m * V_1^2 * N \quad (3.4)$$

E =Impact energy (N m)

m = mass of hammer (kg)

V_I =impact speed (m/s)

N =number of blows

If we assume $\Delta V = V_I$ (i.e. there is no rebound) and then $E = 1/2 * m * (2gh) * N = m * g * h * N$.

As the majority of fracture energy is dissipated by the propagation of surface macro-cracks ([Bazant et al., 1998](#)), a rough measure of fracture energy based on surface macro-crack could

be obtained the total macroscopic surface of the cracks might suffice to explain the energy difference between different mixtures. For this purpose, the formula suggested by [Guo et al. \(2007\)](#) can be also used as follows:

$$W_s/G_f = a * (\delta/a)^{1-D_{1-d}} \quad (3.5)$$

where W_s is the total energy dissipated at the surface of the crack; G_f is the fracture energy at the scale of observation δ (δ is equal to 5 mm- the maximum diameter of sand in concrete); a is the Euclidean length, which is equal to the height of the cross-section and D_{1-d} is the mean value of the fractal dimension of surface cracks on the fractured specimen.

3.5 Concluding Remarks

From this review of background information with reference to the cracking behaviour of concrete under impact loading, it is concluded that

- There has been no study to evaluate the influence of the local properties of the ITZ on the cracking behaviour of conventional/unconventional concrete under impact loading.
- The behaviour of concrete under dynamic loads differs significantly from the behaviour under static loading. This is fundamentally due to the strain rate sensitivity of concrete as a result of its unique microstructure. The generation and interaction of shock waves during an impact even seems the deciding factor on the macro-scale damage.
- It seems that the methods for evaluation of impact damage include variation of elastic modulus, loss of strain energy, and variation of density and so on. However, we need to look at the material response at micro-scale to fully answer the questions

of what happens in the microstructure during an impact event and how do changes at the micro-scale affect failure scenarios at a macro level?

- Although concrete damage originated by impact load is not common, recent natural disasters & terrorist attacks have led to new considerations of the impact response of concrete and concrete structures.
- A crack under impact loading requires more energy to grow than does a crack under static loading, and the higher fracture energy is dissipated under dynamic loading likely due to the increased micro-cracking.
- The incorporation of a small amount of fibres and/or larger aggregates in concrete may increase the fracture energy of concrete under impact loading, and thus the resistance of concrete to cracking. However, further investigations should be taken to understand the role of aggregate factors (stiffness, shape, density etc.) on the concrete cracking mechanism under impact.
- The aggregate bridging is the main toughening mechanism in a plain concrete. However, the heterogeneities and air voids in concrete can also increase the toughness (stress transfer capability) creating new crack branches or blunt tips.

References:

- [1] Banthia, N.P., (1987). “Impact resistance of concrete.” PhD Thesis. University of British Columbia, Canada.
- [2] Bazant, Z.P., and Planas, J., (1998). “Fracture and size effect in concrete and other quasibrittle materials.” CRC Press, Boca Raton, Florida.
- [3] Committee Euro International du Beton- CEB (1988). “Concrete structures under impact and impulsive impact loading.” Bulletin no. 187.
- [4] Clifton, J.R., (1982). “Penetration resistance of concrete a review.” Special Publication, National Bureau of Standards, Washington DC, 480-485.
- [5] Elzafraney, M., and Soroushian, P., (2004). “Assessment of micro-crack development in concrete materials of different strengths.” *Materials and Structures* 37 (10) 724-731.
- [6] Grote, D.L., Park, S.W., and Zhou, M., (2001). “Dynamic behaviour of concrete at high strain rates and pressures: I. Experimental characterization.” *International Journal of Impact Engineering* 25 (9) 869-886.
- [7] Gross, D., and Seelig, T., (2006). “Fracture mechanics with an introduction to micromechanics.” 4th Edition, Springer, New York.
- [8] Guo, L.P., Sun, W., Zheng, K.R., Chen, H.J., and Liu, B., (2007). “Study on the flexural fatigue performance and fractal mechanism of concrete with high proportions of ground granulated blast-furnace slag.” *Cement and Concrete Research* 37 (2) 242-250.
- [9] Hughes, B.P., and Gregory, R., (1972). “Concrete subjected to high rates of loading in compression.” *Magazine of Concrete Research* 24 (78) 25-36.
- [10] Lofgren, I., (2005). “Fibre-reinforced concrete for industrial construction- a fracture mechanics approach to material testing and structural analysis.” PhD Thesis. Chalmers University of Technology, Sweden.

- [11] Millard, S.G., Molyneaux, T. C. K., Barnett, S.C., and Gao, X., (2010). "Dynamic enhancement of blast-resistant ultra-high performance fibre-reinforced concrete under flexural and shear loading." *International Journal of Impact Engineering* 37 (4) 405-413.
- [12] Mindess, S., Young, J.F., Darwin, D., (2002). "Concrete." 2nd Edition, Prentice Hall.
- [13] Mouging, J.P., Perrotin, P., Mommessin, M., Tonnelo, J., and Agbossou, A., (2005). "Rock fall impact on reinforced concrete slab: an experimental approach." *International Journal of Impact Engineering* 31 (2) 169-183.
- [14] Nataraja, M.C., Dhang, N, and Gupta, A.P., (1999). "Statistical variations in impact resistance of steel fibre-reinforced concrete subjected to drop weight test." *Cement and Concrete Research* 29 (7) 989-995.
- [15] Rao, M.C., Bhattacharyya, S.K., and Barai, S.V., (2011). "Behaviour of recycled aggregate concrete under drop weight impact load." *Construction and Building Materials* 25 (4) 69-80.
- [16] Shah, S.P., Swartz, S.E. and Ouyang, C., (1995). "Fracture Mechanics of Concrete". Wiley, New York.
- [17] Song, P. S., Hwang, S., and Sheu, (2005). "Strength properties of nylon and polypropylene fibre-reinforced concretes." *Cement and Concrete Research* 35 (8) 1546-1550.
- [18] Soroushian, P., and Elzafraney, M., (2004). "Damage effects on concrete performance and microstructure." *Cement and Concrete Composites* 26 (7) 853-859.
- [19] Swamy, R.N., and Jojagha, A.H., (1982). "Impact resistance of steel fibre-reinforced lightweight concrete." *International Journal of Cement Composites and Lightweight Concrete* 4(4) 209-220.
- [20] Thilakarathna, H.M., Thambiratnam, D.P., Dhanasekar, M., and Perera, N., (2010). "Numerical simulation of axially loaded concrete columns under transverse impact and vulnerability assessment." *International Journal of Impact Engineering* 37 (11) 1100-1112.

- [21] Wu, W., Zhang, W., and Ma, G., (2010). "Mechanical properties of copper slag reinforced concrete under dynamic compression." *Construction and Building Materials*, 24 (6) 910-917.
- [22] Ying, H. (2010). "X-ray computed tomography to quantify damage of hot-mix asphalt in the dynamic complex modulus and flow number tests." MSc Thesis. Louisiana State University, USA.
- [23] Zhang, M.H., Shim, V.P.M., Lu, G., and Chew, C.W., (2005). "Resistance of high-strength concrete to projectile impact." *International Journal of Impact Engineering* 31 (7) 825-841.
- [24] Zhang, M.H., Sharif, M.S.H., and Lu, G., (2007). "Impact resistance of high-strength fibre-reinforced concrete." *Magazine of Concrete Research* 59 (3) 199-210.
- [25] Zhang, L., (2008). "Impact resistance of high-strength fibre-reinforced concrete." PhD Thesis. University of British Columbia, Canada.

CHAPTER 4

ASSESSING OF MECHANICAL BEHAVIOUR OF CONCRETE MIXTURES UNDER STATIC LOADING

4.1 General:

In this chapter, the mix composition, the properties of aggregates and the static mechanical properties of concrete samples in both compression and flexure are described. Aggregates are assessed with regard to their mineralogical, micro-structural, geometrical and physico-mechanical characteristics. The concrete properties discussed include compressive strength, flexural tensile strength, flexural fracture energy and static and (ultrasonic) dynamic modulus of elasticity. In addition, thermogravimetric and X-ray Computed Tomography analysis results are also presented here to assist in explaining in the static strength behaviour of the mixtures in terms heat of hydration and void characteristics. Finally, in the last section of this chapter, the concluding remarks are drawn.

4.2 Materials, Casting and Concrete Mix Design

4.2.1 Materials used

Considering local and industrial criteria, the following materials were chosen in this experimental study.

Cement: A general purpose blended fly ash Portland cement CEM II/ B-V 32.5 R conforming to [BS EN 197-1: 2000](#) was used as it is widely available and is currently one of the most extensively used cement types. Some of the physical and chemical properties of the cement (provided by the supplier) are given in Table 4.1.

Table 4.1 Physical and chemical properties of cement

Oxide	Determined as (%)
SiO ₂	31.2
Al ₂ O ₃	11.40
Fe ₂ O ₃	2.62
CaO	47.8
MgO	2.24
K ₂ O	0.64
Property	Determined as
Specific gravity	2.80
Blaine fineness	380

Fine Aggregate: Local river sand complying with the requirements of [BS EN 13139:2002](#) with a specific gravity of 2.66 Mg/m³ constituted the fine aggregate in the all mixes. The sand was air-dried in the laboratory. The grading curve of the sand used is given with the standard curves in Fig.4.1.

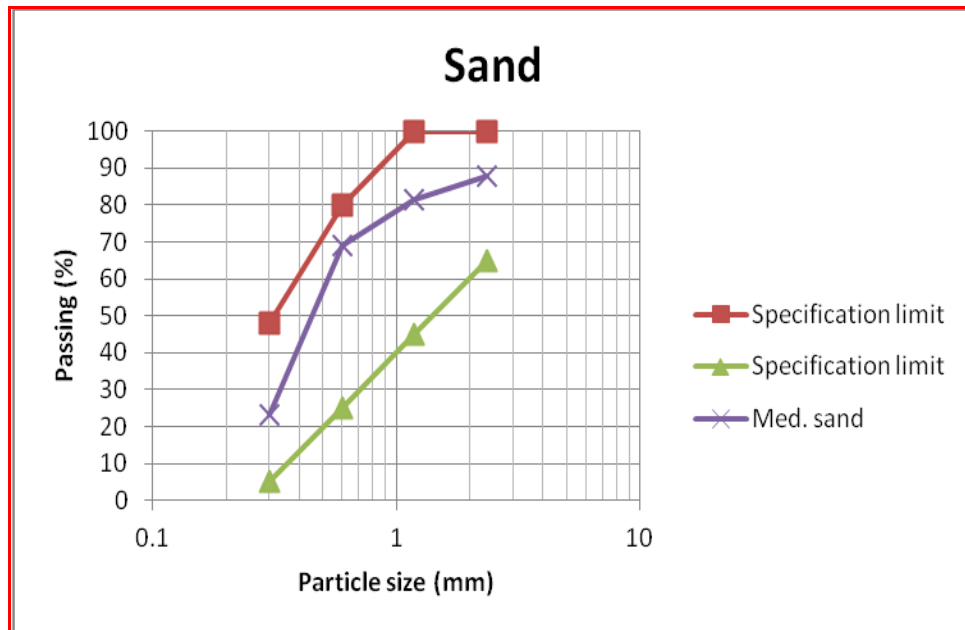


Fig.4.1: Grading curve of the fine aggregate

Coarse Conventional Aggregate: Uncrushed gravel sourced from a local quarry with a nominal maximum size of 10 mm was used to produce a reference mix. The grading curve of the gravel is displayed with the standard curves in Fig.4.2.

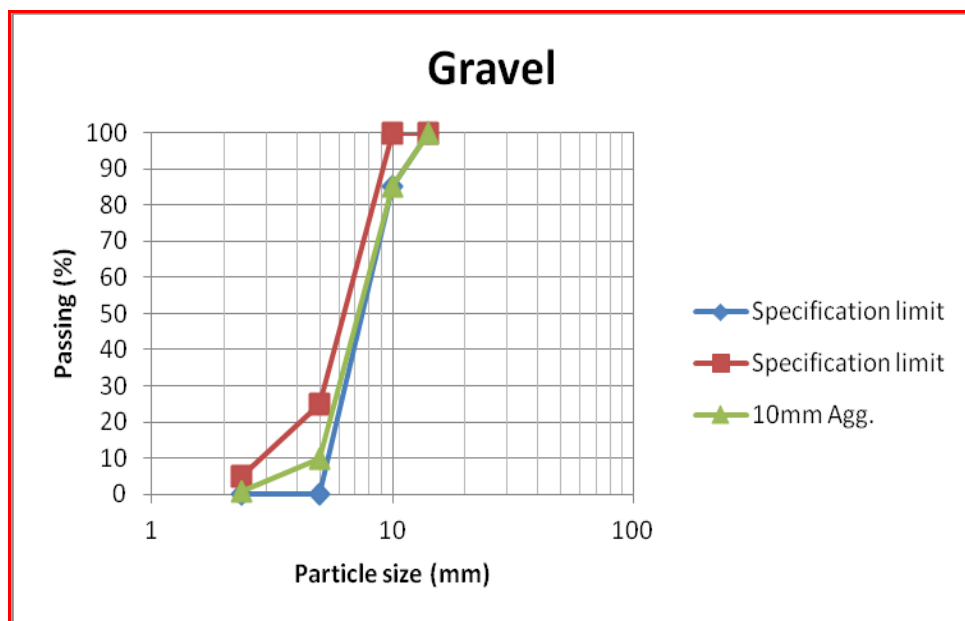


Fig.4.2: Grading curve of the coarse aggregate

Coarse Unconventional Aggregate: Since the main focus of this study is looking at how changes in the performance of concrete subjected to high rates of loading are related to

changes in the ITZ from the viewpoint of coarse aggregate properties, only coarse aggregates from different sources were used while the fine portion was obtained from one source only. Four different types of coarse unconventional aggregates were used: sintered fly ash, demolished blue brick, copper slag and chipped tyre rubber.

Fly ash/Lytag: One type of the unconventional coarse aggregates used in the production of the concrete mixtures was the sintered fly ash lightweight particles (commercially known as Lytag®) manufactured by pelletising the fly ash at a temperature of around 1100 °C. The Lytag particles have extremely porous and had quite rough surface texture which has potential to produce an excellent (strong and dense) interfacial zone. By contrast, the Lytag particles are inherently much weaker than the strength of the surrounding matrix, and strongly heterogeneous at the microscopic level which in turn might lead to a high level of fracture through the particles. Overall, in the case of the lightweight concrete, the aggregate properties were expected to play a profound impact on the overall damage mechanism under loading. The sintered fly ash was also considered due to its availability and consistent properties as well as its potential to offer many benefits in application including ([Kayali, 2008](#)): reduction of dead load, reduction in the sizes of beam and columns, less expensive handling and transportation equipment, higher thermal insulation and enhanced fire resistance.

Copper slag: Copper slag is an industrial by-product obtained during the matte smelting and refining of copper, and major constituents are sulphides and oxides of iron and copper ([Shi et al., 2008](#)). The high density of copper slag concrete may mean that it has greater radiation attenuation characteristics compared to conventional concrete and it has a potential to use in nuclear power reactors which have to be constructed against hazards such as a missile/falling plane or explosion. Among the aggregates used in this study, the copper slag particles had the

highest specific gravity and modulus of elasticity, and the second highest particle strength. Because of much higher strength of the copper slag in comparison with the paste, the interfacial zone and its properties were expected to become of major importance for micro-level damage initiation and propagation in copper slag concrete. In addition, this selection makes it possible to investigate whether the considerable different identities in Young's modulus and specific gravity between the copper slag particles and other constituents of concrete has any effect on the interfacial zone and correspondingly on the failure behaviour. It should also be noted that for every tonne of copper production, approximately 2.2 tonnes of slag is generated and about 24.6 million tonnes of copper slag are generated from world copper production ([Gorai et al., 2003](#)). Decreasing waste copper slag volume stored in landfills by recycling it in construction industry can also prevent environmental problems.

Tyre rubber: Rubber tyre particles are manufactured by processing (i.e. mechanical shredding) of the non-reusable tyres from the automotive industry, and can be classified into three categories: shredded or chipped tyre to replace gravel; crumb rubber to replace sand and ground rubber that may partially replace cement. Length and high elasticity were the most distinctive features of the rubber particles used in this study. The particles had also the smoothest surface texture and the lowest specific gravity. Use of such aggregates in concrete makes it possible to investigate the influence of much higher deformability/softness (low Young's modulus) of the rubber particles compared to the cement matrix on the crack-growth mechanism under loading. Furthermore, the intrinsic smoothness of the rubber particles may produce very poor bond strength (limited crack-arresting capacity), and thus the interfacial zone characteristics may play a profound impact on the overall damage mechanism. It is also worth mentioning that approximately 37 million scrap tyres were annually produced in the United Kingdom in 2002 ([Martin,2002](#)). For many countries, burning the tyres and using as

fuel is still the most preferable strategy which leads to serious environmental hazards (Toutanji, 1996) which could be reduced if scrap rubber could be used in concrete.

Blue brick: New solid blue bricks (free from impurities) of 215x102.5x65 mm working sizes were crushed down into a coarse aggregate and used to produce concrete. The brick samples have an impervious and very hard surface, low water absorption and the highest particle strength. Moreover, the brick samples are composed of angular particles and have a little higher particle density than the natural mineral aggregates. In the case of the blue brick concrete, the interface between the particles and the matrix is expected to represent the weakest link of the composite, and thus the failure mechanism would almost totally be controlled by the bond properties. Use of such aggregates makes it possible to observe how strength incompatibilities between the aggregate and the matrix would affect the bond characteristics, and how a dense, stiff and very low porosity aggregate could change the bond properties compared to highly porous and rounded shape as for the fly ash/Lytag aggregate.

Gravel: Natural gravel forms a major and fundamental part of aggregates for making Portland cement concrete (Smith and Collis, 2001). In the United Kingdom, approximately 151.4 million tonnes of primary aggregates were consumed in 2005 by the construction industry, and almost half of this amount consists of natural mineral aggregates (sand and gravel) (British Geological Survey, 2008). On this basis, the uncrushed gravel samples obtained from a local quarry (in the Trent Valley at Rampton Nottinghamshire, UK) were selected as the reference aggregate in this study.

Fibres: Two groups of fibres; one of hooked-end Dramix ZP 305 steel fibres and one being Barchip synthetic macro fibre (SSM), also known as elasto-plastic fibre, were used in the

lightweight mixture, as shown in Fig.4.3. Some important physical and chemical properties are reported in Table 4.2, as provided by the manufacturers.



Fig.4.3: Steel fibres (a) and synthetic macro fibres (b) used for concrete reinforcement

Table 4.2 The physical and mechanical properties of fibres

Fibre type	Density (gr/cm³)	Tensile strength (mm)	Elastic modulus (GPa)	Cross section	Length (mm)	Diameter (mm)
Steel fibre	7.85	1100	150	Circular	30	0.55
SSM fibre	0.92	550	10	Rectangular	48	0.90

4.2.2 Mixture proportions

All the concrete mixtures were designed by the volume method, and the mix proportions are tabulated in Table 4.3.

Table 4.3: Mix proportions for 1 m³

Material (kg/m³)	Cement	Water	Fine Aggregate	Coarse Aggregate
Quantity kg/m³)	330	198	678	1115

In all mixes, the volume fractions of cement, coarse aggregate, sand and water for hydration were the same. The gravel aggregates (reference) were totally replaced by the unconventional coarse aggregates. Thus, the only difference was the type of coarse aggregate used in the mixtures. Before mixing, the coarse aggregate were first immersed in water for 24 hours until all particles were fully saturated. The aggregates were then spread on a board and left to air-dry for 24 hours. In this condition, the coarse aggregates should absorb no water during mixing and thus requiring no alteration to the quantity of mixing water. The same size percentages were selected for the coarse conventional and unconventional aggregates to eliminate the effect of grading difference on concrete performance. The steel and synthetic fibres were also incorporated in some of the mixtures. Considering practical applications and the literature, the fibre volume was chosen as 1 % by volume of concrete.

4.2.3 Mixing, specimen preparation and curing

In mixing, the dry ingredients (cement, sand and coarse aggregate) were initially blended for 2 min. Then, the water was gradually added and mixed together for another 3 min. For the fibre-reinforced mixes, the fibres were then added and mixed for an additional 3-5 minutes. The fibres were carefully sprinkled by hand in small amounts on the surface of the mix to avoid fibre balling, and thus achieve uniform fibre distribution.

After the mixing process, the fresh concrete was filled into steel moulds in two layers and then compacted by using a vibration table. The concrete in the moulds was then covered with plastic sheet to prevent excessive surface moisture loss. Thereafter, the specimens were left in their moulds for 24 hours. The specimens were demoulded after that and immediately placed in a tank at 20 ± 2 °C. Cubes, prismatic, cylinders and disks were cast for the different tests. All the tests were carried out at an age of 28 days.

Cubes of 100 mm were used for the compressive strength and density tests. Prisms of 100 x 100 x 500 mm were used for flexural strength, flexural toughness parameters and fracture energy. Cylinders, 150 mm in diameter and 300 mm long were used for determining the modulus of elasticity and stress-strain relationships. Disks, 150 mm in diameter and 50 mm in thickness, were used for the impact resistance.

4.3 Test Procedures and Apparatus for Aggregate

4.3.1 X-ray diffraction analysis

X-ray diffraction analysis is best suited for materials with crystalline phases in which the atoms are aligned in regular patterns. This structure enables each atom to produce a characteristic diffracted pattern when subjected to an incident ray. The pattern is produced in accordance to Bragg's Equation.

$$2d\sin\theta^* = n\lambda \quad (4.1)$$

Where

d – the distance between lattice planes in the crystal

θ^* – is the incident/diffracted angle

n* – is an integer

λ^* – is the wavelength of the scattered wave

This formula shows where constructive interference is obtained from the scattered waves reflecting from the lattice planes in the microstructure of the material and hence enables identification of the crystal structure of the sample.

The samples for this test were prepared in a manner similar to those in the TGA analysis. The drying of the sample removed the amorphous phase and finely ground particles improve the surface conditions for diffraction. The samples were placed and levelled in the sample holder and then positioned in the chamber of the Bruker –AXS D8 Advance XRD equipment (see Fig.4.4) which has a Cu-anode x-ray tube, a Göbel mirror, a diffracted beam collimator with a 0.12° Soller slit, and a Sol-X energy-discriminating x-ray detector set to $\text{CuK}\alpha$ radiation. The scanning was conducted between 5 and 70° at a speed of 2° per minute.

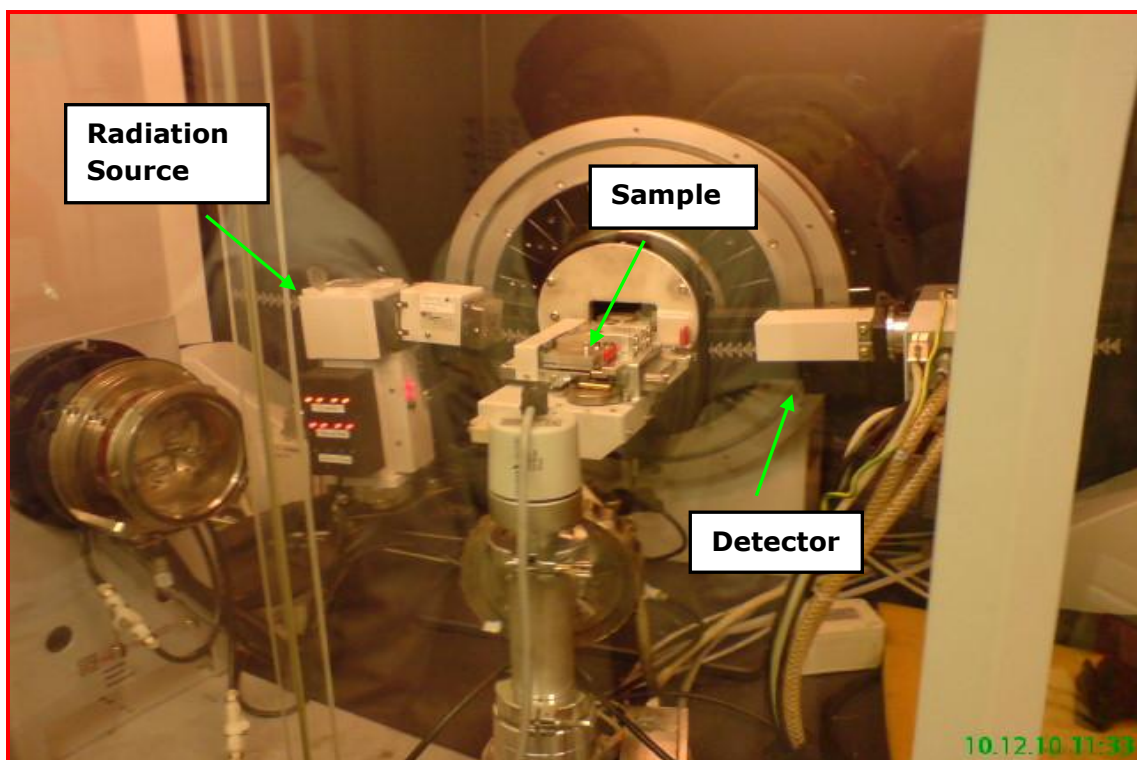


Fig.4.4: Bruker –AXS D8 Advance XRD equipment

4.3.2 Quantification of aggregate shape parameters

A digital image processing (DIP) technique was used to analyze the particle shape characteristics of the coarse aggregates. Image acquisition was performed by the author using a Cambridge Instrument Quantimet 570™ DIP system connected to a CCD camera. Fig.4.5 shows the set up of the system. A sheet of card paper with different colours and different light levels were tried to produce an image with good intensity. After acquiring the images, a computer software program (Image Pro+™) was used for the quantification of aggregate shape characteristics. The main parameters calculated were roundness, angularity and fractal dimension.

The analysis of the processed aggregate images was carried out by the quantification of several geometrical parameters to determine the shape characteristics. As stated [Al-Rousan et al., \(2007\)](#), roundness is measured from a two dimensional image by the following equation:

$$Roundness = \frac{(Perimeter^2)}{4\pi Area} \quad (4.2)$$

A circular object has roundness of 1.0 and a higher value indicates other shapes. Similarly, angularity is calculated using formula given by [Kuo and Freeman \(2000\)](#) in the form of:

$$Angularity = \left(\frac{Perimeter_{convex}}{Perimeter_{ellipse}} \right)^2 \quad (4.3)$$

A circle or an elliptical aggregate will have an angularity of 1, while angular particles have angularity values larger than 1.

The fractal dimension is the fractal dimension of the object's outline and generally used to characterise the irregularity of the aggregate shape profile. The software can directly estimate

it. A circle aggregate will have a fractal dimension of 1, while longer or thinner shapes or particles having rough edges have fractal dimension values larger than 1 (Carr et al., 1990).

Figure 4.6 shows the list of geometrical parameters both Euclidian and fractal geometry which are estimated by the own software.

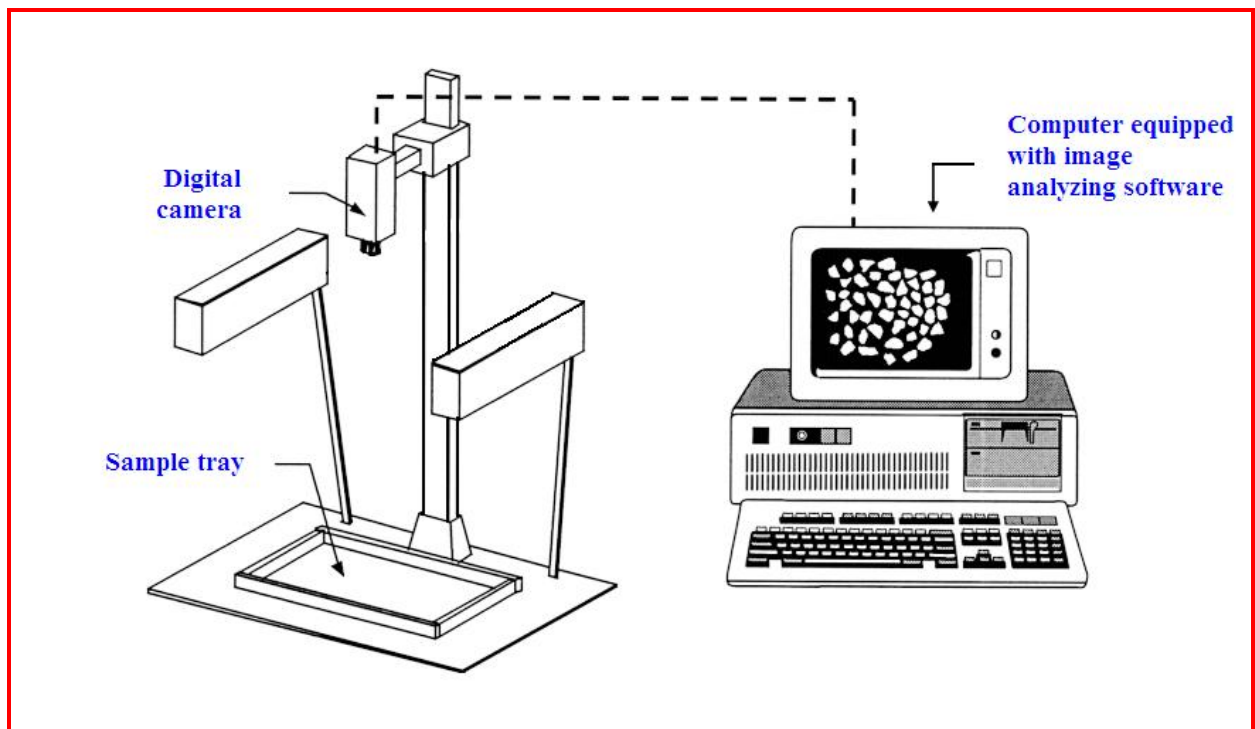


Fig.4.5: Schematic view of image analyzer set up (Adapted from Kwan et al., 1999)

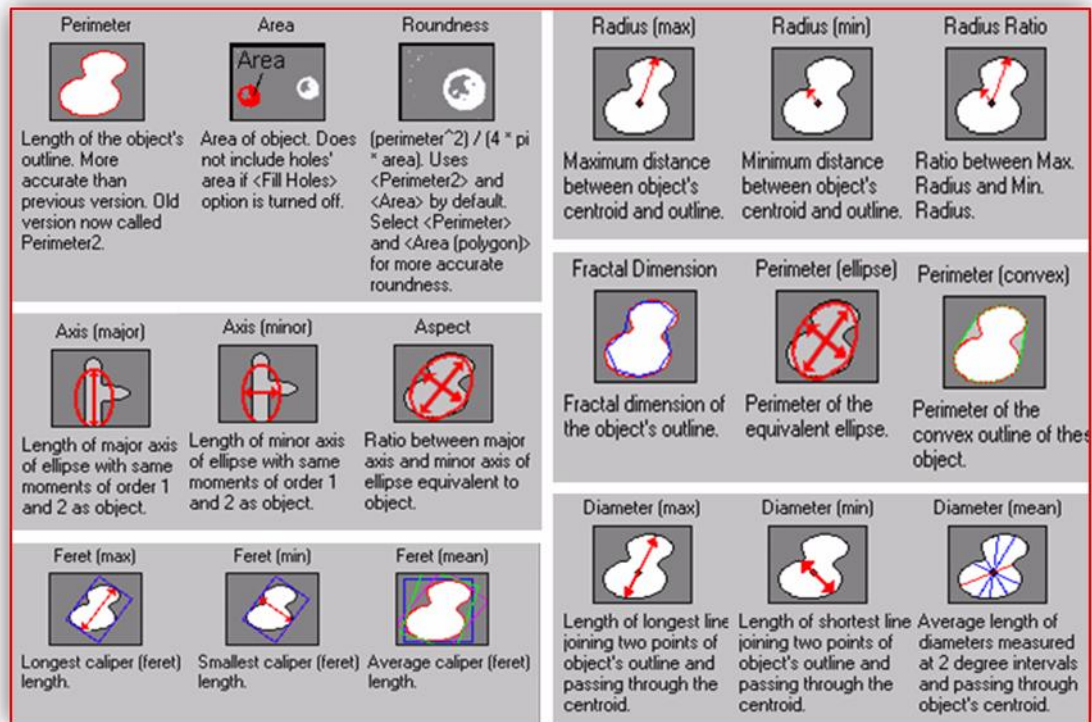


Fig.4.6: Measurement in Image Pro Plus Version 4.5

4.3.3 Surface texture analysis with optical microscope

The surface texture of aggregate particles can range from glassy, through smooth, granular, rough and crystalline, to honeycombed according to BS 812-102 (1989). The surface characteristics of the aggregates were evaluated by means of a Nikon optical microscope with 20x optical magnification. The microscope was equipped with a digital camera.

4.3.4 Total porosity (mercury porosimetry) of aggregates

Pore structure (total porosity and pore size distribution of aggregates) were evaluated by mercury porosimetry with a pressure applied up to 410 MPa. Aggregates with a diameter of smaller than 8 mm were used for the analysis. A small specimen is first dried. Then, it is weighed and transferred to the chamber and subsequently the mercury is introduced to the surrounded specimen.

4.3.5 Surface roughness by contact surface profilometer

Surface roughness of the aggregates used was measured by stylus profilometry using a 2D Mitutoyo Surftest SV 662 profiler with 5 μm stylus, as schematically shown in Fig.4.7. A similar concept to the micro roughness of concrete after impact loading was adopted to evaluate the surface roughness of the aggregates. An auto drive unit was used to measure an evaluation length of 12.5 mm at a speed of 0.5 mm/s. Only asperities bigger than 0.8 μm were assessed.

4.3.6 Physico-mechanical properties of aggregates

The aggregates were also assessed for impact value, the modulus of elasticity, specific gravity and water absorption capacity. The modulus of elasticity of the aggregates was calculated using the formula given by Muller-Rochholz (1979), namely $E_a = 8.1\rho_a^2$ where ρ_a is the density of aggregate.

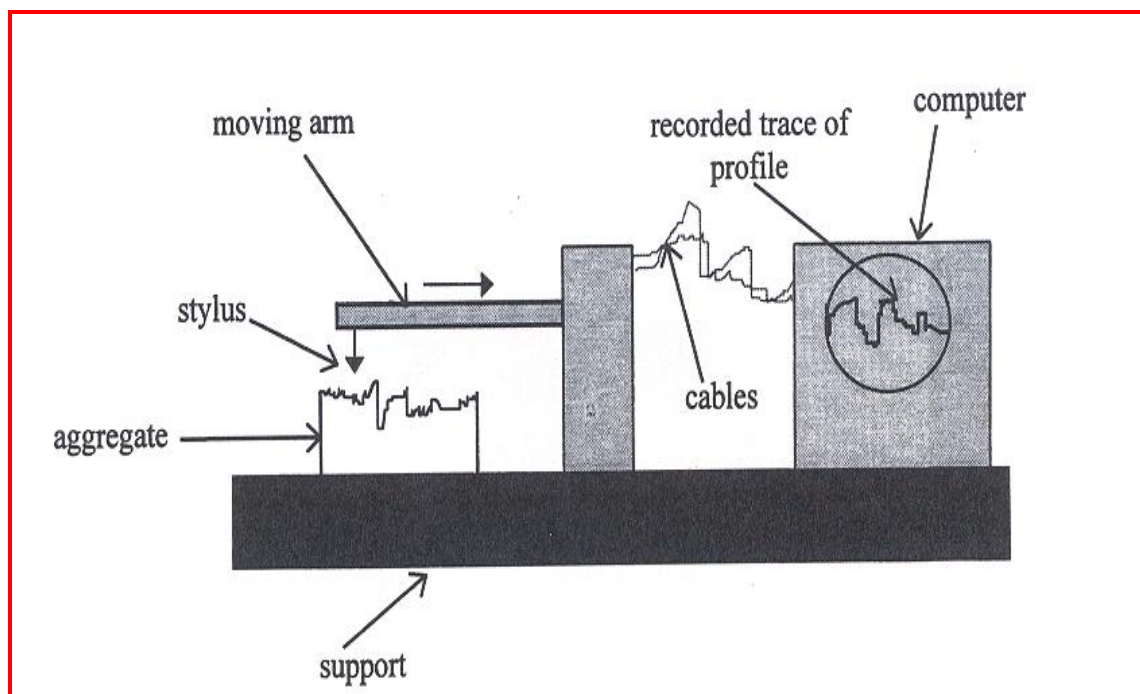


Fig.4.7: Surface profilometer for aggregate roughness (Tasong et al., 1998)

4.4 Routine Mechanical Tests for Concrete

4.4.1 Compressive strength

Compressive strength tests were performed on 100x100x100 mm cubes of three companion specimens at the age of 28 days. The procedure followed during the test was in conformity with [BS EN 12390-3 \(2002\)](#).

4.4.2 Static elastic modulus

The modulus of elasticity of the mixtures was determined using 150 x 300 mm cylinder specimens. Two specimens were tested for each concrete batch at the age of 28 days. The specimens were end-capped using sulphur mortar prior to testing to ensure parallel loading faces and thus to prevent stress concentrations. Each specimen was fixed with four potentiometers at different quadrants to measure the deformation, as shown in Fig.4.8. The test was carried out in accordance with [BS 1881-121 \(1983\)](#). During the testing, all specimens were loaded in the form of cyclic loading. The first two loading cycles were progressively applied until the stress was equal to one-third of compressive strength while the third cycle was applied until the failure of specimens. The load and deformation values were recorded. The static modulus of elasticity in compression was determined from the slope of the stress-strain curves during unloading.

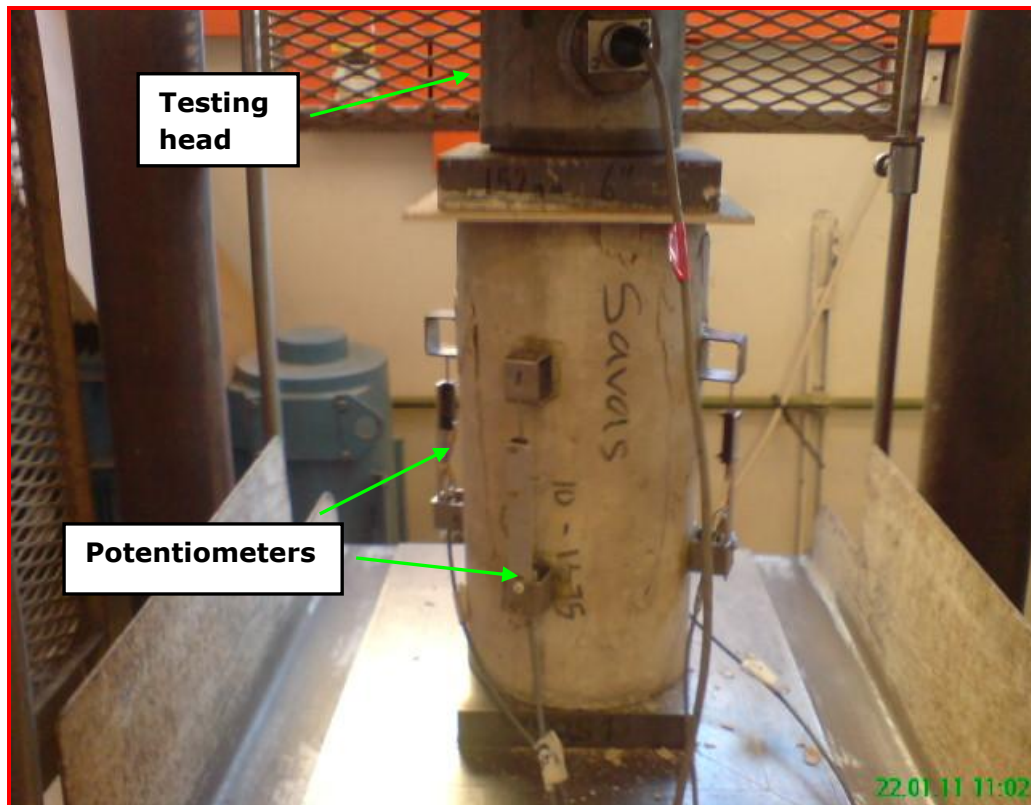


Fig.4.8: Elastic Modulus Test Set Up

4.4.3 (Ultrasonic) Dynamic modulus of elasticity

The dynamic modulus of elasticity of prismatic specimens was determined using a commercially available non-destructive ultrasonic device known as PUNDIT (Portable Ultrasonic Non-destructive Digital Indicating Tester). The measurements were conducted with the transducer firmly coupled to the opposite ends of the specimens using a coupling gel between the transducer and the specimen.

4.4.4 Flexural response and fracture energy

The flexural fracture toughness parameters of the mixtures were determined by testing prism beams having a size of 100x100x500 mm as shown in Fig.4.9. Duplicate specimens were manufactured and tested for each mix. The tests have been performed using a closed-loop deflection controlled Zwick 1484 universal testing machine with a capacity of 200 kN at a

constant deflection rate of 0.10 mm/min. The load was applied through the head of the machine to the top face of the specimen at the mid-span. A steel plate is positioned between the loading head and the specimen to distribute the load over the beam. The head of the test machine was initially lowered so that it was touching but not loading the top steel plate.

Two linear variable differential transducers (LVDTs) were also mounted using a yoke arrangement to measure the deflections at the mid-span of the prisms. The deflections obtained from the LVDTs were averaged and recorded as the net mid-span deflection, ignoring the support deflections. The data were acquired by a PC-based data acquisition system, and then the complete load-deflection curves were plotted via an X-Y plotter for each test specimen. From the load-displacement curves, first cracking loads, defined as the point where the slope of load versus displacement curve first exhibits a deviation from linear elastic behaviour, and the maximum loads as well as displacements at these loads were determined. Moreover, these curves were also analysed to determine flexural strength, and fracture toughness.

The concept of toughness indicates the ability of energy absorption in a failing specimen and can be evaluated on the basis of the area beneath the post-peak portion of the load-displacement curves. In the present work, the flexural toughness was determined using the [ASTM C 1018-1989](#) and [JSCE SF4-1983](#) test methods since they are the most widely used and reported methods for characterising fibre reinforced concrete behaviour.

The ASTM toughness parameters defined in Fig.4.10 are I_5 , I_{10} and I_{20} and calculated by considering the ratios of the area under the load-deflection curve up to a deflection that is 3, 5.5 and 10.5 times the value at first crack detection, divided by the area under the stress-

deflection curve up to the occurrence of the first crack, respectively. On the other hand, in JSCE SF4, the main parameter derived from the toughness (T_{JSCE}) was equivalent flexural strength using the following equation:

$$\sigma_{eq} = [T_{JSCE}L]/[\delta_{JSCE}bh^2] \quad (4.4)$$

where T_{JSCE} is the energy absorbed up to a deflection of 1/150 of span (kN-mm), δ_{JSCE} is deflection of 1/150 of span (mm), and L , b and h are the span, width and depth of the specimen, respectively.

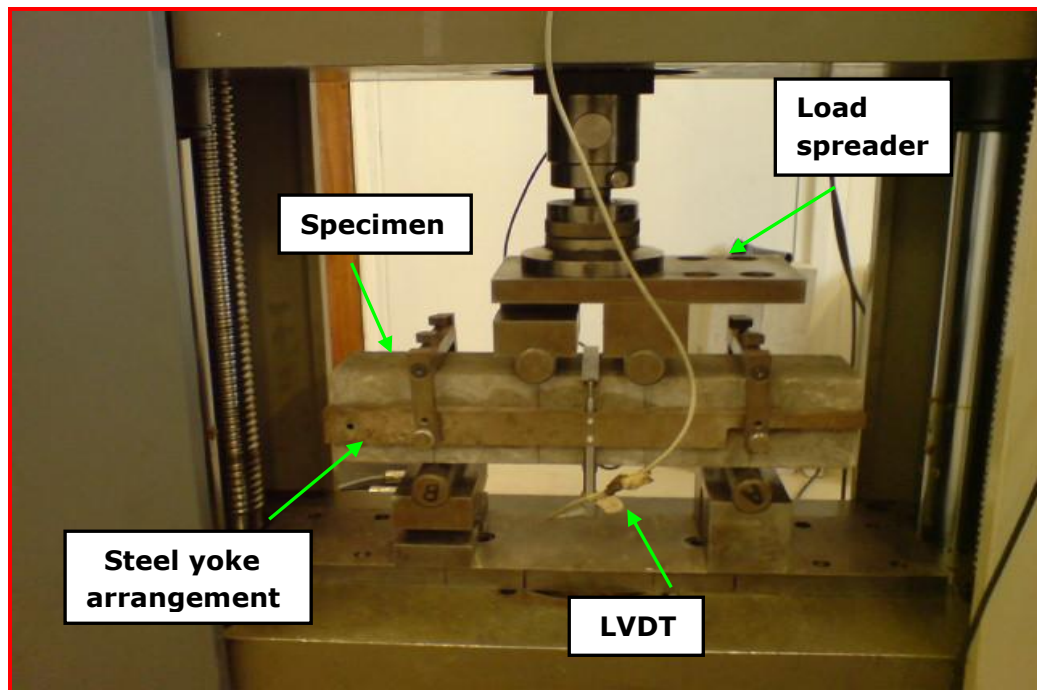


Fig.4.9: Instrumentation of the concrete beam used for the four-point bending test

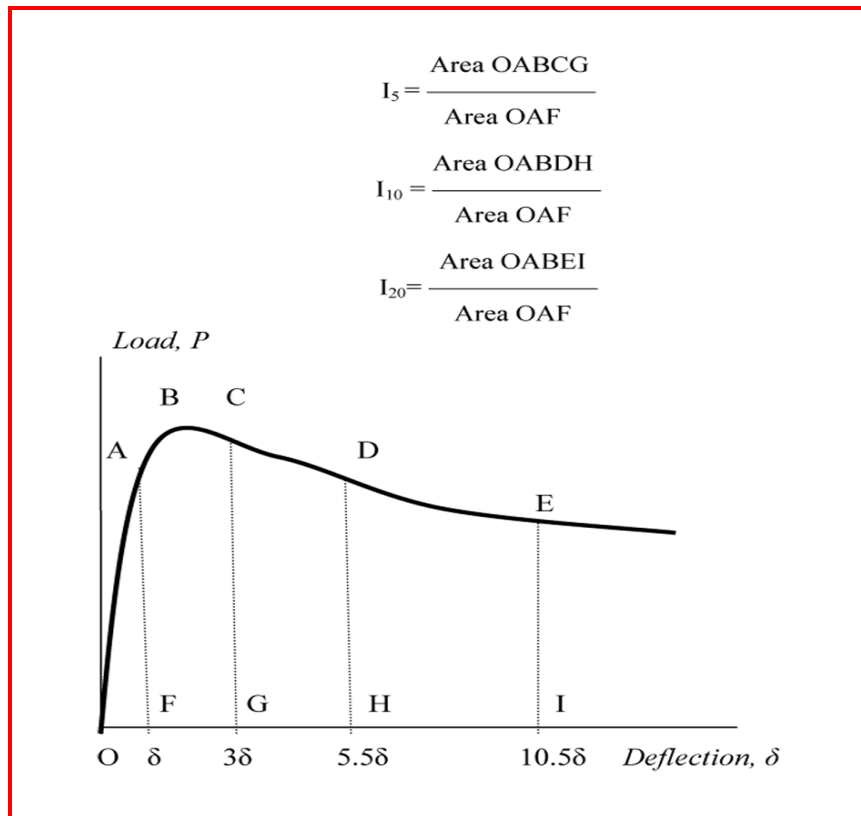


Fig.4.10: Definition of flexural toughness indices: δ is deflection at first observed crack
(ASTM C 1018-1989)

4.5 Thermogravimetric analysis

Thermogravimetric analysis (TGA) was conducted on the hardened mortar samples taken from the crushed concrete cubes after 28 days of curing to determine the quantity of Ca(OH)_2 formed in the mortars. The mortar fragments taken were then pulverised and passed through the 75 micron sieve. Approximately 10 mg of the fraction passing 250 micron sieve was used for chemical analysis.

The samples were placed in pre-weighed aluminium containers and sealed with lids, each having a centrally placed hole 75 micron in diameter. A Perkin Elmer thermogravimetric analyser (Fig.4.11) with ceramic pans was used in the execution of this test. The aluminium containers with the sample were individually placed in the crucibles and precise weights of

the samples were obtained. The analyser was programmed to heat the sample up to 600°C at a rate of 3 °C per minute up to 220°C and 10°C per minute thereafter. The tests were conducted in a nitrogen atmosphere.

Two essential parts of the thermogravimetric analyzer are the microbalance and the furnace. The crucible was suspended from a hang down wire attached to the thermo-microbalance which had a sensitivity of 0.1 µg. This wire facilitated the transfer of the sample to the small vertical furnace. As the furnace was heated a fraction of the sample decomposed at temperature associated with vaporization of specific compounds. The outputs of the experiment were the loss in weight per degree Celsius and the differential thermogravimetric (DTG) curves.

A typical TGA and DTG curve is shown in Fig.4.12. The peak between 420 °C and 500 °C represents the $\text{Ca}(\text{OH})_2$ dehydroxylation ([Loukili et al., 1999](#)) and the amount of portlandite (CH) was determined according to the procedure described by [Peschard et al. \(2004\)](#):

$$\text{CH} (\%) = (\text{WL}_{\text{CH}} (\%) * \text{MW}_{\text{CH}}) / (\text{MW}_{\text{H}}) \quad (4.5)$$

Where $\text{WL}_{\text{CH}} (\%)$ corresponds to the weight loss occurring during CH dehydration; and MW_{CH} and MW_{H} are the molecular weights of portlandite and water, respectively.

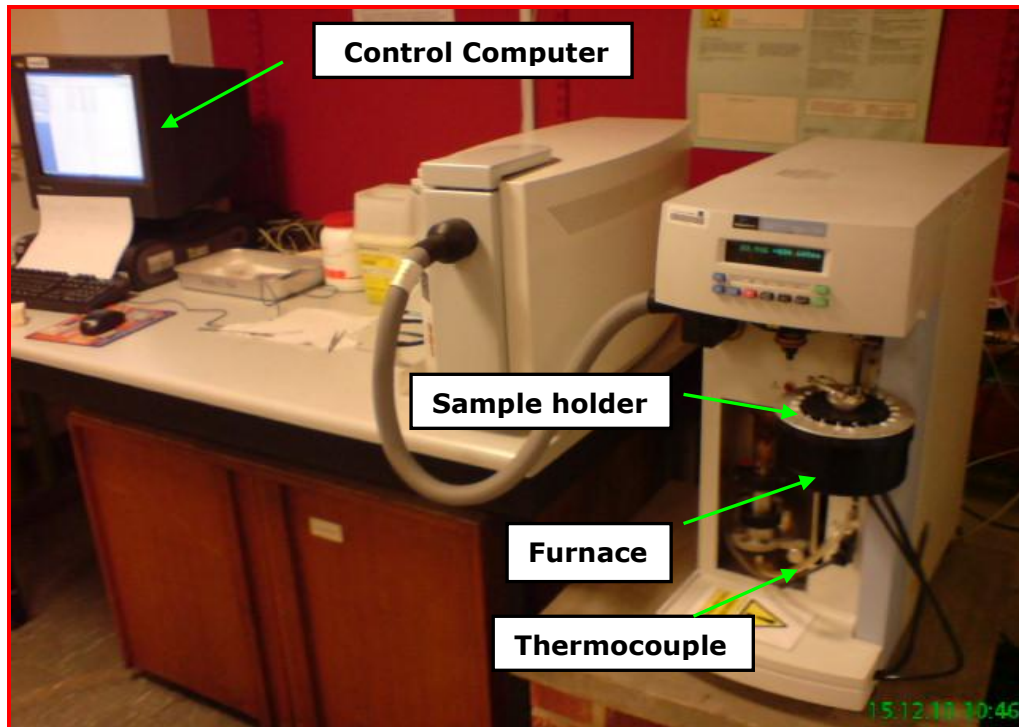


Fig.4.11: Photograph of thermogravimetric analyzer

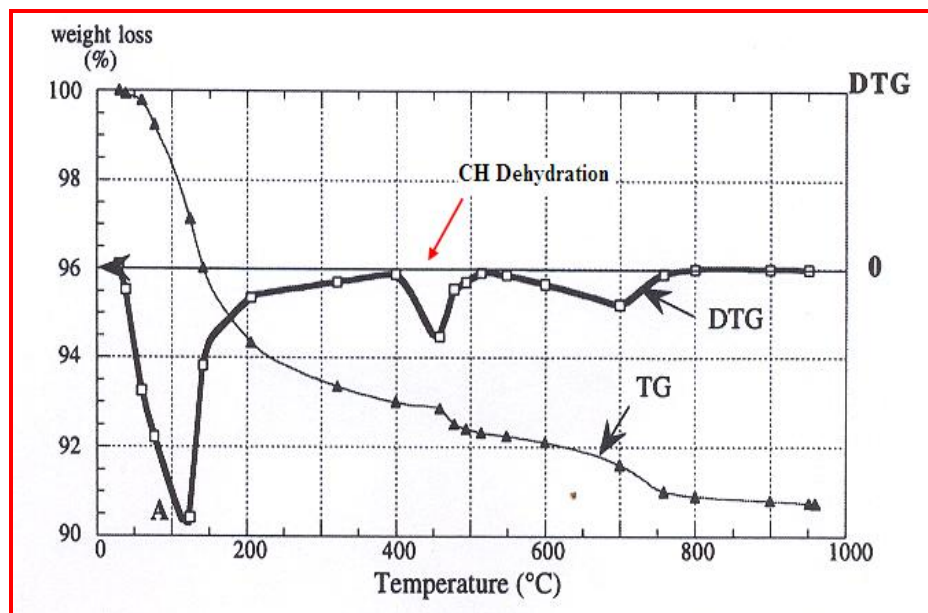


Fig.4.12: Typical TGA and DTG curves (Loukili et al., 1999)

4.6 X-ray Computed Tomography (CT) with digital image analysis

Digital image analysis involves extracting some information from the images by means of digital image processing techniques with the application of various mathematical procedures. This information may be the micro-structural characteristics of concrete such as air voids, aggregate distribution or fibre orientation. An image analysis technique generally consists of three major stages as shown in Fig.4.13.

Image acquisition is a process of getting the image into computer. This is probably the most important part of the entire process because good qualities of captured images are easy to analyse while poor quality images can be almost impossible to process. This step can be done in many different ways, for example using digital cameras, scanners or advanced technologies such as X-ray CT. The second stage is image processing that involves adjustments which are necessary if the image needs correction for problems introduced during image acquisition. Simple adjustments might involve altering the brightness and contrast, removing dust and scratches and particle segmentation.

Image analysis is the final stage of making measurements on the images. It is the process of obtaining numerical data from images. X-ray CT is a completely non-destructive technology and provides a rapid means of gathering the 3D data from a contiguous series of 2D measurements that are needed for such analyses. X-ray CT systems are used to generate a map representing the density at every point in the microstructure. Brighter regions correspond to dense objects such as aggregates and dark regions correspond to low density objects such as air voids. Using an X-ray CT system along with digital image analysis techniques allows cracks, aggregates, air voids (distribution, shape, average size, orientation etc.) to be

visualized and evaluated, and thus the method can be used to study the structure/property relationships in concrete.

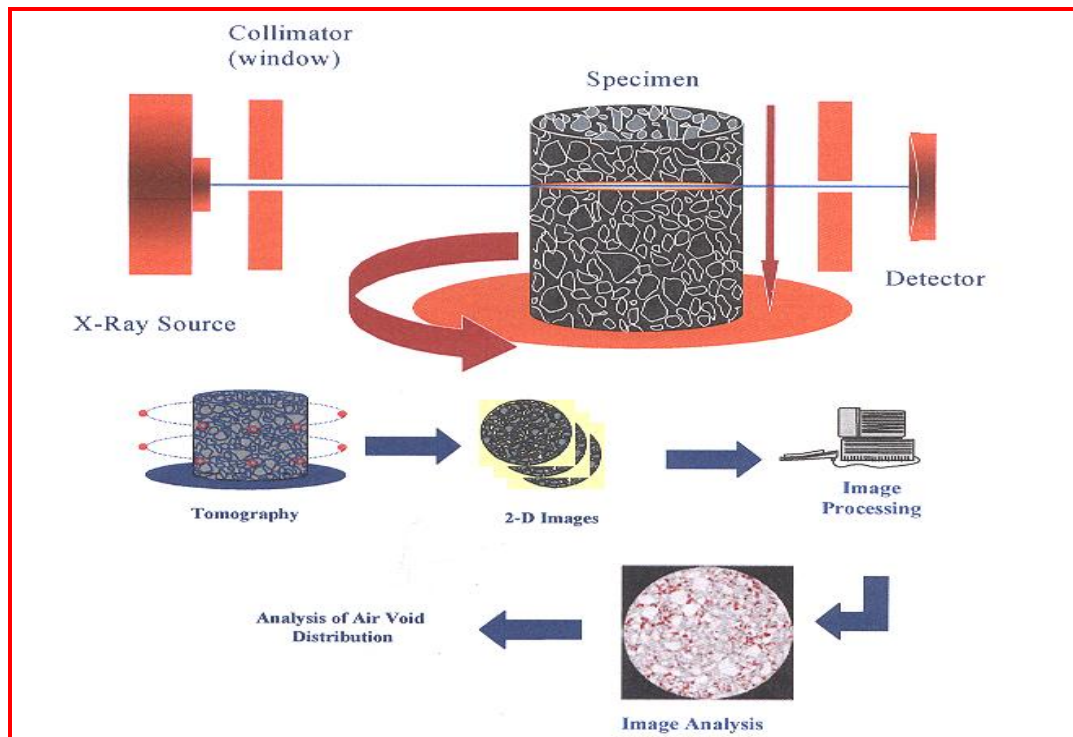


Fig.4.13: Three major stages of image analysis technique (Masad et al., 1999)

In this work, the X-ray CT set up in the Nottingham Transportation Engineering Centre (NTEC), Department of Civil Engineering at the University of Nottingham was used (Fig.4.14). This set-up includes two separate systems placed in the same shielding cabinet. The mini focus system has a 350 kV X-ray source and a linear detector, while the micro-focus system has a 225 kV X-ray source and an area detector. All the experimental measurements in this study were conducted using the mini focus 350 kV X-ray source system, which has the necessary power to penetrate the concrete mix specimens with a reasonable resolution. The resolution of the X-ray CT images was approximately 0.21 mm/pixel.

In order to investigate the micro-structural properties, sequences of X-ray 2D images were captured along the height of the specimens. The captured images from the X-ray CT system were then converted to 3D images using an image analysis software package (Image J). Finally, the converted images were used to identify the constituents and to quantify air voids within the specimen. Images were adjusted in brightness and contrast to enhance the clarity of aggregate and air voids against the surrounding matrix.

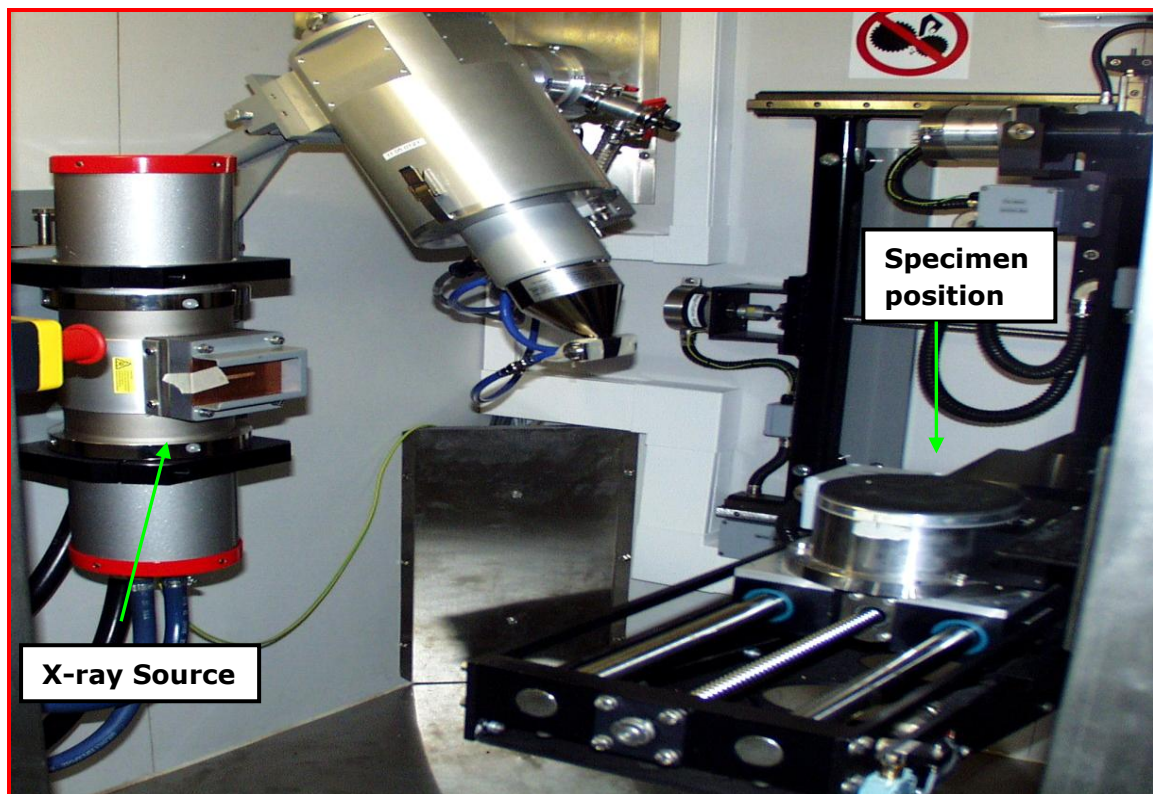


Fig.4.14: X-ray CT system at NTEC, University of Nottingham

4.7 Aggregate Properties Results and Discussion

4.7.1 Mineralogical analysis of the aggregates used

For the four types of aggregates used, the mineralogy patterns, determined by the XRD technique, are shown in Fig.4.15. The main features in the mineralogy of the aggregates are summarized as follows:

Gravel, Copper Slag: are “well-crystallized” in nature. The observed peaks correlate well with the patterns for quartz, calcite and goethite in the gravel; for olivine and illite in the copper slag; and for quartz, mullite, hematite and cristobolite in the blue brick particles.

Fly ash/Lytag and blue rick: It appears both could have significant amorphous content (much obvious in the fly ash/Lytag), most likely silica and thus, pozzolanic characteristics, as “indicated” by the hump in the diffraction pattern arrowed (Fig.4.15). The associated crystalline phases are quartz, mullite, anorthite hematite and cristobolite. It is well-established that mullite exists in the fly ash/Lytag forming from aluminosilicate clay minerals during the combustion process of raw coal, while the formation of anorthite occurs as a result of sintering process ([Kockal, 2008](#)).

It should be noted that the rubber, being basically polymeric, was not assessed for its mineralogy.

4.7.2 Surface roughness of the aggregates used

Fig.4.16 displays typical surface profiles of the aggregates used, and calculated results of surface roughness (Ra) are given in Table 4.4.

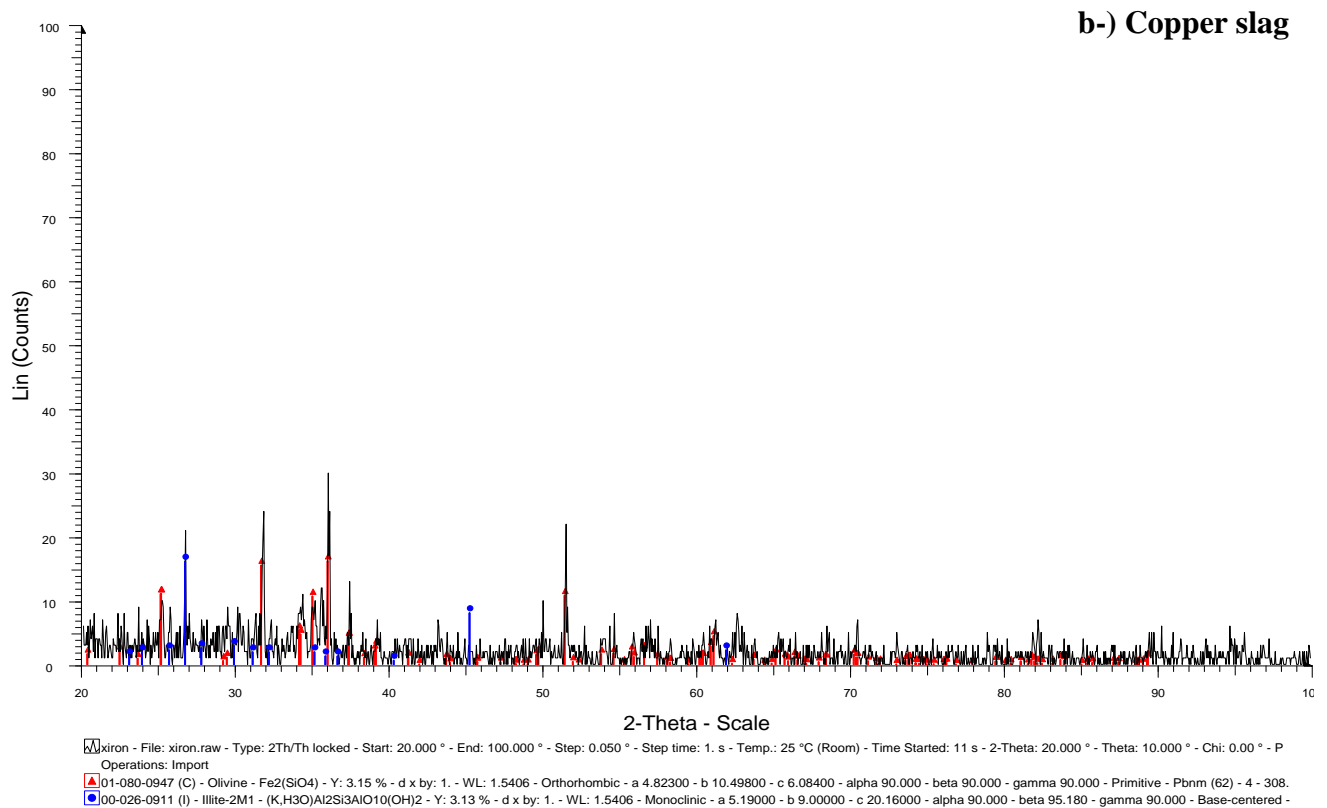
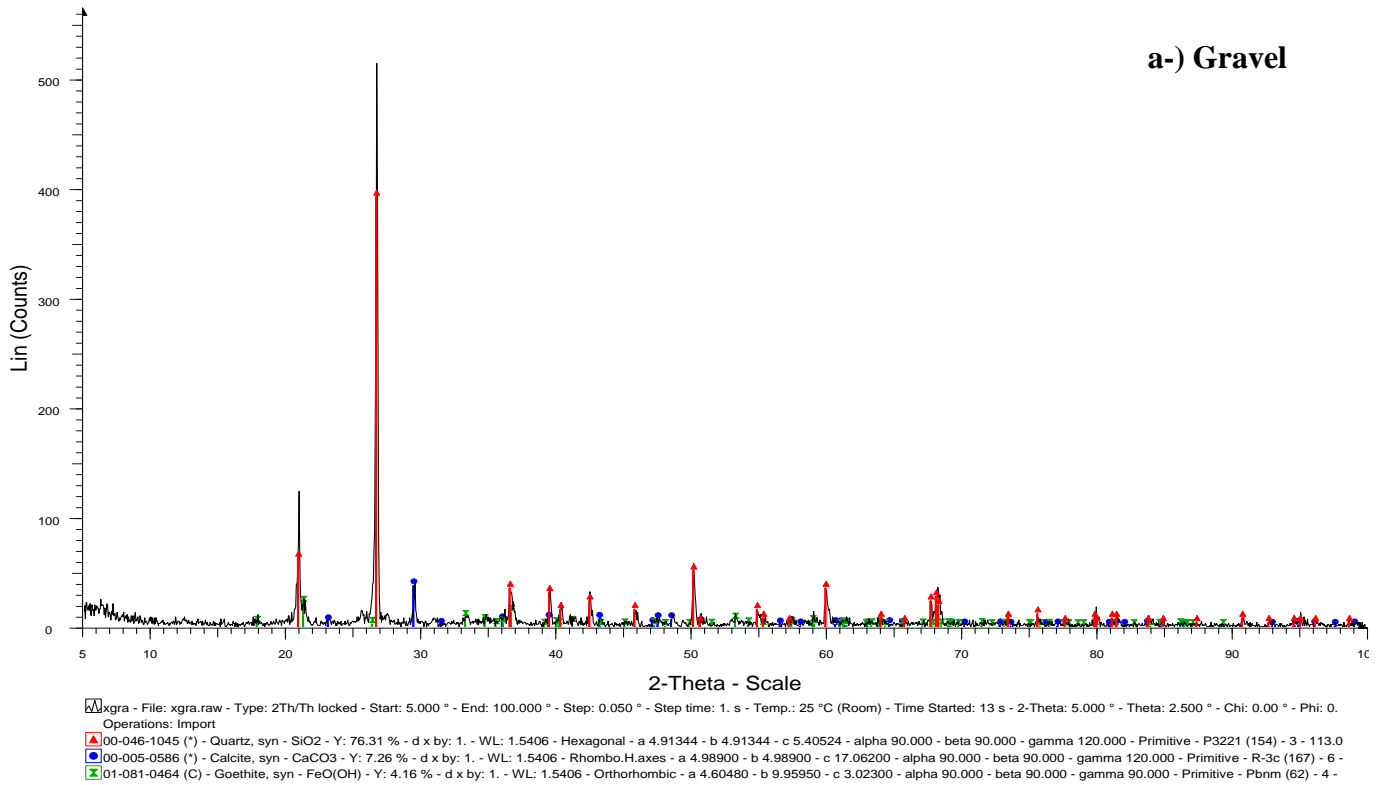


Fig.4.15: XRD patterns of the aggregates used

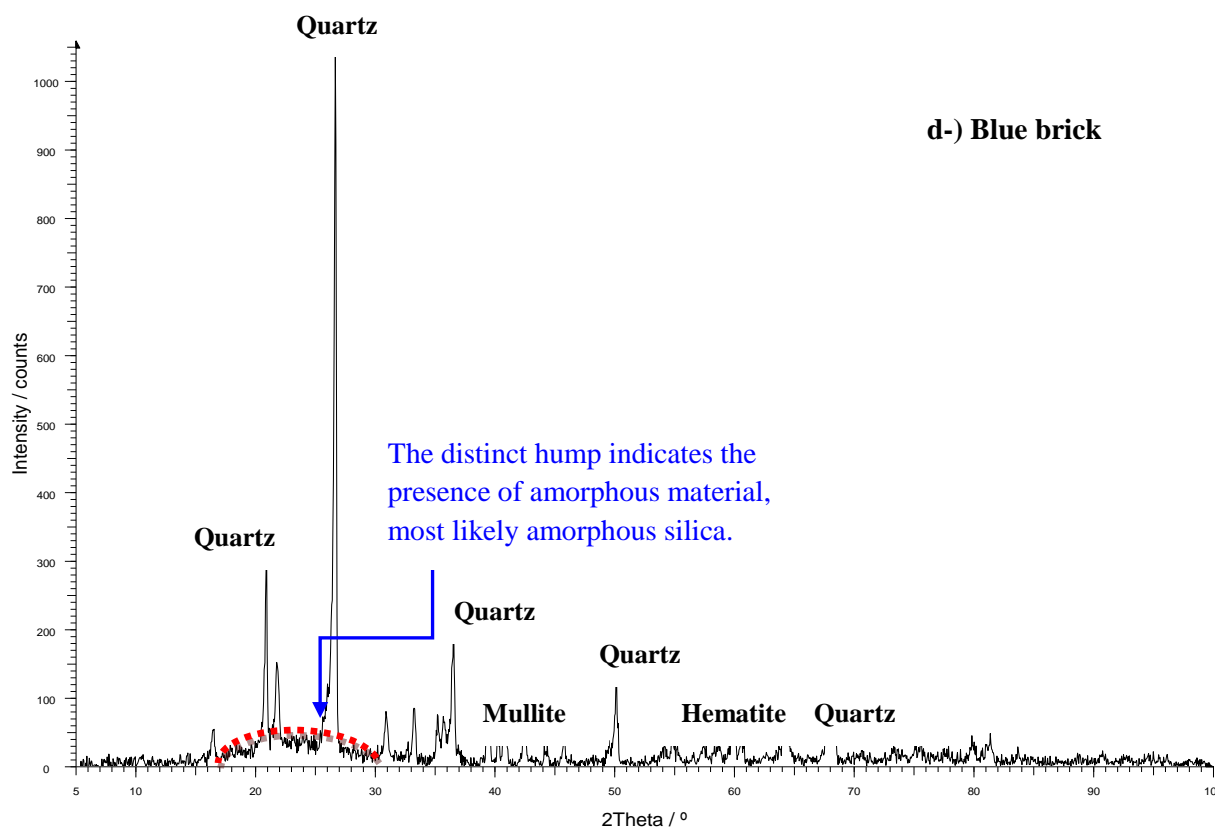
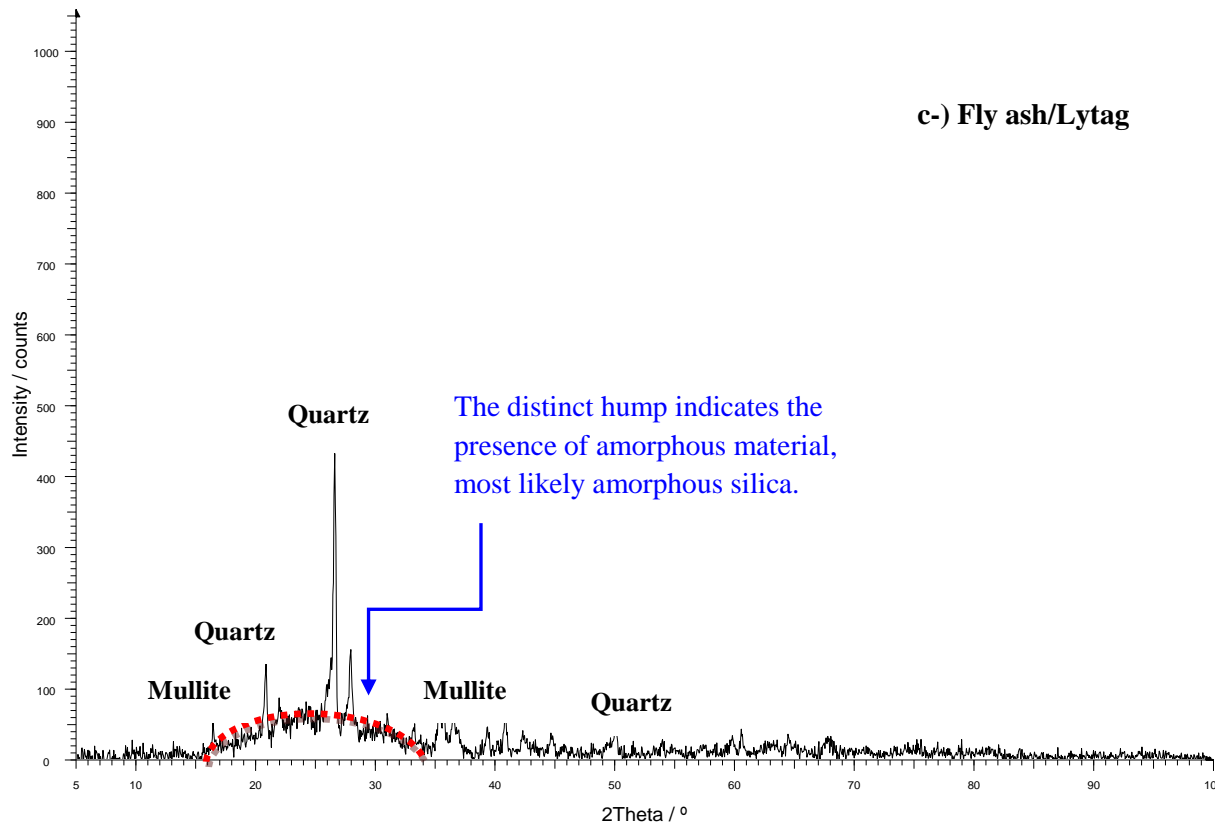


Fig.4.15 continued: XRD patterns of the aggregates used

As would be expected, there were significant differences in the measured profiles and the surface roughness values. The fly ash/Lytag surface was much rougher ($14.3 \mu\text{m}$) than that of blue brick ($12.2 \mu\text{m}$) and copper slag ($8.7 \mu\text{m}$) which were rougher than that of the gravel ($5.6 \mu\text{m}$). The rubber particles had the smoothest surface texture ($1.42 \mu\text{m}$) than the other aggregate types. [Tasong et al., \(1998\)](#) claimed that crystalline texture, hardness and inter granular bonding between the mineral grains are possibly the main reasons for the observed differences in surface texture of the aggregates. For example, the presence of well-defined cleavage planes (or planes of weakness) in calcite, one of the main constituent of the gravel is considered to be the main reason for the low surface roughness of its surface. The images obtained from an optical microscope and a SEM have also shown that the surface texture of the fly ash/Lytag contains large porous and interconnected channels, which could likely affect its water absorption and interfacial bonding behaviour, while the rubber particles have highly smooth surface texture (Fig.4.17).

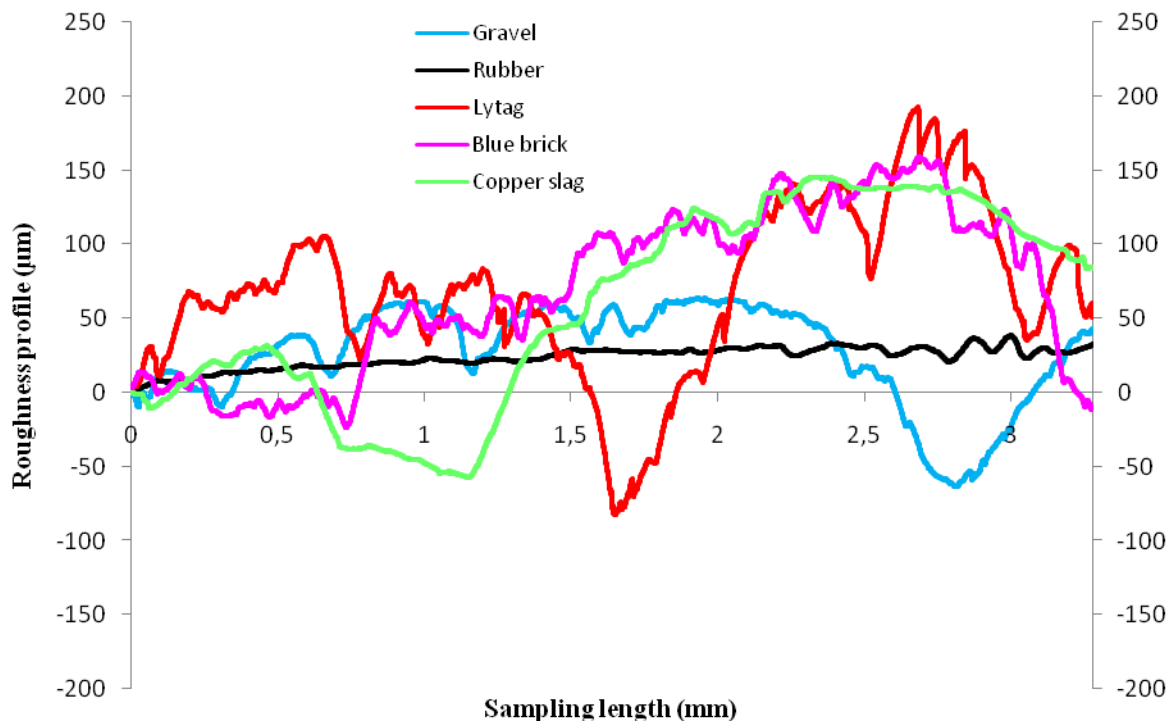


Fig.4.16: Typical surface roughness profiles of the aggregates

4.7.3 Physico-mechanical and geometrical properties of the aggregates

The physico-mechanical properties and geometrical parameters of the aggregates are tabulated in Table 4.4.

Comparison between the properties of the aggregates indicates that the fly ash/Lytag is more porous, much weaker and more rounded than the other aggregates. To give an idea of the pore structures, the pore size distribution curves of the fly ash/Lytag and reference (gravel) aggregate are shown in Fig.4.18. The calculated mercury intrusion porosities of the fly ash/Lytag and gravel aggregates are 52.7 % and 1.62 %, respectively. The higher porosities of fly ash/Lytag aggregates can be attributed to incomplete densification during the sintering process at high temperatures. By contrast, the copper slag aggregate has the highest specific gravity and modulus of elasticity. In addition, the aggregate has a higher degree of angularity than other aggregates. The fractal dimension results indicate that the gravel aggregate is more irregular than the other aggregates. The results also show that the rubber particles are much more elastic, much less dense and have the lowest water absorption value while the blue brick aggregates have the highest particle strength than other aggregates.

Table 4.4 The physico-mechanical properties of the aggregates used

Characteristics	Gravel	Rubber	Copper slag	Fly ash/ Lytag	Blue Brick
Specific gravity (g/cm³)	2.65	1.15	3.75	1.35	2.85
Impact value (%)	12	-	8.30	24.0	6.1
Angularity	1.12	1.16	1.17	1.0	1.14
Roundness	1.25	1.19	1.18	1.01	1.21
Fractal dimension	1.08	1.02	1.02	1.02	1.02
The modulus of elasticity (GPa)	56.9	10.7	113.9	14.8	65.8
Water absorption (%)	1.1	0.4	0.8	27.2	0.6
S.Roughness-Ra (µm)	5.6	1.42	8.7	14.3	12.2

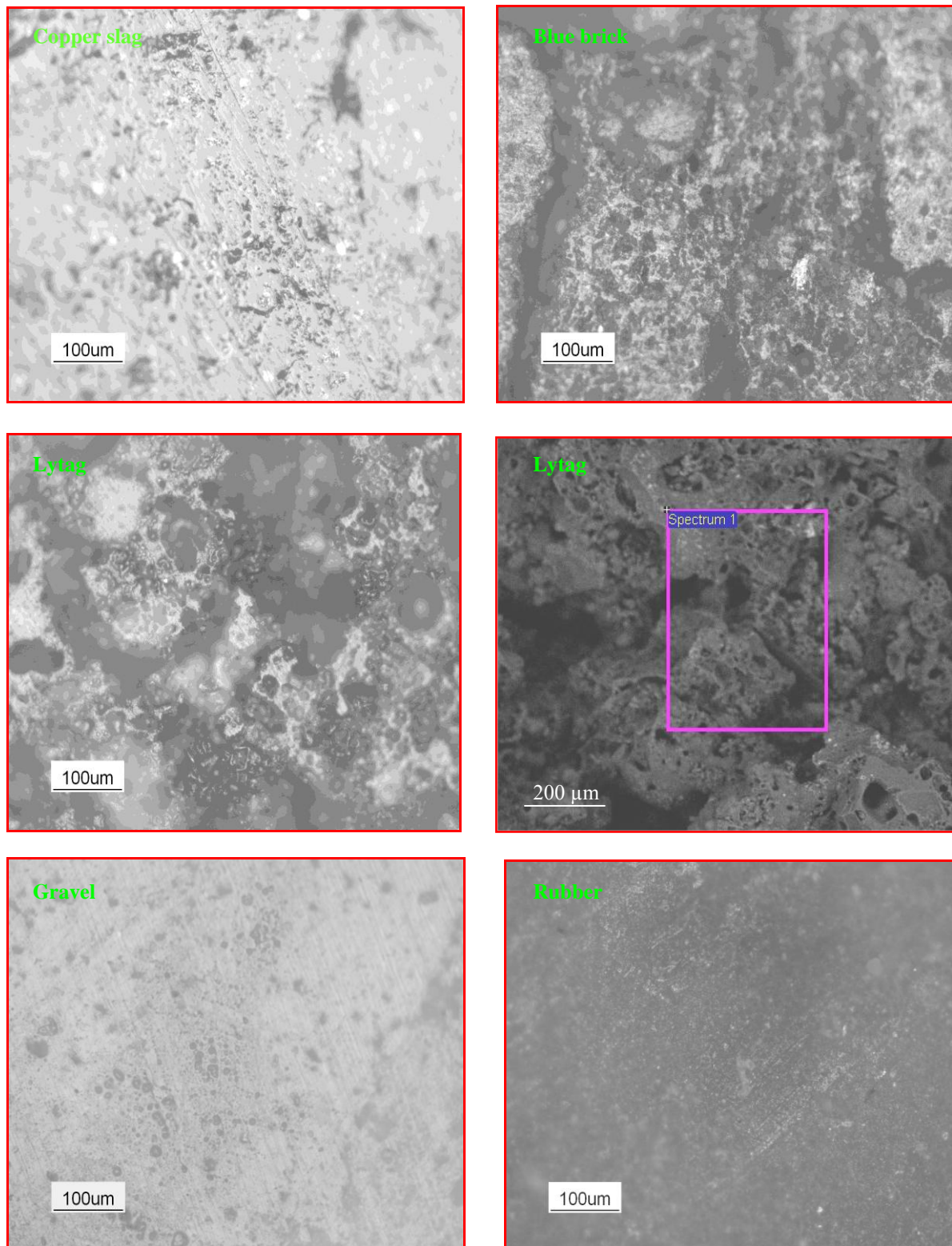


Fig.4.17: Surface texture views of the aggregates via optical microscope

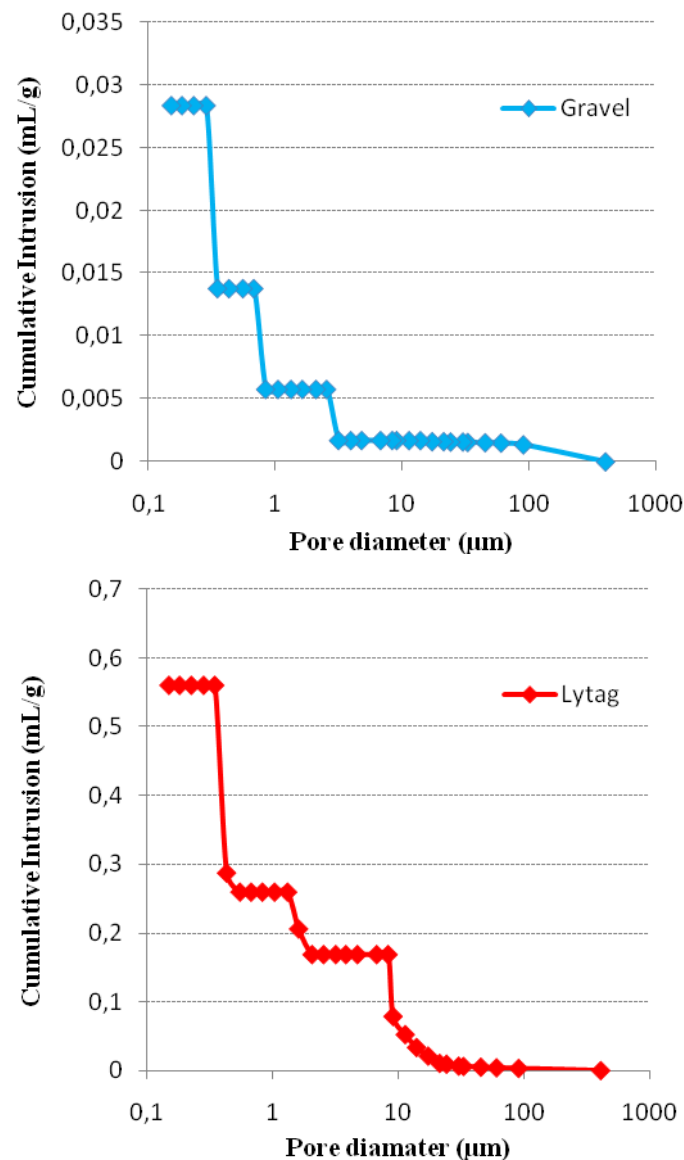


Fig.4.18: Cumulative intrusion vs. pore diameter curves of the fly ash/Lytag and gravel aggregates

4.8 Mechanical Concrete Properties Results and Discussion

4.8.1 Engineering properties of concrete

The basic engineering properties of the concrete mixtures are tabulated in Table 4.5. In general, the results demonstrate that the concrete made with blue brick particles gave the highest strength, followed by the concrete with copper slag aggregate. In addition, it can be seen that there is a very drastic drop in strength when the gravel aggregate is totally replaced

with the rubber particles. The decrease in the compressive strength ranks the same as the density. These results are consistent with those of other studies (Eldin and Senouci 1993; Khatib and Bayomy 1999; Taha et al. 2008; and Khanzadi and Behnood, 2009). However, the most interesting finding was that the concrete with fly ash/ Lytag is stronger in compression than the reference concrete (concrete made with gravel aggregates), which contradicts the results of previous studies (Zhou et al., 1995; Balendran et al., 2002 and Tang et al., 2008). However, Bentz (2007) and Hijazin and Lopez (2011) showed that the mixtures with pre-wetted lightweight aggregates reached a higher compressive strength. The higher strength was attributed to the fact that a higher degree of hydration can overcome the reduction in strength caused by the use of a lower intrinsic strength lightweight aggregate.

Table 4.5: Engineering properties of the concrete mixtures

Concrete ID	Density (kg/m³)	Compressive Strength (MPa)	Flexural strength (MPa)	Dynamic modulus of elasticity (GPa)	Static modulus of elasticity (GPa)
Gravel	2325	25.4	4.0	41.0	20.3
Blue brick	2375	38.0	4.80	42.2	27.1
Copper slag	2720	33.2	4.70	50.9	26.4
Lightweight	1895	28.7	3.15	23.7	18.6
Rubberised	1690	2.50	0.70	9.1	0.65

It is conjectured that the relatively higher compressive strength of the lightweight concrete compared to the gravel aggregate concrete is attributable to the combined effects of the localized high cement content in the vicinity of the pre-wetted aggregate and to the internal

curing effect within the concrete. As wet fly ash/ Lytag aggregate was mixed with cement and sand before water addition, the lightweight aggregates are expected to have been coated in cement, which would affect the local cement content in the ITZ around the aggregates after mixing. In parallel, internal curing water from the lightweight aggregate may have been gradually released into the matrix with the progress of the cement hydration process and, most likely, encouraging pozzolanic reactions with pulverised fly ash (PFA) from the cement. If this is true, there would be considerable influence on the kinetics of the hydration process and further hydrating of the paste. Furthermore, the absorbed water could also have increased the pozzolanic reaction of Ca^{+2} with silica ions in the fly ash/ Lytag as the XRD pattern indicates that the fly ash/ Lytag is of an amorphous nature and possesses pozzolanic characteristics. Measurement of reduced CH content in the mortar of samples would allow the hypothesis of a locally higher degree of hydration within the lightweight concrete to be tested. This will be discussed in the next section.

As can be expected, the flexural strength (Table 4.5) is observed to be much higher for the copper slag and blue brick concrete than for the gravel concrete. The flexural tensile strength of the lightweight concrete was comparable and about 80 % that of the reference concrete. However, the increase in compressive cube strength with fly ash aggregate replacement is not replicated in flexure. This drop may be explained as follows: The flexural behaviour could be dependent on both the surface roughness, which is a leading factor for the interfacial bond strength, and the strength of the coarse aggregate. A deficiency or absence of one of these factors could result in flexural strength loss. However, the increased tension in part of a system subject to tension would seem to be the main difference between compression & tension. Therefore, an explanation in terms of tension would seem most reasonable. Fly ash /Lytag particles are much weaker than the surrounding matrix, and thus can be expected to

crush more readily than do the gravel particles in the conventional concrete, leading to a less tortuous failure surface and a reduced contribution of aggregate interlock to the load transfer from the matrix to the aggregate under flexural loading. Thus, this mechanism would reduce the resistance of the lightweight concrete to tensile strains, thus allowing it to fail at premature flexural strength level.

The concrete mixture prepared with copper slag aggregate exhibited about 25 % higher dynamic modulus of elasticity than the concrete containing gravel aggregate (Table 4.5). This is assumed to be because of higher density of aggregate, primarily. The mortar matrix with copper slag is less porous and has a higher density compared to the reference mortar matrix, and thus the ultrasonic pulse can move faster there. By contrast, the dynamic modulus of elasticity exhibited a dramatic reduction when the gravel aggregate was replaced with rubber particles. This probably reflects the fact that there is delay of velocity of travel time of the ultrasonic wave due to presence of cracks and other internal flaws, and also because rubber is much less stiff. However, the concrete mixture prepared with the fly ash/Lytag aggregate exhibited about 42 % lower dynamic modulus of elasticity than concrete containing gravel aggregate, consistent with the findings by [Tang et al. \(2008\)](#). Given the denser packing of the lightweight concrete, this is assumed to be because of the lower modulus of elasticity of the fly ash/Lytag compared to that gravel.

As can be seen from Table 4.5, the rigidity (static modulus of elasticity) of the mix with crushed brick is much higher than those of the other mixes. By contrast, the mix with rubber particles exhibited a greater deformability and energy absorbing capacity (ductile plastic failure) although its peak stress is very low. Based on the visual observations carried out on the cracking faces, the failure states of the mixtures containing rubber particles did not

exhibit any separation as the rubber particles form a tight bridge across cracks in the matrix. The nature of the aggregate-matrix bond may be responsible for the decrease/increase in the elastic modulus of concrete. For instance, an interfacial bond containing severe defects will quickly degrade and lose its load transferring capacity, and thus the composite would not fully achieve the potential modulus of elasticity (Chan 1998). However, based on composite mechanics, the elastic modulus of concrete depends, to a great extent, on the modulus of aggregate. For the same mix design conditions, the stiffer the aggregate, the stiffer the concrete becomes.

4.8.1.1 Thermogravimetric analysis (Degree of Hydration)

It is well-known that the compressive strength of plain concrete correlates to the formation of the structure of the hardening cement matrix as a result of chemical reaction between cement and water – the degree of hydration (Schutter, 2004). Fig.4.19 shows combined DTA/TGA curves of the mixes in which the points of interest are labelled 1. These peaks show calcium hydroxide being decomposed in the temperature range of approximately 425 to 475 °. The percentage weight loss corresponding to the dehydration of CH was measured as 1.70 %, 3.30 %, 4.30 %, 5.20 % and 5.70 %, for the lightweight, copper slag, rubber, blue brick and gravel mortar, respectively signifying that the most pronounced chemical activity in the development of CSH gels occurred for the lightweight concrete mix. This was followed by the gravel concrete mix which was not the strongest mix. The blue brick and copper slag mixes provided the highest strength yet their lower level of CH suggesting that less hydration has taken place and, hence, a lower mechanical strength could be expected. This mismatch suggests that the strength was dependent on the aggregate strength rather than the degree of hydration in these mixtures. Weakness can also suggest that microstructural development is less uniform. Thus, the large decrease in strength of the concrete with rubber particles relative

to the other two mixes could suggest a partial absence of adequate CSH gels in the ITZ. This will be discussed in more detail in Chapter 5: Quantitative Assessments of Microstructure of the ITZ in Concrete.

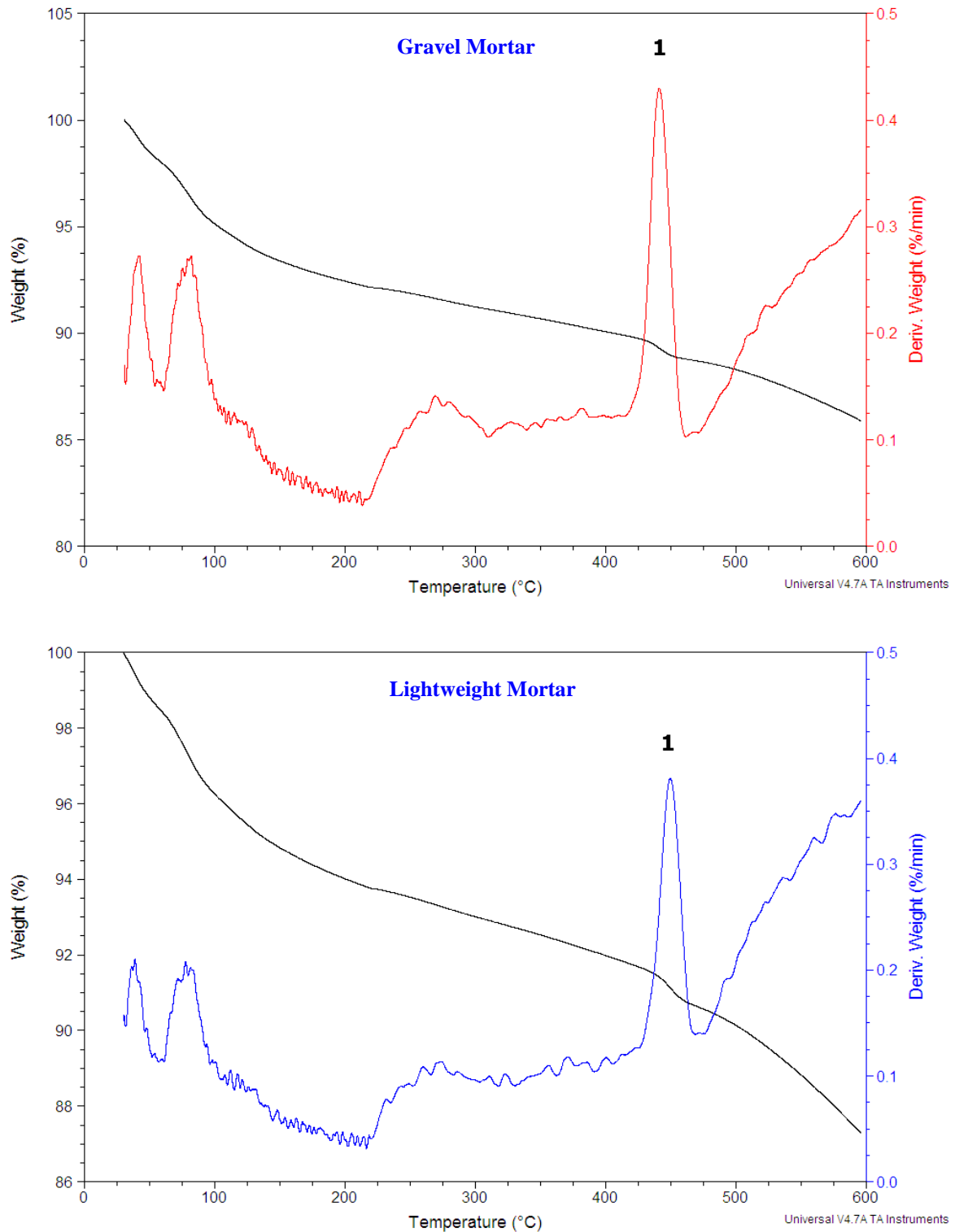


Fig.4.19: DTA/TGA curves of the mixes

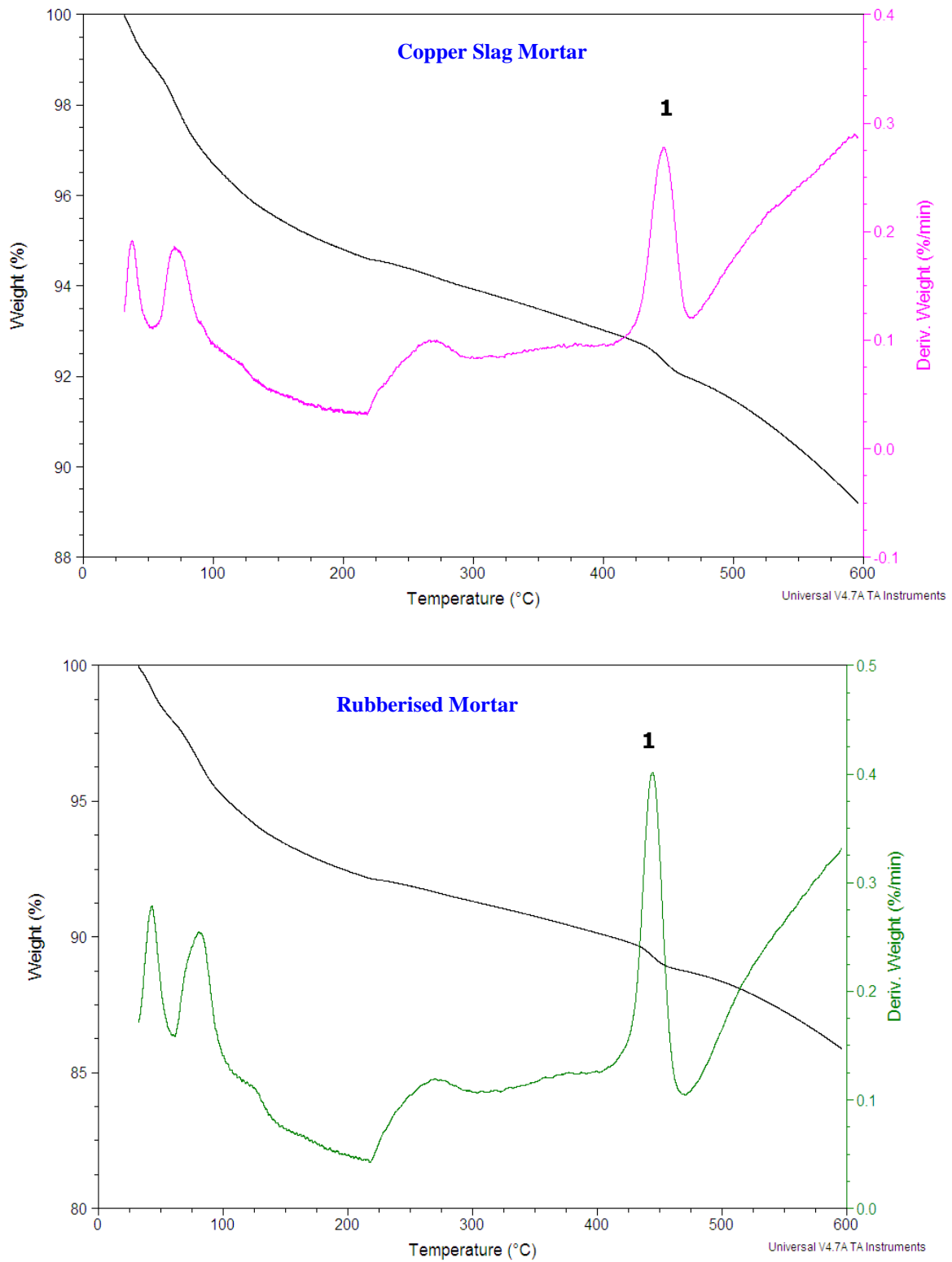


Fig.4.19 continued: DTA/TGA curves of the mixes

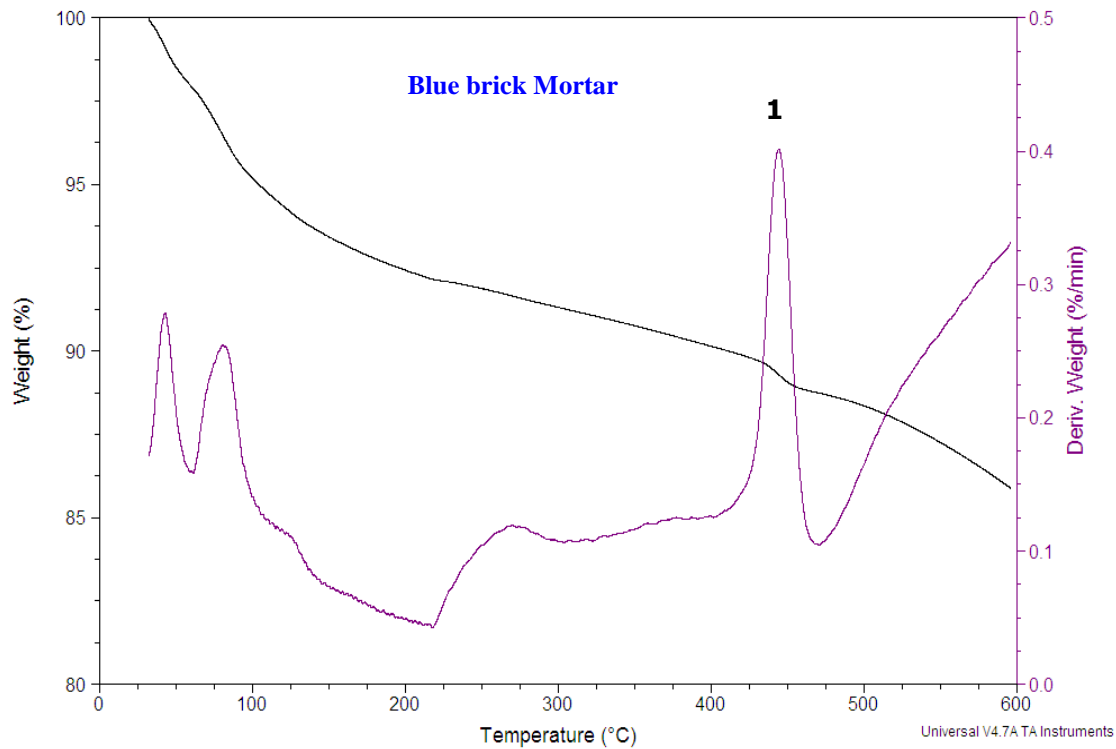


Fig.4.19 continued: DTA/TGA curves of the mixes

4.8.1.2 X-ray Computed Tomography (Void Content)

Using the X-ray CT system along with digital image analysis techniques; aggregates, air voids and other constituents can be visualized and evaluated, and thus this can be used to study the structure/property relationships in concrete. Fig. 4.20 and 4.21 show a typical image of the lightweight and the blue brick mixes obtained by the X-ray technique coupled with digital image analysis. The differences in colours show the different material phases in the mixture. The calculated void contents of all the mixtures derived from multiple horizontal slice assessments made through each specimen's height and 3D visualization of air void distribution are also presented in Fig.4.22.

The analysis clearly shows that the inherent void distribution was not homogeneous for all specimens, and there were three distinct regions with respect to the void distribution except

the rubberised mix: two low void content regions at the top and bottom, and one relatively high void content region in the middle part of the specimens. The void content in the rubberised specimen was much higher than in the other specimens. Such a distribution in the rubberised mix could be attributed to much higher interconnectivity of the ITZ and orientation of the rubber particles which could stop the further movement of the voids during compaction.

According to [Yuan and Harrison \(2006\)](#), such initial defects and heterogeneous microstructure would lead to a significant increase in the destructive transverse tensile strains during the loading and the concentrations of the stresses around the pores in which large pores would intensify the external loading. This, correspondingly, provides a line of weakness for failure to take place on, and accelerates crack growth and strain incompatibilities and, hence, facilitates fracture initiation and propagation leading to premature failure.

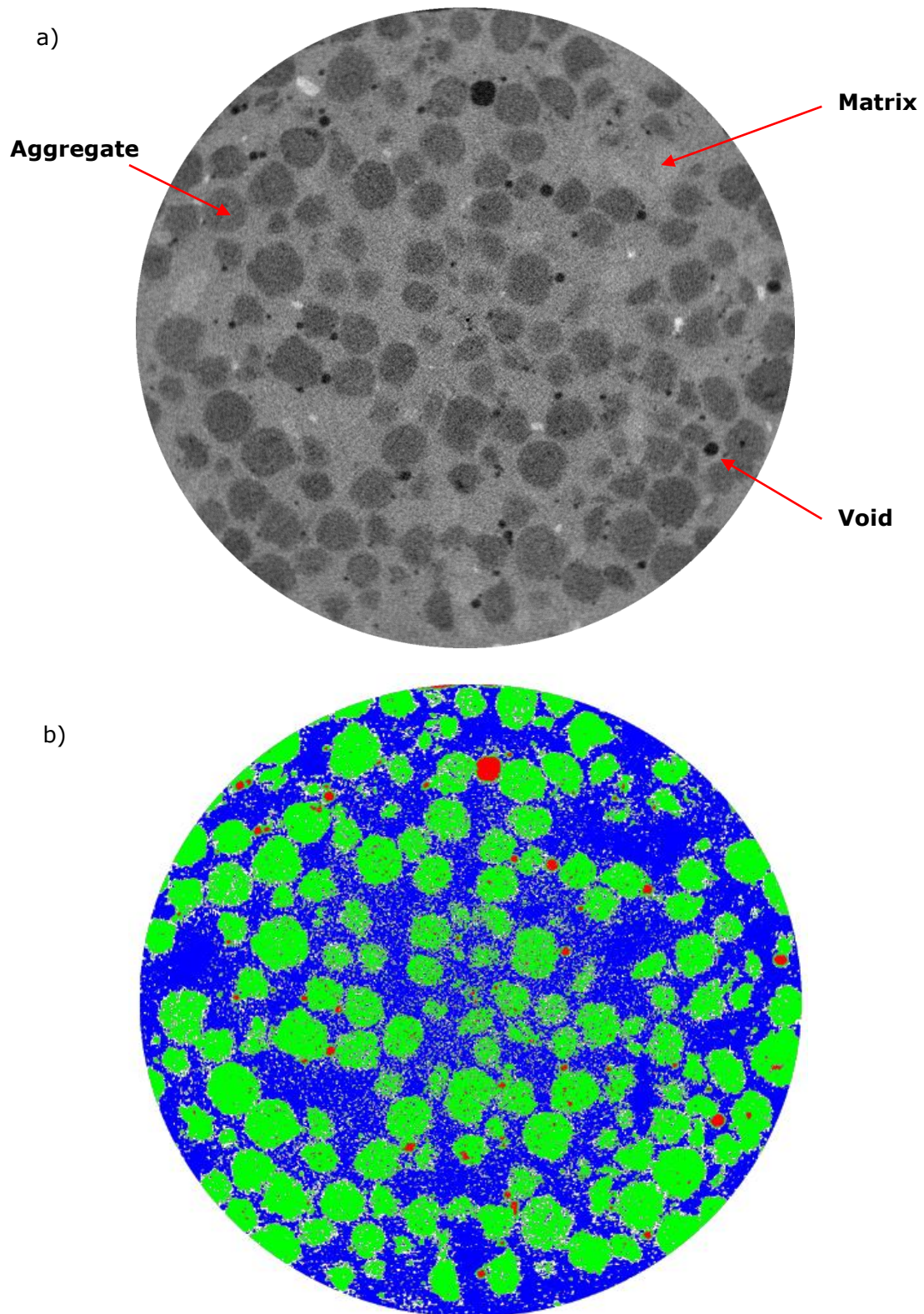


Fig.4.20: Images of lightweight concrete a) original X-ray b-) pseudo colour transformation

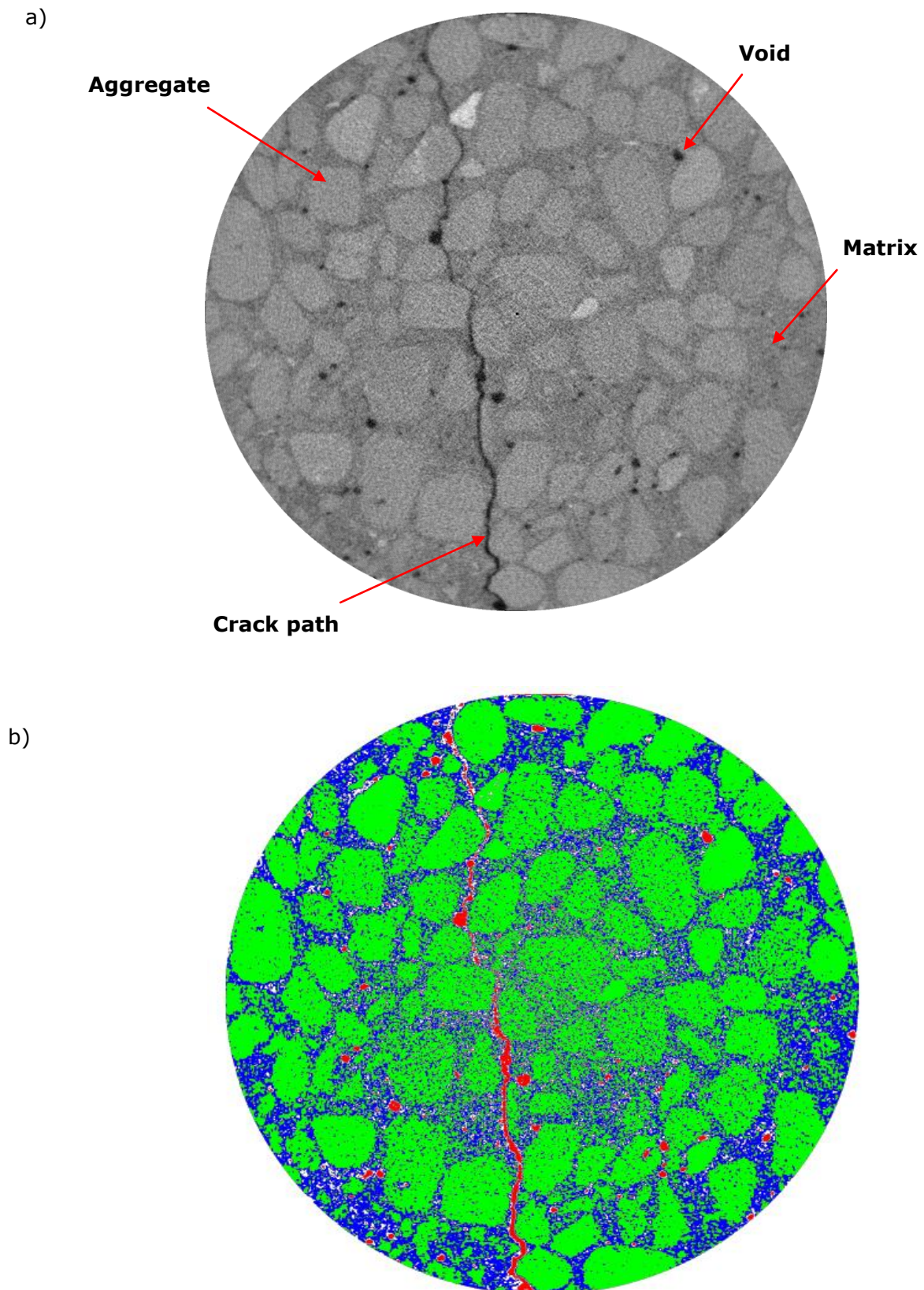


Fig.4.21: Images of blue brick concrete a) original X-ray b-) pseudo colour transformation

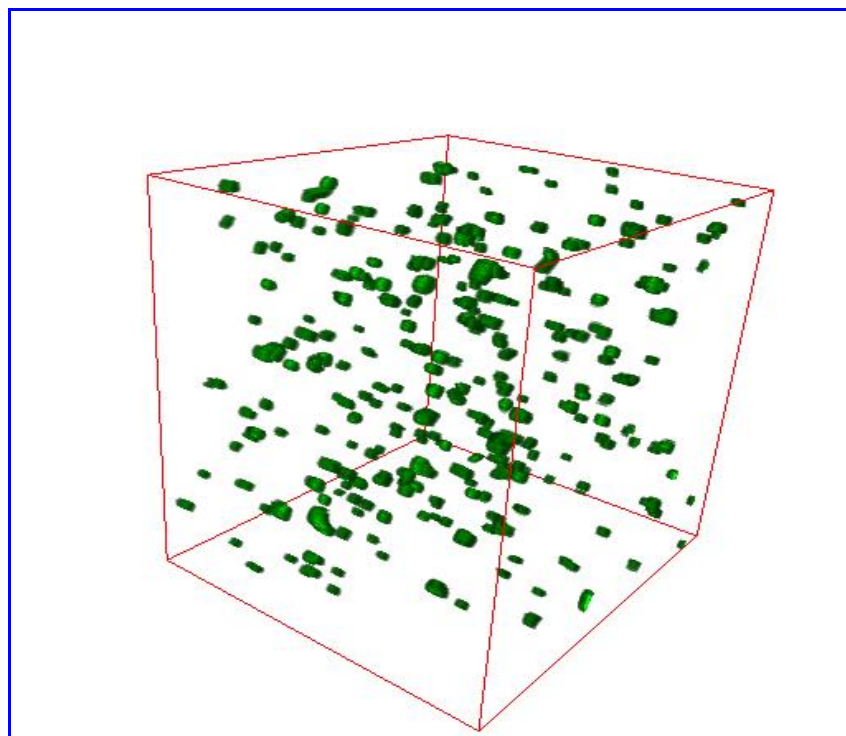
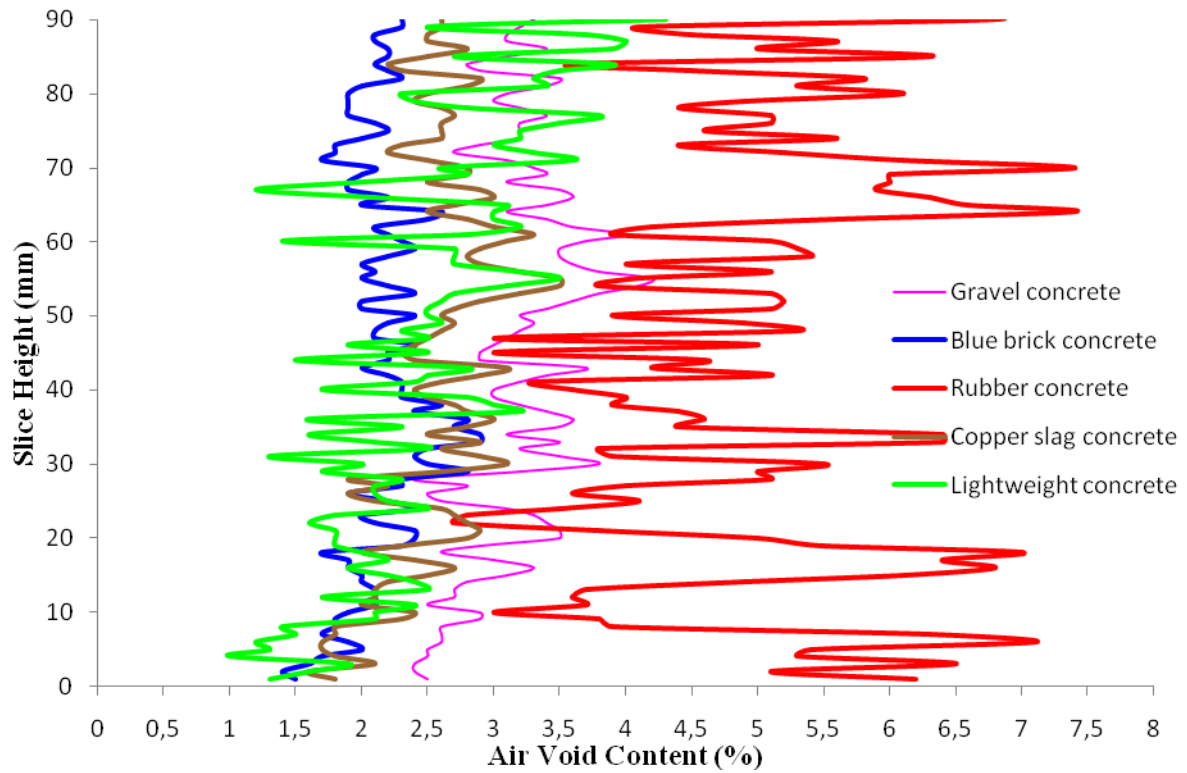


Fig.4.22: Air void distribution of the mixtures (a) and 3D air void simulation (b)

Taking all observations together presented in this section, the most credible explanation of the strength of the lightweight mixes is that pozzolanic products, being the consequence of reaction of the fly ash in the cement with water released from the fly ash/Lytag and hence, hydration of previously unhydrated cement grains, are developing after initial cement hydration process is complete. In this case, the water movements are almost certainly driven by developing matric & osmotic suction in the paste during hydration ([Henkensiefken et al., 2009](#)). These products are helping to fill micro-pores in the paste in the ITZ. Due to the denser paste in the ITZ and rougher surface of the fly ash /Lytag aggregate, a stronger ITZ develops than would otherwise be the case and, certainly, stronger than in the conventional concrete.

4.8.2 Flexural response and fracture energy

The loads versus average mid-span deflection responses for the concrete mixtures are depicted in Fig.4.23.

As expected, after reaching peak load, neither concrete sample except the rubberised mix could carry any significant post-crack loads and collapsed within a very short time. It can be also seen from Table 4.6, that the first cracking and maximum load deflections for the blue brick and gravel concrete are very similar, while the first cracking and maximum load for the lightweight and particularly rubberised concretes are quite different (a much less linear pre-peak stress-strain curve). However, there were remarkable similarities in the post-peak region of the stress-strain curves apart from the rubberised mix. The concrete samples started failing in an unstable manner. This behaviour, from a fracture mechanics standpoint, might be attributable to the fact that the aggregate particles were much stiffer than the surrounding cement matrix. Inhomogeneities cause strain incompatibilities within the mix and consequent

localized stress concentrations and, hence, greater crack initiation and propagation points, eventually leading to accelerated failure accompanied by less energy dissipation within the specimens.

It is also worth highlighting that the deflection at the peak load for the rubberised concrete is distinctively higher than that of the gravel concrete, although its peak load is much lower than that of the gravel concrete. This is basically an effect of mixture: a less stiff aggregate produces a less stiff concrete. A larger deflection is much more preferable under dynamic conditions such as impact or load fluctuations (Newman and Owens, 2003) due to the greater ability to absorb energy without yield. The high deflection value is also beneficial for fracture energy, which is the integral of the load vs. deflection curve, as seen in Table 4.6.

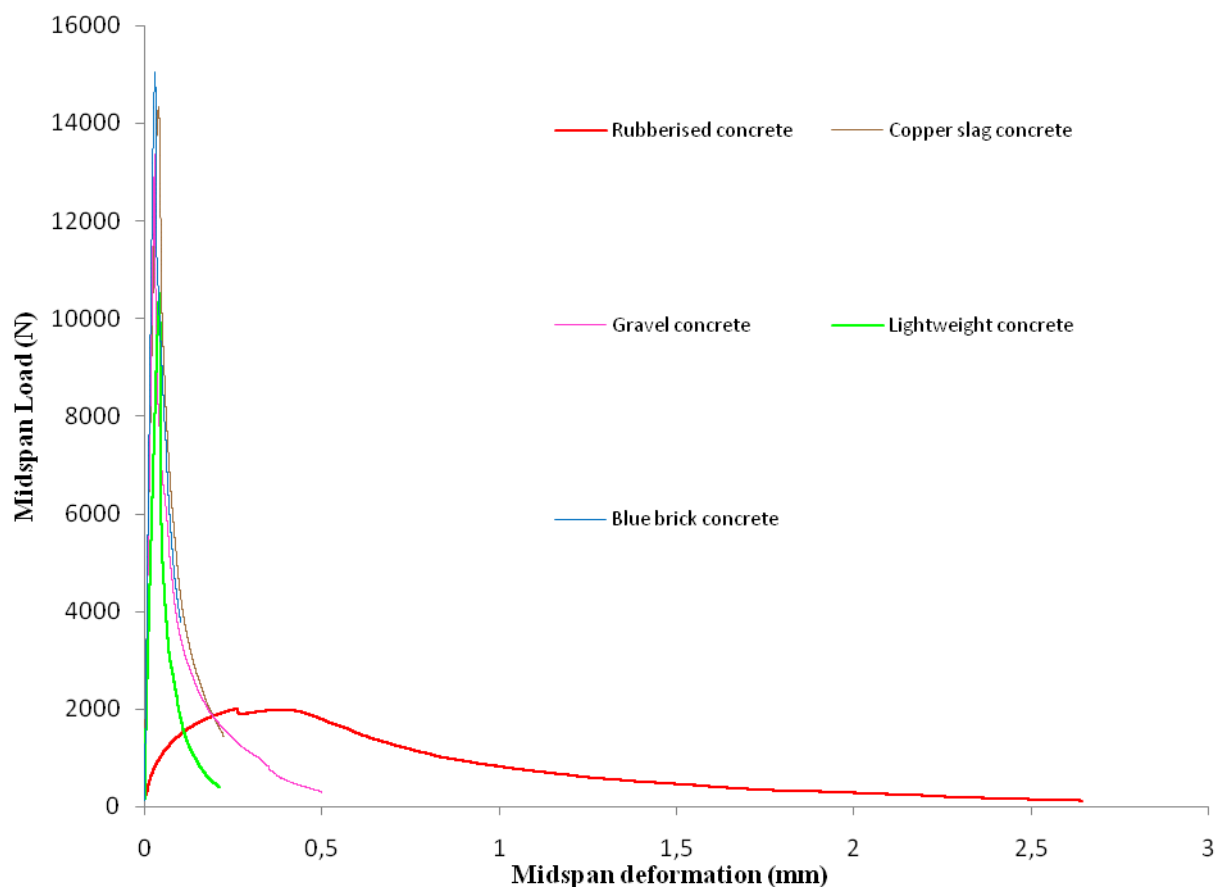


Fig.4.23: Flexural load-deformation curves of the mixtures

Table 4.6: First cracks loads, peak loads and corresponding deflections

Concrete ID	First crack		Peak		Fracture Energy
	Deflection (mm)	Load (kN)	Deflection (mm)	Load (kN)	(kNm)
Gravel	0.028	13.36	0.028	13.36	1.51
Lightweight	0.0041	1.71	0.042	10.50	1.35
Copper slag	0.014	2.36	0.052	14.20	1.74
Blue brick	0.026	14.30	0.034	15.25	1.97
Rubberised	0.123	0.82	0.546	2.1	2.92

4.9 Concluding Remarks

In the light of the findings obtained in this chapter, the following conclusions can be drawn:

- Concrete with fly ash/ Lytag aggregates had a higher compressive strength than the gravel concrete. The higher compressive strength in the lightweight concrete was probably due to enhanced hydration as a result of internal curing process (this interpretation was supported by the thermogravimetric analysis).
- Concrete produced with blue brick aggregates gave the highest compressive strength than the gravel concrete although its degree of hydration is lower than that of the gravel concrete. It cannot be concluded definitively from XRD result that pozzolanic activity was a major contribution to the higher strength in the brick. However, it is postulated that the utilization of water in fresh concrete is partly influenced by the surface and geometrical characteristics of the aggregate particles.
- It is therefore believed that these aggregate characteristics had bearing on the effective w/c ratio and, hence, on the pore water in the ITZ. This will, in turn, result in a better packing of cement particles against aggregate surfaces and less thicker and stronger ITZ.

- Coupled with this phenomenon is the fact that this type of aggregate, because of its inherent strength, plays a dominant role in attenuating crack propagation under loading condition. The cumulative effect of these mechanisms therefore improved the strength of the concrete.
- The concrete mixture prepared with copper slag aggregate exhibited about 25 % higher dynamic modulus of elasticity than the concrete containing gravel aggregate. This is assumed to be because of relatively lower internal vibration damping properties in the material. The mortar matrix with copper slag is less porous and has a higher density compared to the reference mortar matrix, and thus the ultrasonic pulse can move faster there.
- The air void distribution of the concrete mixes was determined from X-ray CT images along with digital image analysis techniques, and reasonable data was obtained. In addition, 3D simulation of air void distribution was successfully done. It has been observed that the air void distribution is not uniform through the specimens' heights, and the voids are more prominent in the middle section of the specimens except the rubberised mix.

References:

- [1] Al-Rousan, T., Masad, E., Tutumluer, E., and Pan, T., (2007). "Evaluation of image analysis techniques for quantifying aggregate shape characteristics." *Construction and Building Materials* 21 (5) 978-990.
- [2] ASTM C1018, Annual Book ASTM Standards, 1989: 4 (04.02).
- [3] Balendran, R.V., Zhou, F.P., Nadeem, A., and Leung, A.Y.T., (2002). "Influence of steel fibres on strength and ductility of normal and lightweight high strength concrete." *Building and Environment* 37 (12) 1361-1367.
- [4] Bentz, D.P., (2007). "Internal curing of high performance blended cement mortars." *ACI Materials Journal* 104 (7) 408-414.
- [5] British Geological Survey Report (2008) "The need for indigenous aggregates production in England". [http://nora.nerc.ac.uk/3711/1/Aggregates - Final Report June 2008.pdf](http://nora.nerc.ac.uk/3711/1/Aggregates_-_Final_Report_June_2008.pdf).
- [6] BS 1881-121 (1983). "Testing concrete. Method for determination of static modulus of elasticity in compression." British Standard Institution.
- [7] BS 812-102 (1989). "Testing aggregates methods for sampling." British Standard Institution.
- [8] BS EN 197-1:2000, Cement Part 1: Composition, specifications and conformity criteria for common cements, British Standard Institution, London, 2000.
- [9] BS EN 12390-3 (2002). "Testing hardened concrete. Part 3: Compressive strength of test specimens." British Standard Institution.
- [10] BS EN 13139: 2002, Aggregates for mortar, British Standard Institution, London, 2002.
- [11] Carr, J.R., Norris, G.M., and Newcomb, D.E., (1990). "Characterization of aggregate shape using fractal dimension." *Transportation Research Record* 1278 (3) 43-50.
- [12] Chan, C., (1998). "Use of recycled aggregate in shotcrete and concrete". MSc Thesis. The University of British Columbia.

- [13] Eldin, N.N., and Senouci, A.B., (1993). "Rubber-tire particles as concrete aggregate." *ASCE Journal of Materials in Civil Engineering*, 5 (4) 478-496.
- [14] Gorai, B., Jana, R.K., and Premchand, (2003). "Characterisation and utilisation of copper slag- a review." *Resources Conservation and Recycling* 39 (4) 299-213.
- [15] Henkensiefken, R., D. Bentz, et al. (2009). "Volume change and cracking in internally cured mixtures made with saturated lightweight aggregate under sealed and unsealed conditions." *Cement and Concrete Composites* 31 (7) 427-437.
- [16] Hijazin, G.E., and Lopez M., (2011). "Extending internal curing to concrete mixtures with w/c higher than 0.42." *Construction and Building Materials* 25 (3) 1236-1242.
- [17] JCI Standards SF 4 (1983). "Method of test for flexural strength and flexural toughness for fibre reinforced concrete." *Japan Concrete Institute* 35-36.
- [18] Kayali, O., (2008). "Fly ash lightweight aggregates in high performance concrete." *Construction and Building Materials* 22 (12) 2393-2399.
- [19] Khanzadi, M., and Behnood, A., (2009). "Mechanical properties of high-strength concrete incorporating copper slag as coarse aggregate." *Construction and Building Materials* 23 (4) 2183-2188.
- [20] Khatib, Z.K., and Bayomy, F.M., (1999). "Rubberized Portland cement concrete." *ASCE Journal of Materials in Civil Engineering* 20 (10) 640-649.
- [21] Kockal, N.U., (2008). "Effects of lightweight fly ash aggregate properties on the performance of lightweight concretes." PhD Thesis. Bogazici University, Turkey.
- [22] Kuo, C.Y., and Freeman, R.B., (2000). "Imaging indices for quantification of shape, angularity and surface texture of aggregates." *Transportation Research Records* 1721 (7) 57-65.

- [23] Kwan, A.K.H., Moro, C.F., and Chan, C.H., (1999). "Particle shape analysis of coarse aggregates using digital image processing." *Cement and Concrete Research* 29 (9) 1403-1410.
- [24] Loukili, A., Khelidj, A., and Richard, P., (1999). "Hydration kinetics, change of relative humidity, and autogenous shrinkage of ultra-high strength concrete." *Cement and Concrete Research* 29(4) 577-584.
- [25] Martin, W., (2002). "Tyre crack-down to help environment." UK Government Environment Agency.
- [26] Masad, E., Muhunthan, B., Shashidhar, N., and Harman, T., (1999). "Internal structure characterization of asphalt concrete using image analysis." *Journal of Computing in Civil Engineering (Special Issue on Image Processing)*, ASCE, 13 (2) 88-95.
- [27] Müller-Rochholz, J., (1979). "Determination of the elastic properties of lightweight aggregate by ultrasonic pulse velocity measurements." *International Journal of Lightweight Concrete* 1 (2) 87-90.
- [28] Newman, J., and Owens, P., (2003). "Properties of Lightweight Concrete (Chapter 2)". In: J. Newman and B.S. Choo, Editors, "Advanced concrete technology constituent materials 3". Wiley, New York, 72–98.
- [29] Peschard, A., Govin, A., Grosseau, P., Guilhot, B., and Guyonnet, R., (2004). "Effect of polysaccharides on the hydration of cement paste." *Cement and Concrete Research* 34 (3) 2153-2158.
- [30] Schutter, G.D., (2004). "Applicability of degree of hydration concept and maturity method for thermo-visco-elastic behaviour of early age concrete." *Cement and Concrete Composites* 26 (5) 437-443.
- [31] Shi, C., Meyer, C., and Behnood, A., (2008). "Utilization of copper slag in cement and concrete." *Resources Conservation and Recycling* 52 (10) 1115-1120.

- [32] Smith, M.R., and Collis, L., (2003). "Aggregates: sand, gravel and crushed rock for construction purposes." Geological Society Special Publication, No 17.
- [33] Taha, M.M.R., El-Dieb, A.S., El-Wahab, M.A.A., and Abdel-Hameed, M.E., (2008). "Mechanical, fracture and microstructural investigation of rubber concrete." ASCE Journal of Materials in Civil Engineering 20 (10) 640-649.
- [34] Tang, W.C., Lo, T.Y., and Chan, W.K., (2008). "Fracture properties of normal and lightweight high-strength concrete." Magazine of Concrete Research 60 (4) 237-244.
- [35] Tasong, W.A., Lynsdale, C.J., and Cripps, J.C., (1998). "Aggregate-cement paste interface ii: influence of aggregate physical properties." Cement and Concrete Research 28 (10) 1453-1465.
- [36] Toutanji, H.A., (1996). "The use of rubber tire particles in concrete to replace mineral aggregates." Cement and Concrete Composites 18 (2) 135-139.
- [37] Yuan, S. C. and Harrison, J. P., (2006). "Development of a hydro-mechanical local degradation approach and its application to modelling fluid flow during progressive fracturing of heterogeneous rocks." International Journal of Rock Mechanics and Mining Sciences 42 (7-8) 961-984.
- [38] Zhou, F.P., Lyndon, F.D., and Barr, B.I.G., (1995). "Effect of coarse aggregate on elastic modulus and compressive strength of high performance concrete." Cement and Concrete Research 25 (1) 177-186.

CHAPTER 5

QUANTITATIVE ASSESSMENTS OF MICROSTRUCTURE OF THE INTERFACIAL ZONE IN THE CONCRETE MIXTURES

5.1 General:

The main focus of this study is to evaluate the differences generated in the impact load-induced cracking behaviour and mechanical performance of concrete associated with the changes in the micro-mechanical properties of the ITZ (as influenced by the characteristics of the coarse aggregate). Thus, this chapter first describes test procedures for quantifying the structure and mechanical properties of the ITZ. Following that, the results of micro-structural characteristics of the transition zone (namely; surface roughness, porosity and thickness, chemical nature, interconnectivity, hardness) will be discussed, highlighting the influence of the characteristics of the coarse aggregates on this zone. Finally, the last section of this chapter draws concluding remarks.

5.2 Test Procedures for Characterization of the ITZ

5.2.1 Scanning Electron Microscopy (SEM)

5.2.1.1 Working principle of the SEM

An understanding of the fundamental principles of Scanning Electron Microscopy (SEM) will help us to accurately interpret and analyse the micrographs obtained from this technique. Therefore, the first part of this chapter introduces some of the basic principles of the SEM.

The specimen in a SEM is bombarded by a focused beam of high-speed electrons. When the electron beam (called primary electron) hits the specimen surface, a number of interactions take place with the specimen, as shown in Fig.5.1. For example, the beam electrons might be scattered by the atomic structure in the sample and their directions might be changed over a wide range with only very small loss of their energies (elastic scattering). In other case, the primary electrons might be scattered inside the sample at low angles, losing detectable amount energy. In essence, energy from the primary electrons is conveyed to the atoms in the sample (inelastic scattering). Overall, these processes generate three major types of electrons, backscattered electrons, secondary electrons and X-rays photons ([Fens, 2000](#)).

Backscattered electrons (BSE) are those electrons in the electron beam and have high energy. BSE imaging is highly sensitive to the differences in the atomic number of the materials irradiated. Phases including lower atomic number elements appear darker than those containing higher atomic number elements. Therefore, phases in concrete such as unhydrated cement particles, crack and voids and C-S-H solids can be easily distinguished and measured, based on the grey level intensities ([Sahu et al., 2004](#)). Secondary electrons are those electrons which escape from within a few nanometres of the sample surface due to their low energy. Thus, they can only provide information about the surface topography. X-rays are generated when a

specimen is bombarded by high energy electrons and allows the study of chemical constituents of surfaces (Clarke and Eberhardt, 2002).

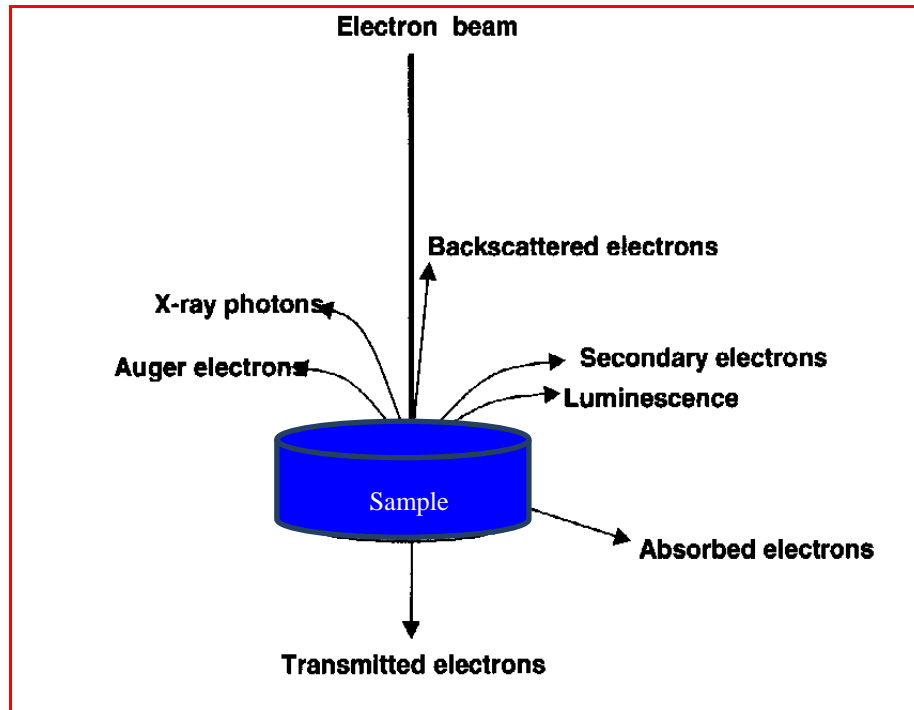


Fig.5.1: Interaction between the beam and sample (Adapted from Fens, 2000)

Generation of these three major of signals occurs in a volume of tear drop shape (Fig.5.2) that is known as the excitation volume. Understanding of the excitation volume is really important as the lateral resolution of the image generated from each signal depends, to a great extent, to its size. The penetration depth and shape of the interaction volume are dependent three major parameters: the applied accelerating voltage (the beam energy), the average atomic number of sample and the beam electron density (Fens, 2000 and Hemavibool, 2007). With the higher accelerating voltage, the incident electrons tend to penetrate deeply into the specimen resulting in a larger interaction volume. Similarly, material with a higher atomic number generate much more scattering near the specimen surface and consequently, most of the incident electrons are scattered resulting in a larger but less deeper interaction volume, as shown in Fig.5.3.

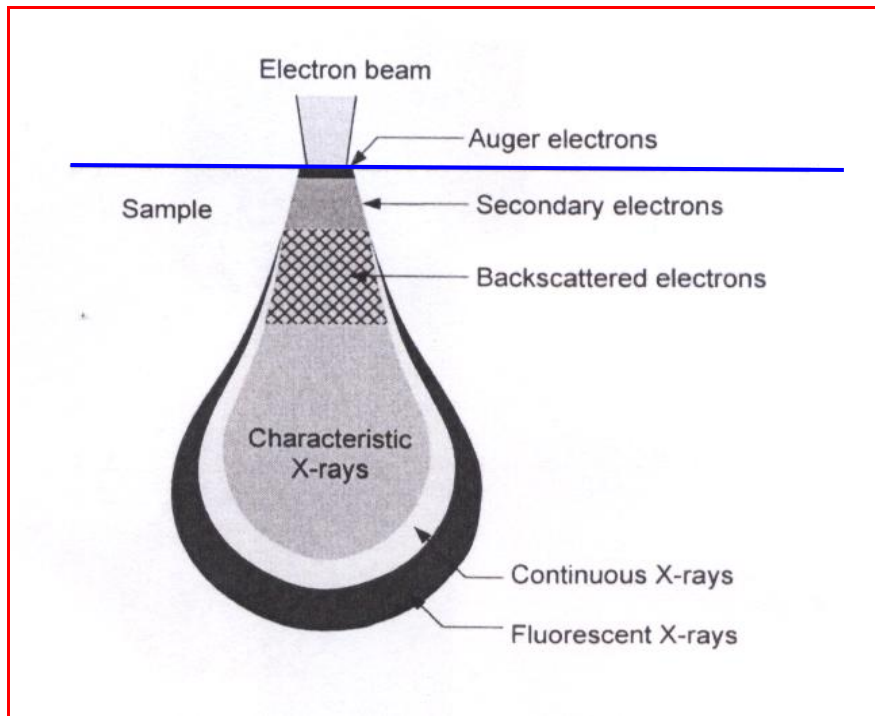


Fig.5.2: Schematic view of the interaction volume and the regions of the various signals (Hemavibool, 2007)

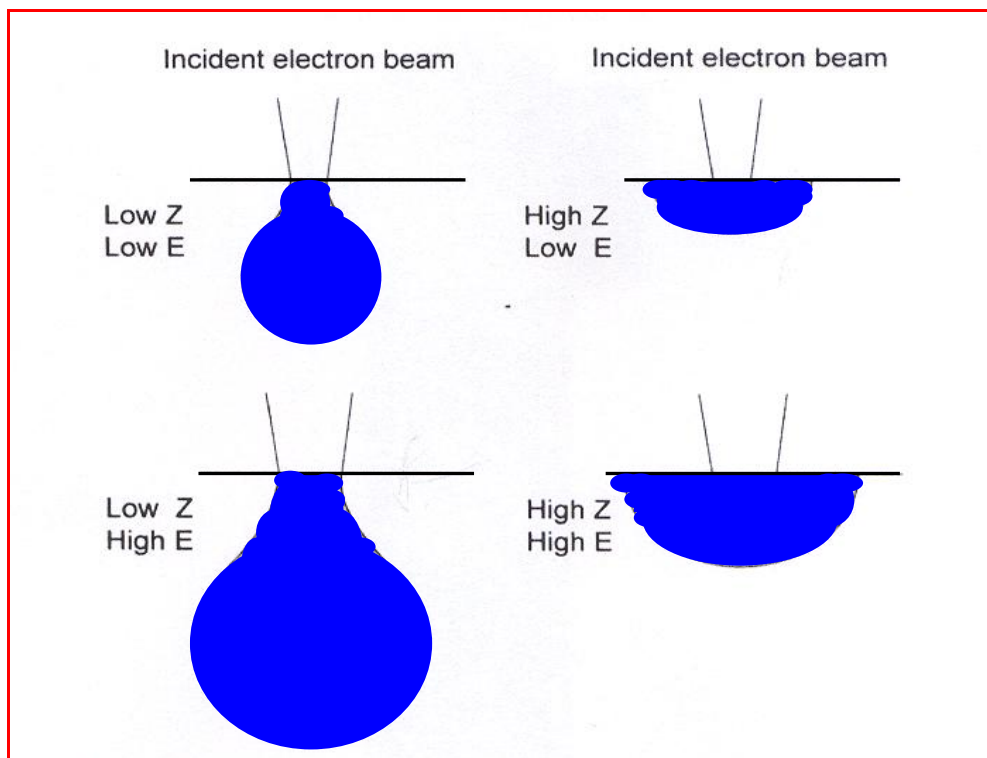


Fig.5.3: Illustration of the variation in the interaction volume shape, E: electron beam accelerating voltage and Z: the average specimen atomic number (Hemavibool, 2007)

5.2.1.2 Sample preparation

The morphological features of the microstructures were investigated by using a Philips XL 30 SEM fitted with an Oxford Instruments INCA model spectrometer for energy-dispersive X-ray (EDX) analysis. The samples were prepared by taking small pieces from the crushed specimens. The microstructure and morphology of the mixtures were observed on fractured surfaces using the secondary electron mode of the SEM. Fractured small samples were mounted on the SEM stubs and left under high vacuum, and then coated with carbon before capturing an image. The samples were then stored in a vacuum dessicator until they were required for the SEM analysis to prevent or minimize the surface carbonation likely due to the exposure of the samples to the CO₂ in the atmosphere. The SEM micrographs were captured using an accelerating beam voltage of 15-25 kV with different magnifications.

5.2.2 Micro-mechanical Properties of the ITZ

5.2.2.1 Porosity in ITZ

The quantification of the porosity in the ITZ has been mainly performed by means of the technique developed by [Scrivener and Pratt \(1987\)](#). The observations were made on the flat polished sections of the concretes by using the BSE mode of the SEM. For this purpose, the specimens were first mechanically ground with 200, 400, 800 and 1200 grit abrasive papers and then polished sequentially using 6, 3 and 1 µm diamond paste. Finally, the specimens were cleaned in ethanol and distilled water and ultrasonically dried before putting into the vacuum chamber.

The BSE images were captured at 540x magnification and digitized into grey level images of 512x512 pixels resolution. It was decided to analyze the porosity profile for ITZ up to 50 µm

from the aggregate surface as the thickness of ITZ is around 20-50 μm (Akçaoğlu et al., 2004). The profile for the bulk paste was also determined using a similar technique, but the analysis was carried out at least 50 μm away from the nearest aggregate surface. The ITZ and the bulk paste images were analysed using Scandium image software.

As is well-established, segmentation of the features of interest from background can be carried out by defining a range of brightness (grey) value in the original image. This process is known as thresholding. Any pixels having grey value within this range are set to the foreground (grey value = 255) and all of the rest are rejected to the background (grey value = 0). Fig.5.4 shows a typical grey level histogram of cement paste material. The grey level limits for the percent of detectable porosity was determined after carefully examining a number of images to make sure the limits are valid for all of images processed. The threshold limits for the grey level of the detectable pores has been selected in the range 0-90 with an error of ± 5 for all images. However, it should be highlighted that the results presented are for the detectable feature and do not represent the absolute value.

5.2.2.2 Measurement of ITZ thickness

The ITZ thickness has been regarded as the distance from the aggregate surface until the point where the porosity value reaches that of the observed porosity of the bulk paste.

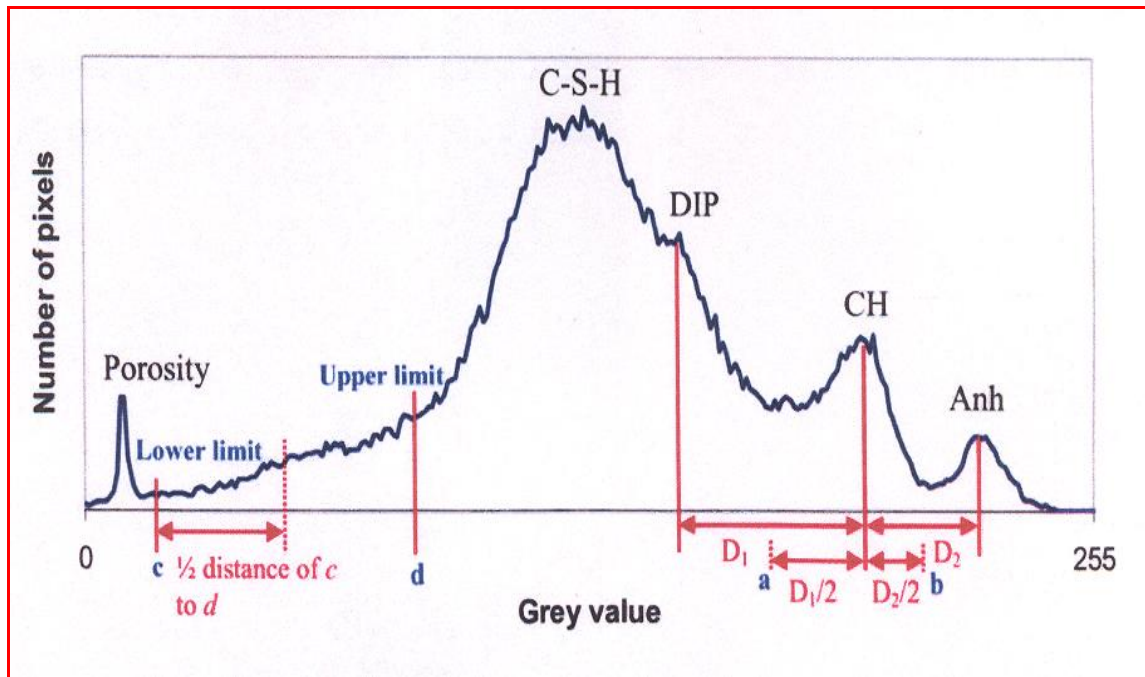


Fig.5.4:Thresholding criteria for the segmentation of the constituents in concrete, DIP: dense inner hydration products, Anh: unhydrated cement particles (Hemavibool, 2007)

5.2.2.3 Measurement of ITZ micro-hardness

A Vickers micro-hardness test was carried out to determine the micro-hardness in the transition zone between aggregates and hardened cement paste. The test load was 0.01 kg with 10 s contact time. The measured range was up to 100 μm away from the surface of aggregates. Six determinations were performed on the surface of each sample.

5.2.2.4 Elements analysis in ITZ

X-ray line scanning analyses were made in the region of the aggregate-cement paste interfaces of the specimens using a 25 kV accelerating voltage. This is to allow deep penetration of electrons and generate a greater number of characteristics X-rays, whilst the larger interaction volume did not adversely obscure the line scan resolution. The counting rate for each analysis obtained was 100s. The analysis was obtained between 5 and 20 μm

from the aggregate interface. Trägårdh (1999) used the following classification in order to distinguish hydrates. The same classification was used in this study.

C-S-H: $0.8 \leq \text{Ca/Si} \leq 2.5$, $(\text{Al} + \text{Fe})/\text{Ca} \leq 0.2$

CH: $\text{Ca/Si} \geq 10$, $(\text{Al} + \text{Fe})/\text{Ca} \leq 0.4$, $\text{S/Ca} \leq 0.04$

AFm: $\text{Ca/Si} \geq 4$, $(\text{Al} + \text{Fe})/\text{Ca} \leq 0.40$, $\text{S/Ca} > 0.15$

5.2.2.5 Measurement of surface roughness of ITZ

The surface roughness of the ITZs was measured using a vertical scanning interferometer (Fogale Nanotech Photomap 3D, Ville Active, Nimes, France-Fig.5.5). The same concrete samples prepared for the SEM investigation were also used in this analysis. A quantitative evaluation of each file was digitally carried out to calculate the surface roughness. A mean value of four measurements in at least two different locations was used as a response value for each experiment.

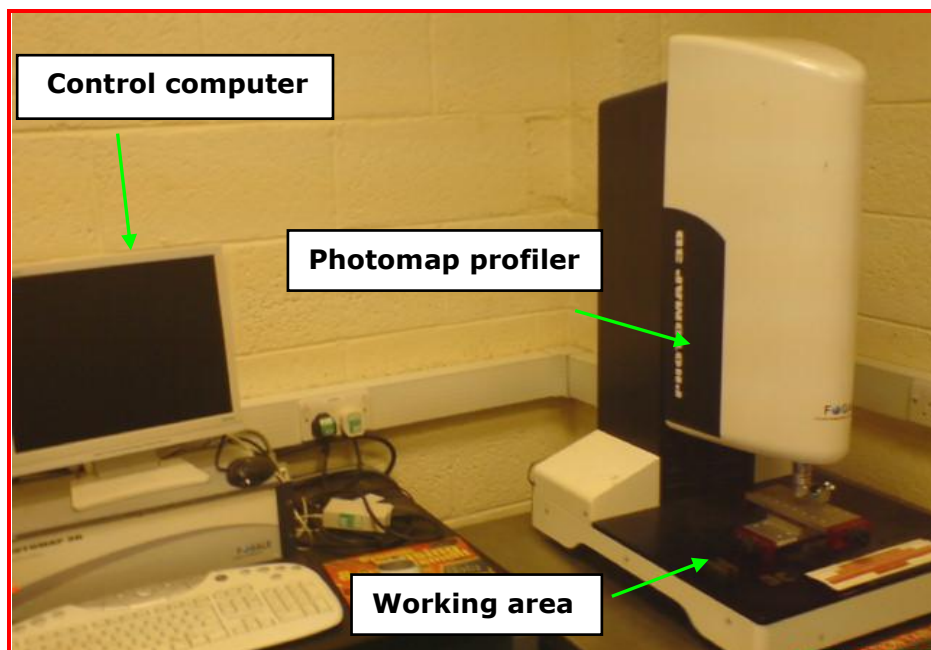


Fig.5.5: Nanotech vertical scanning interferometer

5.3 Results and Discussion of Micro-mechanical Properties of the ITZ

5.3.1 Surface Roughness of the ITZ

Three dimensional micro-graphs of the ITZ surfaces were constructed using a vertical scanning interferometer (Nanotech Photomap 3D). They are presented in Fig. 5.6 to 5.9. The calculated Ra (surface profile roughness) values are also illustrated in the figures. In general, the figures indicate that the paste surface in the case of the lightweight concrete has the smoothest profile (Fig.5.9) while the paste region of the rubberised concrete has the highest irregularity (Fig.5.8b) followed by those of the blue brick (Fig.5.8a), copper slag (Fig.5.7) and gravel mixtures (Fig.5.6), respectively.

The differences in the profile and roughness values of the specimens could be attributed to the degree of hydration of the mixtures and the shape properties of the aggregates used. Partly, this was explained by [Ficker et al. \(2010\)](#) who concluded that stronger hydrated Portland cement pastes will have smoother fracture surfaces as the finer products of hydration reactions will fill the gaps between the grains resulting in a more uniform and less porous structure. Similarly, it is well-known that rounded particles usually pack together more closely than angular particles ([Kwan and Mora, 2001](#)). This is because particle asperity breakage and/or significant dilation would be needed to achieve the same relative displacement of angular particles, and both of these need more energy than does the rolling or particle slip largely achieved in rounded aggregate mixes. Thus proper interlocking of angular aggregates is hindered, and this leads to a more random distribution of fine and coarse hydration products as well as cementitious particles which, in turn, may lead to an increase in the local capillary porosity in the hardened paste. This results in peaks and troughs of strength across the length of an aggregate-paste boundary. Such a difference leads to the question that will be fully answered in the following chapters “how do changes in the paste-

aggregate surface roughness affect the deformation behaviour and energy dissipation characteristics of the concrete that is subjected to impact loading?”

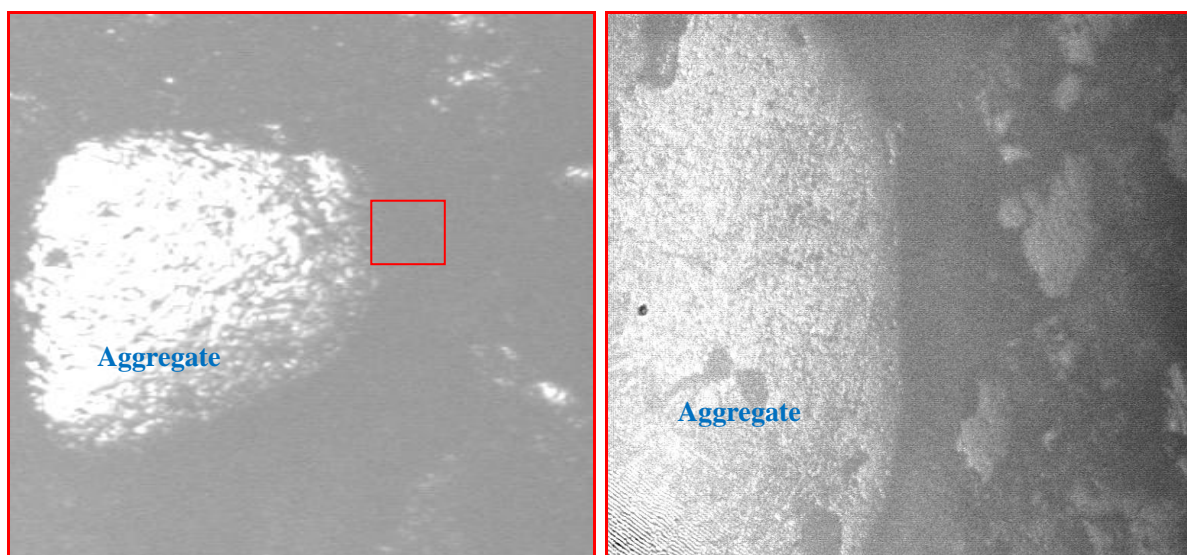
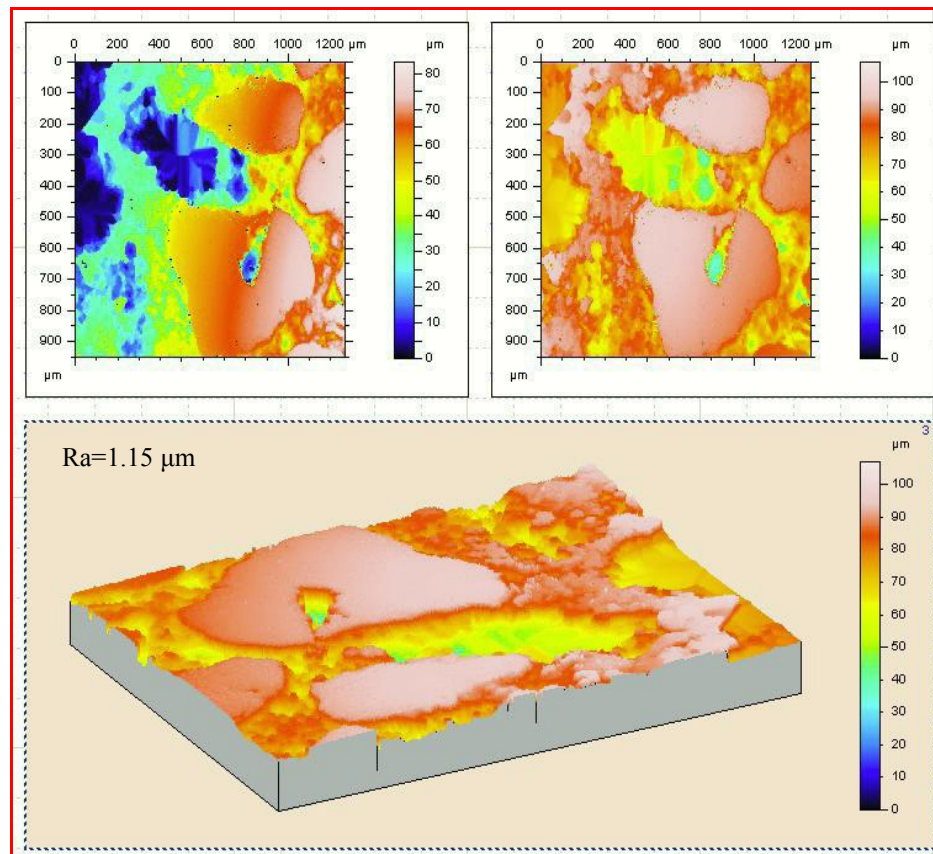


Fig.5.6: Surface roughness profile of the ITZ in the gravel mixtures and an example of camera view of the area

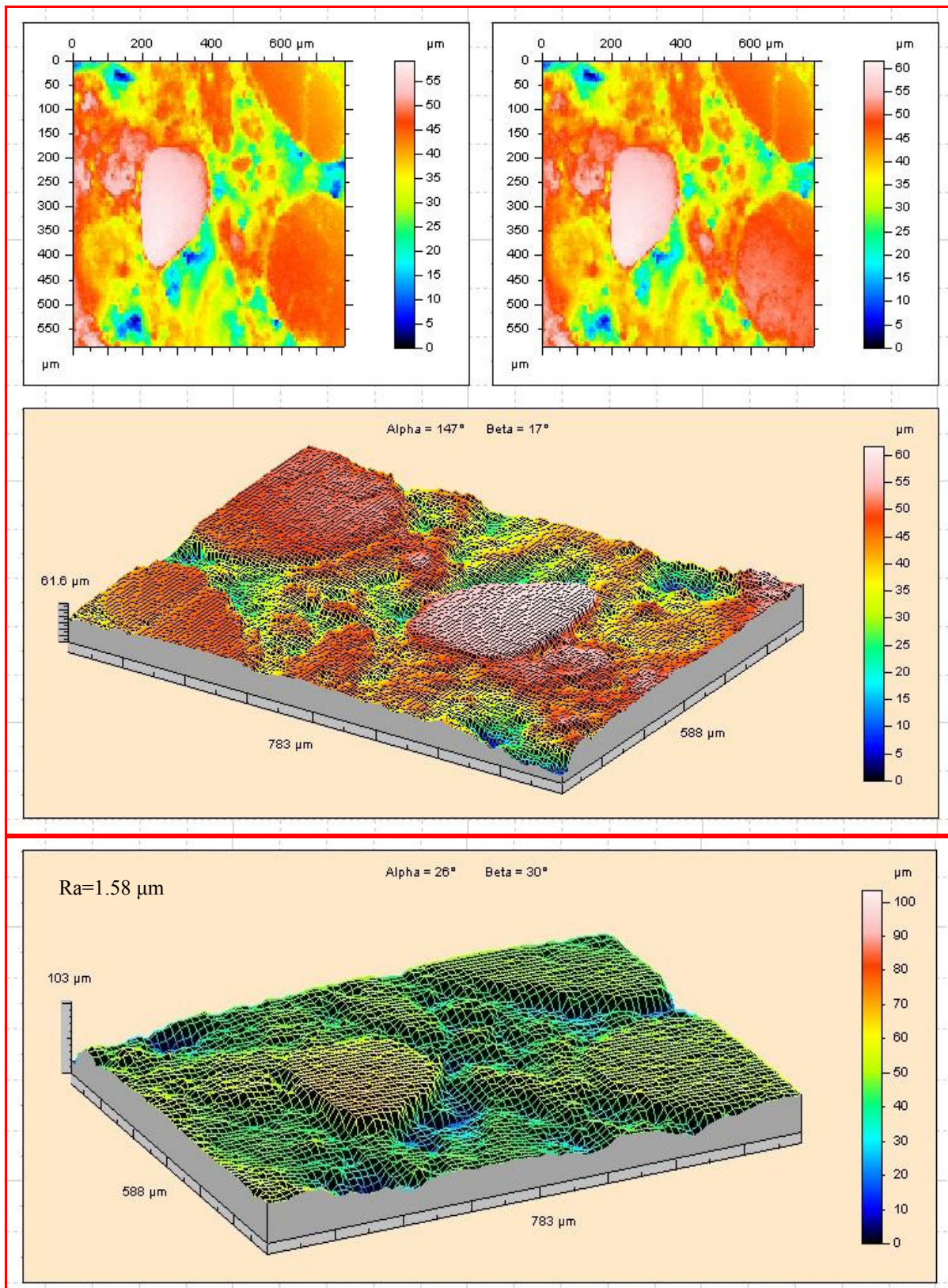
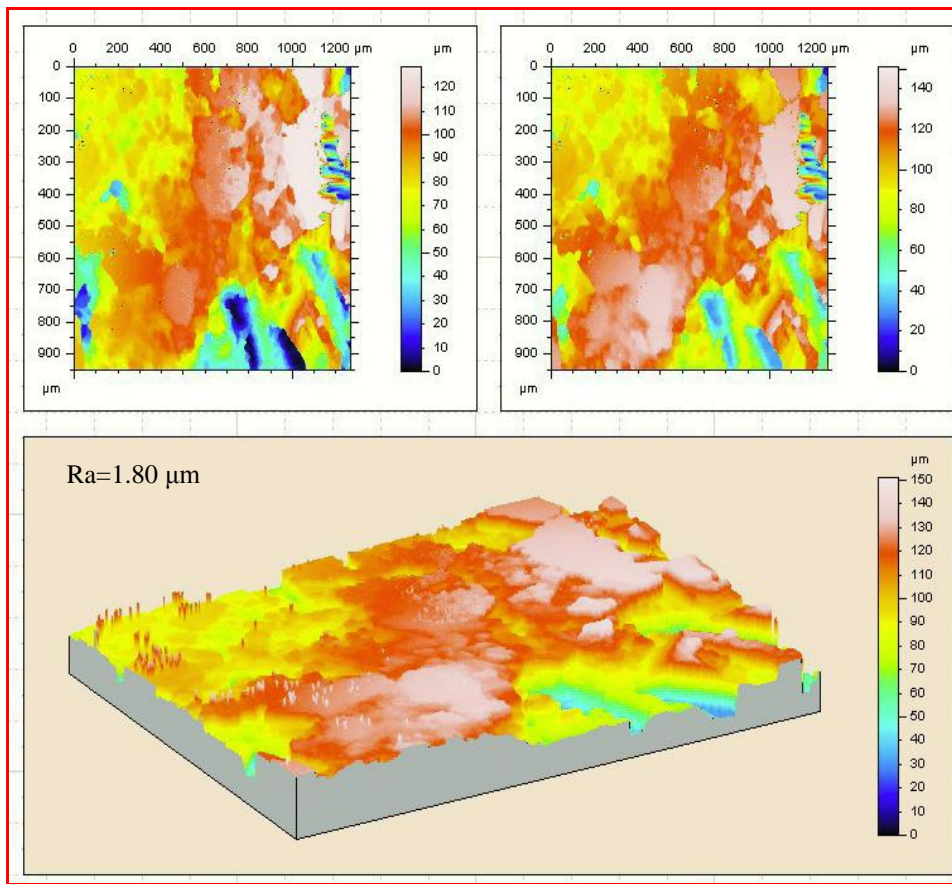


Fig.5.7: Surface roughness profiles of the paste matrix in the copper slag mixtures with mesh application and different view of angles

a)



b)

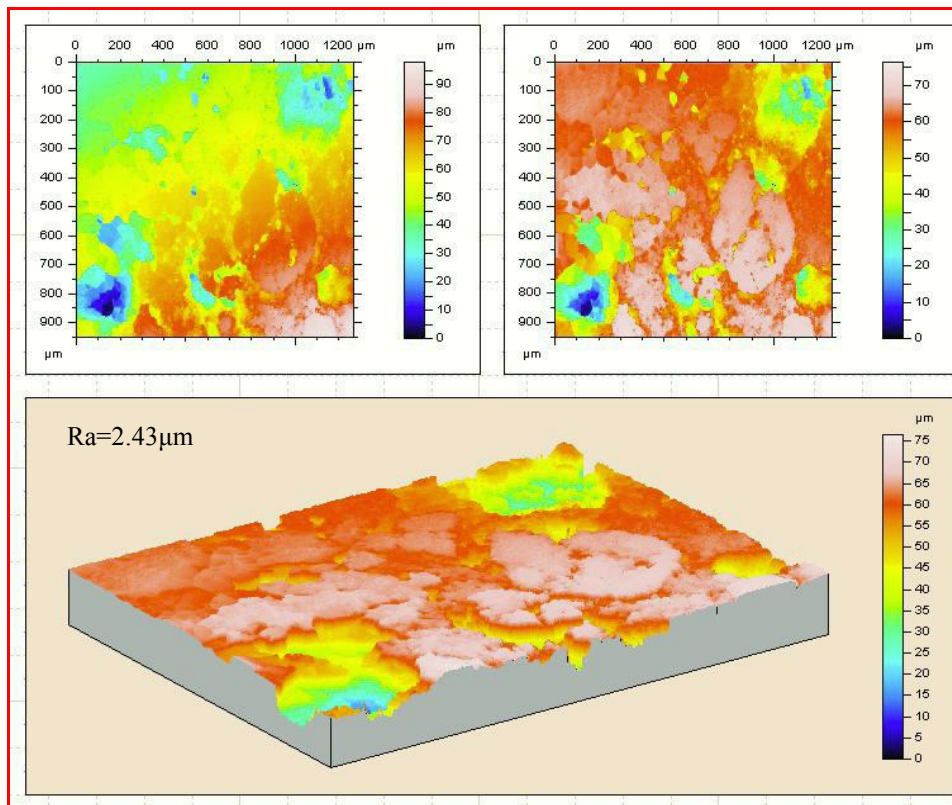


Fig.5.8: Surface roughness profile of the ITZ of the blue brick (a) and rubberised mixtures (b)

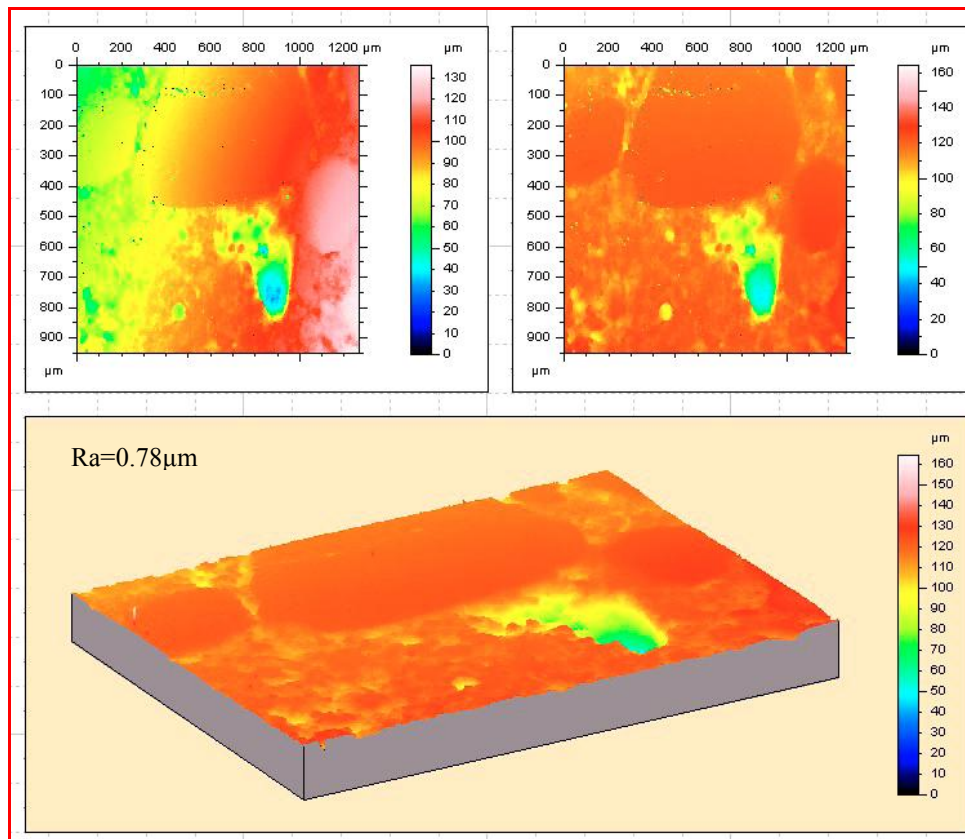


Fig.5.9: Surface roughness profile of the ITZ of the lightweight mixture

5.3.2 Chemistry of the hydrous phases in the ITZ

The average atomic ratios of the hydrous phases in the ITZ of the mixtures measured by SEM coupled with EDX are listed in Table 5.1. X-ray line scanning analyses were made in the region of the aggregate-cement paste interfaces of the specimens to investigate the presence of various elements.

An example of the analysis conducted by the author is given in Fig.5.10. In addition, an example of the EDX spectrum profile for the elements detected is displayed in Fig.5.11. Interested readers can be found more details about the analysis in the attached excel worksheet (see Appendix D).

The analysis revealed that there was significant difference in the Ca/Si, (Al + Fe)/Ca and S/Ca ratios of the ITZs of the concrete mixtures. Significant differences in all three ratios also existed between the intermixed phases and C-S-H gels. The intermixed phases in the ITZ in the copper slag and rubberised concrete had lower Ca/Si but higher (Al + Fe)/Ca and S/Ca ratios. The ratios of (Al + Fe)/Ca and S/Ca indicate that the intermixed material in the copper slag and rubberised concrete predominantly consisted of a monosulfate phase (Fig.5.12a). Such a structure may promote secondary ettringite formation in the microstructure of the impact-damaged concrete. The most interesting finding was that there is a fairly constant Ca/Si ratio and a relatively large quantity of C-S-H throughout the microstructure of the lightweight cement paste (Fig.5.12b). Such a structure suggests that the micro-structural development is much more uniform and that the extra C-S-H would reduce weakness in the ITZ somewhat. More importantly, giving some support to the hypothesis (mentioned in the previous chapter) of pozzolanic reaction occurring around the fly ash/Lytag particle because of significant amount amorphous content present in the aggregate.

Table 5.1 Average atomic ratios of analyses in the ITZ of hydrous materials

Concrete ID	ITZ (Hydrous phases)	Ca/Si	(Al+Fe)/Ca	S/Ca
Gravel	Intermixed	2.66	0.34	0.041
Copper Slag	Intermixed	1.44	0.75	0.057
Lightweight	C-S-H and Intermixed	1.18	0.19	0.023
Blue Brick	Intermixed	1.52	0.52	0.045
Rubber	Intermixed	1.84	0.25	0.024

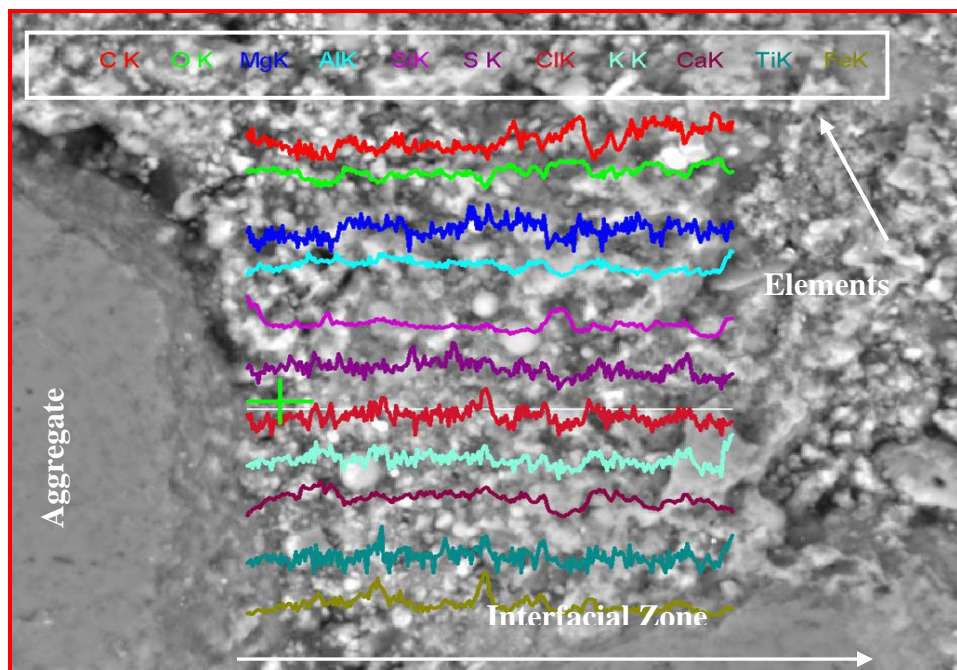


Fig.5.10: Energy dispersive spectroscopy analysis in the ITZ (at 1400x magnification)

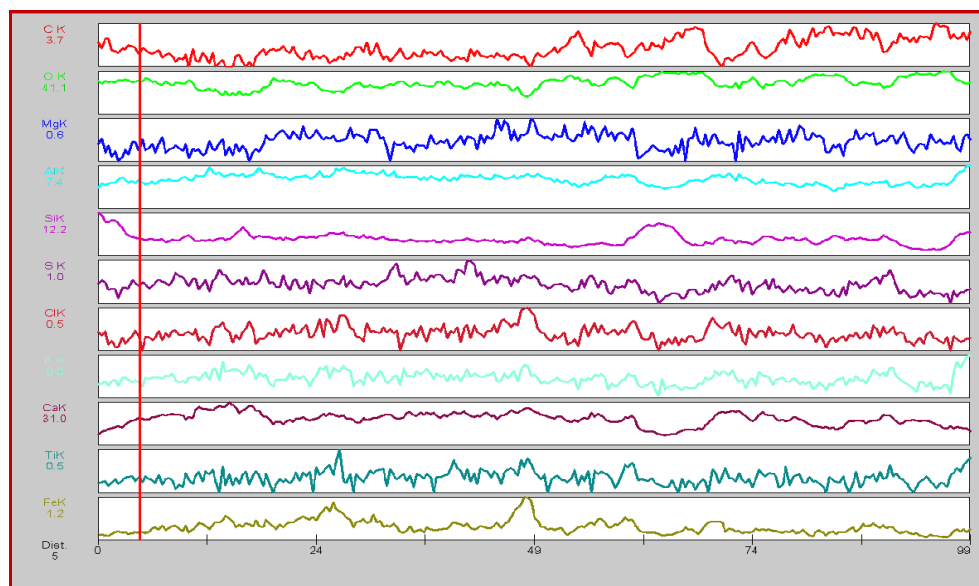


Fig.5.11: EDX spectrums of the elements

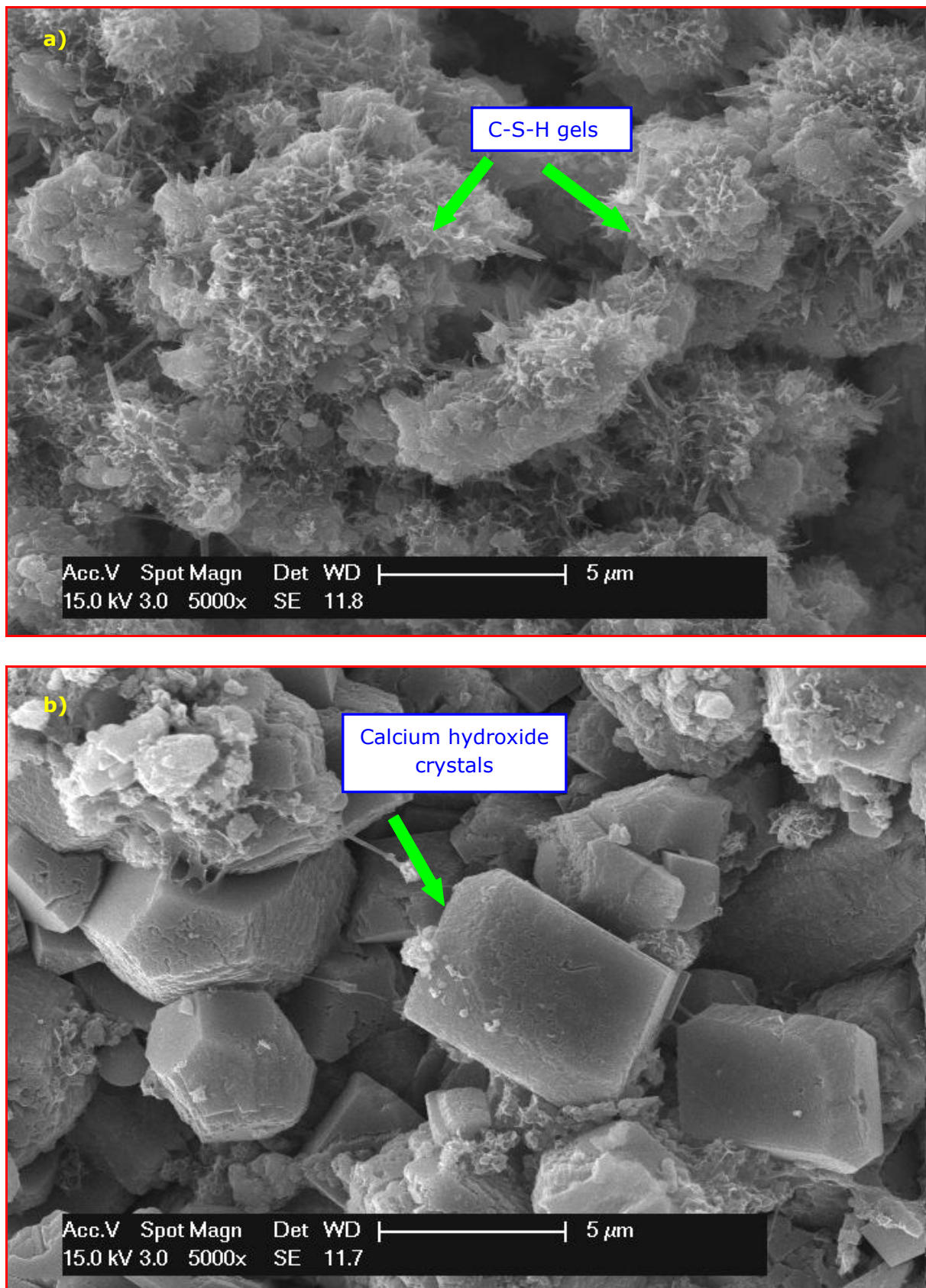


Fig.5.12: Internal structure of the lightweight (a) and the rubberised mix (b)

On the basis of the evidence so far discussed, it is also believed that the w/c ratio used in this study may contribute to the development of pozzolanic reactions somewhat as the progress of cement hydration, which is a relatively fast process at a high w/c ratio, leads to moisture loss and thus releasing of the absorbed water from the pores of the material ([Tuan et al., 2011](#)).

5.3.3 Thickness and Porosity of the ITZ

A SEM micrograph for the paste surrounding an aggregate is reproduced in Fig.5.13. The porosity of the pastes deduced from the image analysis of the micrographs as a function of the distance from the aggregate surface is also shown in Fig.5.14.

From the figure, it can be seen that in all types of concrete, the volume of pores in the ITZ decreases with increase in distance from the aggregate surface. The porosity of the paste surrounding the lightweight concrete at all distances was distinctively smaller than that of the paste around the gravel concrete. The error bars confirm the reliability of this comparison. By contrast, the porosity of the paste surrounding the rubber particles at all distances was significantly larger than that of paste around the reference concrete. In addition, the blue brick and the copper slag mixes exhibited quite similar porosity patch. Fig. 5.15 illustrates the close-up views of the ITZs in the concrete mixtures (the region of interest in a green frame). It seems that a reduced amount of CH crystals and penetration of hydration products into surface pores of the fly ash/Lytag (an example of EDX analysis is shown in Fig.5.16) contributes to the development of a better bond and produce a relatively unfavourable place for crack formation in the ITZ, as also suggested by [Wasserman and Bentur \(1996\)](#), and signifies that a higher local paste density has been achieved.

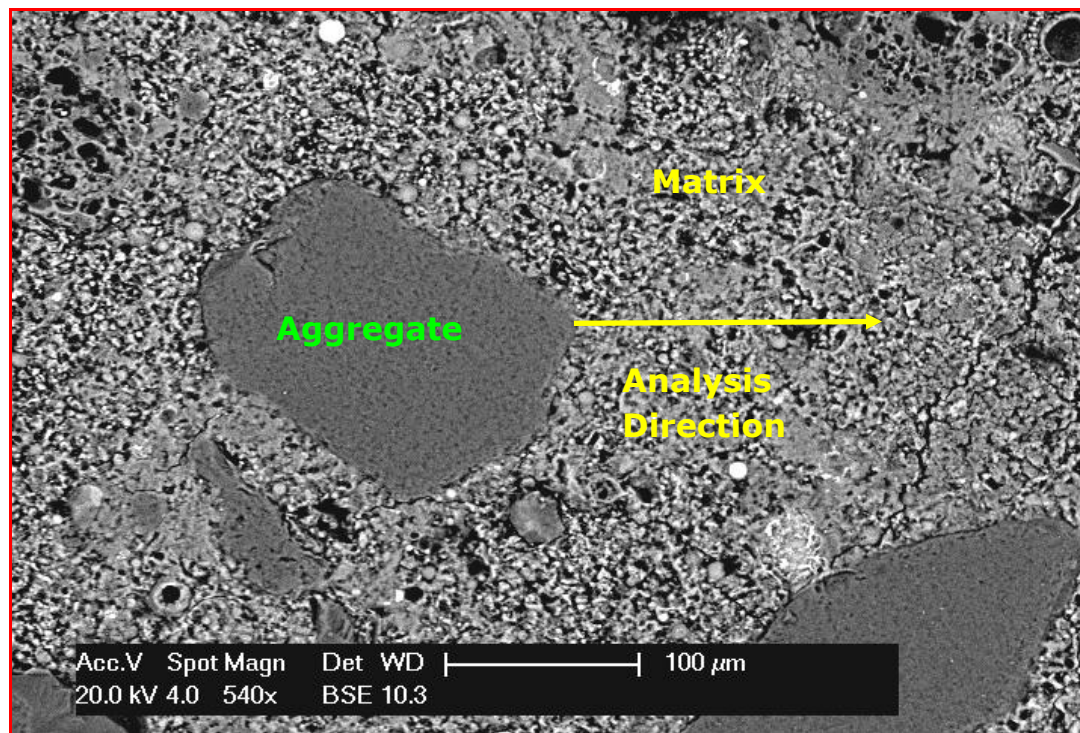


Fig.5.13: SEM micrographs of the pastes surrounding the aggregates

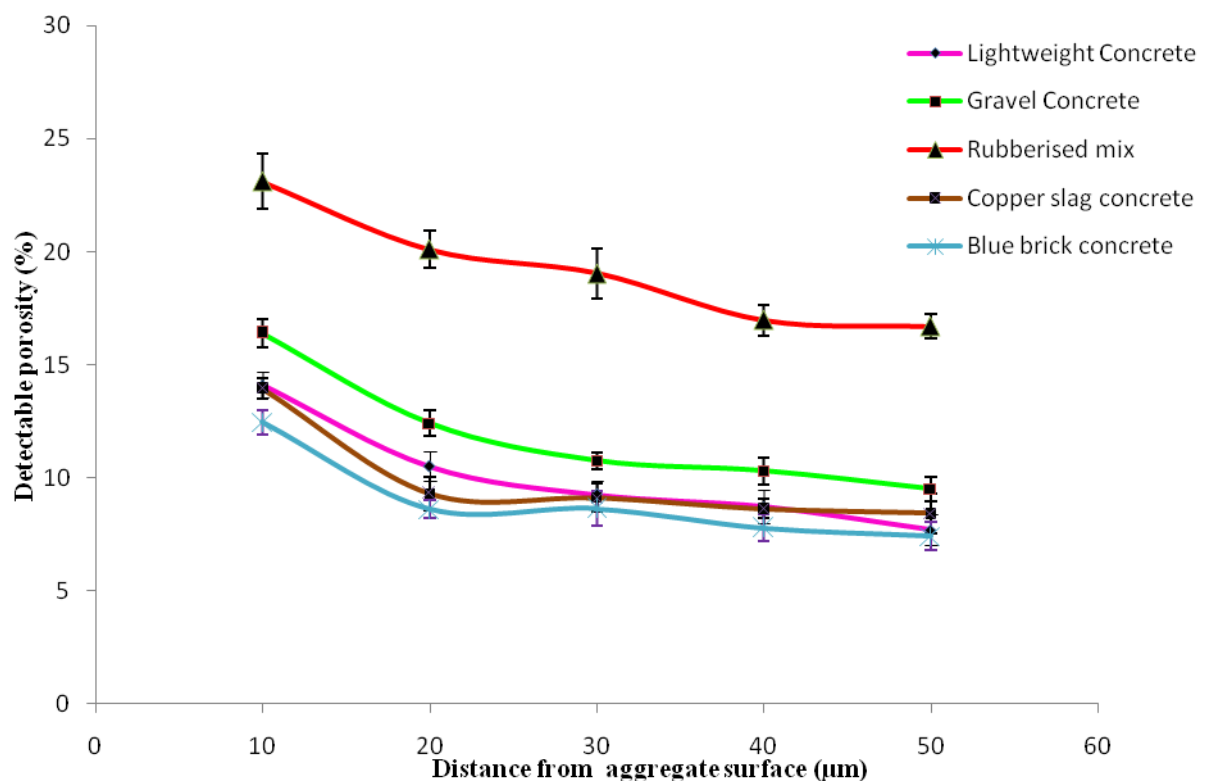


Fig.5.14: Interfacial porosity profiles of the mixes as a function of the distance from the aggregate surface

Fig.5.13 also shows that the thickness of the interfacial transition zone, where the porosity approaches to the level observed in the bulk paste, was approximately 15 μm , 18 μm , 20 μm , 28 μm and over 50 μm for the lightweight, blue brick, copper slag, gravel and rubberised concrete mixtures, respectively. The reduction in the thickness of the ITZ may increase the integrity of the concrete which in turn may contribute to enhancement of the strength. This is because, in the elastic case, the effect of increasing porosity is to make the moduli smaller, so that the ITZ elastic moduli are less than the bulk value, and increase with distance away from the aggregate surface (Garboczi and Bentz, 1997). Very recent work about the influence of impact loading on the nanomechanical properties of reactive powder concrete by Allison et al. (2011) showed that a majority of degradation in the microstructure of the specimens was associated with reductions in the elastic modulus and hardness, which were determined using a nano-indenter. Unfortunately, it was not possible to include this type of in-depth analysis and it was not conducted in this study due to lack of the facilities.

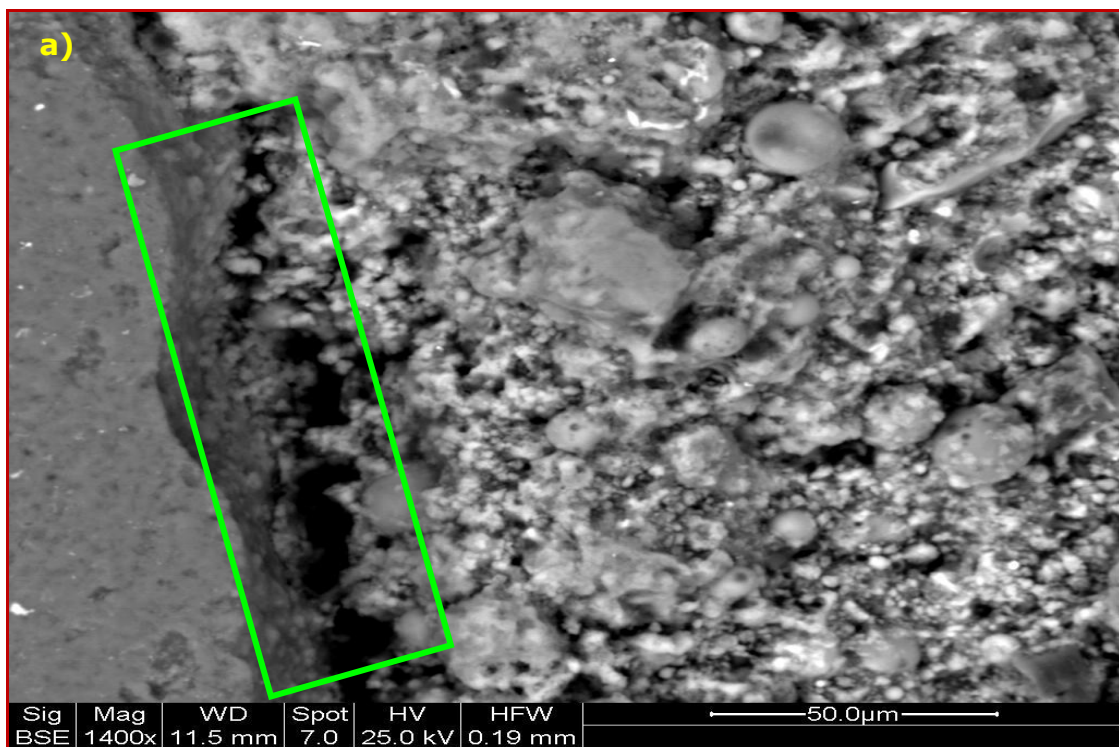


Fig.5.15: Close-up views of the ITZs of some of the mixtures

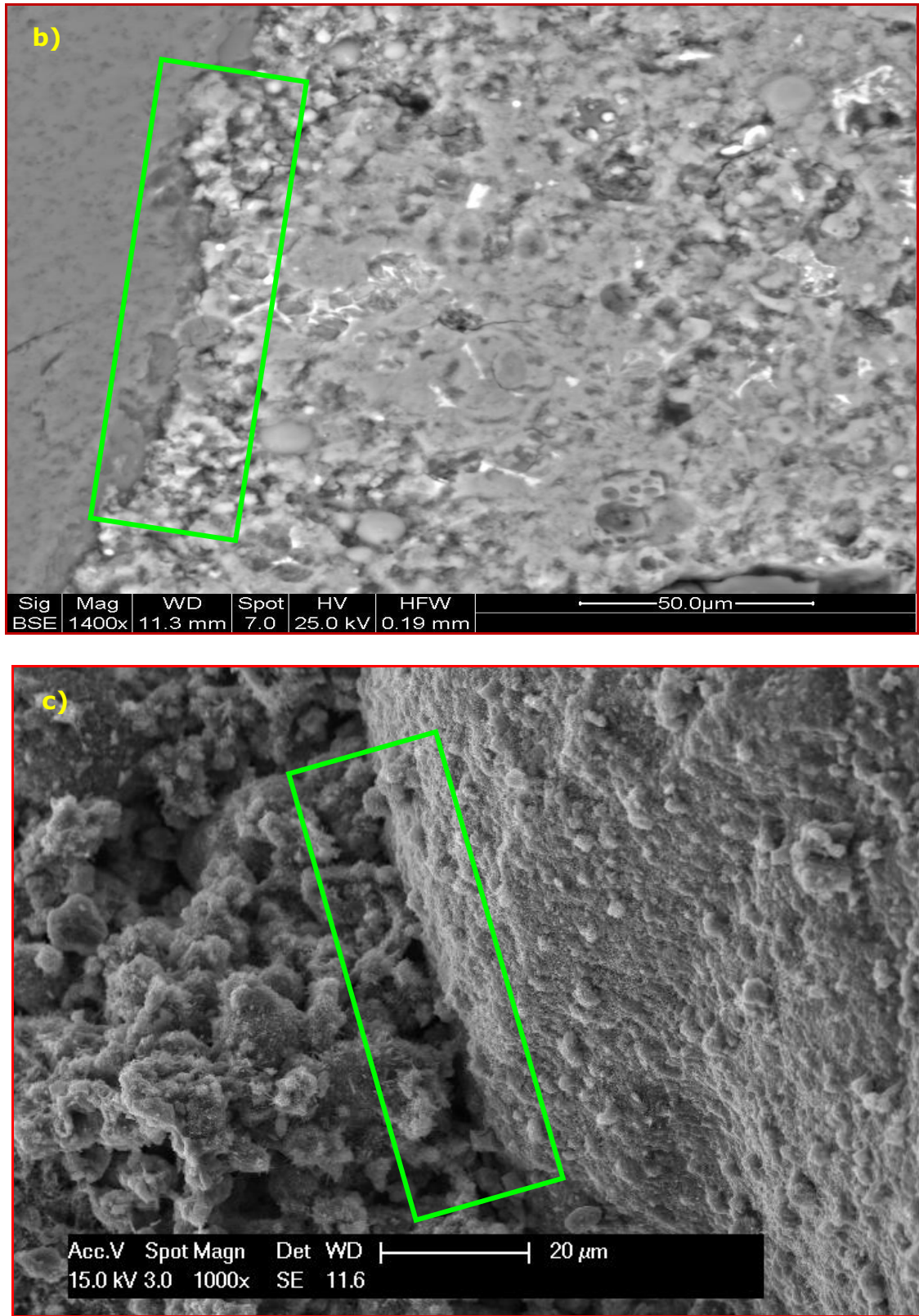
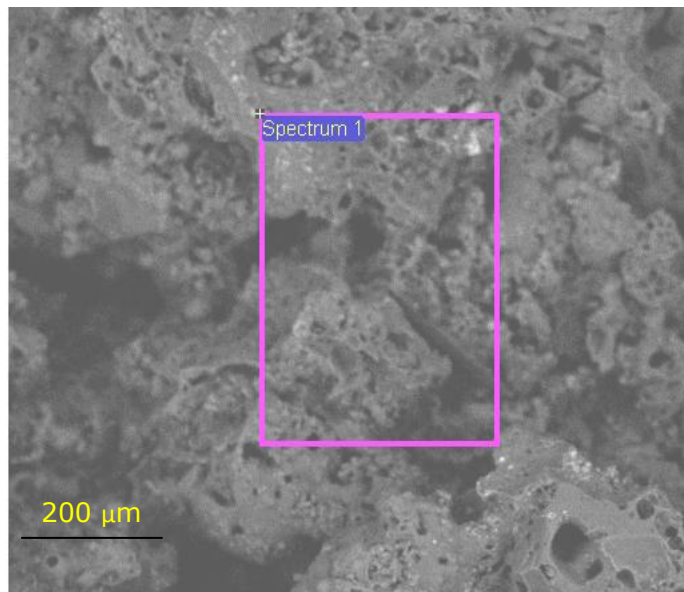


Fig.5.15 continued: Close-up views of the ITZs of gravel mix (a), lightweight mix (b) and blue brick mix (c)



Element	Weight %	Atomic %	Compound %	Formula
C K	18.03	25.14	66.06	CO ₂
Na K	0.34	0.25	0.46	Na ₂ O
Mg K	0.90	0.62	1.50	MgO
Si K	8.84	5.27	18.91	SiO ₂
P K	0.21	0.12	0.49	P ₂ O ₅
S K	0.18	0.10	0.46	SO ₃
Cl K	0.06	0.03		
K K	0.99	0.43	1.20	K ₂ O
Ca K	2.91	1.22	4.07	CaO
Ti K	0.30	0.11	0.50	TiO ₂
Fe K	4.73	1.42	6.09	FeO
Ni K	0.16	0.02	0.21	NiO
O	62.33	65.26		
Totals	100.00			

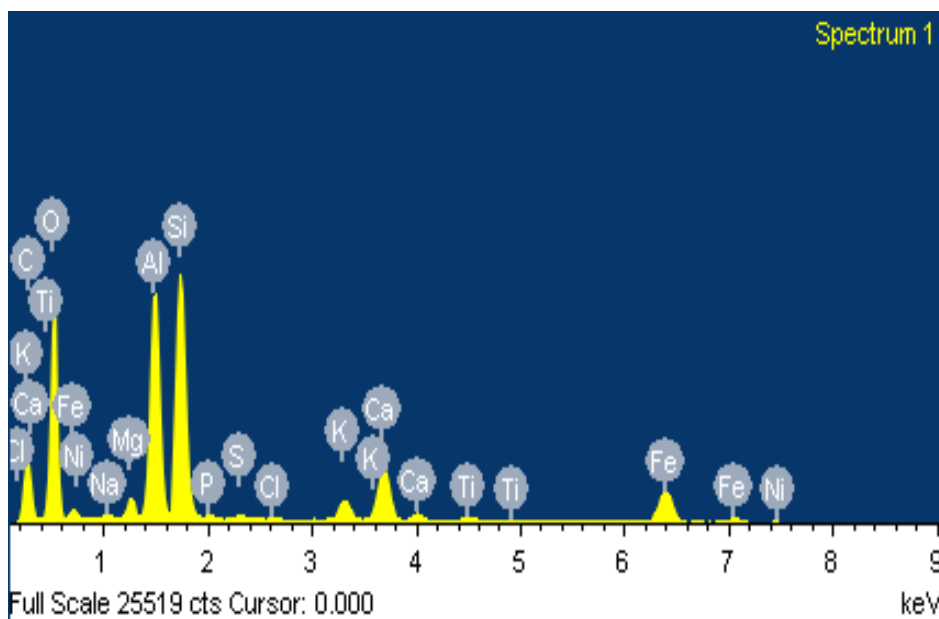


Fig.5.16: EDX spectrum analysis of the fly ash/Lytag Aggregate

5.3.4 Interconnectivity of the ITZ

The degree of interconnection of the ITZ of the mortar was calculated using the results of a previous work carried out by [Snyder et al. \(1992\)](#) running various numerical simulations (in each case assuming a different thickness of the ITZ). This model approximates the mortar matrix to an arrangement of randomly distributed spherical shape sand grains and assumes that the ITZ surrounding aggregate particles have a fixed thickness. The results of these simulations are displayed in Fig.5.17.

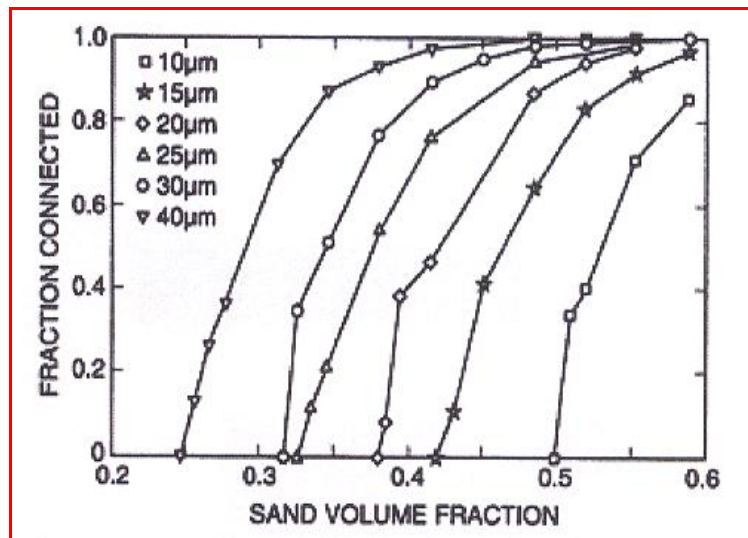


Fig.5.17: Results of continuum model used to determine interfacial zone percolation in mortars with varying sand contents and ITZ thickness ([Snyder et al., 1992](#))

The analysis revealed that for 55 % sand volume and greater, the interfacial zones are almost totally interconnected except when the ITZ thickness is less than 15 µm to some extent. In addition, it can be seen that interconnection requires at sand fractions of 52 % and 33 % respectively, for an interfacial zone thickness of 10 µm and 25 µm. As highlighted by [Snyder et al. \(1992\)](#), the results of this continuum model may also be extrapolated to concrete. The authors claim that one can expect the ITZ in concrete to be interconnected for interfacial zones as small as 10 µm for a typical sand content of about 50 % in the mortar fraction of

concrete. If a portion of the mortar is replaced with a large aggregate, the mortar can remain interconnected. This is because the addition of large aggregates helps to connect a mortar's interfacial zone phase that is not already interconnected, for geometrical reasons, as illustrated, schematically, in Fig.5.18.

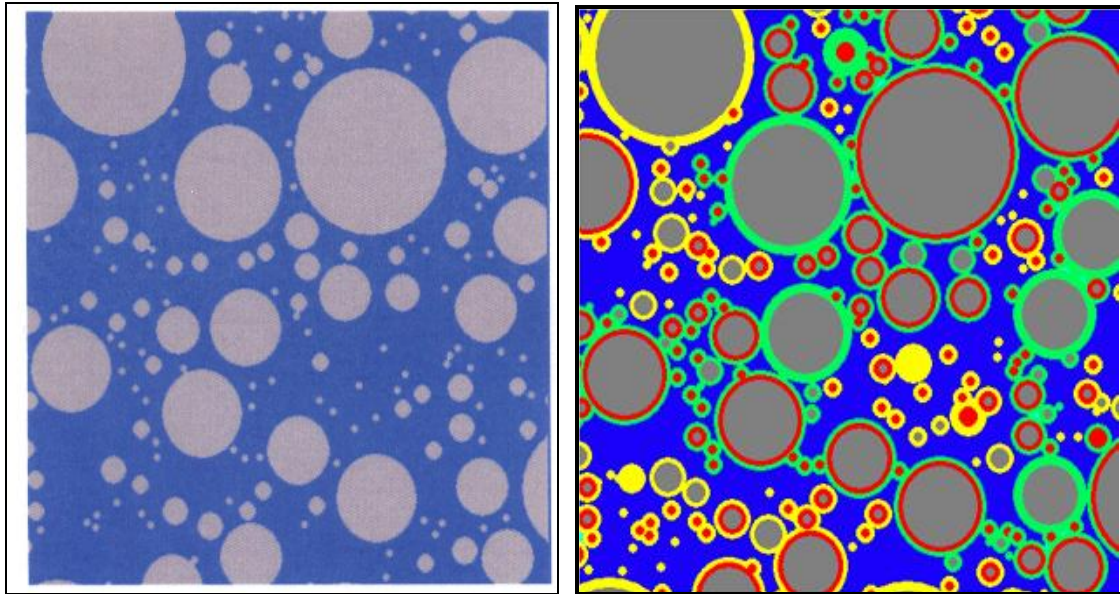


Fig. 5.18: Connectivity of the ITZ zone a) initial stage and b) connectivity of solid phases
Grey: coarse and fine aggregate, Red: voids in the ITZ, Green: ITZ between the coarse and matrix, Yellow: ITZ between the fine and matrix, Blue: matrix (Ye, 2003)

5.3.5 Micro-hardness of ITZ

The average micro-hardness (strength) distribution measured in the ITZ of each mix is plotted against the distance from the aggregate surface in Fig.5.19.

The results suggest that there are noticeable differences between the specimen behaviours. In the specimen manufactured with the copper slag, the micro-hardness at 50 μm away from the aggregate surface reached a level of 36 HV 0.01, whereas it was only 29 HV 0.01 for the gravel specimen. From a material science point of view, such behaviour of the specimen

prepared with the copper slag could be attributed to a higher crystallinite proportion in the copper slag aggregate. As stated by Perkins (1999), increased crystallinite usually results in a higher yield stress and Young's modulus, and vice-versa. Thus, it could be expected that the inclusion of stiffer and denser material (such as copper slag and blue brick) in the specimen would increase its micro-hardness value. In parallel, interestingly, the micro-hardness pattern of the lightweight mix indicated and confirmed that absorption of water into the aggregate led to densification of the interfacial matrix and provided superior bonding. However, when the local micro-hardness of the cement paste is normalized to bulk paste values (see Fig.5.20); the gains of the slag disappear. It is well-known that the presence of rigid and well-bonded stiff inclusions (such as fibre and aggregate) or other inhomogeneities (such as large pores) can restrain the stress fields developed under the indenter, leading to an indentation size that is smaller than would be expected from the nature of the paste alone and thus, the hardness of the paste is expected to increase when these inhomogeneities exist (see Fig.5.21).

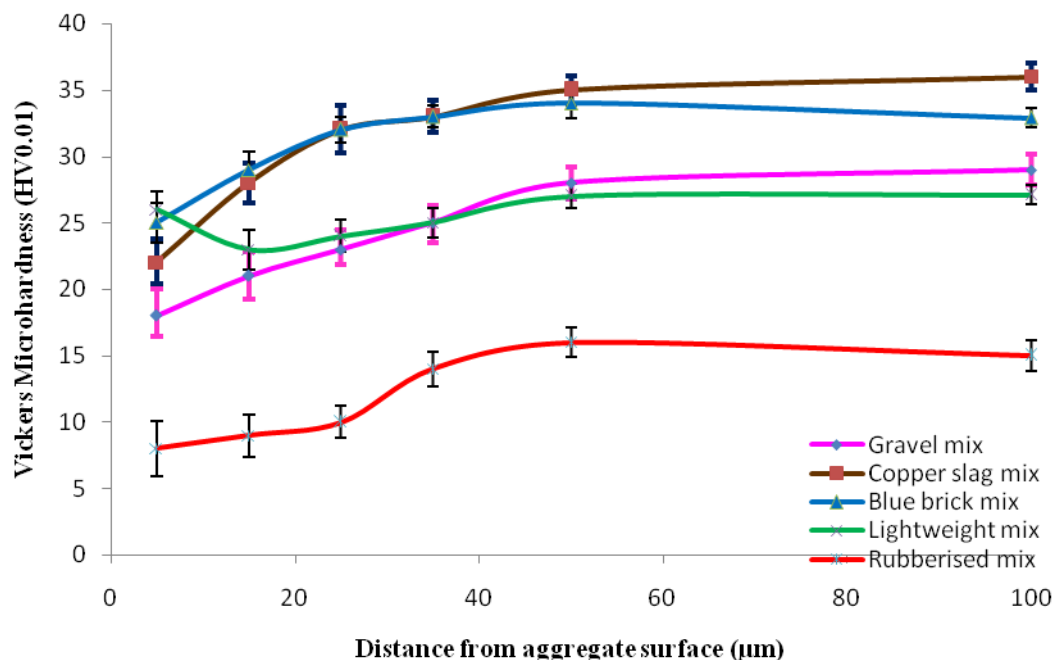


Fig.5.19: Micro-hardness values of the ITZs of the concrete mixes

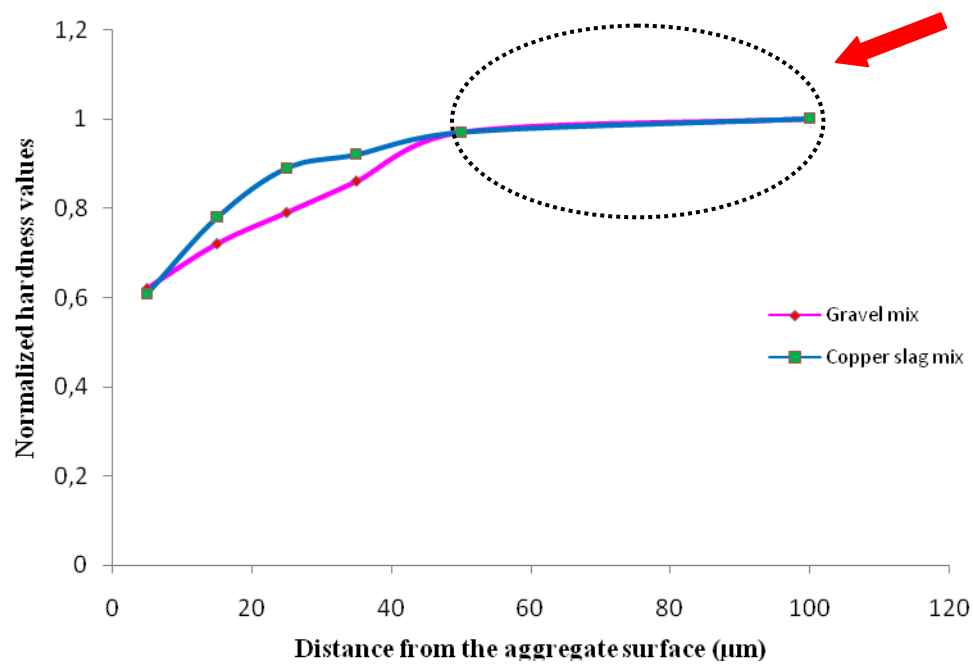


Fig.5.20: Normalized hardness values of the copper slag and gravel aggregate mixes

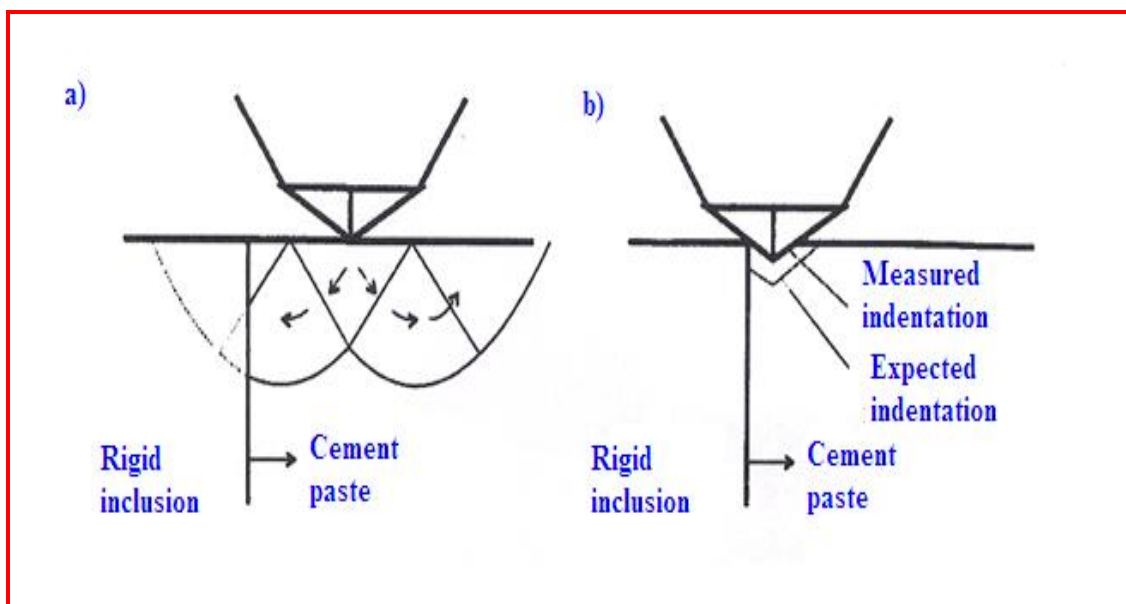


Fig.5.21: Schematic description of the process for the reduction due to restraint of the stress field (a) and reduction due to physical interaction of the penetrating indenter and the rigid inclusion (Igarashi et al., 1996).

5.4 Concluding Remarks

- The paste surface in the case of the lightweight concrete has the smoothest profile while the paste region of the rubberised concrete has the highest irregularity followed by those of the blue brick, copper slag and gravel mixtures respectively. The differences in the profile and roughness values of the specimens could be a result of either the degree of hydration of the mixtures and the shape properties of the aggregates used.
- A micro-structural study revealed that a relatively dense and homogeneous interface with a moderate amount of C-S-H gels was present between the fly ash/Lytag aggregate and cement matrix in the lightweight concrete, while a more porous and loose interface existed in the rubberised mix due to the presence of calcium hydroxide crystals, monosulfate and internal voids that could, presumably, provide a line of weakness for failure to take place along, and thus lead to less strength.
- Highly porous fly ash/Lytag aggregate can produce a very dense interfacial zone as the hydration products tend to migrate into the pores and fill the gaps.
- Increase in the thickness of the ITZ could lead to a reduction in the moduli of elasticity of the ITZ. In parallel, interconnectivity of a poor ITZ would have a subtle effect on the overall performance of concrete.
- Much denser, stronger and rougher, and higher crystalline copper slag aggregate produced a dense, stronger and much rougher ITZ, which, in turn, could improve concrete performance.
- The presence of rigid and well-bonded stiff inclusions or other inhomogeneities can restrain the stress fields developed under the indenter, leading to an indentation size

that is smaller than would be expected from the nature of the paste alone and thus; the hardness of the paste is expected to increase.

- The thickness and porosity of the ITZ define two different characteristics of the interfacial transition zone. The thickness is the measurement of the more porous band that surrounds the aggregate while the porosity is ratio between the volume of the pores and the total volume enclosed in this band.
- Micro-hardness on the other hand is a mechanical property of the cementitious constituent of the concrete at the micro level, that is, when the hardness is determined over a distance of about 10 – 20 μm increment. The value of hardness is directly related to the strength of the material.

References:

- [1] Akçaoğlu, T., Tokyay, M., and Çelik, T. (2004). “Effect of Coarse Aggregate Size and Matrix Quality on ITZ and Failure Behaviour of Concrete Under Uniaxial.” *Cement and Concrete Composites* 26 (6) 633-638.
- [2] Allison, P.G., Moser, R.D., Chandler, M.Q., Rushing, T.S., Williams, B.A., and Cummins, T.K., (2011). “Nanomechanical structure-property relations of dynamically loaded reactive powder concrete.” *USACE Infrastructure Conference*, June 15th, USA.
- [3] Clarke, A.R., and Eberhardt, C.N., (2002). “Microscopy techniques for Materials Science.” *Woodhead Publishing Limited*, Cambridge.
- [4] Fens, T.W.F., (2000). “Petro-physical properties from small rock samples using image analysis techniques.” *PhD Thesis*. Technical University of Delft, Netherlands.
- [5] Ficker, T., Martisek, D., and Jennings, H.M., (2010). “Roughness of fracture surfaces and compressive strength of hydrated cement pastes.” *Cement and Concrete Research* 40 (6) 947-955.
- [6] Garboczi, E.J., and Bentz, D.P., (1997). “Analytical formulas for interfacial transition zone properties.” *Advanced Cement Based Materials* 6 (3-4) 99-108.
- [7] Hemavibool, S., (2007). “The microstructure of synthetic aggregate produced from waste materials and its influence on the properties of concrete.” *PhD Thesis*. University of Leeds, UK.
- [8] Igarashi, S., Bentur, A., and Mindess, S., (1996). “Micro-hardness testing of cementitious materials.” *Advanced Cement Based Materials* 4 (2) 48-57.
- [9] Kwan, A.K.H., and Mora, C.F., (2001). “Effects of various shape parameters on packing of aggregate particles.” *Magazine of Concrete Research* 53 (2) 91-100.
- [10] Perkins, W.G., (1999). “Polymer toughness and impact resistance.” *Polymer Engineering Science* 39 (12) 2445-2460.

- [11] Sahu, S., Badger, S., Thaulow, N., and Lee, R.J., (2004). "Determination of water-cement ratio of hardened concrete by scanning electron microscopy." *Cement and Concrete Composites*, 26 (8) 987-992.
- [12] Scrivener, K.L., and Pratt, P.L., (1987). "A preliminary study of the microstructure of the cement/sand bond in mortars. Proceedings of 8th International Congress of the Chemistry of Cement, Rio de Janeiro, 466-471.
- [13] Snyder, K.A., Winslow, D.N., Bentz, D.P., and Garboczi, E.J., (1992). "Advanced cementitious systems: Mechanism and properties." *MRS Symposium proceedings*, 265-270.
- [14] Trägårdh, J., (1999). "Micro-structural features and related properties of self-compacting concrete." In: A. Skarendahl and O. Petersson (Editors), *Proceedings of the First International RILEM Symposium on Self Compacting Concrete*, RILEM, Cachan, Cedex ,175-186.
- [15] Van Tuan, N., Ye, G., Breugel, K.V., and Copuroglu, O., (2011). "Hydration and microstructure of ultra-high performance concrete incorporating rice husk ash." *Cement and Concrete Research* 41(11) 1104-1111.
- [16] Wasserman, R., and Bentur, A., (1997). "Effect of lightweight fly ash aggregate microstructure on the strength of concretes." *Cement and Concrete Research* 27 (4) 525-537.
- [17] Ye, G., (2003). "Numerical simulation of the development of the microstructure, porosity and permeability of cement-based materials." PhD Thesis. Technical University of Delft, Netherlands.

CHAPTER 6

DAMAGE ANALYSIS OF THE CONCRETE MIXTURES UNDER IMPACT LOADING

6.1 General:

In the previous chapter, it was revealed that aggregate characteristics have a profound effect on the local mechanical and micro-structural properties of the ITZ. In order to establish a link between the scales (from the micro to macro), the studies in this chapter involve investigation of the effect of different types of unconventional aggregates on the impact responses of concrete mixtures from a quantitative micro-structural point of view. The results presented can be divided into two main sections:

- In the first section, the impact test results of the mixtures from a manual drop-weight impact test set up are presented.
- In the second section, impact responses of the mixtures using an automatic drop-weight impact testing machine are studied.

6.2 Equipment Development for Impact Testing

6.2.1 Review

Unfortunately, there is still missing a standard test method that can be universally accepted to assess the impact resistance of concrete. Because of the lack of a standard method, researchers have developed several techniques to evaluate the impact resistance but it has been observed that previous research tends to favour a drop weight apparatus for the testing.

Up to now, the most popular types of the test methods are

- The Drop-Weight Impact Test ([ACI Committee 544, 1988](#))
- The Modified Charpy and Izod Method ([Yue, 1997](#))
- The Split Hopkinson Pressure Bar Test ([Lok et al., 2002](#))

A drop-weight impact testing apparatus has been proposed by the [ACI Committee 544 \(1988\)](#) to compare the merits of fibre reinforcement. In this method, a hammer of mass 4.54 kg drops from a height of 457 mm repeatedly on a hardened steel ball that is positioned on top of the test specimen. The test specimen is a cylinder with a diameter of 63.5 mm and a height of 150 mm. For each specimen, the number of blows required to cause the first visible crack and the ultimate failure is recorded. These numbers refer to the first-crack impact resistance and the ultimate impact resistance (strength), respectively. It is generally agreed ([Badr and Ashour, 2005](#); [Barr and Baghli, 1988](#)) that this method is widely used because it is economical and could be easily fabricated. However, the large variation in the number of blows to initiate first visible cracking has been a reason for it to be commonly criticised. The schematic representation of the drop-weight impact test machine developed by [Banthia et al., \(1987\)](#) is illustrated in Fig.6.1 below.

The Charpy test is another popular test which has been widely used for impact testing of metal. Standard sized specimens (10 mm square and 60 mm long) containing a sharp notch to localize stress are pendulum hammer-impacted and then the energy absorbed during this fracture process is measured. As the pendulum hammer has a fixed weight and drops the same distance each time its kinetic energy when it strikes the specimen is always the same. Part of this energy is consumed in breaking the specimen: the energy remaining in the hammer leads it to continue its upward swing. By measuring the difference in the height of the upward swing after the pendulum has fallen freely, and after it has broken the sample, the energy absorbed in breaking the sample can be calculated (Rollet, 2007).

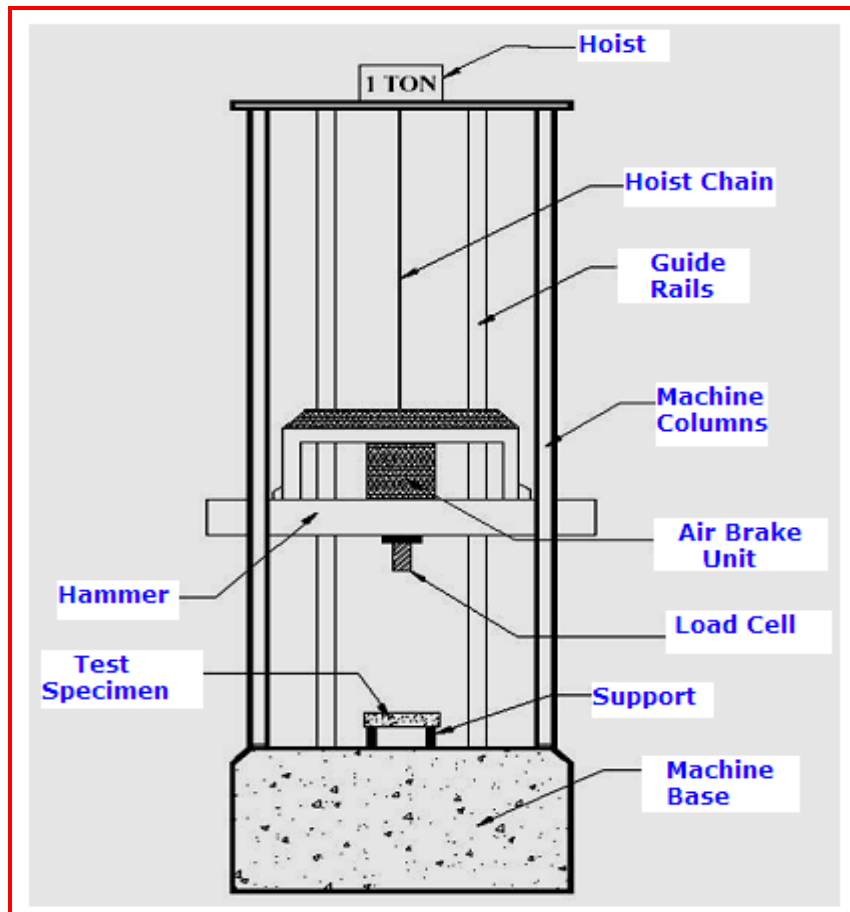


Fig.6.1: The drop-weight impact test set up (Adapted from Banthia et al., 1987)

Another type of impact test technique that has been known for a long time is the split Hopkinson pressure bar (SHPB). The test facility consists of a projectile, an instrumented input bar, an instrumented output bar and a short cylindrical specimen, as illustrated in Fig.6.2. In the SHPB test, the specimen is sandwiched between the bars. The projectile impacts the input bar and generates a compressive stress wave which propagates through the input bar, pierces the specimen and propagates again in the output bar. At the interfaces between the specimen and the input and output bars, the stress is partially reflected into the input bar and partially transmitted through the specimen into the output bar. After several reflection of the compressive wave, the specimen breaks, and measurements (strain) are recorded on the two bars (Lok et al., 2002).

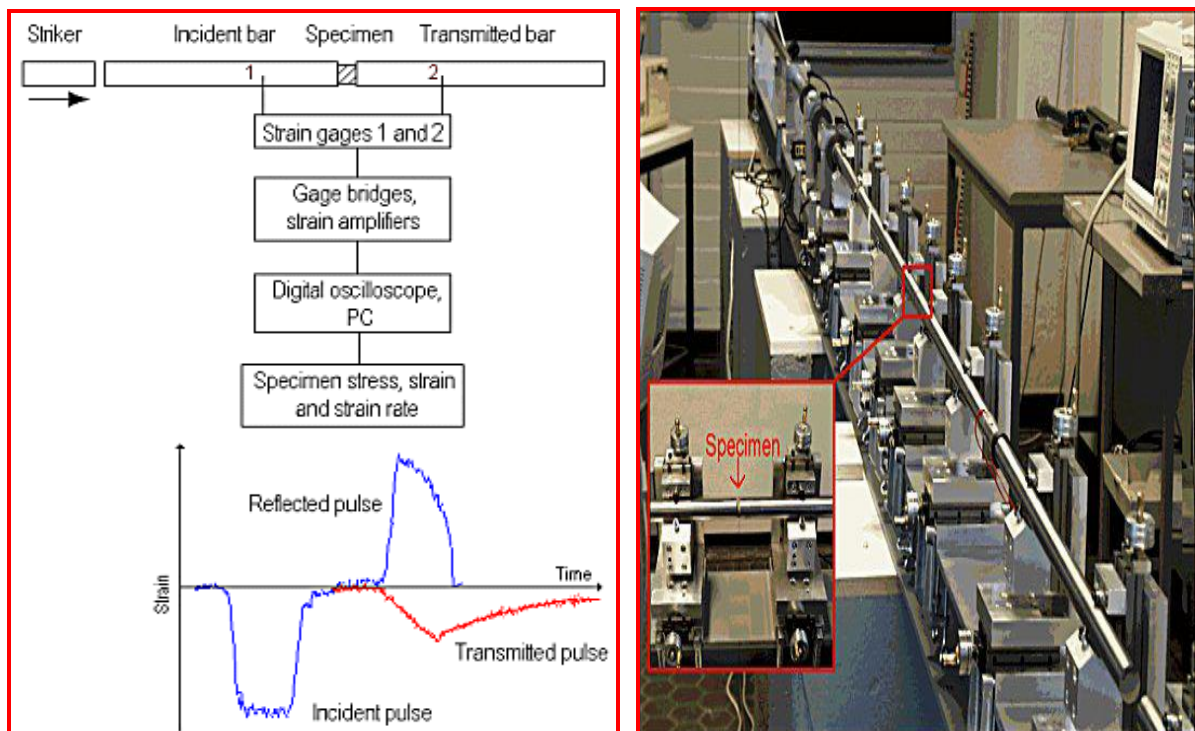


Fig.6.2: Split Hopkinson Pressure Bar Test Apparatus (Jialiang, 2004)

6.2.2 Initial Apparatus Development in the Present Study

The impact resistance of the concrete specimens was initially determined by an instrumented drop weight impact test arrangement that the author developed in accordance with the suggestions of [ACI Committee 544 \(1988\)](#).

The first step for the design of the drop weight system was to find a relatively simple way to guide the dropping mass down to the concrete specimen. After some discussion, it was decided that the use of a plastic pipe would be a simple but effective way to guide the weight to the specimen. The key factor in choosing the most appropriate pipe was the dropping mass. The space between the pipe and the mass should be sufficient to minimize or eliminate the risk of friction but not so much space as to permit an uncontrolled drop path. A steel mass that consists of a cylinder base and a semi-circle end, shown in Fig.6.3, was manufactured with a diameter of 80 mm and a weight of about 5 kg. A top ring was also attached to the top of the dropping mass to provide an easy hoisting system. After designing the falling mass, a pipe that was slightly larger (100mm) in inner diameter than the outer diameter of the drop-mass was obtained.

In the next step, clips were used to prevent slip out of the pipes. The clips were set roughly equal distances from each other with the lowest being from the base of the pipe, and were attached to wooden pieces (40*40*250mm) to construct supports, as illustrated in Fig.6.4. Finally, these supports were anchored to the wall in the laboratory using steel bolts to establish a safe test set up.

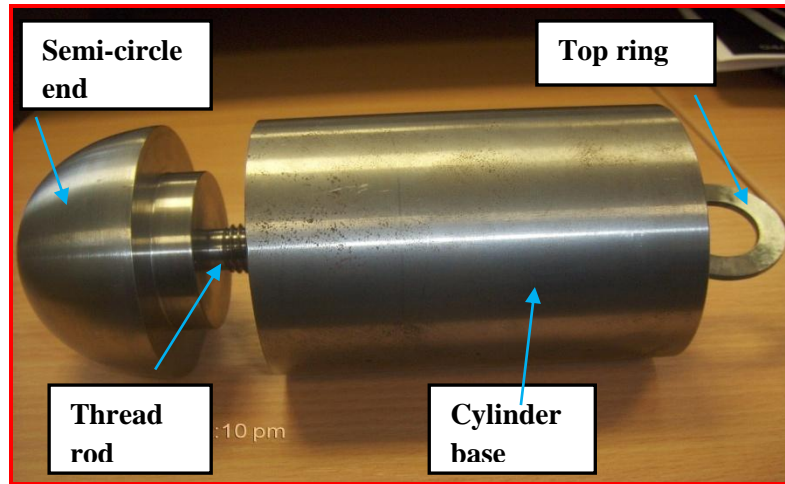


Fig.6.3: The Falling Mass for the Test Set up

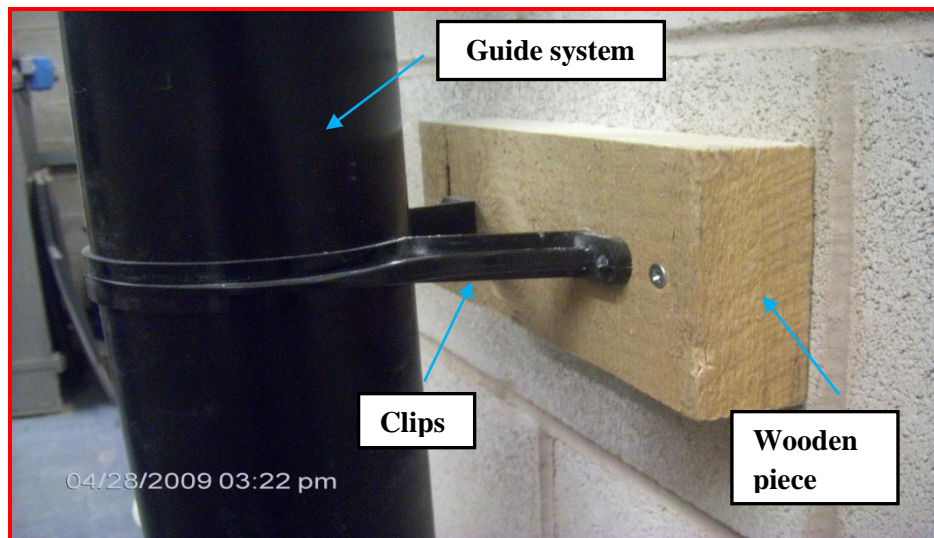


Fig.6.4: Support Connection for the Drop Weight Test Set Up

The next step was to find an appropriate quick release mechanism which should be incorporated to allow the mass to free fall when released. It was thought that the quick release system should not significantly restrict or reduce the velocity of the falling mass during free fall. A pulley and nylon rope system was considered acceptable.

Another important point that must be mentioned is support conditions of the specimen. In order to minimize and restrict variability in results, the test should be performed on a base

with controlled properties. The 100 mm cubical specimens were placed on a steel base plate that rests upon the concrete laboratory floor. A rubber sheet with a thickness of 3 mm was also placed between the specimen and the base plate to prevent stress concentrations. Four steel lugs were also welded to each corner of the base plate to prevent excessive rotation of the specimen after the impact. A steel plate, 10 mm thick, were then positioned on the top of the concrete specimen to help generate uniform load distribution. With time, repeated drops caused slight distortion in this top plate changing the contact arrangement. Therefore, a disposable 25 mm diameter contact plate made of copper-coated mild steel (approximately 2 mm thick) was placed beneath the top plate to keep the contact constant on each specimen. The impact resistance of the specimens was determined in terms of the number of blows required either to produce the first visible crack or to cause complete failure of the specimens. The general schematic view of the equipment developed is illustrated in Fig. 6.5.

Nevertheless, this apparatus had a number of significant limitations; in particular the author did not have direct means to measure the load-deflection histories, energy-time histories etc. of specimens. In order to overcome this problem, another impact test equipment was also used in the later stages of the project which is described next.

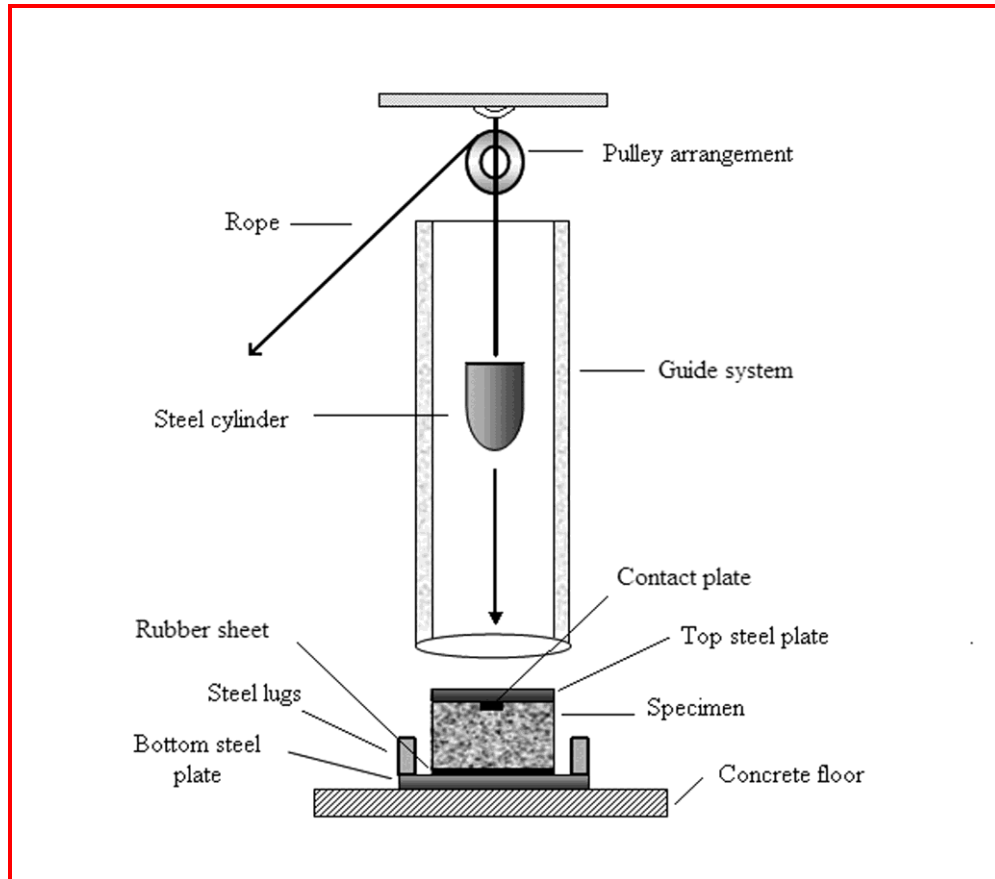


Fig.6.5: Schematic view of the impact test set up developed by the author

6.2.3 Rosand Falling Weight Apparatus

The latter equipment used was a Rosand instrumented falling weight impact tester Type 5 in the Innovative Research Technology Centre, Department of Materials, Mechanics and Manufacturing Engineering, University of Nottingham. The machine is capable of dropping a 120 kg mass from heights of up to 3m on to the target specimen. The machine is floor mounted and uses a free falling, weighted crosshead with a striker, guided by two long steel rods, to impart an impact as illustrated schematically in Fig.6.6 and shown in the photograph of Fig.6.7. The drop tower striker imparts a load on the moving carriage which, in turn, loads the specimen in tension. The hoist chain controls the height of the impactor mechanically.

The specimen (150 mm in diameter and 60 mm in height) was held in the fixture placed on a cylindrical steel base located at the centre of the impact machine. A pneumatic rebound brake was also fitted to ensure that the specimens received only one impact. The hammer was dropped from about 500 mm height, corresponding to a speed and impact energy of 2.92m/s^{-1} and 34.6 J, respectively. A crosshead mass of approximately 8.1 kg was used in the dynamic test.

The drop weight device was equipped with data acquisition system to obtain force versus time data. An accelerometer attached to the impact hammer was also used to acquire acceleration and displacement during the impact event. By assuming that the hammer displacement was essentially equal to the specimen deformation, the velocity and the displacement of the specimen could be computed using the following equations (Sukontasukkul et al., 2004):

From the initial potential energy, the velocity of the impactor at the beginning of the impact event is

$$\dot{u}(0) = \sqrt{2gh} \quad (6.1)$$

where g is the corrected gravitational acceleration ($0.91g$); h is the drop height.

At any time t during the impact, the velocity of the hammer is equal to

$$\dot{u}_h(t) = \dot{u}_h(0) + \int_0^t \ddot{u}_h(t) dt \quad (6.2)$$

where $\ddot{u}_h(t)$ is the recorded acceleration by the accelerometer.

Then, the displacement of the hammer and the displacement of the specimen at any time t become

$$u_h(t) = \int_0^t [\dot{u}_h(0) + \int_0^t \ddot{u}_h(t) dt].dt \quad (6.3)$$

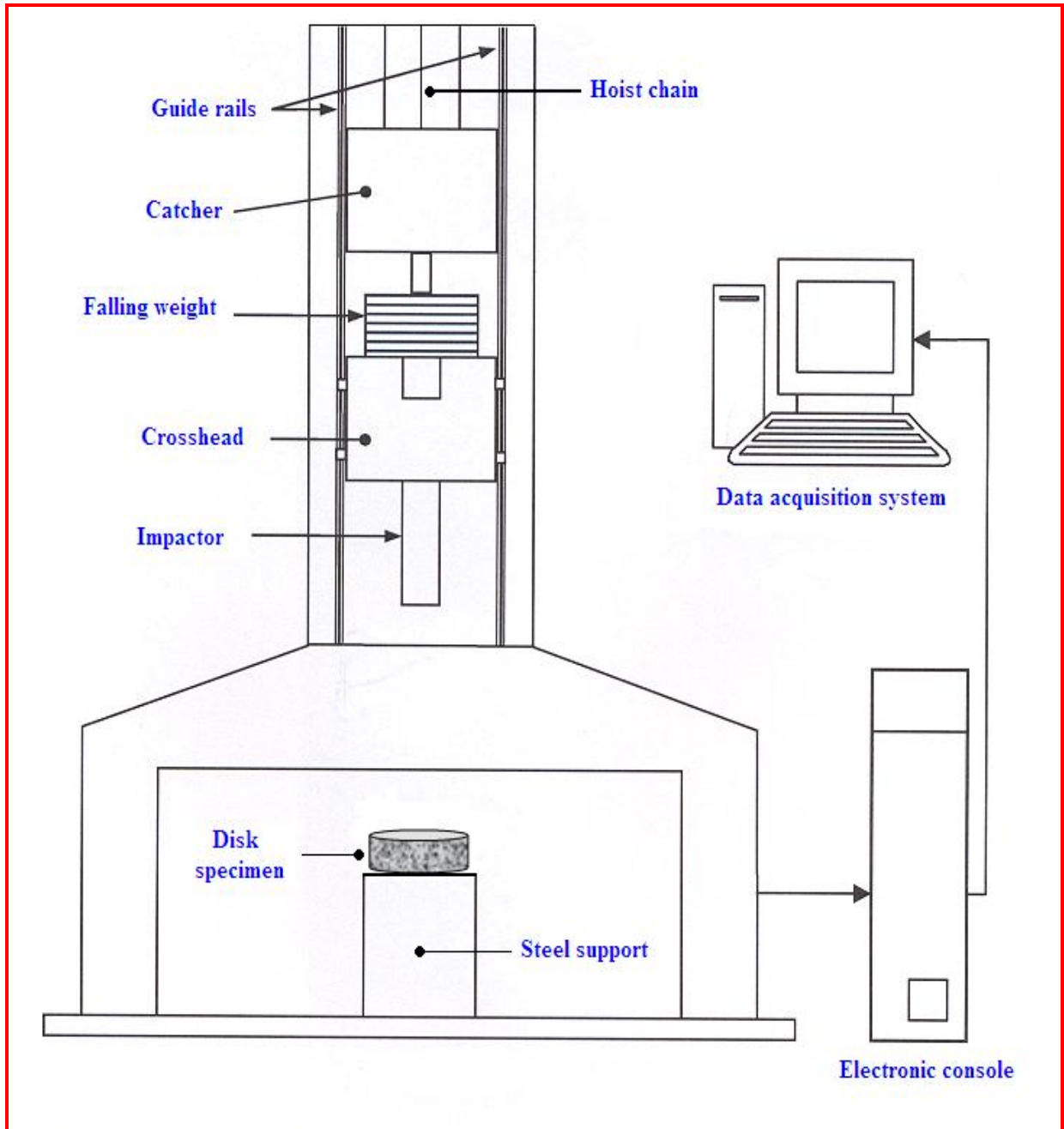


Fig.6.6: Schematic of Rosand Instrumented Falling Weight Drop Tower

(Adapted from Brown, 2007)

6.2.3.1 Instrumentation used

Force sensors and strain gauges

The impact force between the hammer and the specimen is measured by a piezoelectric load cell (made by Kistler Group); model 9051A, the measurement range is up to 120 kN. Strain data was recorded with Kyowa 120 Ohms strain gauges (KFG-20-120-C1). Both load cell data and strain gauge readings were recorded at a sample rate of 40 kHz on to a personal computer. The calibrations of the sensors were supplied by the manufacturers.

Accelerometers

The accelerometer used in this study was also piezoelectric sensors, with a resonant frequency greater than 70 kHz. The accelerometer can read up to ± 1000 g (where g is the Earth's gravitational acceleration). The calibrations of the sensors were also supplied by the manufacturer.

Data acquisition system

The data acquisition system consisted of a signal conditioner, a 16 channel analogue to digital (A/D) convertor, a data logging program and a computer.



Fig.6.7: Photograph of drop tower impact machine

6.3 Characterization of Fracture Surfaces

6.3.1 Fracture roughness using 3D laser non-contact surface profilometer

As important post-mortem evidence, the fracture surface can help to reveal the micro mechanism of fracture and plays a significant role in the evaluation of fracture mechanics properties of cementitious-based materials (Yan et al., 2003).

The quantitative analysis of the fracture roughness was made using a three-dimensional (3D) non-contact profilometer with a laser scanner, Talysurf CLI 1000 (Taylor Hobson) at the laboratory of the University of Nottingham`s Technology Centre, as shown in Fig.6.8. The surface inspection was carried out on one of the cracked halves of the specimen. The scanning analyses were undertaken with a CLA Confocal gauge 300 HE (300 µm range and 10 nm vertical resolution). The profile points were recorded every 20 µm along the path with a resolution of 0.3 µm in height and at a scan speed of 2 mm/s with 100 µm increments. The measurement length of the profiles was kept constant for all specimens so that the results are comparable.

Micro roughness (Ra) values were calculated for each mix. A mean value of three measurements was used as a response value for each experiment. These values were then used to reveal the micro mechanism of fracture (fracture energy- micro structural aspect relationship during the impact event). The mean micro roughness value of Ra was defined as the mean value of the surface relative to the centre plane calculated according to the following equation:

$$Ra = \frac{1}{L} \int_0^L [z(x)] dx \quad (6.4)$$

where $z(x)$ is the central-line profile and L is the length of the projected profile. Definition of the surface profile and the different roughness regimes are displayed in Fig.6.9.

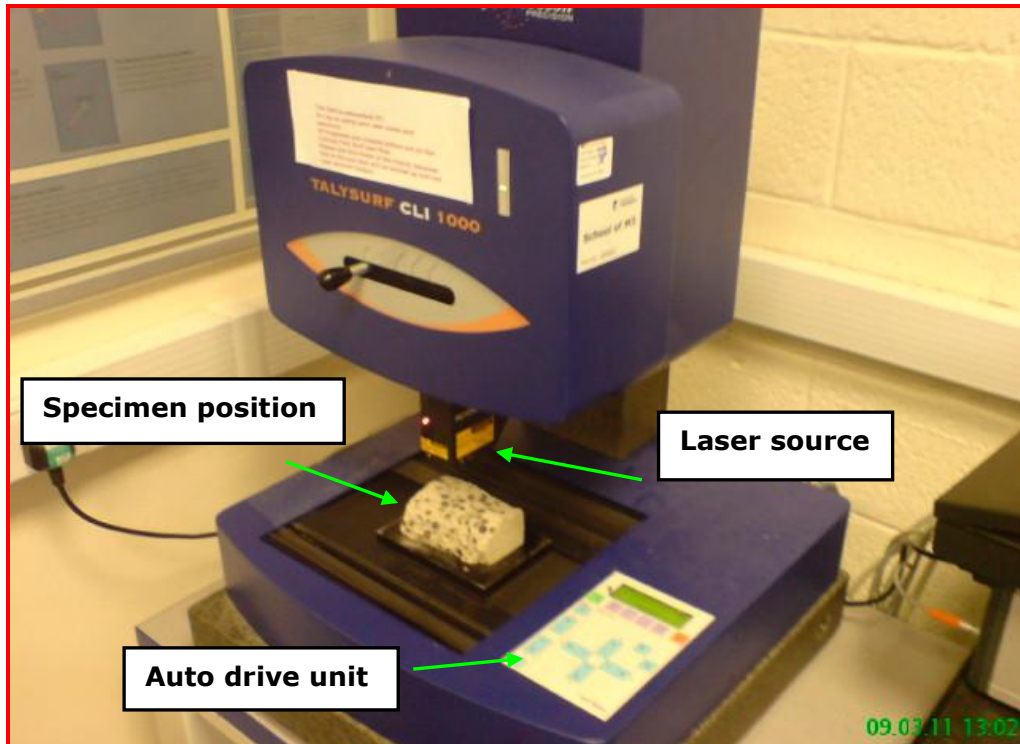


Fig.6.8: Talysurf CLI 1000 Laser Profilometer

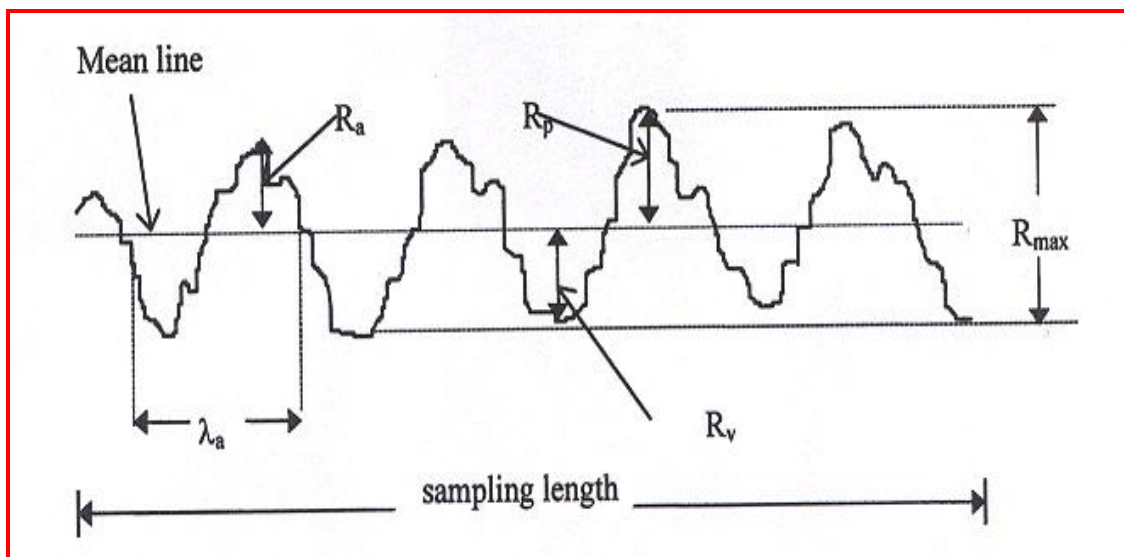


Fig.6.9: Texture profile and different roughness regimes (Tasong et al., 1998)

6.3.2 Crack tortuosity and density

The technique suggested by [Akhavan et al., \(2011\)](#) was used to quantify the tortuosity of the surface cracks. The surface profile was first digitized and the x and z coordinates on the crack surfaces were identified (Fig.6.10). Then, the profile was then divided into the segments of length λ . In each segment, a reference Z line was drawn which connected the beginning and end points at where the segment intersected the profile. The entire nominal length (X_{max}) and the lengths of the reference Z lines were determined. By summation of the Z lengths, the effective length (L_e) was determined, and then used for the calculation of tortuosity. The tortuosity was obtained as follows: $\tau = (X_{max}/L_e)^2$. The crack density ($1/\mu\text{m}$), equal to the micro-crack length per area unit, was calculated from the SEM images by dividing the total length of the cracks (μm) by the total examined surface area (μm^2).

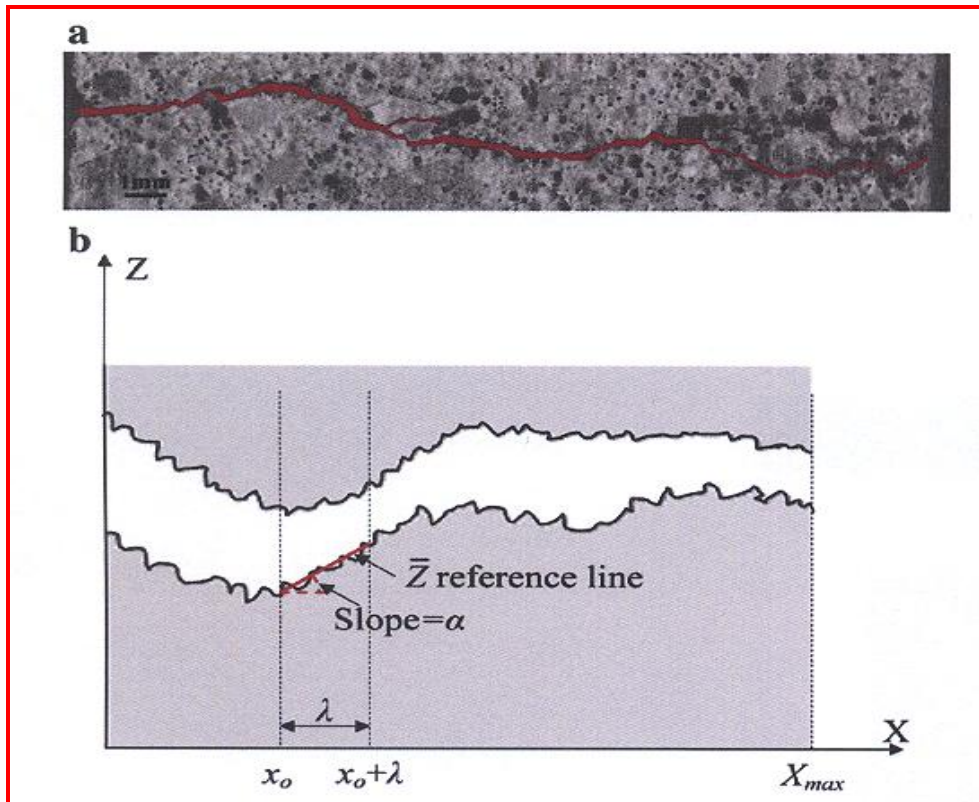


Fig.6.10: Digitized actual crack profile (a) and schematic of crack profile (b)

(Akhavan et al., 2011)

6.3.3 Fractal dimension and dissipated fracture energy

For a rough measure of fracture energy based on surface macro-crack, the formula suggested by Guo et al., (2007) was adopted as follows: $W_s/G_f = a^* (\delta/a)^{1-D_{1-d}}$ where W_s is the total energy dissipated at the surface of the crack; G_f is the fracture energy at the scale of observation δ (δ is equal to 5 mm- the maximum diameter of sand in concrete); a is the Euclidean length, which is equal to the height of the cross-section and D_{1-d} is the mean value of the fractal dimension of surface cracks on the fractured specimen.

The profiles of the crack maps of the specimens were obtained using Image J software. Then the fractal dimensions of cracks are computed by means of the box-counting method in the same image software. In this method, digitized crack patterns are covered by rectangular grids of progressively decreasing linear size. The fractal dimensions are then secured by computing the logarithmic density of the measure of these covering, as illustrated in Fig.6.11 (Chiaia et al., 1997).

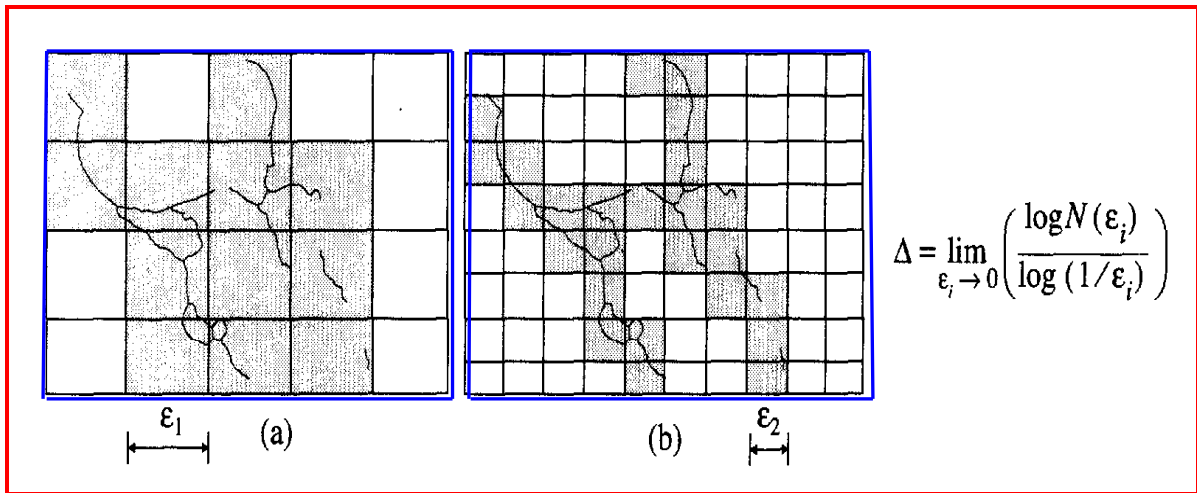


Fig.6.11: The box-counting method (Chiaia et al., 1997)

6.4 Impact Response Test Results and Discussion

6.4.1 Results from the manual drop-weight apparatus

Table 6.1 presents the impact strength results of the specimens in terms of the number of blows to cause first crack and ultimate failure. The data for three samples of each are recorded. As can be seen from Table 6.1, a relatively small number of blows were required to produce failure in the concrete specimens except the rubberised mix. The specimens could endure only a few additional blows after the appearance of the first visible cracks.

Table 6.1: The results of drop-weight impact test

Concrete ID	No. of blows for first crack			Average	No. of blows for ultimate failure			Average
Sample No	1	2	3		1	2	3	
Gravel	4	3	3	3	6	5	6	6
Lightweight	2	2	1	2	3	5	3	4
Rubberised	17	22	24	21	38	45	42	42
Copper slag	4	6	4	5	10	8	13	10
Blue brick	3	5	5	4	11	16	13	13

The concentrations of the micro-cracks in the ITZ could be an important parameter to help understand the failure process of the specimens subjected to impact loading. Table 6.2 shows the measured crack densities in the ITZ of the mixtures. As can be seen from Table 6.2, a much more concentrated damage occurred in the ITZ of the lightweight, blue brick and copper slag concrete compared to that of the other concrete mixtures. As highlighted by [Akçaoğlu et al. \(2005\)](#), the bigger the difference between the strengths of the ITZ and surrounding the matrix, the higher the tendency of micro-cracking in the ITZ. From this may

be inferred that the enhanced bond at the interface of the lightweight concrete could possibly lead to a reduction in the grain-grain interlock and inter-particle friction within the aggregate pieces as the crack growth intercepts the aggregates themselves, resulting in a smoother fracture surface. By contrast, concrete made with gravel aggregates or particularly rubber particles exhibited a different behaviour; many interfaces between the matrix and the aggregate were debonded (as shown in Fig.6.12) most likely due to the weaker interface and the concrete had a much more tortuous fracture surface as a consequence.

Table 6.2: Micro-crack density of the ITZ

Concrete ID	Maximum crack width (μm)	Total crack length (μm)	Total crack area (μm^2)	Crack density ($1/\mu\text{m}$)
Conventional	28.90	705.9	9360.6	0.075
Lightweight	20.50	607.5	3627.55	0.167
Copper slag	32.10	817.3	4280.1	0.191
Blue brick	26.10	745.6	5038.8	0.148
Rubberised	38.20	616.3	4480.2	0.137

As a contribution to the discussion of the failure mechanism involved in these concretes, a quantitative roughness analysis of the fracture surfaces was conducted to determine the micro-roughness number-Ra. The roughness profiles and calculated results of micro roughness are presented in Fig. 6.13 for the concrete mixtures. The results show that the micro-roughness of the rubberised and blue brick mixes, which exceed those of the copper slag and gravel mixes is much larger than that of the lightweight concrete. There is already a theory that higher micro-roughness usually results in higher fracture energy consumption during the fracture and vice versa (Wu et al., 2001). Fig.6.14 and 15 show digitized crack maps of the surface, calculated fractal dimension of the cracks and fracture energies based on

surface macro-crack measurement of some of the mixtures-gravel and lightweight. All results are tabulated in Table 6.3. The results give some support to the theory just mentioned and confirm that, for the concrete with rubber and blue brick particles, greater fractal energies are dissipated during the impact event, likely due to their more zigzag surface macro-crack pattern. By contrast, in the case of the lightweight mix, more likely a dynamic effect due to the high stiffness difference between aggregate and paste (the ITZ paste was strong- see Chapter 5) prevents the mix from resisting high level of deformation and produces less tortuous fracture path.

Table 6.4 compares the variation in relative dynamic modulus of elasticity of the concrete mixtures during impact exposure. The measurements have been performed in both horizontal and vertical (loading) directions just before and just after impact. It is obvious that the reduction in dynamic elastic modulus for the rubberised concrete was more pronounced, while the lightweight mix and blue brick mix exhibited less reduction. This can be explained by the greater development of discontinuities at weak regions along the cement paste-aggregate bond and/or within the paste matrix of the rubberised specimen due to impact-induced stress waves.

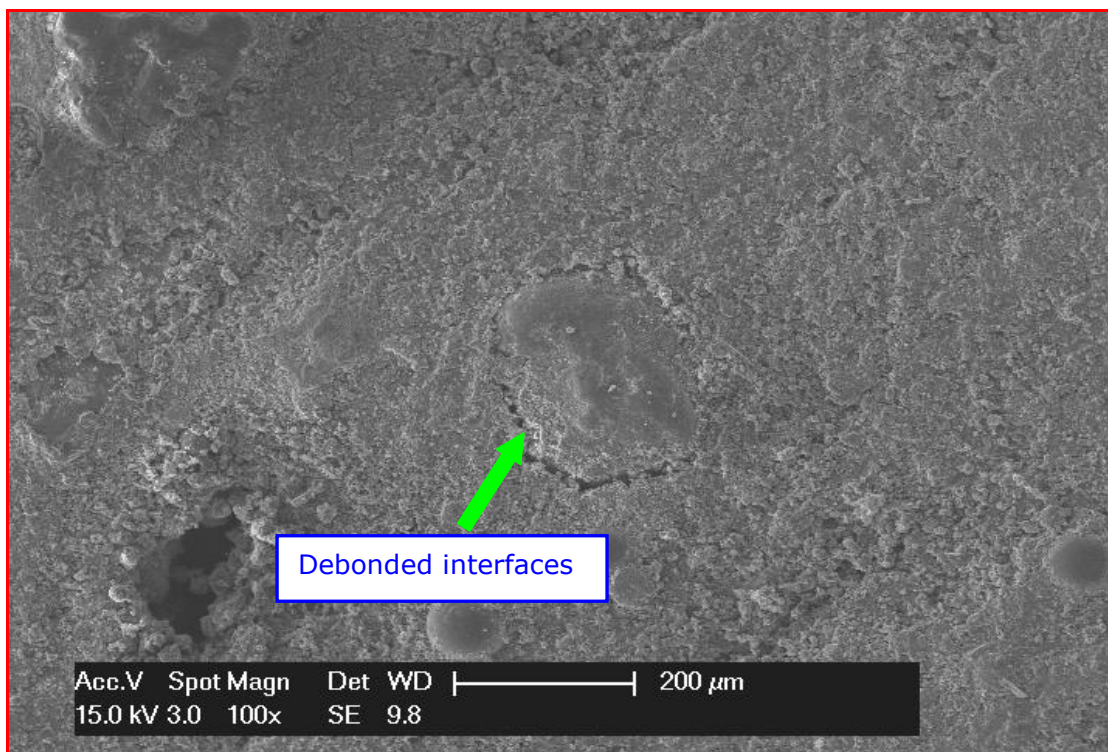
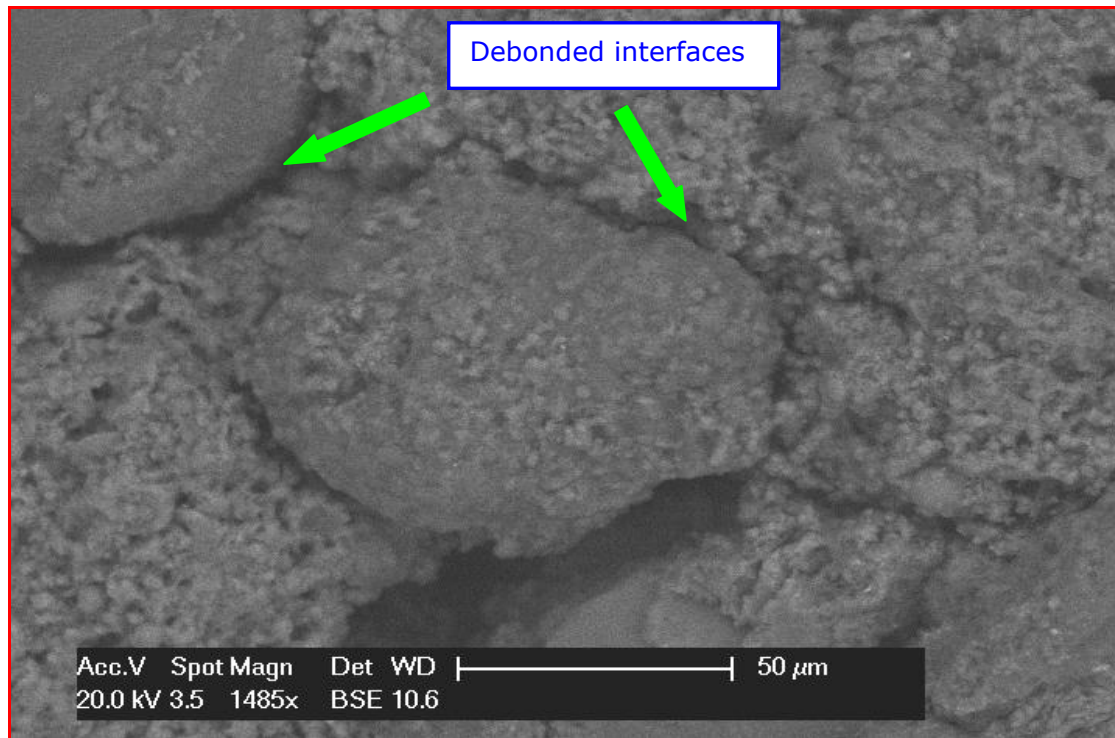


Fig.6.12: Debonded interfaces after impact

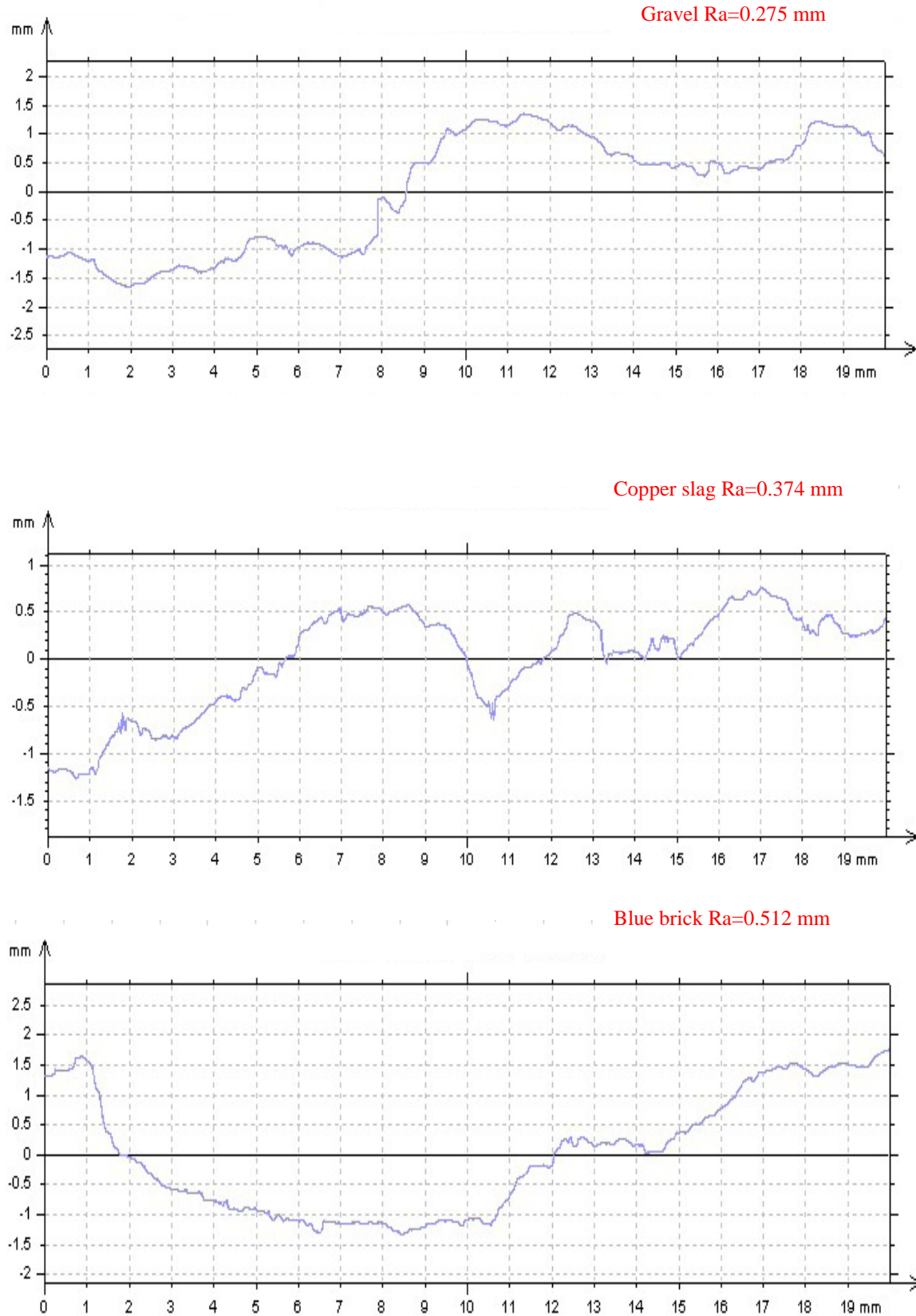


Fig.6.13: Micro roughness profiles of the concrete mixes

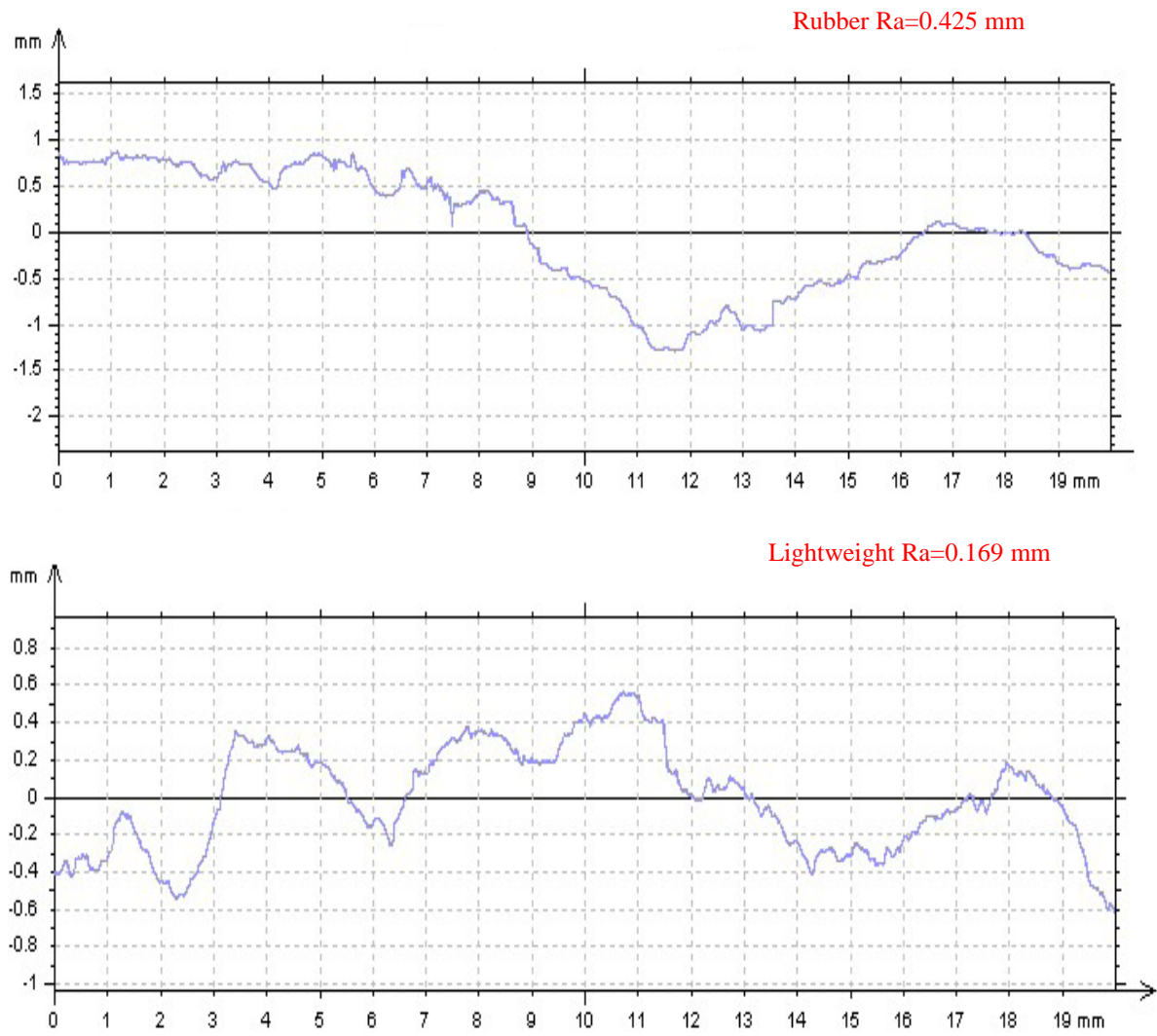


Fig.6.13 continued: Micro roughness profiles of the concrete mixes

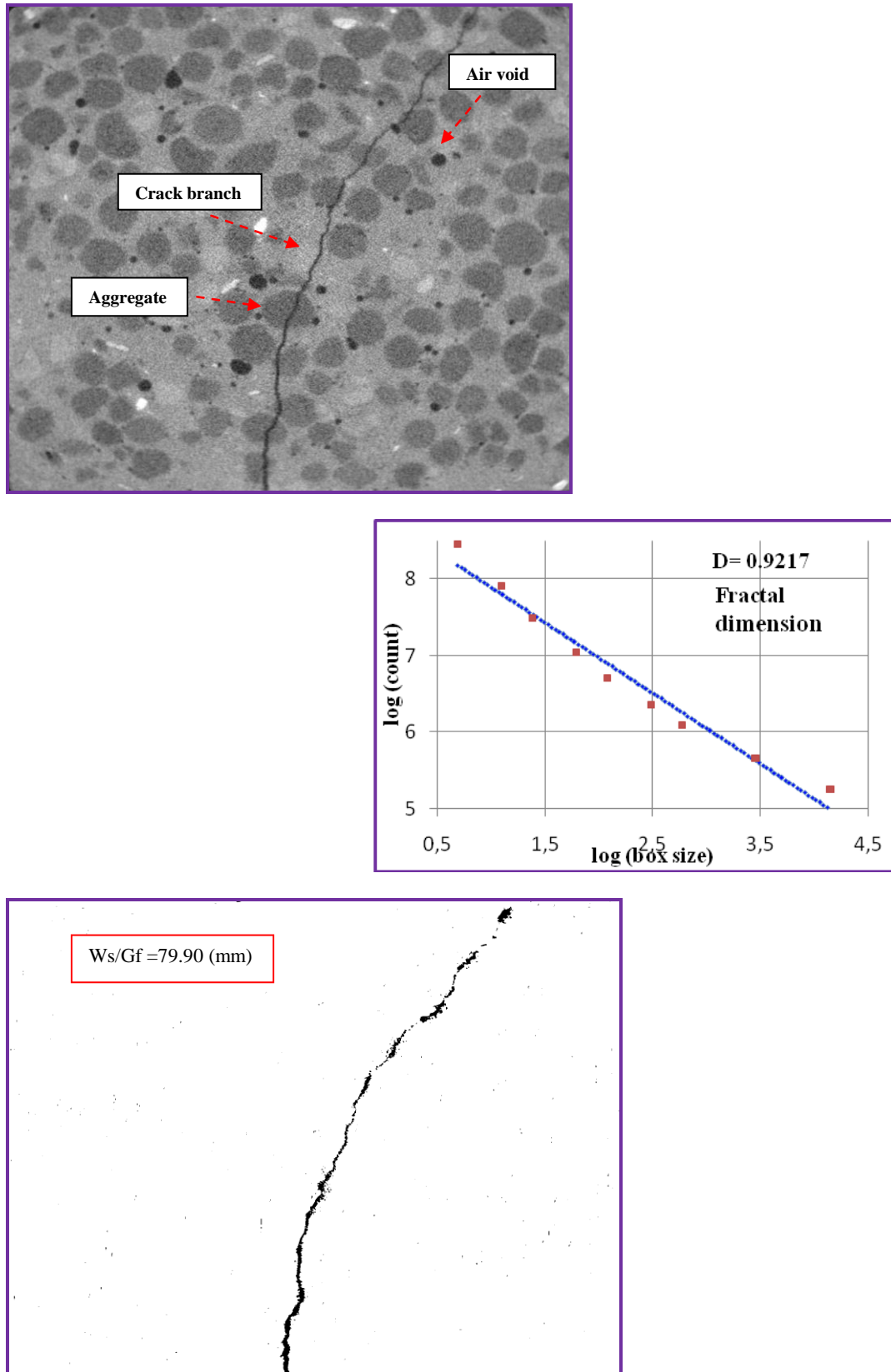


Fig.6.14: Digitized crack maps and fractal fracture energy of the lightweight concrete

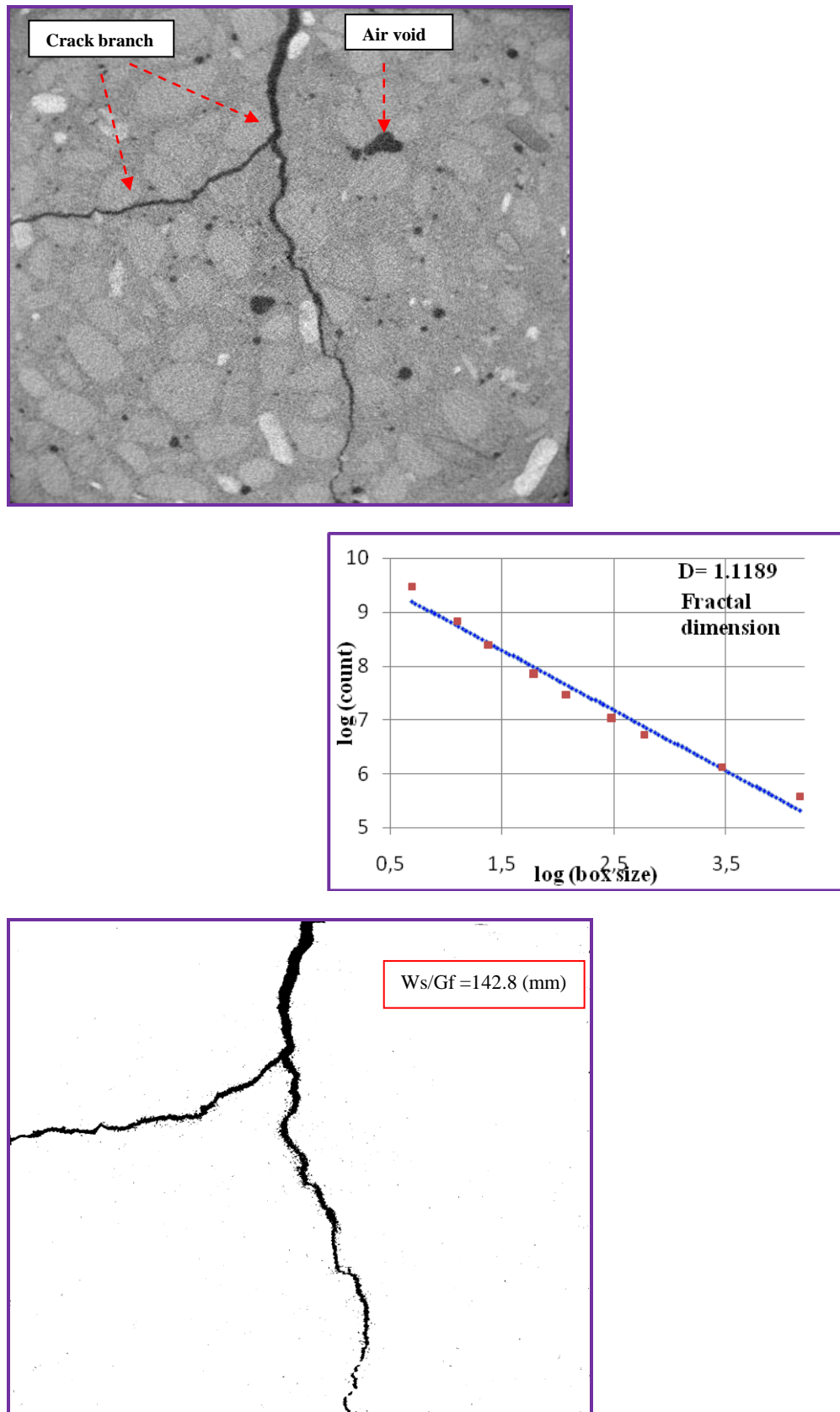


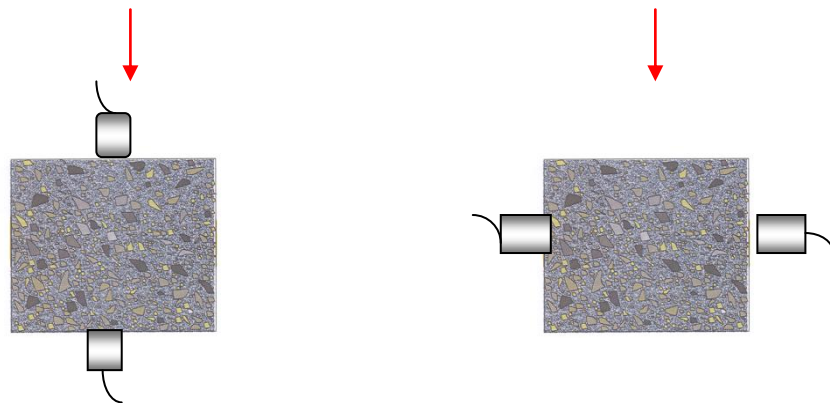
Fig.6.15: Digitized crack maps and fractal fracture energy of the gravel concrete

Table 6.3: Internal cracking features of the concrete mixtures

Concrete ID	D- Fractal dimension	Ws/Gf (mm)- Dissipated Energy	T- Tortuosity
Gravel	1.1189	142.8	0.636
Lightweight	0.9217	79.90	0.142
Copper slag	1.1522	157.8	0.704
Blue brick	1.1724	167.60	0.730
Rubberised	1.1964	180.10	0.758

Table 6.4: Changes in the dynamic modulus of specimens after impact failure

	Load Direction	Load Direction	Load Parallel	Load Parallel
	Before	After	Before	After
Gravel	41.0	23.7	41.9	22.5
Lightweight	23.7	15.9	22.5	14.1
Copper slag	50.9	27.3	50.1	17.40
Blue brick	42.2	30.7	42.5	20.4
Rubberised	9.10	0.7	9.3	0.2



According to continuum damage mechanics, damage is caused as a result of nucleation, growth and coalescence of micro-voids. These voids may grow and generate new micro defects during the deformation process ([Khan, 2009](#)). Thus, changes in air void distribution and content could also provide valuable information that can be linked to the damage process of concrete under impact.

Fig. 6.16 presents the change in air void distribution across the depth of the specimens as a result of testing. These results also suggest that most of the damage is taking place in the top part of the lightweight specimens compared to its middle and bottom sections signifying that the damage is a localized phenomenon occurring in a critical location in a heterogeneous material in accordance with the findings of [Ying \(2010\)](#). By contrast, the middle and top part of copper slag and blue brick specimens were damaged almost equally, while the top section had a relatively less damage. In parallel, the conventional specimen had a relatively higher damage in bottom and top parts while the middle sections were less damaged. In the case of the rubberised mix, the damage developed in a highly unstable manner but the polar graph shows that the damage mostly accumulated in the upper-mid section of the specimen.

In general, the results indicate that all specimens experienced a significant increase in air voids after being subjected to the high rates of loading. This confirms that the impact loading would tend to form a network of interconnected cracks between the micro-pores and pre-load existing micro-cracks, thereby leading to stress concentrations around the ITZs and reduce peak stress.

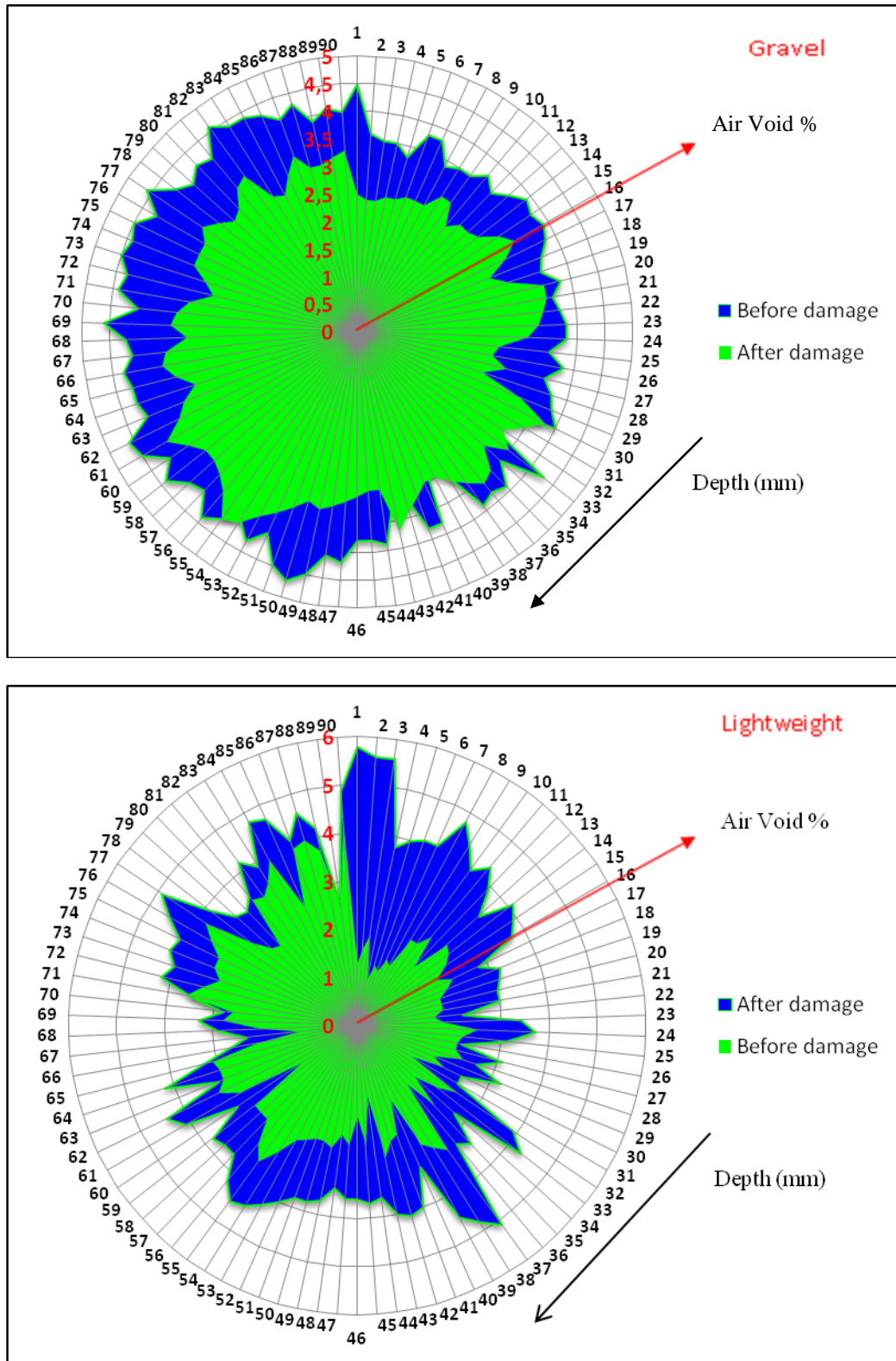


Fig.6.16: Polar diagrams for the changes in air void distribution across the depth of the concrete mixes

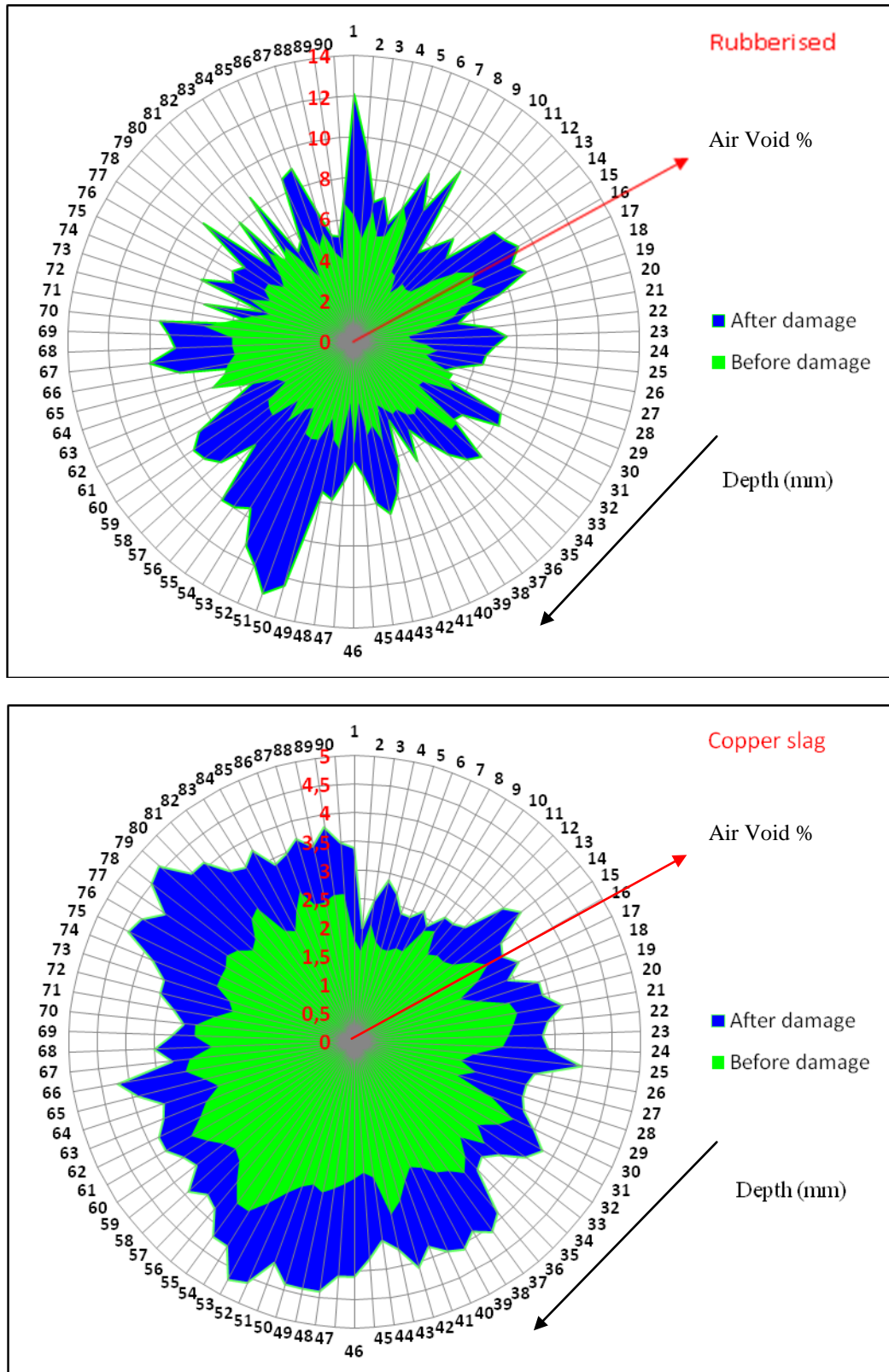


Fig.6.16 continued: Polar diagrams for the changes in air void distribution across the depth of the concrete mixes

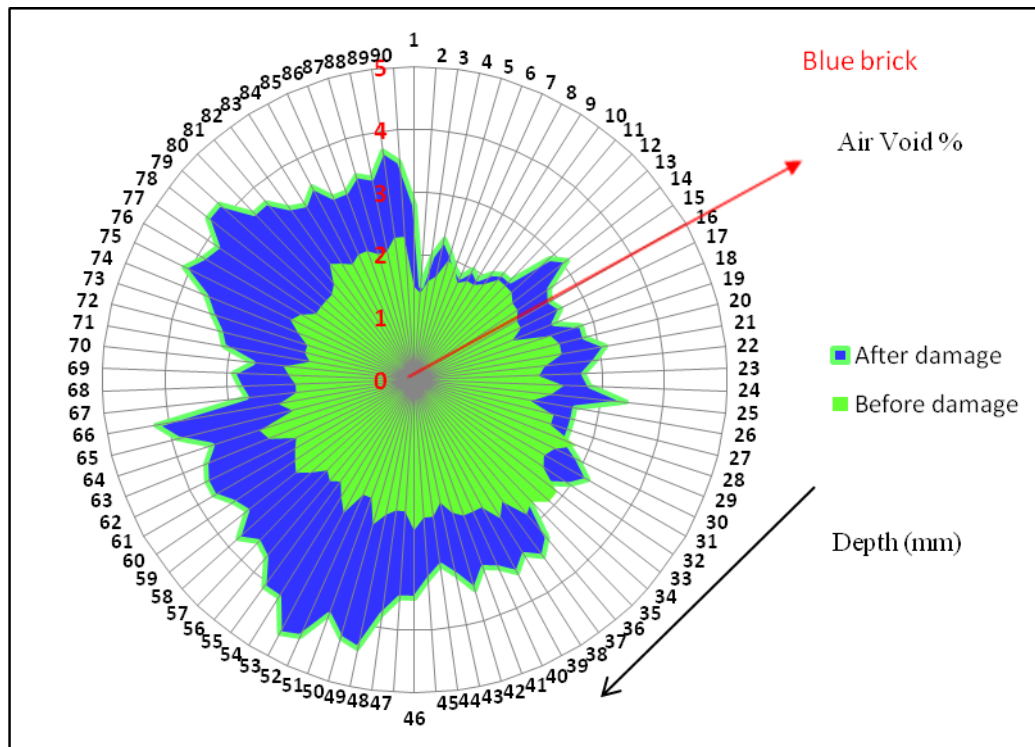


Fig.6.16 continued: Polar diagrams for the changes in air void distribution across the depth of the concrete mixes

6.4.2 Results from the Rosand Impact Equipment

Since parameters such as the velocity and mass of the hammer, shape of the hammer nose, thickness of the concrete disks and boundary conditions of the concrete disks etc. were fixed, the resistance of the concrete disks to impact loading is assumed to be mainly related to the mechanical properties of the concrete disks themselves so differences in response should be a function of the coarse aggregate used as this is major difference between mixtures.

Fig.6.17 shows reaction force-time histories for concrete mixtures during the first drop of impact. It is observed that in the first cycle of wave propagation, the magnitude of load for the blue brick specimen is much higher than those of the other specimens. The peak value of load is 21.20 kN compared to a peak force of 17.2 kN, 13.10 kN, 11.8 kN and 4.20 kN for the copper slag, lightweight, gravel and rubberised concrete mixes, respectively. Since the

loading is constant ($\text{drop height} \times \text{mass} \times \text{gravitational constant}$) in this study, different peak heights correspond to different times of loading indicating different dynamic stiffness and plastic strains. Therefore, the blue brick mix (highest peak force) is likely to convey stress waves with less crack propagation when it is subjected to impact loading. Based on composite mechanics, the elastic modulus of concrete is, to a great extent, positively related to the modulus of the aggregate. According to this theory, when the specimen is subjected to high rates of loading, the concrete with rigid aggregates (such as blue brick and copper slag) would mainly be able to dissipate energy by cracking rather than rebounding or deforming. As cracks preferentially travel through the path of least resistance, the ITZ properties become of major importance for the behaviour of these concretes under loading. The stronger ITZ in these concretes (as confirmed in Chapter 5) would efficiently participate in transferring stress through the composite, resulting in a greater vertical impact reaction force. It should also be mentioned that observation of the fractured surfaces indicated that a higher percentage of the blue brick aggregates were pulled from their cavities compared to the reference concrete or lightweight concrete (see Fig.6.18), and the failure surface is more tortuous as observed in broken faces.

The higher interfacial surface roughness in the blue brick specimen may also contribute to the bearing capacity. As it is concluded by [Zampini et al. \(1995\)](#), the paste-aggregate interface can toughen the paste by increasing its roughness, which in turn may result in an increase in toughness of the concrete. Overall, an increased interfacial roughness may enhance the material strength against the angle of frictional resistance by improving the contact point interactions and may increase the area needed to be created on the surface during fracture, and thus the concrete can withstand a high level of load and consume more energy.

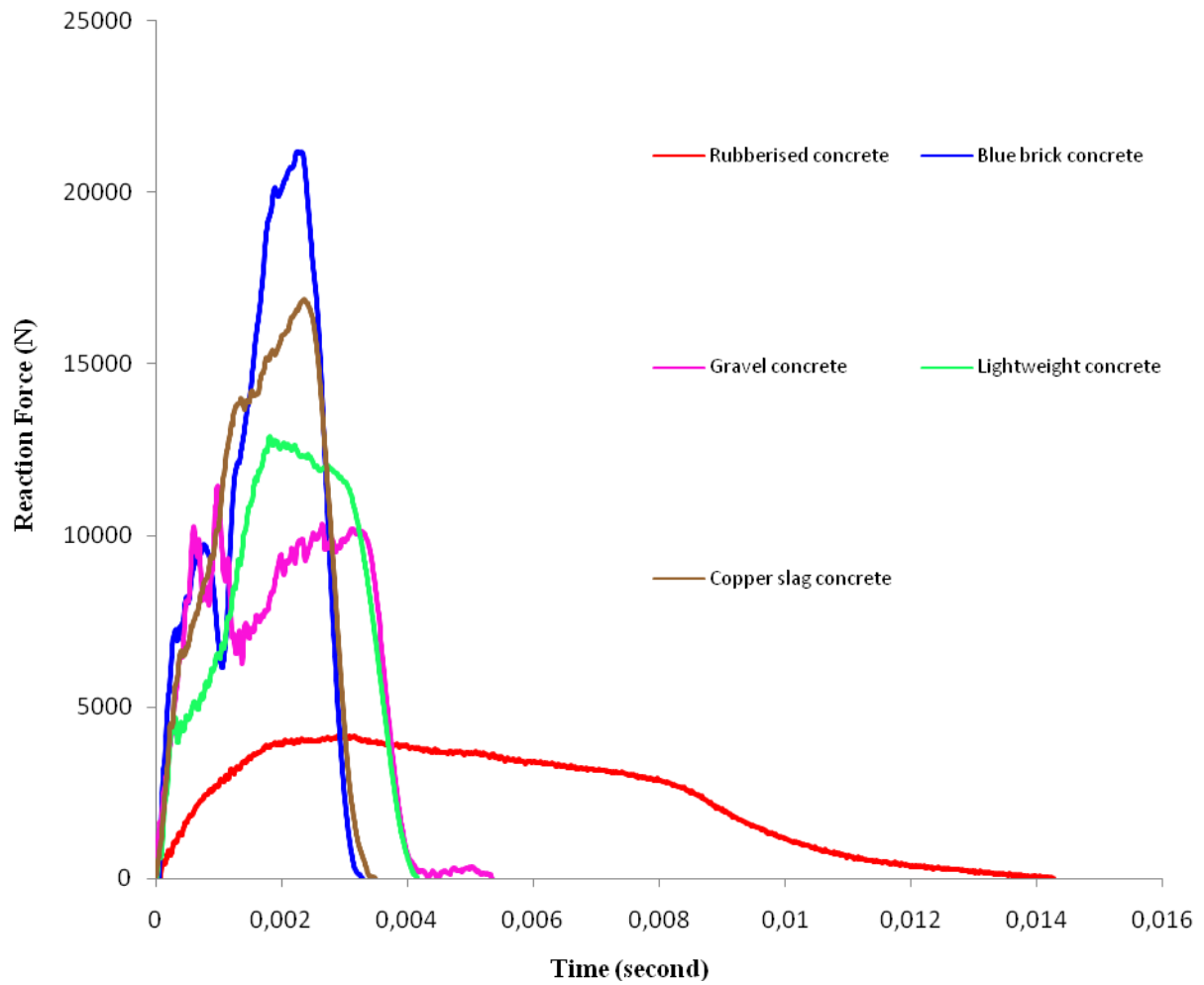


Fig.6.17: Force-time curves of all specimens at the first drop of impact



Figure 6.18: Broken surfaces of the specimens after impact

Shear wave velocity in a continuum is given by the Newton- Laplace equation as $V_s = \sqrt{G/\rho}$ where V_s is shear wave velocity, G is shear modulus and ρ is the density. Thus, the shear wave velocity is controlled by the shear modulus and increases with the stiffness of the material and decrease with the density. On this basis, it is worth also highlighting that the time taken for the compression stress waves to travel from the impact point to the bottom of the rubberised specimen was 3 to 5 times higher than for the other specimens (Fig.6.17). This is a further demonstration of the lower overall stiffness of the rubberised mix and a weaker structural integrity at micro-scale.

The presence of the ettringite needles in air voids of the impact-damaged specimen is illustrated in Fig.6.19. It is supposed that the chemical composition of the ITZ (i.e. release of sulphate or high amount of Al, Fe and S) may promote ettringite re-crystallization in cracks and air-voids (secondary ettringite formation). Although, it is common to see ettringite in the voids and cracks of deteriorated concrete (Tomas and Ramlochan, 2002) yet so far, there is no clear evidence that the ettringite crystals are the cause of crack formation.

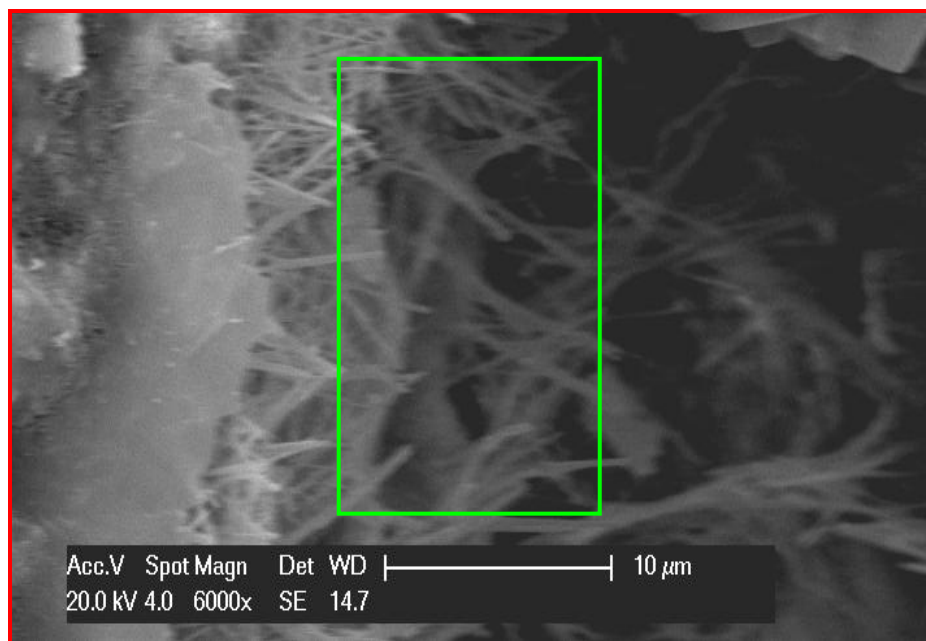


Fig.6.19: Ettringite deposition in air void

The force-displacement histories of the specimens during the first drop of impact are presented in Fig.6.20. Interestingly, the ascending branch of the force-deflection curves of the specimens is both irregular and highly non-linear (most obvious in the gravel concrete). This could be attributable to the reflections of the stress waves from the specimen boundaries and their interactions, and to the anisotropic nature of concrete itself ([Mindess and Zhang, 2009](#)). Presumably, generation of compression shock waves during impact would accelerate interlinking and dissipation of micro pores and other flaws in the contact area of the paste matrix by highly perturbed stress fields. This, in turn, may weaken the bond at the paste-aggregate interface and may further increase the plastic anisotropy.

The recovered strain is lower in the case of the blue brick mix in the same way as it is much stiffer. The figures also indicate that the rubber mix exhibits high plastic deformation while the gravel and brick mixes have a similar plastic response but these are much smaller than that of the rubber mix. This could be attributed to cracks that pass through the interfacial zone (see Fig.6.21) or presumably, the cracks could extend at velocities many orders of magnitude higher than subcritical crack growth, which is the slow growth of cracks that are too small to cause failure under the prevailing stress ([Young et al., 1998](#)). This, in turn, could lead to relatively high degeneration in the stiffness and hardness values of C-S-H particles and thus, could cause easy slippage and bonding. However, unfortunately, there is no experimental data on the crack growth velocities under impact in this study to support this hypothesis.

The force-displacement histories of the specimens in each impact are also recorded and illustrated in Fig.6.22. As can be observed from the figure, the copper slag specimen exhibits much larger deformation before fracture. This confirms that the response of concrete under impact is quite different. In the static condition, modification of concrete usually diverts the

fracture path from the ITZ to the aggregate, as in high-strength concrete, producing a destructive brittle failure. However, it is seen that in the dynamic condition, a strong interface in the case of the copper slag specimen would have a higher ability to redistribute stress accompanied by (relatively) higher energy dissipation, and ultimately a more ductile failure has taken place. Here, the specimens exhibited elasto-viscoplastic behaviour when the load was removed (most pronounced in the gravel specimen), possibly leading to generation of larger stress perturbations at the interface. Correspondingly, a weaker interface having a lower ability to redistribute stress would contribute to the comparatively sudden failure.

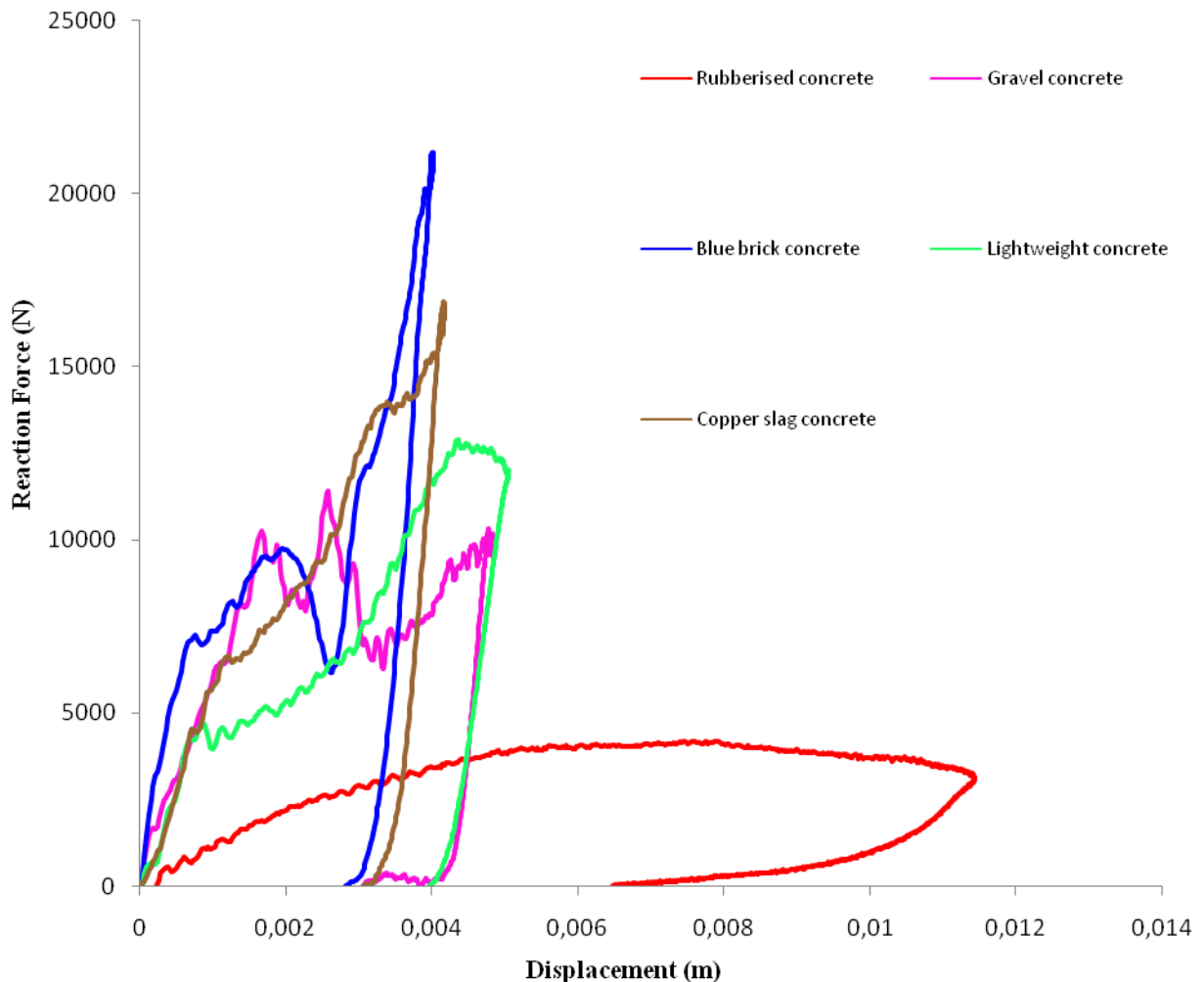


Fig.6.20: Force-deflection curves of the specimens at first drop of impact

The author believes that there is another important point that must be highlighted. It was found that the rate of curve peak decrease is better controlled in some specimens. For example, the curve peak of the 2nd impact in the case of the copper slag is higher than the peak of the 1st or 3rd impacts, and just before the failure (at the fourth drop), the amplitude of the load that was carried significantly increased. By contrast, surprisingly, the peak of the final (third) drop in the gravel specimen was even higher than the curve peaks of the first and second impact (incremental collapse).

According to [Wang et al. 2011](#), this phenomenon could be attributed to the fact that the hardening effect of strain-rate may prevail over the effect of damage softening. In parallel, this may indicate that the inherent microstructure of some specimens makes them more vulnerable to stiffness loss under the applied load as recently proposed by [Rao et al. \(2011\)](#) for the behaviour of recycled aggregate concrete under impact. The crack pattern and failure surfaces of disk specimens for both gravel and copper slag concretes are presented in Fig.6.23. The failure patterns shows that the failure was usually initiated by a radial tensile crack at or near the impact point and then the cracks propagated sideways, eventually breaking the specimens into several pieces, as shown in Fig.6.23.

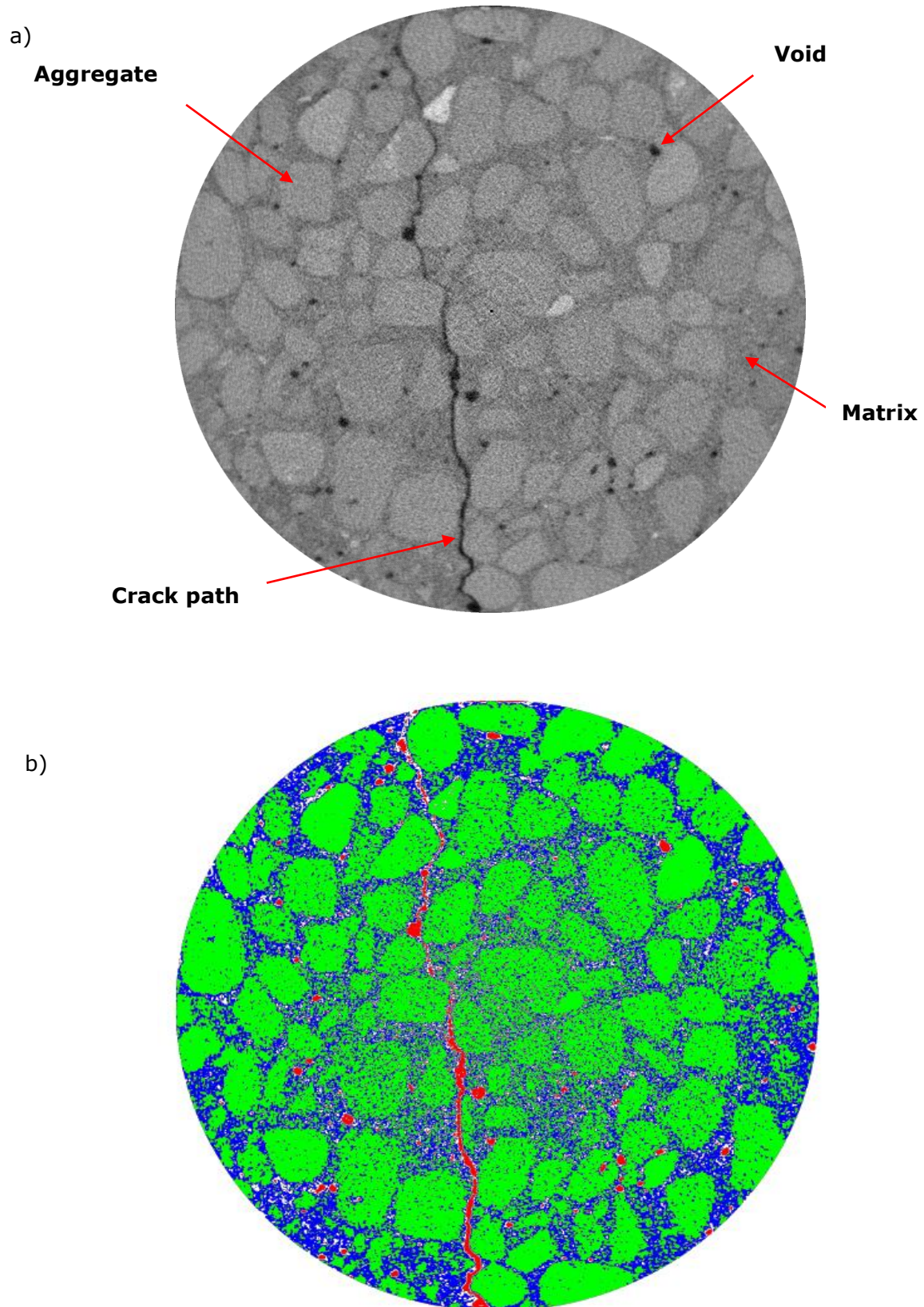


Fig.6.21: Images of impact failed blue brick concrete a) original X-ray b-) pseudo colour transformation

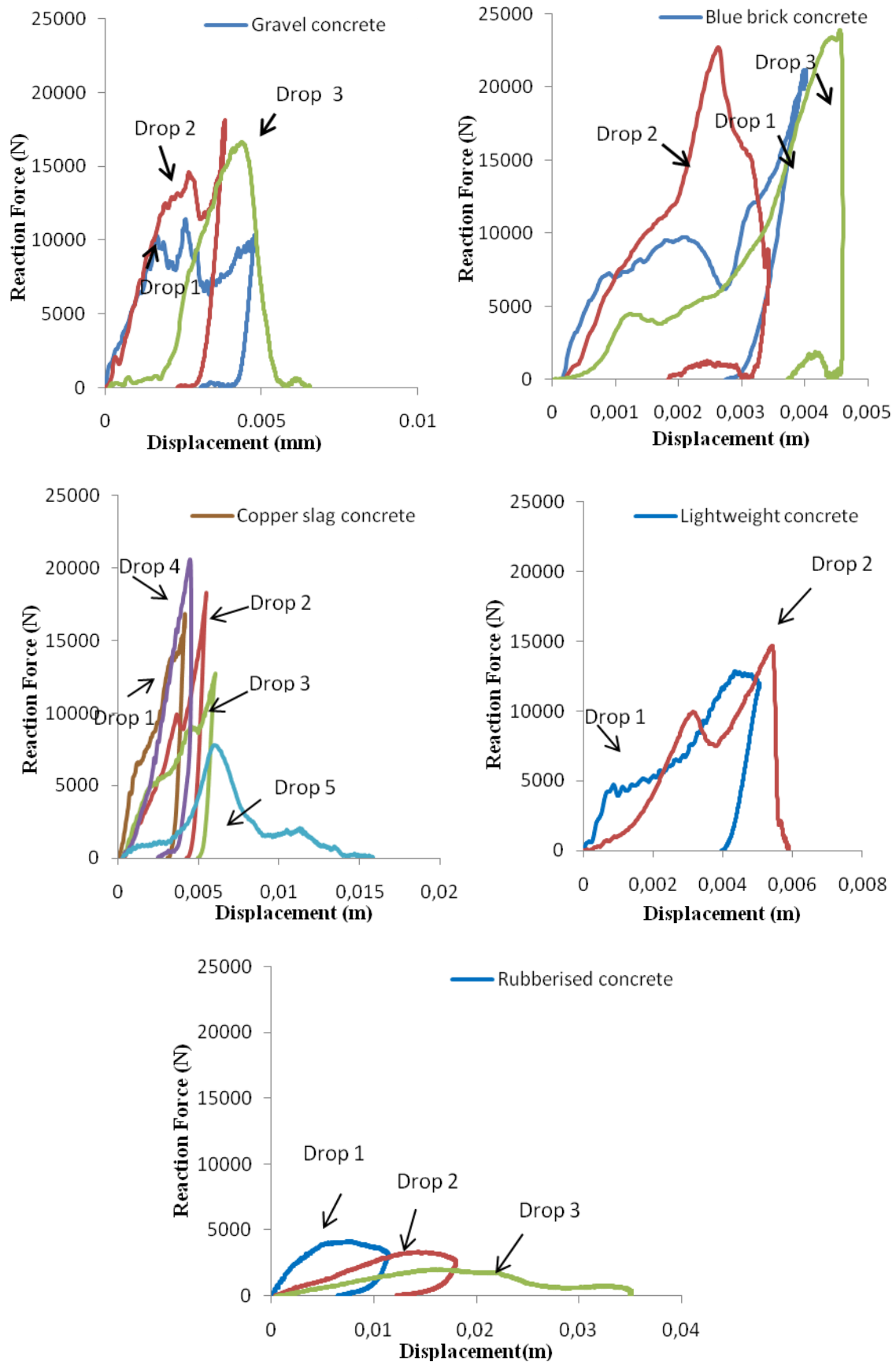


Fig.6.22: Force-displacement curves of the specimens



Fig.6.23: Failure pattern of the specimens after impact

6.4 Concluding Remarks

In the light of the findings obtained in this chapter, the following conclusions can be drawn:

- The air void distribution of the concrete mixes was determined from X-ray CT images along with digital image analysis techniques, and reasonable data was obtained. In addition, 3D simulation of air void distribution was successfully done. It has been observed that the air void distribution is not uniform through the specimens' heights, and the voids are more prominent in the middle section of the specimens except the rubberised mix.
- The time taken for the stress waves to travel from the impact point to the bottom of the rubberised specimen was 3 to 5 times higher than for the other specimens. This is

a demonstration of the lower overall stiffness of the rubberised mix and a weaker structural integrity at micro-scale as confirmed by the ITZ micro-hardness results.

- An ITZ with higher surface roughness may result in a higher force-carrying capacity of concrete by contributing to more energy dissipation within the mixture, and thus more resistance to impact but this will make it more brittle.
- The chemical elemental composition of the ITZ may promote the secondary ettringite formations in the voids of the damaged specimen.
- The rubberised concrete showed a more ductile and elastic response. In parallel, the blue brick and lightweight mixes exhibited less vulnerability to stiffness loss under impact likely (as confirmed by the changes in dynamic modulus results just before and after impact) due to a stronger and denser ITZ, and more homogeneous microstructure.
- Under impact loading, failure of concrete containing gravel aggregates occurred through the ITZ; mainly including pull-out of individual aggregate pieces from their cavities. Concrete prepared with the fly ash/Lytag failed through the aggregates; primarily including splitting of the aggregates across their diameter.
- Analysis for the real fracture profiles with a non-contact laser profilometer confirmed that the physical and microstructural aspects of aggregate may lead to a reduction in microroughness and correspondingly the amount of fracture energy.
- The changes in air void distribution and dynamic modulus of elasticity are demonstrated to provide a good basis on which to evaluate the deterioration of concrete subjected to impact loading.

References:

- [1] ACI Committee 544 (1988). "Measurement of properties of fibre reinforced concrete." ACI Material Journals 85(11) 583-93.
- [2] Akçaoğlu, T., Tokyay, M., and Çelik, T. (2005). "Assessing the ITZ micro-cracking via scanning electron microscope and its effect on the failure behaviour of concrete." Cement Concrete and Research 35 (2) 358-363.
- [3] Akhavan, A., Shafaatian, S.M.H., and Rajabipour, F., (2011). "Quantifying the effects of crack width, tortuosity, and roughness on water permeability of cracked mortars." Cement and Concrete Research, doi: [10.1016/j.cemconres.2011.10.002](https://doi.org/10.1016/j.cemconres.2011.10.002).
- [4] Badr, A., Ashour, A. F., and Platten, A.K., (2006). "Statistical variations in impact resistance of polypropylene fibre-reinforced concrete." International Journal of Impact Engineering 32 (11) 1907-1920.
- [5] Banthia, N., Mindess, S., Bentur, A., (1987). "Impact behaviour of concrete beams." Materials and Structures 20 (4) 293-302.
- [6] Barr, B., and Baghli, A., (1988). "A repeated drop weight impact testing apparatus for concrete." Magazine of Concrete Research 40 (144) 167-176.
- [7] Brown, A.K., (2007). "Finite element modelling of the static and dynamic impact behaviour of the thermoplastic composite sandwich structures". PhD Thesis. The University of Nottingham.
- [8] Chiaia, B., Van Mier, J.G.M., and Vervuurt, A., (1998). "Crack growth mechanism in four different concretes: Microscopic observations and fractal analysis." Cement and Concrete Research 28 (1) 103-114.
- [9] Fedroff, D., Ahmad, S., and Savas, B.Z., (1996). "Mechanical properties of concrete with ground waste tire rubber." Transport Research Record 1532 (10) 66-72.

- [10] Guo, L.P., Sun, W., Zheng, K.R., Chen, H.J., and Liu, B., (2007). "Study on the flexural fatigue performance and fractal mechanism of concrete with high proportions of ground granulated blast-furnace slag." *Cement and Concrete Research* 37 (2) 242-250.
- [11] Jialiang, L., (2004). "Dynamic modelling of lightweight high-strength concrete under impact." MSc Thesis. National University of Singapore.
- [12] Khan, R., (2009). "Quantification of micro-structural damage in asphalt." PhD thesis. University of Nottingham, United Kingdom.
- [13] Lok, T.S., Li, X.B., and Zhao, P.J., (2002). "Testing and response of large diameter brittle materials subjected to high strain rate." *ASCE Journal of Materials in Civil Engineering* 14 (3) 262-269.
- [14] Mindess, S., and Zhang, L., (2009). "Impact resistance of fibre-reinforced concrete." *Proceedings of Institution of Civil Engineering-Structures and Buildings* 162 (3) 69-76.
- [15] Rao, M.C., Bhattacharyya, S.K., and Barai, S.V., (2011). "Behaviour of recycled aggregate concrete under drop weight impact load." *Construction and Building Materials* 25 (1) 69-80.
- [16] Rollet, A.D., (2007). "Microstructure-Properties: I Lecture 6A: Fracture." http://neon.mems.cmu.edu/rollett/27301/L6A_GriffithEq-15Oct07.pdf
- [17] Sukontasukkul, P., Nimityongskul, P., and Mindess, S., (2004). "Effect of loading rate on damage of concrete." *Cement and Concrete Research* 34 (3) 2127-2134.
- [18] Tasong, W.A., Lynsdale, C.J., and Cripps, J.C., (1998). "Aggregate-cement paste interface ii: influence of aggregate physical properties." *Cement and Concrete Research* 28 (10) 1453-1465.
- [19] Thomas, M.D.A., and Ramlochan, T., (2002). "Field cases of delayed ettringite formation." In: K. Scrivener and J. Skalny (Editors), *International RILEM TC 186- ISA Workshop (Villars) on Internal Sulphate Attack and Delayed Ettringite Formation*, 85-97.

- [20] Yan, A., Wu, K.R., Zhang, D., and Yao, W., (2003). "Influence of concrete composition on the characterization of fracture surfaces." *Cement and Concrete Composites* 25(1) 153-157.
- [21] Ying, H., (2010). "X-ray computed tomography to quantify damage of hot-mix asphalt in the dynamic complex modulus and flow number tests." MSc thesis. Louisiana State University.
- [22] Wu, K., Yan, A., Yao, W., Zhang, D., (2001). "Effect of metallic aggregate on strength and fracture properties of HPC." *Cement and Concrete Research* 31 (1) 113-118.
- [23] Wang, Z. L., Z. M. Shi, et al. (2011). "On the strength and toughness properties of SFRC under static-dynamic compression." *Composites Part B: Engineering* 42 (5) 1285-1290.
- [24] Wu, K., Yan, A., Yao, W., and Zhang, D., (2001). "Effect of metallic aggregate on strength and fracture properties of HPC." *Cement and Concrete Research* 31 (1) 113-118.
- [24] Zampini, D., Jennings, H.M., Shah, S.P., (1995). "Characterization of the paste-aggregate interfacial transition zone surface roughness and its relationship to the fracture toughness of concrete." *Journal of Material Science* 30 (12) 3149-3154.

CHAPTER 7

OVERALL DISCUSSION AND EVALUATION: MICROMECHANICAL STRUCTURE-PROPERTY RELATIONSHIPS

7.1 General:

The aim of this chapter is to collate and discuss the whole set of test results presented in previous chapters.

At first section, method to characterize the pore structures of the mixes will be described and some general consideration about the characteristics of each mix will be summarized. Each assessment and its possible implications will be also tabulated here. Next, some correlations between micro and macro-scale properties will be presented and discussed. The correlations presented can be summarized as follows:

- In the first part, the relationships between the micro-structure of the interfacial zone and the composite mechanical properties will be analyzed.
- In the following part, the relationships between the micro-structural features of the zone at the cement paste-aggregate interface and the impact load-induced micro-damage will be studied.

7.2 Pore Structure Testing

It is now widely accepted that the microstructure of concrete has a profound effect upon its macro-mechanical properties. Thus, to a certain degree, the variation of pore structure can be expected to relate to the deterioration of concrete subjected to impact loading.

Porous space characterisation in cement-based materials can be achieved by different techniques such as nitrogen adsorption, vapour sorption, thermoporometry, mercury porosimetry (MIP) and image analysis. Among these methods, the MIP is extensively used over a long time because of its ease and simplicity, and can measure larger capillary pores 0.005-10 μm (Abell et al., 1999). Thus, the technique of MIP was used to characterize the pore structures (total porosity and pore size distribution) of concretes in this study. However, as highlighted by Abell et al., (1999), the MIP assumes that the geometry of the pores is regular and the pores are interconnected (continuous pore, continuous pore with ink bottle and dead-end pore with ink bottle) and thus isolated pores cannot be detected by mercury intrusion.

For MIP measurement, small fragments of hardened cement paste were obtained from the middle part of concrete specimens after being subjected to impact loading. Then, the selected samples were immersed in acetone in order to stop further hydration. The extracted pieces were then dried in a vacuum oven at about 60 °C for 48 hours until constant mass was achieved. The porosity and pore size distribution of the concrete samples were then measured using a Micrometrics Autopore IV mercury porosimeter (see Fig.7.1) with a maximum intrusion pressure of 210 MPa which means the smallest pore diameter that can be measured is about 7 nm.

The whole MIP testing procedure including first intrusion, extrusion and the second intrusion is schematically shown in Fig.7.2 (Ye, 2003). During the first intrusion, mercury is intruded into the pore spaces with the increase of pressure (Fig.7.2 b). When the pressure is reached the highest value, the mercury is sucked out of the pore space with a gradual decrease of the applied pressure except for the pores having ink-bottle and dead-end parts (Fig.7.2 c). In the second intrusion, the same procedure is followed as for the first intrusion part (Fig.7.2 d).

The mercury intruded pore diameter d_p at an intrusion pressure of P_{In} was then calculated using Washburn equation as follows:

$$d_p = -4\gamma \cos\theta / P_{In} \quad (7.1)$$

where $\gamma = 0.483 \text{ Mm}^{-1}$ the surface tension of mercury and $\theta = 140^\circ$ the contact angle between mercury and solid.



Fig.7.1: Micromeritics Autopore IV mercury porosimetry

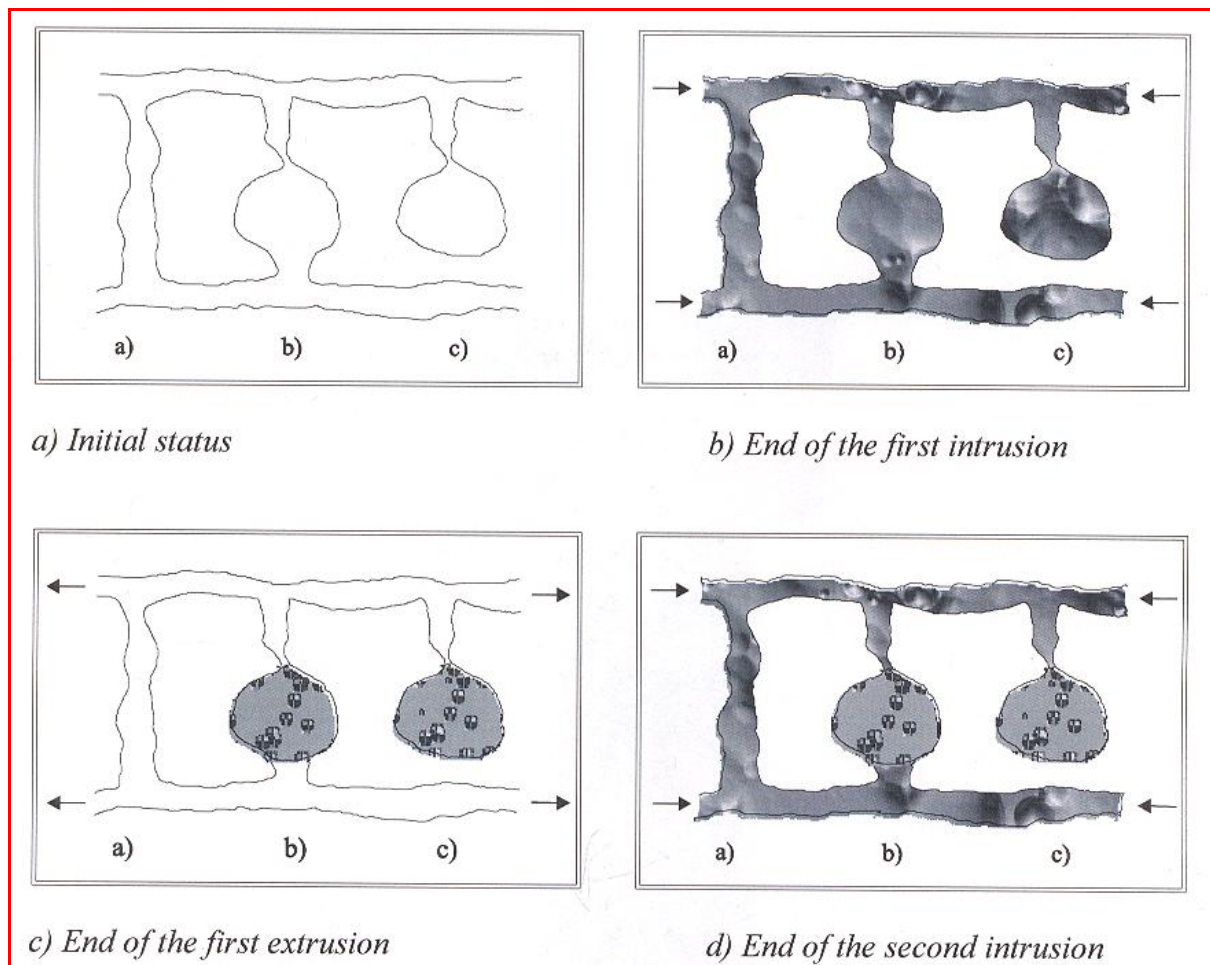


Fig.7.2: Schematic illustration of mercury intrusion and extrusion (Ye, 2003)

7.3 Summary of Material Behaviours:

The in-depth micro-structural analysis of the mixtures revealed some morphological differences in the cracking behaviour and the corresponding mechanical differences. The analysis strongly suggests that the microscopic damage mechanism under impact loading is highly complex, and the aggregate causes a change in the initial ITZ condition and it is this altered ITZ condition that has a major effect on overall mix behaviour.

It was deduced that the osmotic forces yielded water transfer from the highly porous and rough fly ash/Lytag aggregate to the cement paste with the progress of hydration process.

This supplied water and in turn further hydrated the paste matrix and thus, produced a very dense, thin and strong interfacial zone, leading to more homogeneous behaviour. However, there seem to be some contradictions when the ITZ characteristics are taken into consideration to explain the observed differences in the micro-damage features of the concrete mixes. The less porous and narrow ITZ in the lightweight mix was associated with fractures that penetrated into the aggregate in many cases. The fracture was not properly arrested by the particles due to their intrinsic weakness and low stiffness, and thus lower stress accumulated near the position where the crack left the aggregate -due to the aggregate geometry- and less energy was required in order to advance the fracture again. As a result, secondary crack branches were rarely produced, leading to a smoother fracture profile associated with a smaller fractal dimension in this type of concrete.

On this basis, one might expect less crack concentrations at the interface. This was not the case as the crack density was higher than in the gravel and blue brick mixes. This indicates that other factors in addition to the ITZ contribute to the damage phenomena of the concrete mixtures studied. As stressed by [Chiaia et al. \(1998\)](#), the Lytag particle itself is strongly heterogeneous at the micro-scale, and thus the fractal dimension of cracks through these particles can be much higher than that at the macro-level of observation. This could be the reason for the relevant ductility under impact in this concrete, which is not trivial when compared to its low nominal dissipated fracture energy. The less anisotropic distribution of pores in the ITZ or the presence of fewer numerous interconnected interfaces could have an influence on this behaviour as well.

When the particles have much higher strength than the paste matrix, the ITZ and its properties became of major importance for micro-level damage initiation and propagation. The

rougher surface rugosity and more angular shape of the aggregates improved mechanical interlocking, resulting in a strong ITZ, while a smooth shape of aggregate reduced the adhesion and provided only a weak obstacle to crack propagation. If the particles are highly rigid, such as copper slag, the tendency to develop local stress concentrations and corresponding micro-cracking at the paste-aggregate interface was increased. However, in this case the deflection and arresting of cracks occurred probably due to the higher roughness of the ITZs and this in turn caused a slower propagation of interfacial cracks slower via the relatively thinner ITZ. Thus, more energy was required for the interfacial cracks to reach critical length and more energy is consumed for the coalescence of the cracks, resulting in a fracture surface with a high degree of roughness.

Taking these observations together, it appears that the rubber aggregate has deleteriously affected a wider zone of paste around each particle resulting in a thicker ITZ with less ability to carry stress waves effectively and a weaker overall performance. Poorer aggregate characteristics alone could be responsible for a greater ITZ deterioration after loading as it might be expected to have had to play a greater role in carrying the stress of the first load pulse. But the initial observation demonstrates that, in fact, the aggregate causes a change in the initial ITZ condition and it is this altered ITZ condition that has a major effect on overall mix behaviour. The good performance of the blue brick mix also supports this interpretation because, although the individual pieces of fly ash/Lytag are not as strong as those in the gravel, yet the mix is the strongest. Thus the benefit must be coming from the paste and the results show that it is in the form of an improved ITZ. Similarly, the higher fractal dimension of the rubberised mix indicates that although the rubber particles reduce mechanical interlocking (owing to the surface texture of the particles) producing a large number of pores

in the ITZ, these weak heterogeneities, in turn, disorder the fracture pattern leading to an increase in tortuosity.

It is also supposed that the high rates of loading would tend to form a network of inter-connected cracks between the micro-pores and pre-existing micro-cracks (Fig.7.3). Micro-cracks exist even before loading due to the incompatibility between the modulus of elasticity and shrinkage of the aggregate and the matrix ([Acker et al. 1987](#); [Van Mier 1997](#)), thereby leading to stress concentrations around the interfacial zone. These dissipate some of the impact energy and reduce the peak stress, which is very obvious from the rubberised specimen impact test results.

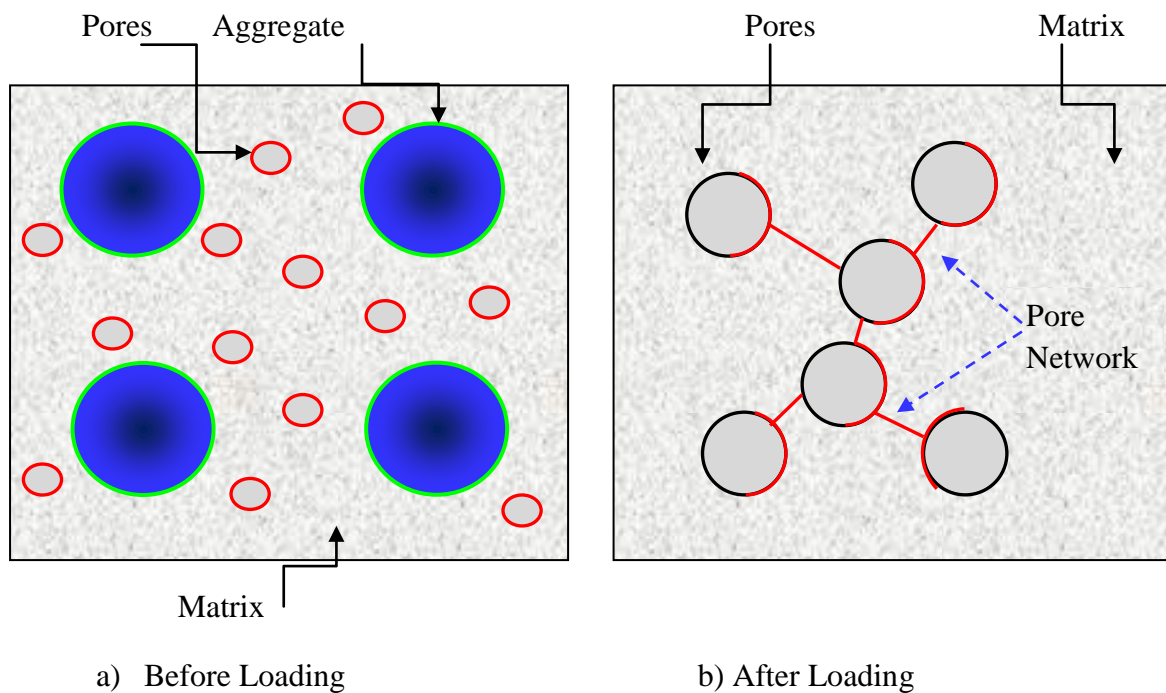


Fig.7.3: Schematic representation of pore connectivity in matrix under loading

Each assessment and the possible implications are now considered in turn. Results are summarized in Table 7.1.

Table 7.1: Relative values of results for all mixes

Factor	Gravel	Lightweight	Blue brick	Copper slag	Rubberised
Impact Reaction Force	Moderate	Good	Very good	Very good	Poor
Density	High	Moderate	High	Very high	Low
Static strength	Moderate	Good	Very good	Very good	Rather poor
ITZ porosity	Moderate	Dense	Dense	Dense	Highly porous
Dissipated surface fracture energy after impact	Moderate	Low	High	High	High
ITZ roughness	Smooth	Quite smooth	Highly rough	Highly rough	Highly rough
The time for stress wave to pass through the specimens	Long	Moderate	Short	Short	Very long
ITZ thickness	Thick	Very thin	Thin	Thin	Very thick
Plastic deformations	Low	Moderate	Low	Low	Very high
ITZ micro-hardness	Moderate	Moderate	Strong	Strong	Very weak
ITZ cracks and fractures	Low density	High density	Moderate	High density	Moderate

7.4 Results and Discussion - Bridging between the Scales

7.4.1 Micro-hardness- Strength Relationship

Fig.7.4 shows the compressive strengths of the mixtures as a function of the ITZ micro-hardness. The trend has very little scatter and clearly rises almost linearly as a function of micro-hardness with a correlation coefficient of 0.9944. This is consistent with the findings of Mindess et al. (1998) who also found linear correlations between micro-hardness and compressive strength, but the correlations were more linear. As is well-established, micro-hardness is a parameter dependent on various characteristics of the ITZ including mean crystal size, crystal orientation index of CH and pore microstructure (Gao et al. 2005). It is thus supposed that a weaker ITZ (i.e. porous and large CH deposition) could yield a lower micro-hardness values and correspondingly, poor mechanical performance in the specimen.

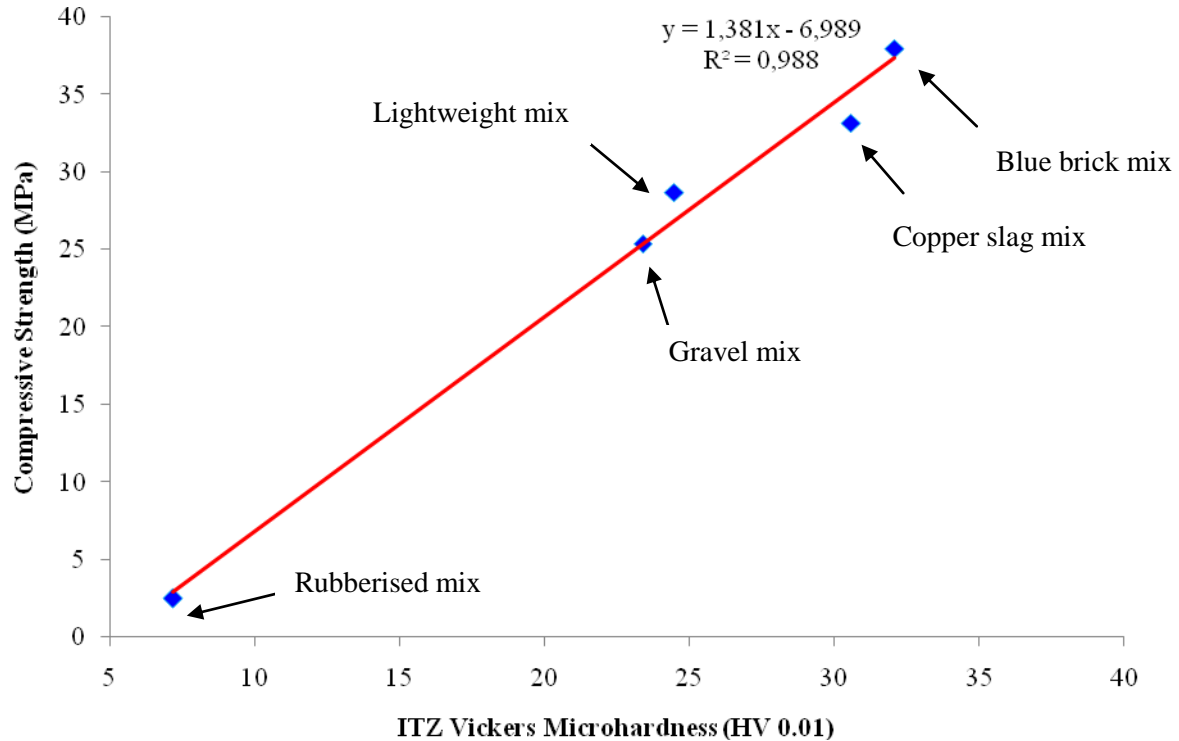


Fig.7.4: Relationships between the ITZ micro-hardness and concrete compressive strength

7.4.2 Compressive Strength vs. ITZ Porosity

Fig.7.5 illustrates the relationship between the static strengths of the concrete mixtures and the ITZ porosity. As can be seen, the strength has a very strong dependence (correlation coefficient 0.9872) upon the variation in the ITZ porosity, showing a linear inverse relationship. This data is also a complement of the strength vs. ITZ micro-hardness correlation. The analysis also suggests that a denser and less porous ITZ provides a better bond likely due to the absence of large crystals of CH in the vicinity of the aggregate particles signifying that a high packing density has been achieved. The denser packing would reduce the volume of open pores in the microstructure of the cement paste, which, in turn, leads to a smaller amount of cement paste needed to fill up the voids and thus reduce concentrations of CH in this region as the CH is mainly deposited in the open pores (Scrivener et al., 2004).

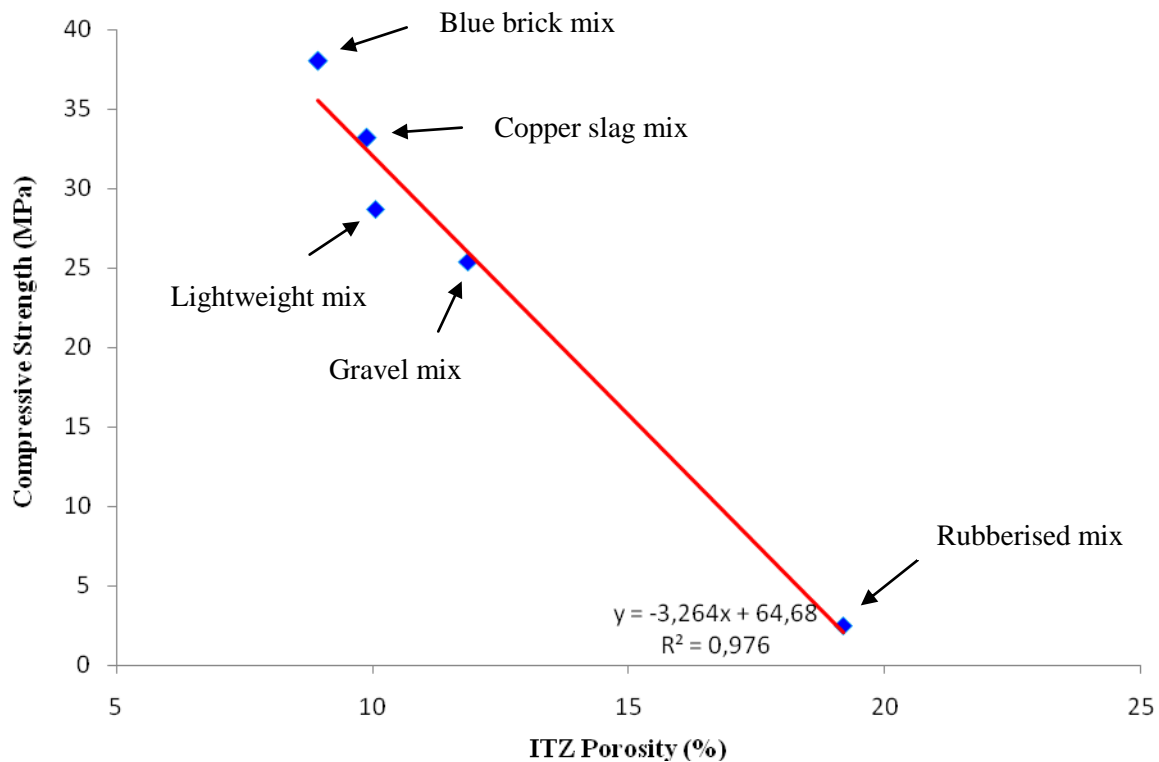


Fig.7.5: Relationships between the ITZ porosity and concrete compressive strength

7.4.3 ITZ Micro-hardness vs. Impact Reaction Force

As suggested by [Copuroglu \(2005\)](#), considering the global tensile strength of the material may not be an appropriate approach to assess the damage response of a concrete material, since the tensile strength is strongly dependent on the strength of the ITZ. Therefore, assessment of local micro-mechanical properties seems to be a much more realistic means of assessing the impact-resistance of a particular material.

Fig. 7.6a and b display the changes in micro-hardness values after the first drop of impact, and the peak load values in the first cycle of impact, respectively. It is obvious that the impacted specimens displayed degradation in the mean hardness values likely due to crack development in the ITZ. This is most pronounced for the rubberised specimen. This is probably due to the fact that the weak ITZ could not transfer the load efficiently and led to narrower spacing between the cracks in the mix. For these reasons, the specimen would not be able to withstand more loading before failure is observed. The results also provide a strong support for the interpretation that the different height of peaks is a consequence of different times of loading- indicating different dynamic stiffnesses and plastic strains.

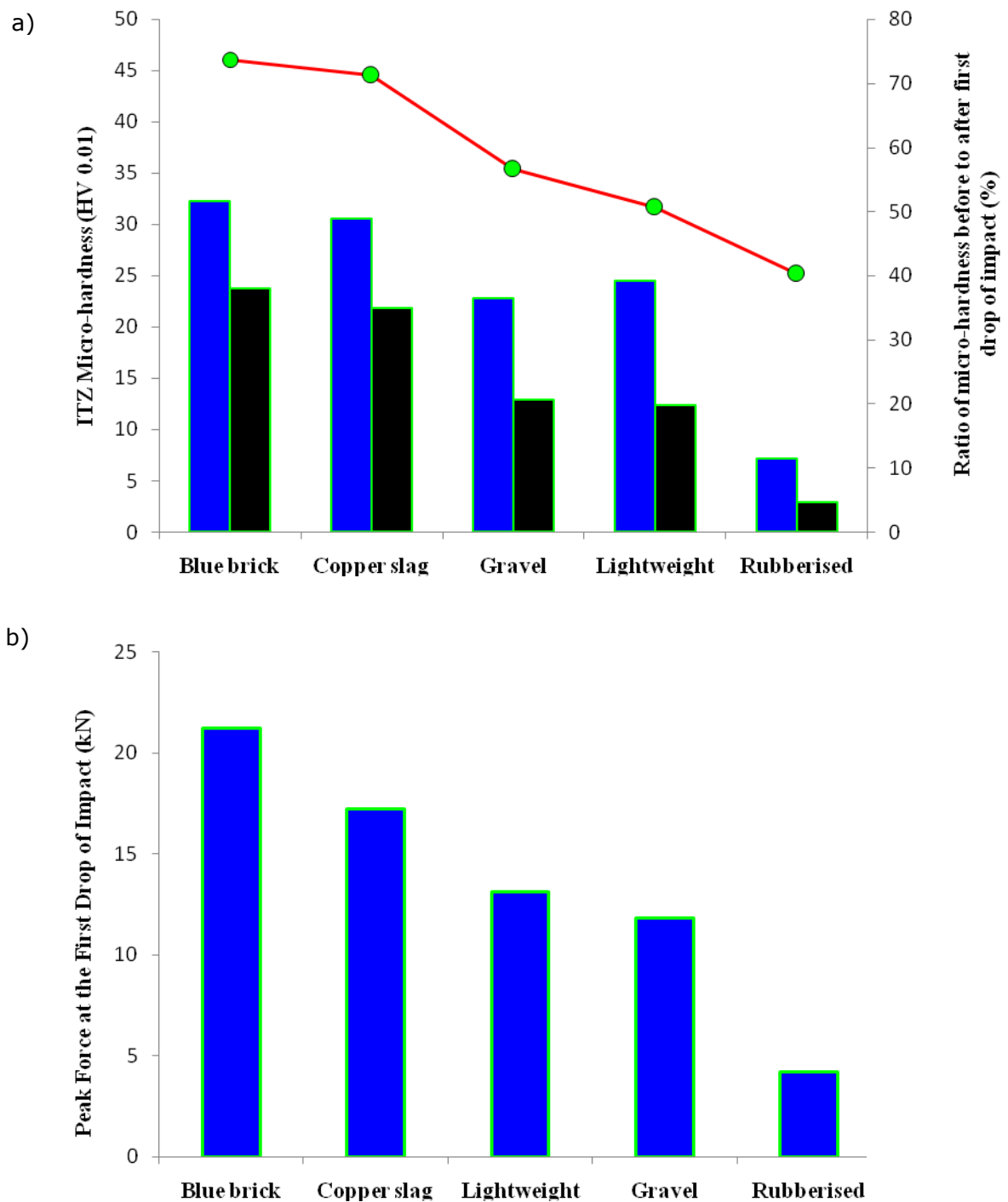


Fig.7.6: The micro-hardness before and after first drop of impact (a) and the peak force at first cycle of impact (b)

7.4.4 ITZ Surface Roughness vs. Dissipated Fracture Energy

Fig.7.7 shows digitized contour crack maps of typical failure surfaces. These crack maps were used to calculate the fractal dimensions of the specimens. The analysis, using the approach suggested by [Guo et al. \(2007\)](#), indicates that concrete with rubber particles dissipate much greater fracture energy during the impact, followed by the blue brick mix, copper slag and the gravel mix. It is supposed that this was basically due to the fact that very elastic rubber particles compared to the surrounding matrix may produce localized stress concentrations and, hence, more crack initiation and propagation points, leading to larger fractal dimensions. The results are also consistent with the findings presented in the previous paragraphs and give some support to the theory that higher micro-roughness usually results in higher fracture energy consumption during the fracture and lower micro-roughness results in lower energy consumption ([Wu et al. 2001](#)). It is also very interesting to note that the increase in roughness number (Ra) of the paste results in an increase in the energies absorbed up to peak load. In addition, there is almost a linear correlation between the Ra values and the absorbed energy values of the specimens, as shown in Fig.7.8.

As schematically explained by [Katsaga \(2010\)](#), when an aggregate is located in front of the fracture tip, the fracture cannot propagate straight to the aggregate due to the confinement field below and above the aggregate (if load is applied vertically). These confinement fields are created as a consequence of the elastic incompatibility between the aggregate and matrix, and friction between them along the boundary. Therefore, avoiding these confinement cones, the fracture travels along the weak aggregate-matrix interface on the sides (Fig.7.9). This mechanism causes fracture path fluctuation and helps to explain the higher fractal dimension and correspondingly greater energy dissipation in some of the mixtures such as copper slag or rubberised mix.

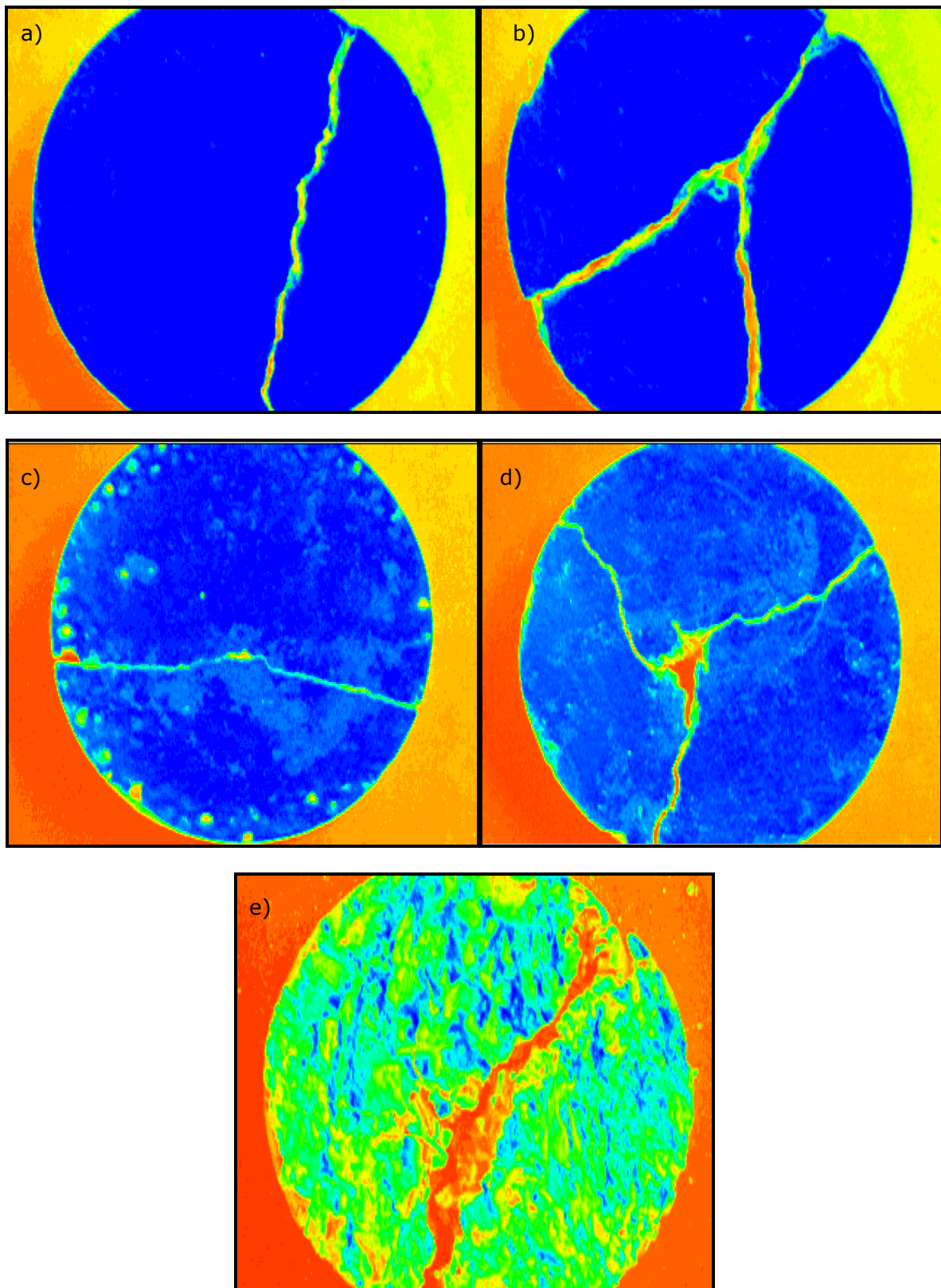


Fig.7.7: An example of the digitized crack path of the surfaces of the concrete mixtures: a) gravel, b) blue brick, c) lightweight, d) copper slag and e) rubberised mix.

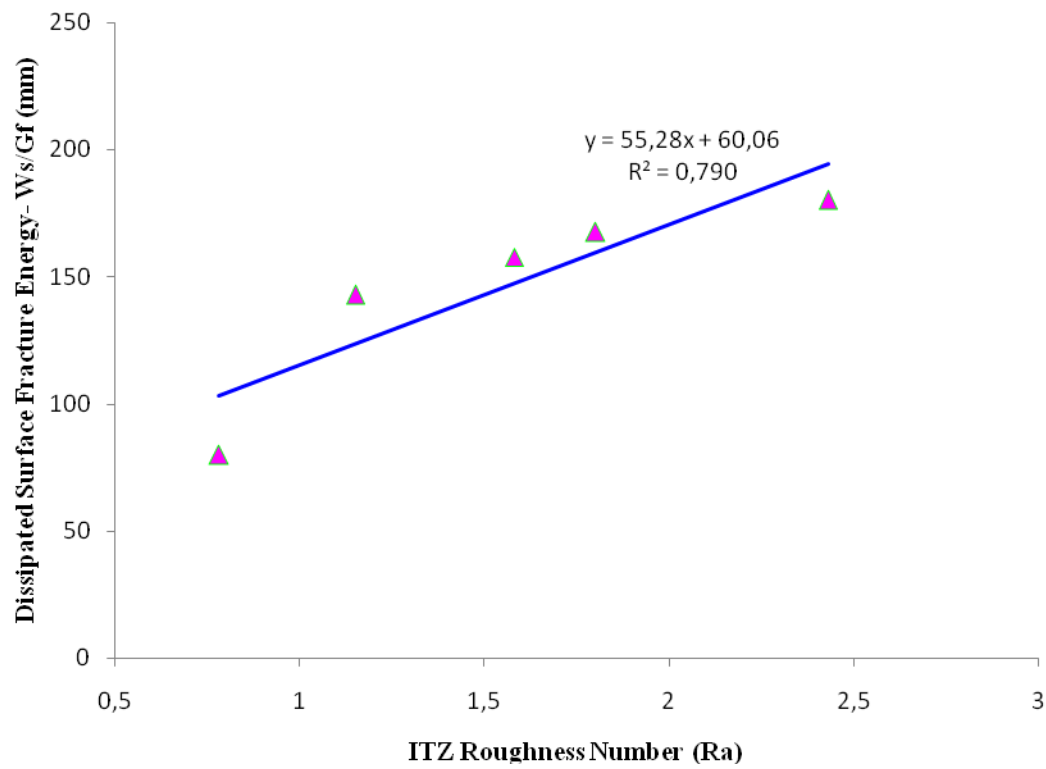


Fig.7.8: Relationships between the ITZ roughness and dissipated surface fracture energy

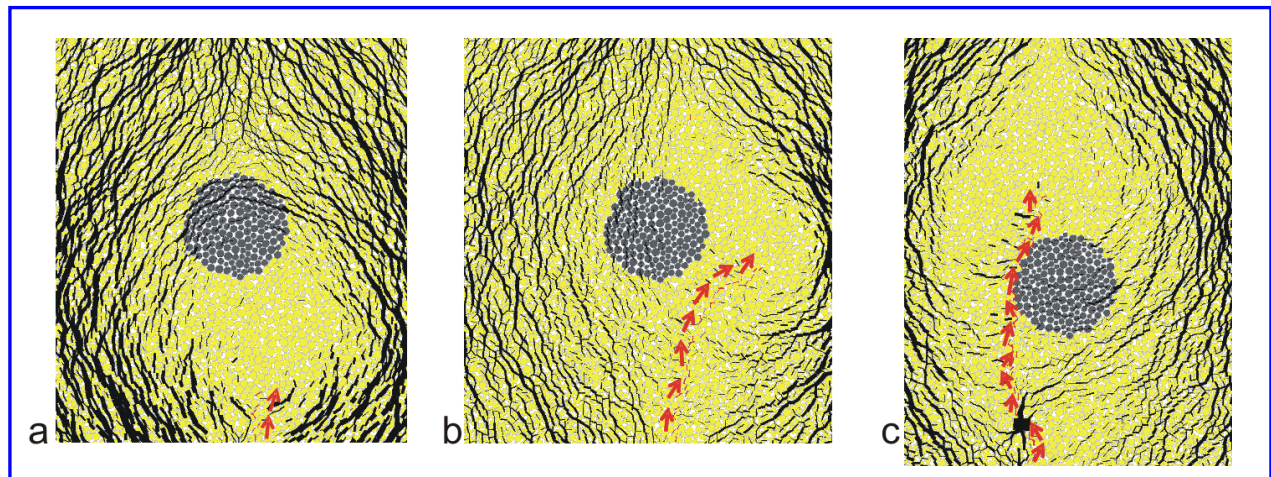


Fig.7.9: Fracture propagation with a single aggregate: black lines show contact forces
(Katsaga, 2010)

7.4.5 ITZ Crack Width vs. Coarse Aggregate Type

Fig.7.10 shows plot of the type of coarse aggregate in concrete mix versus the ITZ crack width under impact testing conditions. The comparison in crack widths between the rubber and the other aggregates shows that the crack width for the rubberised case, 38.20 μm , is much greater than those for the other aggregate. This could be explained by considering the much larger volume change in the air void content of rubberised concrete as presented in Chapter 6. It is also believed that pre-load cracks (see Fig.7.11) due to the significant disparity in the moduli of elasticity of the aggregate and the matrix, and more importantly the differential shrinkage and thermal expansion of the two materials could also contribute to less reliable concrete aggregate interlock at the crack in the case of rubberised case. The results also indicate a more reliable concrete-aggregate interlock in the lightweight and blue brick mixes.

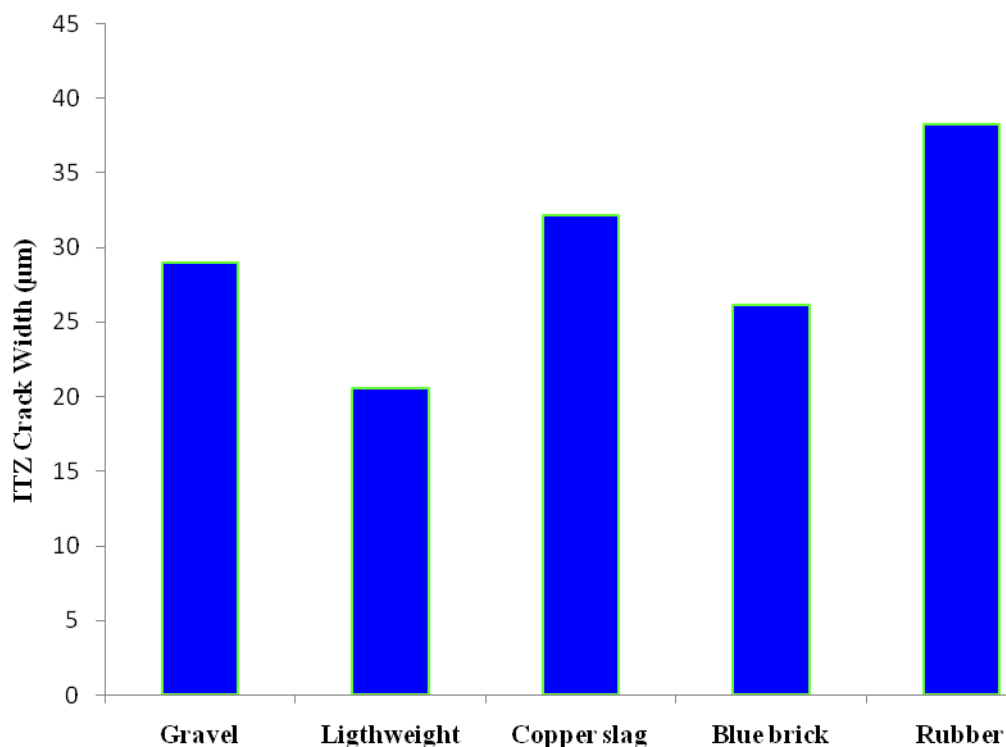


Fig.7.10: Measured ITZ crack widths

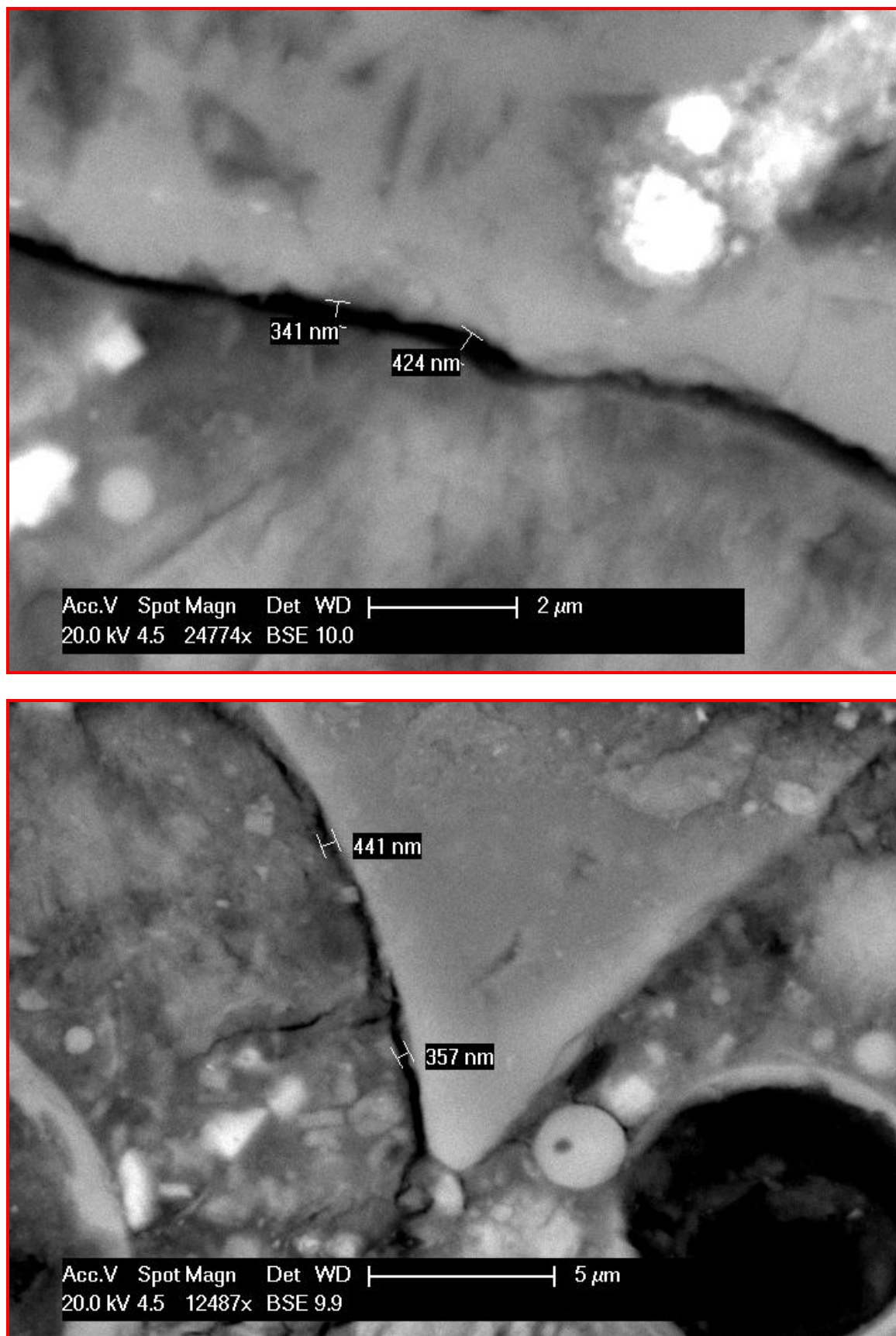


Fig.7.11: Pre-loading cracks in the rubberised mix

7.4.6 ITZ Thickness vs. Impact Induced-Stress Wave Propagation Time

Fig.7.12. presents the ITZ thickness and the corresponding time for the stress wave to pass through the specimen at the first drop of the impact. As can be from the figure, when the ITZ is thicker, it requires a longer time for the stress wave to travel through the specimen body. However, the analysis reveals that this is only valid when a specimen has both a thin and strong ITZ (i.e. the lightweight mix specimens). This probably reflects the fact that a thin but less strong interface would have a relatively lower ability to redistribute stress which makes the material brittle.

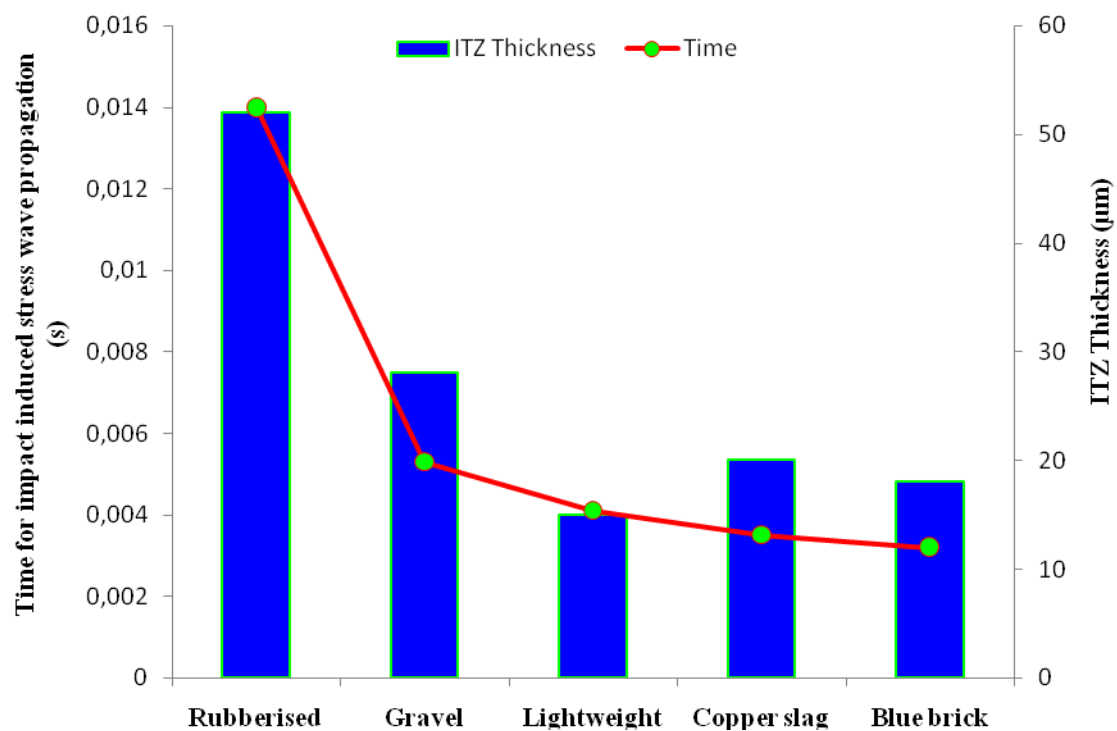


Fig.7.12: Relationships between the ITZ thickness and the time for stress wave propagation

7.4.7 ITZ Surface Roughness vs. Surface Crack Tortuosity

The relationship between the ITZ roughness and surface macro-crack tortuosity can be seen in the graph in Fig.7.13. The correlation coefficient is 0.7920, indicating a moderately strong relationship between the tortuosity and ITZ roughness. This data is also a complement to the

strength vs. ITZ micro-hardness correlation. Investigation on the characteristics of the cracks at the interface would contribute to a more in-depth understanding of the fracture process. A very recent work by [Katsaga \(2010\)](#) visualized and processed the crack characteristics and showed that in the case of the interfacial cracks, a number of secondary intercept directions can exist. This was probably the case for some of the mixes in this study and it explains why its fracture surface's had a high degree of tortuosity.

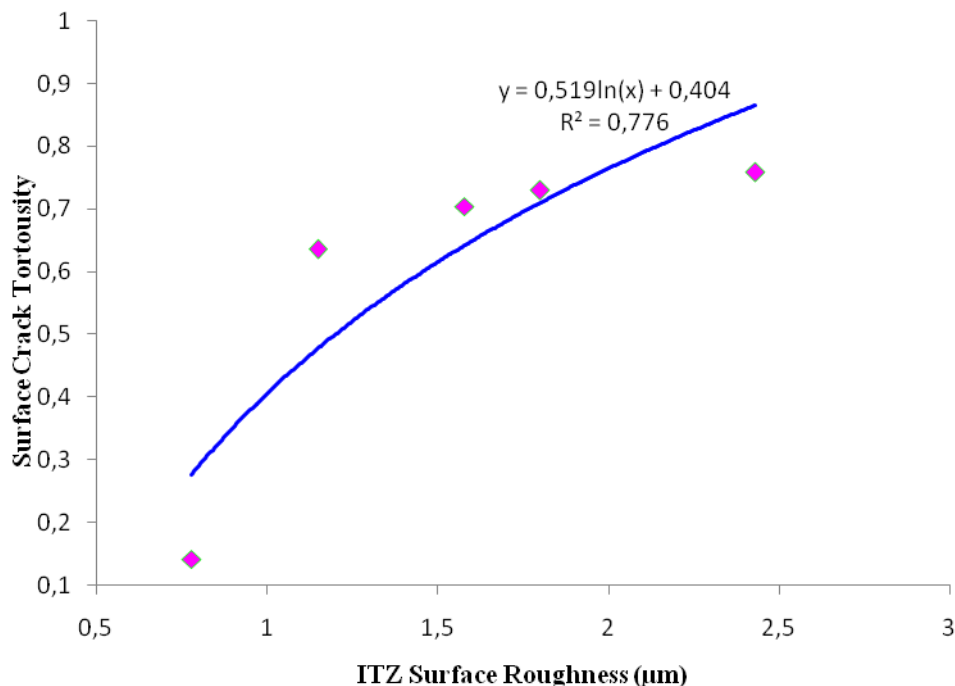


Fig.7.13: Relationships between the ITZ roughness and surface crack tortuosity

7.4.8 Compressive Strength/Flexural Energy vs. Impact Strength/Impact Energy

Fig.7.14 gives the relationship between the impact strength and compressive strengths of the mixtures. [Neville \(2009\)](#) reported that the impact strength of concrete is more closely related to its flexural strength rather than its compressive strength, and for the same compressive strength, the impact strength is greater for coarse aggregate of greater angularity and surface roughness. The results support this suggestion to some extent. It can be seen that the concrete made with highly angular and rough blue brick and copper slag aggregates have withstood

higher numbers of impacts than the gravel mix. By contrast, the porous internal structure and rough internal texture of the Lytag particles could possibly lead to a reduction in the grain-grain interlock and inter-particle friction between aggregate pieces, resulting in a less stiff material. In the case of the rubber, the specimen is able to absorb considerable amounts of energy before failure due to the highly elastic nature of the particles.

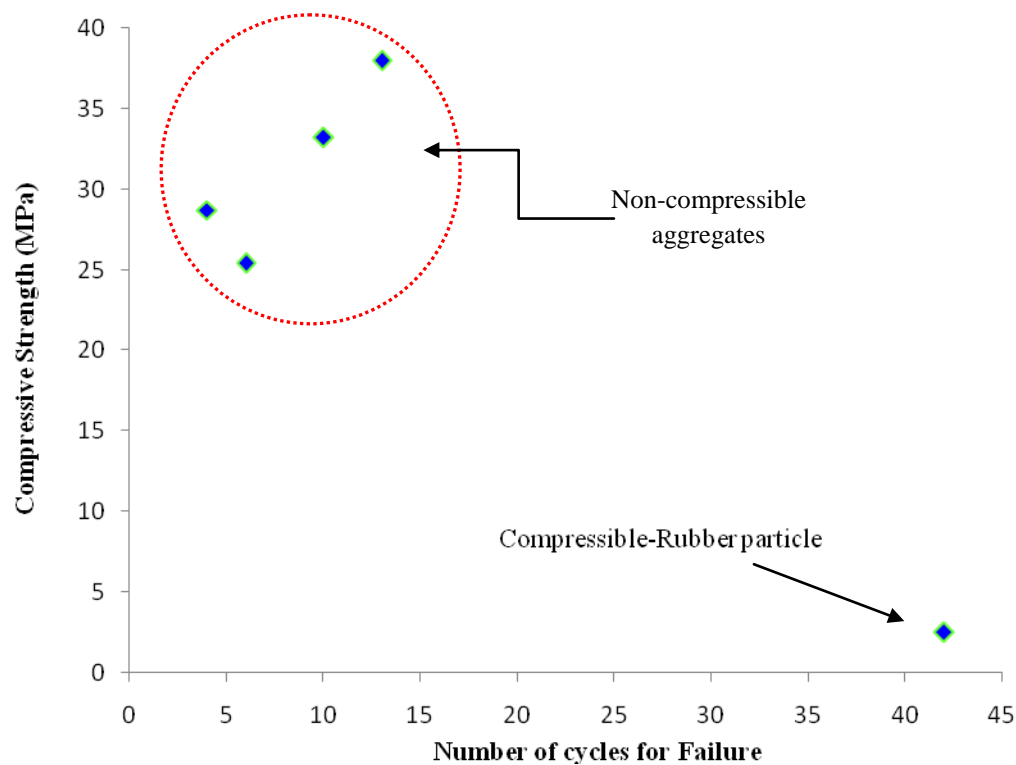


Fig.7.14: Relationship between the compressive and impact strength

The results indicate that in general, the impact resistance of concrete increases with an increase in compressive strength but more specifically, the non-compressible aggregates behave in a similar manner and absorb less energy compared to the compressible aggregate and thus, last less longer under impact loading. In parallel, Fig.7.15 shows that the impact energy increases almost linearly with increase in flexural toughness energy. A correlation coefficient of 0.9867 indicates a very strong relationship between these variables.

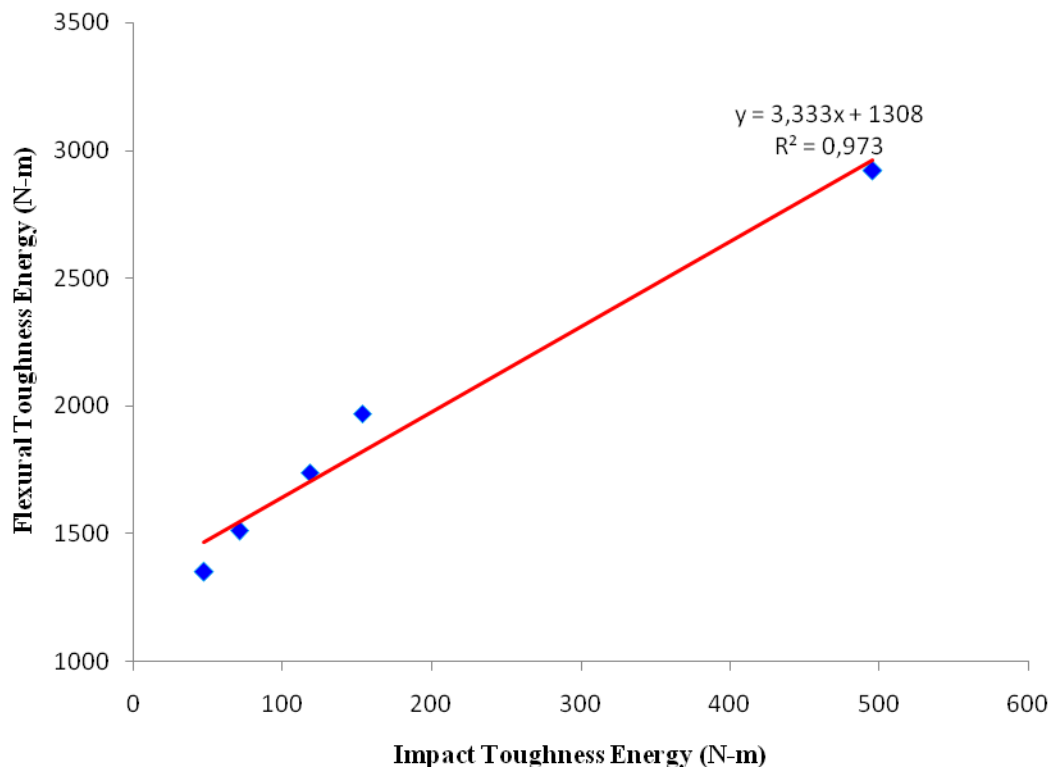


Fig.7.15: Relationship between flexural toughness energy and impact energy

7.5 Pore Structure Characterisation after Impact

Fig.7.16 shows cumulative MIP intrusion volume against pore diameter curves of the mixtures after exposure to impact loading. The reference point for the porosity is based on the control mix. It would be interesting to obtain the porosity of the different types of concrete before subjection to impact but the normal method of preparing the samples for MIP on undisturbed concrete requires some kind of impact (usually from rather variable manual effort) to obtain little fragments of mortar. Since the controlled impact from the equipment reduces the influence of manual variability, it is believed that using the impact force to produce the specimens is better for ensuring a fair comparative analysis.

The calculated percent total pore space (micro and macro pores) is also tabulated in Table 7.2. In general, the analysis indicates that the impact loading enlarged the mean pore diameter and caused clustering and coarsening of the interconnected pores. The microscopic analysis (see Fig.7.17) seems to confirm the connectivity in the air void layers. The coalescence of pores will inevitably reduce effective interparticle contact area on the fracture surfaces, which is undesirable under dynamic conditions because much of the imparted energy is normally lost in plastic deformations ([Hallett et al., 1995](#)). The MIP test results clearly indicate that the percentage of the pore volume in the rubberised specimen occupied by macro pores (pores larger than 100 nm) after impact was significantly lower than in both the gravel and blue brick mixes and the least degeneration in the pore structure occurred in this mix. In addition, the analysis indicates that a refinement of pore structure- this is the case in which the volume of micro pores is bigger 65 %- has taken place for the rubberised specimen.

The cement matrices of the mixtures used in this study show a higher fluidity due to the high w/c ratio. In this case, stabilization of air voids is more important than generations of air voids ([Lee et al. 2010](#)). The non-polar nature of rubber particles may attract air voids and perhaps air voids get against into their jagged surface textures ([Fedroff et al. 1996](#)). In addition, the rubber particles absorb a relatively low proportion of the energy that is required for the effective flow of the cementitious material due to their low density during mixing. For these reasons, on the one hand, the pores will inevitably expand in the transition area and will be very hard to stabilize. On the other hand, the micro-cracks will develop around the perimeter of the rubber particles, which provides a more gentle crack propagation compared to other mixes.

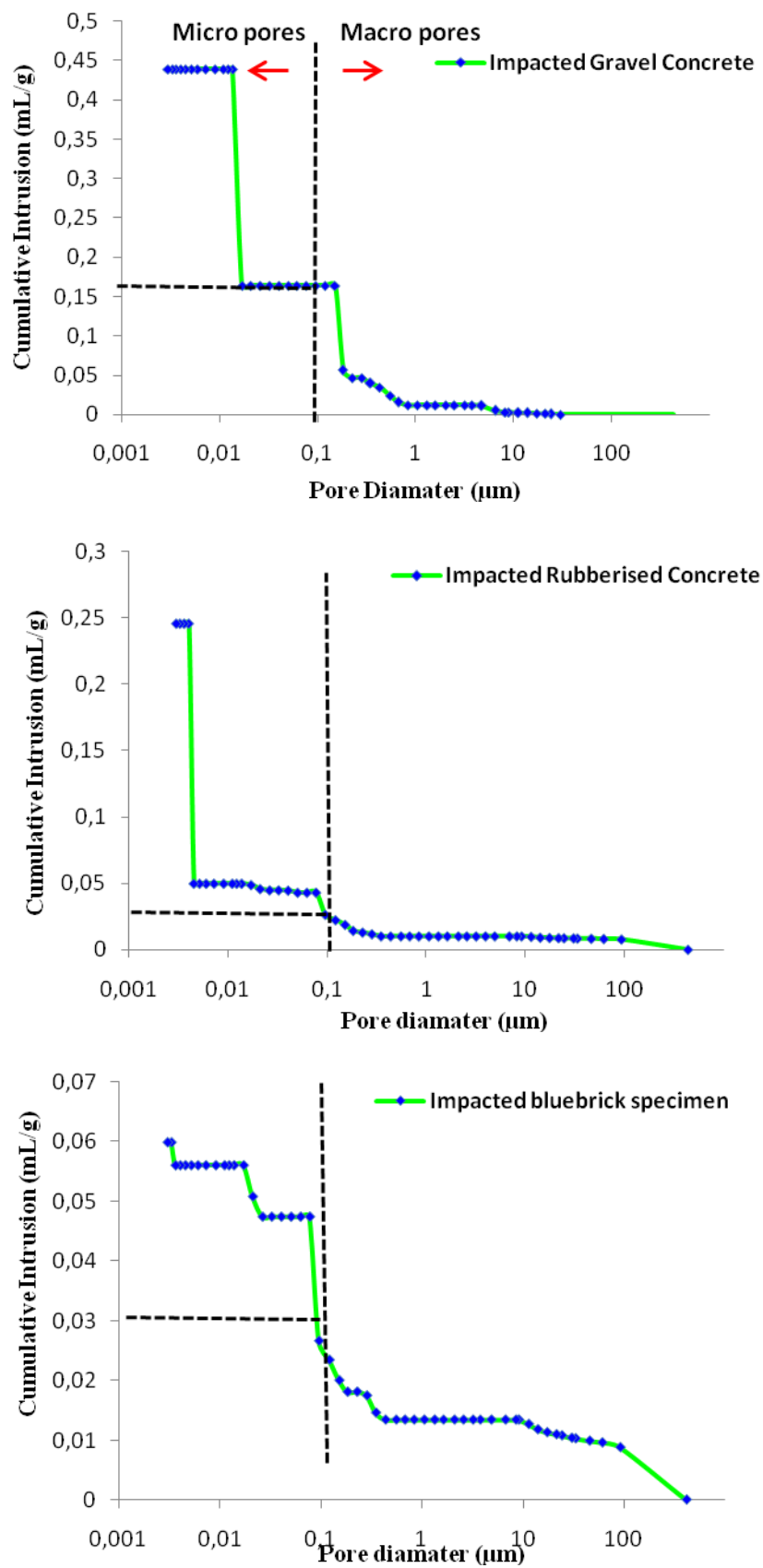


Fig.7.16: Cumulative intrusion volume against pore diameter curves after impact

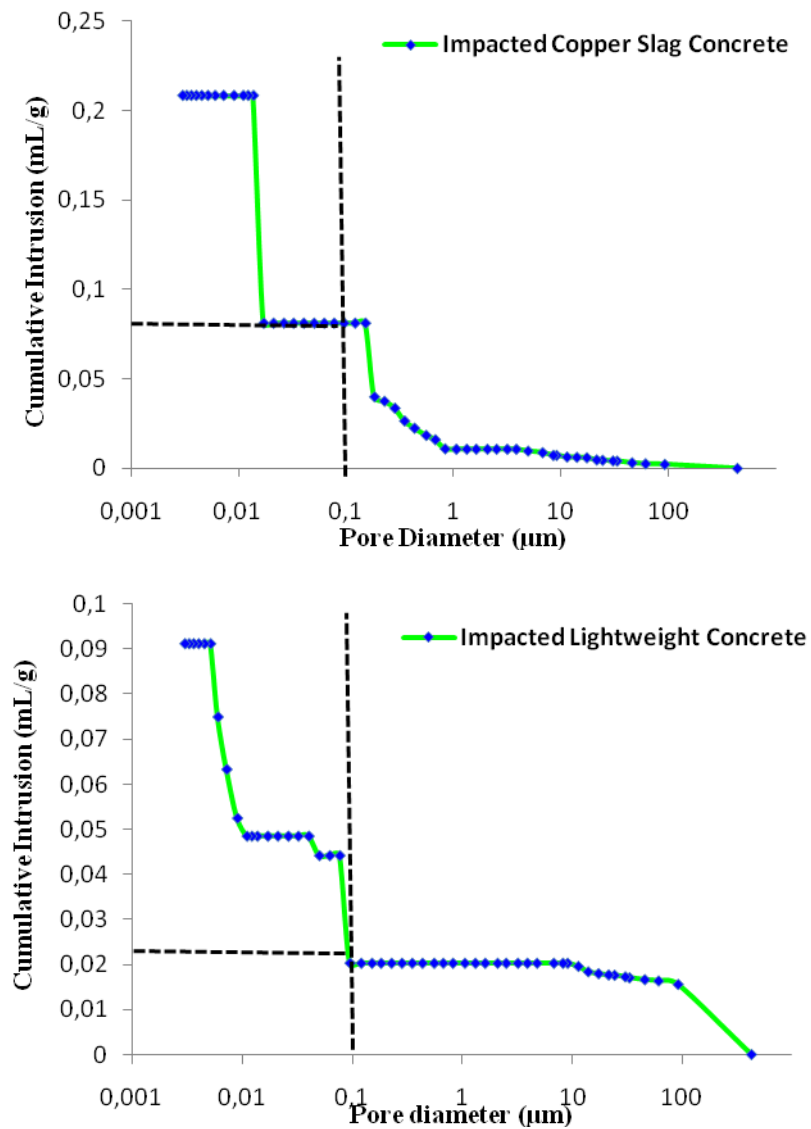


Fig.7.16 continued: Cumulative intrusion volume against pore diameter curves after impact

Table 7.2 The calculated percentage of the micro and macro pores after impact

Specimen ID	Micro pores (%)	Macro pores (%)	Critical diameter (μm)
Gravel mortar	62.40	37.60	0.020
Copper slag mortar	61.60	38.40	0.020
Rubberised mortar	89.80	10.20	0.007
Lightweight mortar	78.10	21.90	0.006
Blue brick mortar	56.60	43.40	0.090

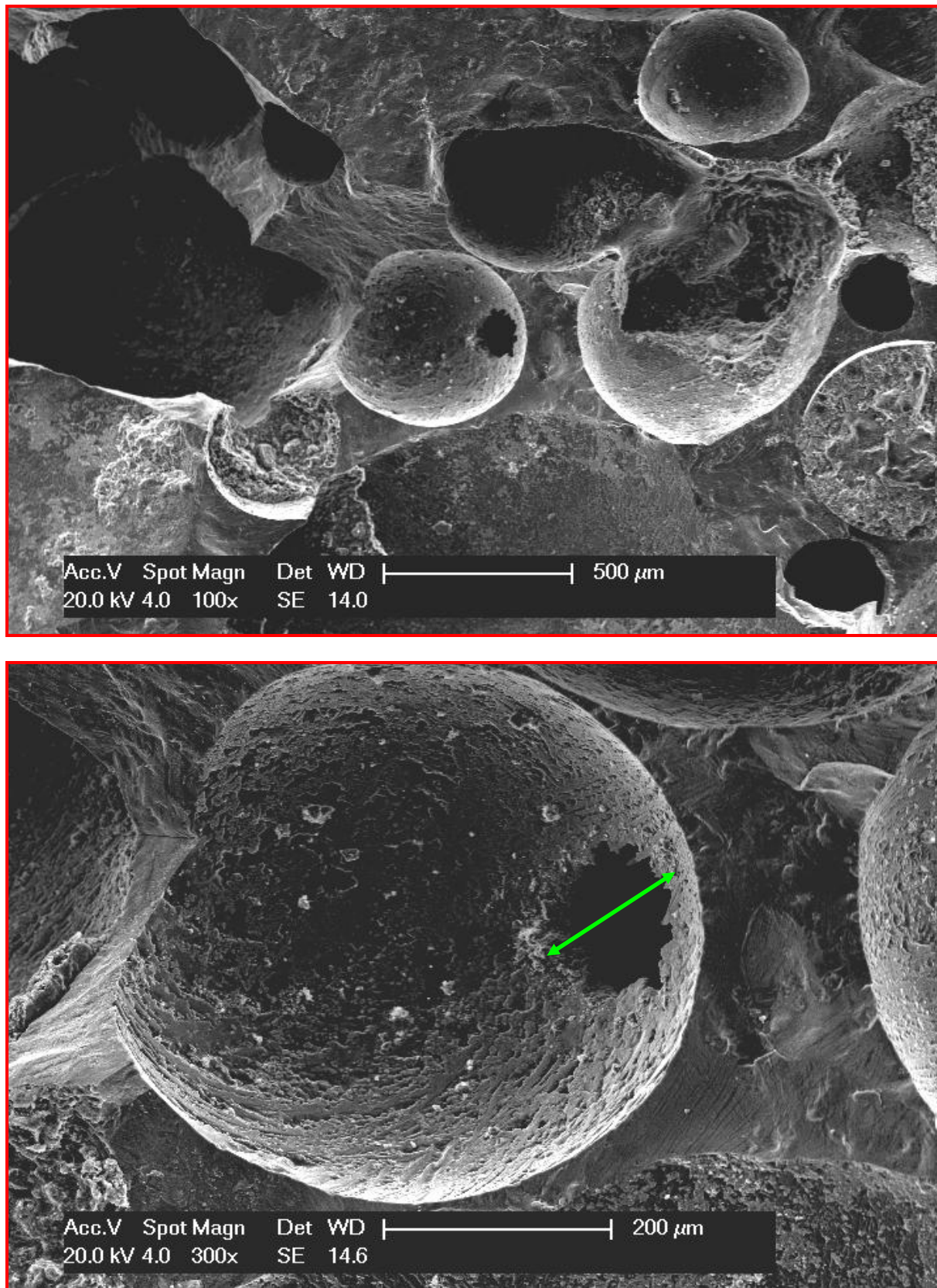


Fig.7.17: (a) Low-resolution image of air voids and (b) high-resolution images of air void showing connectivity in air-void layer

7.6 Concluding Remarks

Based on the correlations obtained, it can be concluded that:

- The analysis suggests that the aggregate's principal effect is to cause a change in the initial ITZ condition and this condition, in turn, has the major effect on overall mix behaviour.
- In several of the figures, the data point belonging to the rubberised mix does not fit. The different relationships of the other four points on each graph tell us that the non-compressible aggregates behaved in a smaller manner.
- The compressive strength of concrete was shown to be a function of the ITZ micro-hardness and porosity.
- The changes in micro-hardness value and pore structure are demonstrated to provide a good basis on which to evaluate the deterioration of concrete subjected to impact loading.
- The impact resistance of concrete increases with increasing compressive strength. The concrete with rubber particles did not conform to this pattern and this may be attributable to the distinct compressible characteristics of the particles which resulted in the generation of greater fractal energy. In addition, if the flexural toughness energy is obtained, impact energy can be predicted.
- Surface macro-crack tortuosity and dissipated energy increases with increasing the ITZ roughness which is primarily a function of the aggregate characteristic.
- Secondary crack directions that may exist at the interface cracks are largely responsible for the high degree of surface tortuosity.
- Interface cracks and aggregate characteristics (in particular shape and strength) have a profound influence on the roughness topography of fracture surfaces.

- ITZ crack width refers to the width of individual minute crack that may appear in the vicinity of an aggregate particle. Cracking may occur in the mortar in the vicinity of the aggregate as a result of tensile stress arising from differential movement between the aggregate and the cement paste. ITZ porosity can be defined as the porosity of the mortar that invariably occupies a 30 - 50 μm band around the aggregate particle. The porosity of this zone is usually higher than the bulk mortar mainly because of what is described as type of 'wall effect'. Therefore ITZ cracking can be considered to be a subset of ITZ porosity when it exists and therefore could be measured by MIP.

References:

- [1] Abell, A.B., Willis, K.L., and Large, D.A., (1999). "Mercury intrusion porosimetry and image analysis of cement-based materials." *Journal of Colloid and Interface Science* 211(1) 39-44.
- [2] Acker, P., Boulay, C., and Rossi, P., (1987). "On the importance of initial stresses in concrete and of the resulting mechanical effects." *Cement and Concrete Research* 17 (1) 755-764.
- [3] Chiaia, B., Van Mier, J.G.M., and Vervuurt, A., (1998). "Crack growth mechanism in four different concretes: Microscopic observations and fractal analysis." *Cement and Concrete Research* 28 (1) 103-114.
- [4] Copuroglu, O., (2005). "The characterisation, improvement and modelling aspects of frost salt scaling of cement-based materials with high slag content." PhD Thesis. The Technical University of Delft, Netherlands.
- [5] Fedroff, D., Ahmad, S., and Savas, B.Z., (1996). "Mechanical properties of concrete with ground waste tire rubber." *Transport Research Record* 1532 (10) 66-72.
- [6] Gao, J.M., Qian, C.X., Liu, H.F., Wang, B., and Li, L., (2005). "ITZ microstructure of concrete containing ggbs." *Cement and Concrete Research* 35 (7) 1299-1304.
- [7] Guo, L.P., Sun, W., Zheng, K.R., Chen, H.J., and Liu, B., (2007). "Study on the flexural fatigue performance and fractal mechanism of concrete with high proportions of ground granulated blast-furnace slag." *Cement and Concrete Research* 37 (2) 242-250.
- [8] Hallett, P.D., Dexter, A.R., and Seville, J.P.K., (1995). "Identification of pre-existing cracks on soil-fracture surfaces using dye." *Soil Tillage Research* 33(3-4) 163-184.
- [9] Katsagana, T., (2010). "Geophysical imaging and numerical modelling of fractures in concrete." PhD Thesis. University of Toronto, Canada.

- [10] Lee, H.K., Kim, H.K., and Hwang, E.A., (2010). "Utilization of power plant bottom ash aggregates in fibre-reinforced cellular concrete." *Waste Management* 30 (2) 274-284.
- [11] Mindess, S., Igarashi, S., and Bentur, A., (1998). "Characterization of cementitious materials using micro-hardness testing." *International RILEM conference on concrete: from Material to Structure*, Edits: Bournazel, J.P., and Malier, Y., RILEM Publications SARL, Airles-France.
- [12] Neville, A.M. (1996). "Properties of Concrete." (4th edn. ed.), Wiley, New York, USA.
- [13] Scrivener, K.L., Crumbie, A.K., and Laugesen, P., (2004). "The interfacial transition zone (ITZ) between cement paste and aggregate in concrete." *Interface Science* 12 (4) 411-421.
- [14] Van Mier, J.G.M., (1997). "Fracture processes of concrete." CRC Press, New York.
- [15] Wu, K., Yan, A., Yao, W., and Zhang, D., (2001). "Effect of metallic aggregate on strength and fracture properties of HPC." *Cement and Concrete Research* 31 (1) 113-118.
- [16] Ye, G., (2003). "Numerical simulation of the development of the microstructure, porosity and permeability of cement-based materials." PhD Thesis. Technical University of Delft, Netherlands.

CHAPTER 8

CONCLUSIONS AND SUGGESTIONS FOR FUTURE RESEARCH

8.1 Introduction

Understanding the correlation between the mix proportions, micro structural characteristics, and macro-scale properties of concrete (i.e. the process-structure-properties relationship) is fundamental to achieving a more advanced understanding of how to apply and optimise this abundant engineering material. Due to the recently elevated threat of terrorist attacks around the world, one of the macro-level properties of concrete which has been the subject of growing interest is its impact resistance. While significant efforts have been made to analyze the impact resistance of concrete, the behaviour of concrete under a high-strain rate of loading has still not been fully understood, e.g. the micro-structural origins of strength are complex and not fully understood. This research was intended to make a quantitative assessment of impact load-induced micro-structural damage in concrete and, more particularly, to investigate the influence of ITZ local properties (as influenced by aggregate characteristics) on the impact load-induced cracking behaviour of concrete.

8.2 Main conclusions

Several parameters determine the local properties of the ITZ and the formation of micro-structural damage. The relative strength and stiffness of the aggregate and the paste matrix significantly influence the micro-structural damage features of concrete under impact loading. A number of other parameters, such as the thickness and roughness of the ITZ, the variations in the porosity of the aggregate, and particle shape also have an effect. Similarly, strength depends also on the physical-chemical interactions taking place between the ITZ and the aggregate.

Based on the results obtained, a possible mechanism for micro-structural damage in concrete has been proposed. The surface roughness, strength, stiffness and mineral composition of the aggregate are responsible for ITZ deterioration after loading, but the results indicate that the aggregate's principal effect is to cause a change in the structure of the ITZ.

One effect of the aggregate on the resulting damage after loading is seen in the change in the ITZ porosity which is manifested in the level of pore connectivity. This effect was shown in work done by other researchers on fracture analyses of concrete subject to compressive loading and it is now confirmed that this effect is also prevalent in concrete subject to impact loading. Additionally, this research work also determined the characteristic that accounts for this type of change. From quantitative analysis, it is shown that aggregates with low surface roughness increased the regional porosity which resulted in a reduction in the pore connectivity and aggregate with high surface roughness produced an opposite effect. Further, it was realized that these changes helped to control the moduli of elasticity at the micro-level, in that thicker ITZ resulted in a reduction of the modulus of elasticity and vice versa.

Another effect of the aggregate is the influence of its shape and chemical composition on the unhydrated and hydrated constituents of the cement. It is postulated that the shape and composition of aggregate particles have an effect on the structure of the hydration products in the early stages of hydration and it is now shown that these features of the aggregate also impact on the structure of cementitious constituents after impact loading. The different types of aggregate produced unique changes that resulted from disturbances in the packing of the coarse and fine hydrated products and in the unhydrated cement particles. This was evident in the peaks and troughs of strength across the length of the aggregate-particle boundary.

Finally, the effect of the aggregate on the surface area roughness of the ITZ was established for the first time in the concrete literature. The roughness number of the area near the ITZ was found to positively correlate with dissipated surface fracture energy. An increase in the roughness number is associated with an increase in the dissipated fracture energy. As it is shown that the level of surface fracture energy depends on the type of aggregate, it can be concluded, with the exception of rubber, that as the aggregate changes from smooth and rounded (as in gravel) and more to rough and angular (as in copper slag and blue brick) there is a corresponding increase in roughness in the vicinity of the ITZ. The concrete with rubber particles did not conform to this pattern and this may be attributable to the distinct compressible characteristics of the particles which resulted in the generation of greater fractal energy. The significance of this correlation however, lies in the fact that the rougher near – ITZ fraction of the bulk paste is more resistant to cracking at the macro level.

It is also possible to conclude that the presence of a weak and porous ITZ has two opposite effects on the failure process. First, the chemical and porosity heterogeneities within the ITZ can cause fluctuations/disordering in the cracking (fracture) path, resulting in an increase in

the tortuosity and corresponding fracture energy dissipation. Second, a weak and porous ITZ transfers less stress from the matrix to the aggregate particles. This leads to a lower compressive strength but increased toughness due to micro crack path lengthening and energy dissipation. One can now conclude that the macro-scale strength decrease is a result of an increase in the porosity at the boundary of the aggregate-matrix interface and a decrease in the percolation of solids due to a partial absence of adequate CSH gels in the ITZ. Similarly, it can be concluded that the relatively isotropic distribution of pores at the interface would contribute to localized micro-damage in concrete under high rates of loading.

8.3 Suggestions for Future Research

























According to the review of current and recent research, and the findings obtained from this research project, suggestions for further research should address the following items:

- ✓ Concrete made with Recycled Concrete Aggregate (RCA) has two ITZs; i) the ITZ between the original aggregate and the adhesive mortar, and ii) the ITZ between the adhesive mortar and the new mortar matrix. In this respect, work is needed to better understand the more complex microstructure of RCA and its behaviour when exposed to impact loading. A multi-scale approach, combining 3D laser scanning confocal microscopy and SEM coupled with EDX micro analysis, might be employed to achieve this.
- ✓ The micro-structural data obtained using SEM and X-ray CT during impact and mechanical testing of the concrete mixtures could be used to develop a micro-mechanical model to simulate and predict 3D behaviour and fracture damage of concrete subjected to dynamic loading. The developed model could also be used to enhance the existing damage models of concrete for different load conditions.

- ✓ In a future research study, the load-deformation response and thus the elastic moduli of the ITZ should be determined using nano-indentation techniques. Its influence on the impact load-induced micro-damage process of concrete made with unconventional aggregates can then be studied.
- ✓ In this research, a number of crack features were quantitatively analyzed as damage indicators. However, further analysis could be carried out to characterize numerically the geometrical aspects of the cracks, such as the degree of orientation and branching, using stereological analysis. Crack velocities could also be measured using a high-speed video camera system. This would assist in developing a better understanding of the damage process in concrete under high-strain rates of loading.
- ✓ As a result of recently elevated and changing terror threats around the world, studies on concrete when subjected to high temperatures would be useful. The residual impact performance and microstructure of concrete produced with different types of alternative aggregates and fibres could be studied in such conditions. The thermogravimetric analyzer, mercury porosimetry and scanning electron microscopy techniques could be applied, for a more in-depth understanding of the degeneration process.
- ✓ In this study, the constituents of paste in the mixes were not changed, but changes in the paste were observed as a consequence of aggregate interaction. On this basis, further work could be done to determine the optimum paste that will yield the desired outcome.

APPENDIXES

The list below describes the Appendixes to this thesis. The relevant appendixes that may represent cumbersome amount of data but may be used in a future work in addition to a further understanding of the work carried out were included in a CD.

	Description	Copy Format	File Type
Appendix A	Rosand drop-weight impact data of the mixes		
Appendix B	Aggregate surface roughness data		 
Appendix C	MIP data for the aggregates and mortars		
Appendix D	X-ray CT and other microscopic images of the mixes		  
Appendix E	ITZ surface roughness data		  
Appendix F	Experimental test photos		 
Appendix G	Thermogravimetric analysis data of the mortars		
Appendix H	Flexural load-deformation response data		
Appendix I	Published journal and conference papers		
Appendix K	XRD original data of some mixes	